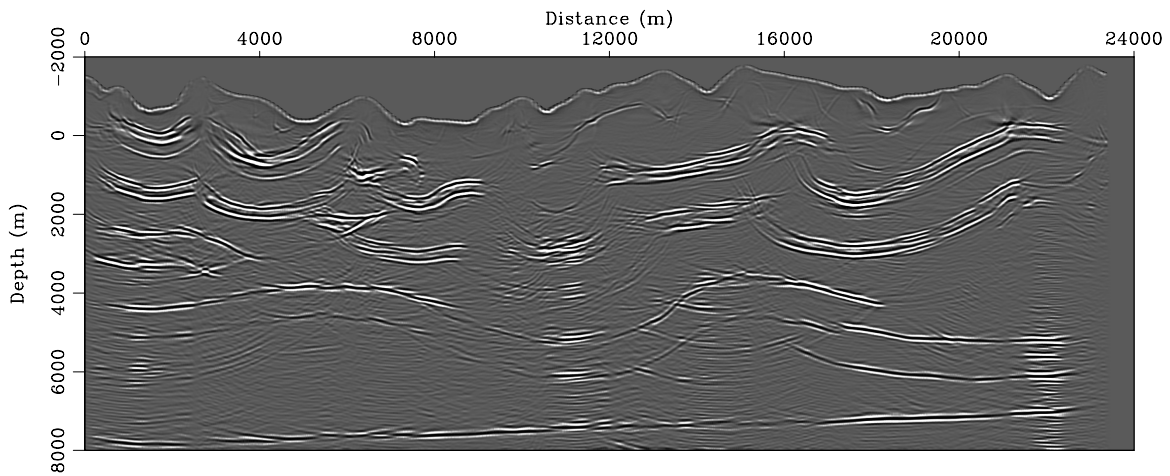
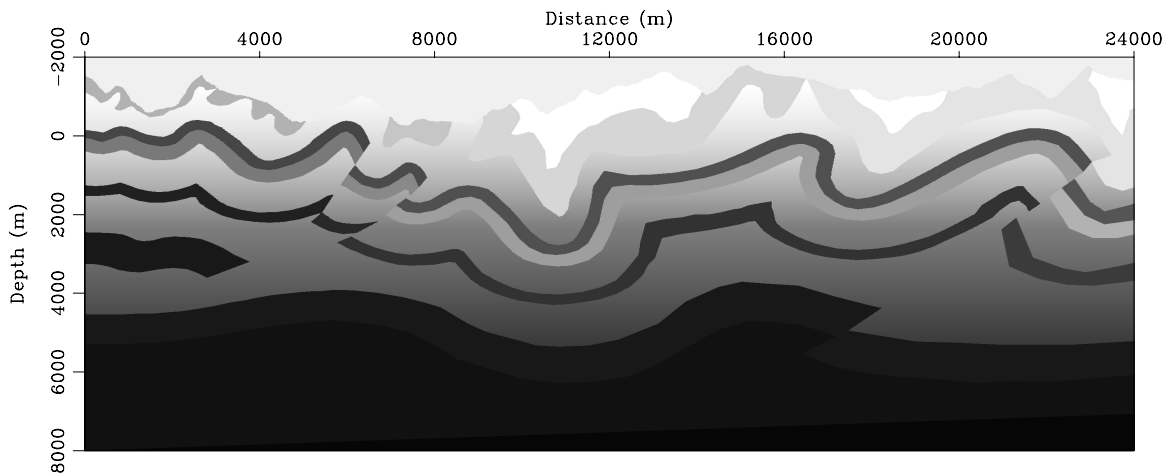


STANFORD EXPLORATION PROJECT

*James Berryman, Biondo Biondi, Robert Clapp, Marie Clapp, William Curry,
Antoine Guitton, Chris Liner, Jesse Lomask, Daniel Rosales, Paul Sava, Guojian Shan,
Jeff Shragge, Alejandro Valenciano, Ioan Vlad, and Charles Wilson*

Report Number 117, October 2004



Copyright © 2004

by the Board of Trustees of the Leland Stanford Junior University

Stanford, California 94305

*Copying permitted for all internal purposes of the Sponsors of
Stanford Exploration Project*

Preface

The electronic version of this report¹ makes the included programs and applications available to the reader. The markings [ER], [CR], and [NR] are promises by the author about the reproducibility of each figure result. Reproducibility is a way of organizing computational research that allows both the author and the reader of a publication to verify the reported results. Reproducibility facilitates the transfer of knowledge within SEP and between SEP and its sponsors.

ER denotes Easily Reproducible and are the results of processing described in the paper. The author claims that you can reproduce such a figure from the programs, parameters, and makefiles included in the electronic document. The data must either be included in the electronic distribution, be easily available to all researchers (e.g., SEG-EAGE data sets), or be available in the SEP data library². We assume you have a UNIX workstation with Fortran, Fortran90, C, X-Windows system and the software downloadable from our website (SEP makerules, SEPlib, and the SEP latex package), or other free software such as SU. Before the publication of the electronic document, someone other than the author tests the author's claim by destroying and rebuilding all ER figures. Some ER figures may not be reproducible by outsiders because they depend on data sets that are too large to distribute, or data that we do not have permission to redistribute but are in the SEP data library.

CR denotes Conditional Reproducibility. The author certifies that the commands are in place to reproduce the figure if certain resources are available. SEP staff have only attempted to make sure that the makefile rules exist and the source codes referenced are provided. The primary reasons for the CR designation is that the processing requires 20 minutes or more, or commercial packages such as Matlab or Mathematica.

M denotes a figure that may be viewed as a movie in the web version of the report. A movie may be either ER or CR.

NR denotes Non-Reproducible figures. SEP discourages authors from flagging their figures as NR except for figures that are used solely for motivation, comparison, or illustration of the theory, such as: artist drawings, scannings, or figures taken from SEP reports not by the authors or from non-SEP publications.

Our testing is currently limited to LINUX 2.4 (using the Portland Group Fortran90 compiler), but the code should be portable to other architectures. Reader's suggestions are welcome. For more information on reproducing SEP's electronic documents, please visit

<<http://sepwww.stanford.edu/research/redoc/>>.

¹<http://sepwww.stanford.edu/private/docs/sep117>

²http://sepwww.stanford.edu/public/docs/sepdatalib/toc_html/

SEP-117 — TABLE OF CONTENTS

Wavefield Extrapolation Imaging

<i>Shan G. and Biondi B.</i> , Wavefield extrapolation in laterally-varying tilted TI media	1
<i>Sava P.</i> , High-order kernels for Riemannian wavefield extrapolation	11
<i>Shragge J. and Sava P.</i> , Incorporating topography into wave-equation imaging through conformal mapping	27

Inversion and Optimization

<i>Clapp M. L.</i> , Regularized inversion for imaging: Effect on the data space	43
<i>Guitten A.</i> , Bound constrained optimization: Application to the dip estimation problem . . .	51
<i>Valenciano A. A. and Biondi B.</i> , Target-oriented computation of the wave-equation imaging Hessian	63

Velocity Analysis

<i>Clapp R. G.</i> , Velocity uncertainty: Non-linearity and the starting guess	77
<i>Clapp R. G. and Wilson C. K.</i> , The effect of model covariance description on global seismology tomography problems	89
<i>Vlad I.</i> , The influence of multiples and imaging approximations on focusing-effect AVA detection and removal	95
<i>Rosales D. A.</i> , An educated guess on the V_p/V_s ratio	105

Multiples

<i>Rosales D. A. and Sava P.</i> , Multiple suppression in the image space: A Mahogany field example	113
<i>Liner C. and Vlad I.</i> , Analytical traveltimes for arbitrary multiples in constant velocity . . .	121

Interpolation

<i>Lomask J.</i> , Estimating a 2D stationary PEF on sparse data	129
--	-----

<i>Curry W.</i> , Midpoint-offset vs. source-receiver coordinates for PEF-based interpolation	141
---	-----

Rock Properties Estimation

<i>Berryman J. G.</i> , Bounds on transport coefficients of porous media	151
<i>Berryman J. G.</i> , Bounds on geomechanical constants for a model of heterogeneous reservoirs	159

Cluster Computing

<i>Clapp R. G.</i> , Fault tolerant parallel SEPlib	175
<i>Clapp R. G.</i> , A Python solver for out-of-core, fault tolerant inversion	183

3-D Seismic Imaging

<i>Biondi B.</i> , Chapter 7 – Efficient wavefield-continuation methods for prestack migration . . .	191
<i>Biondi B.</i> , Chapter 12 – Migration Velocity Analysis by wavefield methods	221

SEP article published or in press, 2003-04	259
SEP phone directory	263
Research personnel	265
SEP sponsors for 2003-04	271

Wavefield extrapolation in laterally-varying tilted TI media

Guojian Shan and Biondo Biondi¹

ABSTRACT

A new wavefield extrapolation method has been developed that allows the propagation of waves in an anisotropic medium. The anisotropic medium considered here is transversely isotropic (TI) with an axis of symmetry. Our method applies an asymmetric explicit correction filter after the normal isotropic extrapolation operator. It is stable and suitable for laterally varying TI media. This new scheme is useful to extrapolate wavefields in a vertical transversely isotropic (VTI) medium in tilted coordinates. The explicit correction operator, designed by a weighted least-square method, is stable and accurate for the desired wavenumbers. Impulse responses from this scheme and the anisotropic phase-shift method are compared to illustrate the algorithm.

INTRODUCTION

Anisotropy has been shown to exist in many sedimentary rocks (Thomsen, 1986). If it is neglected in wavefield-extrapolation operators, reflectors in the subsurface, especially steeply dipping reflectors, will be mispositioned. Most sedimentary rocks can be approximated by a transversely isotropic medium with a symmetry axis. The symmetry axis can be vertical or tilted, and the corresponding media are called VTI or tilted TI media, respectively.

Although Kirchhoff migration can incorporate anisotropy into migration, it fails to handle the multi-pathing problem. Wave-equation-based methods are able to handle the multi-pathing problem and image the complicated subsurface structure. However, it is still challenging to image steeply dipping reflectors in the subsurface, such as a salt flank. Wavefield extrapolation in tilted coordinates (Etgen, 2002; Shan and Biondi, 2004) is useful for these steeply dipping reflectors. The energy related to these steeply dipping reflectors propagates almost horizontally and is greatly affected by the anisotropy of the sediment. In tilted coordinates, VTI media become tilted TI media in the extrapolation direction. It is useful therefore to develop a wavefield-extrapolation scheme for tilted TI media.

During the last decade, methods have been developed to incorporate anisotropy into wavefield extrapolation in TI media. As with isotropic extrapolation operators, anisotropic extrapolation operators include the implicit method (Ristow and Ruhl, 1997), phase-shift-plus-interpolation (PSPI) (Rousseau, 1997), non-stationary phase-shift (Ferguson and Margrave, 1998), explicit operator (Uzcategui, 1995; Zhang et al., 2001a,b), and reference anisotropic

¹email: shan@sep.stanford.edu, biondo@sep.stanford.edu

phase-shift with an explicit correction filter (Baumstein and Anderson, 2003).

In this paper, we incorporate anisotropy into wavefield extrapolation by adding an explicit anisotropic correction operator to the normal isotropic extrapolation operator. This new extrapolation scheme is capable of propagating waves in an anisotropic, heterogeneous medium with strong lateral variation. The explicit correction operator is designed by weighted, least-squares fitting to the true anisotropic phase-shift operator in the wavenumber domain (Thorbecke, 1997). In our method, we handle the lateral velocity variation by using a mixed-domain isotropic operator and the lateral anisotropic parameter variation by using explicit correction operator. At each depth level, we don't need to run the explicit correction operator for isotropic points. Therefore, it is efficient for a medium with both isotropic and anisotropic points. Furthermore, it is useful for VTI media with tilted coordinates where for each depth level most points are isotropic.

ANISOTROPIC PHASE-SHIFT IN TILTED TI MEDIA

In a VTI media, the phase velocity of qP- and qSV-waves in Thomsen's notation can be expressed as (Tsvankin, 1996):

$$\frac{V^2(\theta)}{V_{P0}^2} = 1 + \varepsilon \sin^2(\theta) - \frac{f}{2} \pm \frac{f}{2} \sqrt{\left(1 + \frac{2\varepsilon \sin^2(\theta)}{f}\right)^2 - \frac{2(\varepsilon - \delta) \sin^2(2\theta)}{f}}, \quad (1)$$

where θ is the phase angle of the propagating wave, and $f = 1 - (V_{S0}/V_{P0})^2$. V_{P0} and V_{S0} are the qP- and qSV- wave velocities in the vertical direction, respectively. ε and δ are anisotropy parameters defined by Thomsen (1986):

$$\varepsilon = \frac{C_{11} - C_{33}}{2C_{33}}, \delta = \frac{(C_{11} + C_{44})^2 - (C_{33} - C_{44})^2}{2C_{33}(C_{33} - C_{44})},$$

where C_{ij} are elastic moduli. In equation (1), $V(\theta)$ is the qP-wave phase-velocity when the sign in front of the square root is positive, and the qSV-wave phase velocity for a negative sign.

If we rotate the symmetry axis from vertical to a tilted angle φ , we obtain the phase velocity of a tilted TI medium whose symmetry axis forms an angle φ with the vertical direction:

$$\frac{V^2(\theta, \varphi)}{V_{P0}^2} = 1 + \varepsilon \sin^2(\theta - \varphi) - \frac{f}{2} \pm \frac{f}{2} \sqrt{\left(1 + \frac{2\varepsilon \sin^2(\theta - \varphi)}{f}\right)^2 - \frac{2(\varepsilon - \delta) \sin^2 2(\theta - \varphi)}{f}}. \quad (2)$$

Here, in contrast to equation (1), ε and δ are now defined in a direction tilted by the angle φ from the vertical direction. V_{P0} is the qP-wave velocity in the direction parallel to the symmetry axis.

For plane-wave propagation, the phase angle θ is related to the wavenumbers k_x and k_z by:

$$\sin \theta = \frac{V(\theta, \varphi)k_x}{\omega}, \quad \cos \theta = \frac{V(\theta, \varphi)k_z}{\omega}, \quad (3)$$

where ω is the temporal frequency. Squaring equation (2) and substituting (3) into (2), we can obtain a dispersion relation equation:

$$d_4 k_z^4 + d_3 k_z^3 + d_2 k_z^2 + d_1 k_z + d_0 = 0, \quad (4)$$

where the coefficients d_0, d_1, d_2, d_3 , and d_4 are as follows:

$$\begin{aligned} d_0 &= (2 + 2\varepsilon \cos^2 \varphi - f) \left(\frac{\omega}{V_{P0}} \right)^2 k_x^2 - \left(\frac{\omega}{V_{P0}} \right)^4 - \left[(1 - f)(1 + 2\varepsilon \cos^2 \varphi) + \frac{f}{2}(\varepsilon - \delta) \sin^2 2\varphi \right] k_x^4, \\ d_1 &= [2\varepsilon(1 - f) \sin 2\varphi - f(\varepsilon - \delta) \sin 4\varphi] k_x^3 - \left(\frac{\omega}{V_{P0}} \right)^2 2\varepsilon \sin 2\varphi k_x, \\ d_2 &= [f(\varepsilon - \delta) \sin^2 2\varphi - 2(1 - f)(1 + \varepsilon) - 2f(\varepsilon - \delta) \cos^2 2\varphi] k_x^2 + \left(\frac{\omega}{V_{P0}} \right)^2 (2 + 2\varepsilon \sin^2 \varphi - f), \\ d_3 &= [f(\varepsilon - \delta) \sin 4\varphi + 2\varepsilon(1 - f) \sin 2\varphi] k_x, \\ d_4 &= f - 1 + 2\varepsilon(f - 1) \sin^2 \varphi - \frac{f}{2}(\varepsilon - \delta) \sin^2 2\varphi. \end{aligned}$$

The dispersion relation equation (4) is a quartic equation. It can be solved analytically (Abramowitz and Stegun, 1972) or numerically by Newton's Method (Stoer and Bulirsch, 1992). Equation (4) has four roots, which are related to up-going and down-going qP- and qSV- waves, respectively. For a medium without lateral change in the velocity V_{P0} and anisotropy parameters ε and δ , the wavefield can be extrapolated by the phase-shift method (Gazdag, 1978):

$$P(z + \Delta z) = P(z) e^{-ik_z^a \Delta z}, \quad (5)$$

where k_z^a is one of the roots of equation (4).

EXTRAPOLATION OPERATOR IN Laterally Varying Media

The phase-shift method is effective, but it is not suitable for a strongly heterogeneous medium, where strong lateral changes are present in velocity as well as in the anisotropy parameters, ε and δ . This can be remedied by PSPI (Rousseau, 1997), explicit operator (Zhang et al., 2001a), or reference anisotropic phase-shift with an explicit correction filter (Baumstein and Anderson, 2003).

In this paper, we use an explicit anisotropic correction filter in addition to the normal isotropic operator. For each z step, we first regard the medium as an isotropic medium and extrapolate the wavefield using an isotropic operator with the velocity in the direction parallel to the symmetry axis. The isotropic operator can be the split-step method (Stoffa et al., 1990), the general screen propagator (Huang and Wu, 1996), or Fourier finite difference (FFD) (Ristow and Ruhl, 1994). Then we correct the wavefield with an explicit correction operator.

After we extrapolate the wavefield with an isotropic operator, the resulting error relative to anisotropic extrapolation is:

$$F(k_x) = e^{i\Delta z \Delta \phi(k_x)}, \quad (6)$$

where $\Delta\phi(k_x)$ is the difference between the isotropic wavenumber, k_z^i , and the anisotropic wavenumber, k_z^a , that satisfies

$$\Delta\phi(k_x) = k_z^a(V_{P0}, \delta, \varepsilon, \varphi) - k_z^i(V_{P0}), \quad (7)$$

where,

$$k_z^i(V_{P0}) = \pm \sqrt{\left(\frac{\omega}{V_{P0}}\right)^2 - k_x^2},$$

and k_z^a is one of the four roots of the dispersion-relation equation (4). We design the explicit correction operator by weighted least squares. The obtained explicit operator is approximately the same as $F(k_x)$ in the wavenumber domain for desired wavenumbers.

EXPLICIT CORRECTION OPERATOR

Explicit extrapolation operators have been proved useful in isotropic wavefield extrapolation (Holberg, 1988; Blacquiere et al., 1989; Hale, 1991b,a; Thorbecke, 1997). They are also applied in wavefield extrapolation for TI media (Zhang et al., 2001a). For an isotropic or VTI medium, the extrapolation operator is symmetric and can be approximated by a cosine function series. For a tilted TI medium, k_z is not an even function of k_x , and the extrapolation operator is asymmetric. Thus, we need both the sine and cosine function series to approximate the correction operator in the wavenumber domain. In equation (6), $F(k_x)$ is not an even function, but can be divided $F(k_x)$ into two parts: even function $F^e(k_x)$ and odd function $F^o(k_x)$,

$$F^e(k_x) = \frac{1}{2}(F(k_x) + F(-k_x)), \quad (8)$$

$$F^o(k_x) = \frac{1}{2}(F(k_x) - F(-k_x)). \quad (9)$$

To design the explicit correction operator, we specify $F^e(k_x)$ in the form

$$F^e(k_x) = \sum_{n=0}^N a_n \cos(n \Delta x k_x), \quad (10)$$

and $F^o(k_x)$ in the form

$$F^o(k_x) = \sum_{n=1}^N b_n \sin(n \Delta x k_x), \quad (11)$$

where a_n, b_n are complex coefficients. These coefficients can be determined by the following weighted least-squares fitting goals:

$$\mathbf{W}(\mathbf{Aa} - \mathbf{f}^e) \approx \mathbf{0}, \quad (12)$$

$$\mathbf{W}(\mathbf{B}\mathbf{b} - \mathbf{f}^o) \approx \mathbf{0}, \quad (13)$$

where

$$\mathbf{a} = (a_0, a_1, \dots, a_N)^T,$$

$$\mathbf{b} = (b_1, b_2, \dots, b_N)^T.$$

\mathbf{A} is an $(M+1) \times (N+1)$ matrix with elements $A_{mn} = \cos(mn\Delta k_x \Delta x)$, $m = 0, 1, 2, \dots, M$, and $n = 0, 1, 2, \dots, N$. \mathbf{B} is an $M \times N$ matrix with elements $B_{mn} = \sin(mn\Delta k_x \Delta x)$, $m = 1, 2, \dots, M$, and $n = 1, 2, \dots, N$. \mathbf{f}^e is a vector with elements $F^e(m\Delta k_x)$, $m = 0, 1, 2, \dots, M$. \mathbf{f}^o is a vector with elements $F^o(m\Delta k_x)$, $m = 1, 2, \dots, M$. \mathbf{W} is a diagonal matrix with proper weights for the wavenumber k_x . One way to solve the fitting goal (12) is to do QR decomposition (Golub and Van Loan, 1996) of the matrix \mathbf{WA} : $\mathbf{WA} = \mathbf{QR}$, where \mathbf{Q} is an orthogonal matrix and \mathbf{R} is an upper triangular matrix. Then the coefficient vector \mathbf{a} is given by

$$\mathbf{a} = \mathbf{R}^{-1}\mathbf{Q}^T\mathbf{W}\mathbf{f}^e. \quad (14)$$

We can solve the fitting goal in equation (13) and obtain the coefficient vector \mathbf{b} in the same way. After we have the coefficient vectors \mathbf{a} and \mathbf{b} , we can combine them into the coefficients for the explicit correction operator. From Fourier transform theory, it is well known that the inverse Fourier transform of the function $\cos(n\Delta x k_x)$ and $\sin(n\Delta x k_x)$ are:

$$\mathcal{F}^{-1}\{\cos(n\Delta x k_x)\} = \frac{1}{2}(\delta(x - n\Delta x) + \delta(x + n\Delta x)), \quad (15)$$

$$\mathcal{F}^{-1}\{\sin(n\Delta x k_x)\} = \frac{1}{2i}(\delta(x - n\Delta x) - \delta(x + n\Delta x)). \quad (16)$$

Thus, the inverse Fourier transform of the function $a_n \cos(n\Delta x k_x) + b_n \sin(n\Delta x k_x)$ is

$$\mathcal{F}^{-1}\{a_n \cos(n\Delta x k_x) + b_n \sin(n\Delta x k_x)\} = \frac{1}{2}(a_n + ib_n)\delta(x - n\Delta x) + \frac{1}{2}(a_n - ib_n)\delta(x + n\Delta x).$$

Therefore, the explicit correction operator is:

$$(c_{-N}, c_{-(N-1)}, \dots, c_{-1}, c_0, c_1, \dots, c_{(N-1)}, c_N), \quad (17)$$

where $c_0 = a_0$, and

$$c_{-n} = \frac{1}{2}(a_n - ib_n), \quad n = 1, 2, \dots, N,$$

$$c_n = \frac{1}{2}(a_n + ib_n), \quad n = 1, 2, \dots, N.$$

In 3-D, based on the following trigonometric identity,

$$\cos(n\theta) = 2\cos(\theta)\cos[(n-1)\theta] - \cos[(n-2)\theta], \quad (18)$$

we can run McClellan transformations (McClellan and Parks, 1972; McClellan and Chan, 1977; Hale, 1991a) for the cosine terms. Similarly, based on the trigonometric identity:

$$\sin(n\theta) = 2\sin(\theta)\cos[(n-1)\theta] - \sin[(n-2)\theta], \quad (19)$$

we can design a recursive operator similar to McClellan transformations for the sine terms.

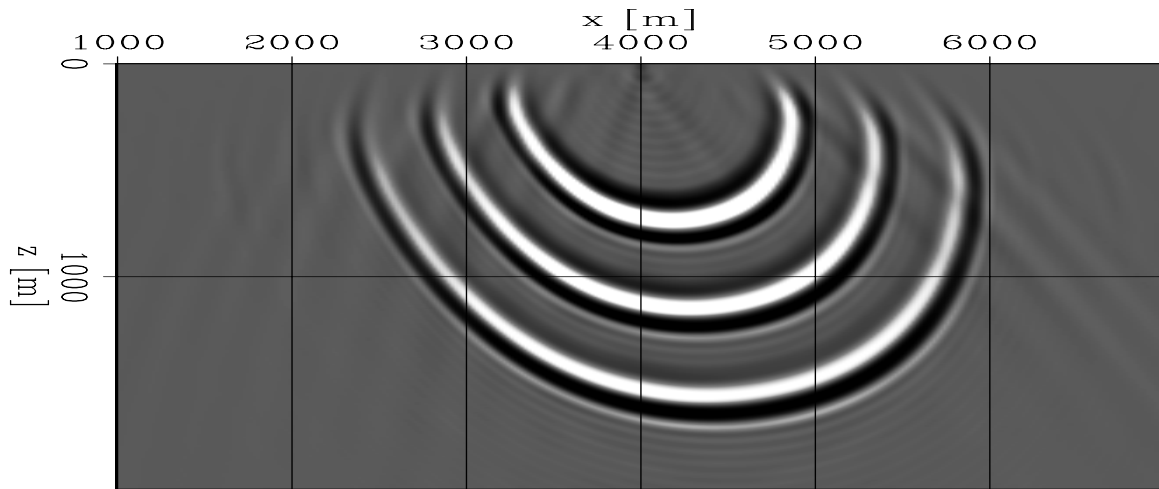


Figure 1: Impulse response of isotropic phase-shift with an anisotropic correction operator.
`guojian1-ico` [CR]

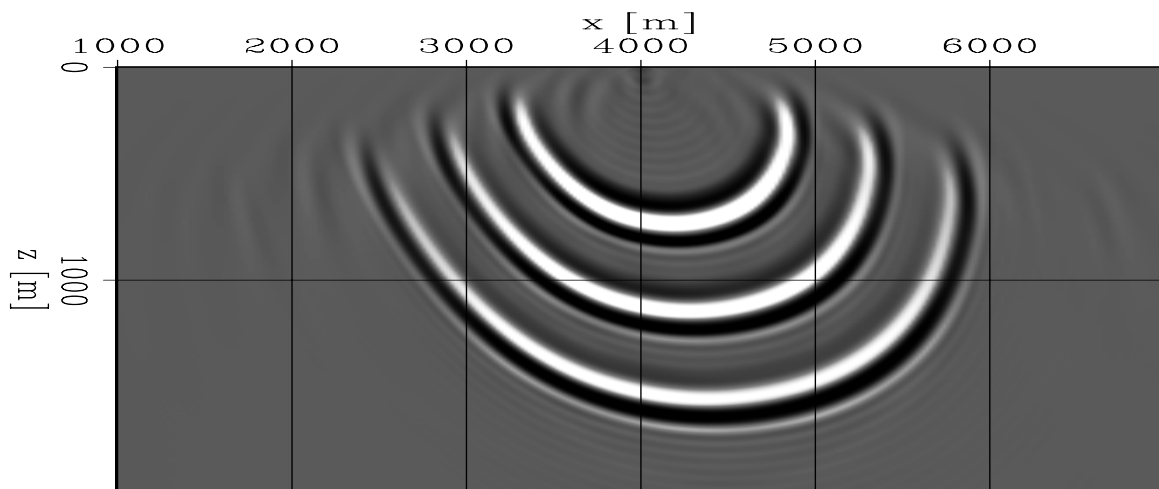


Figure 2: Impulse response of isotropic FFD with an anisotropic correction operator.
`guojian1-icoffd` [CR]

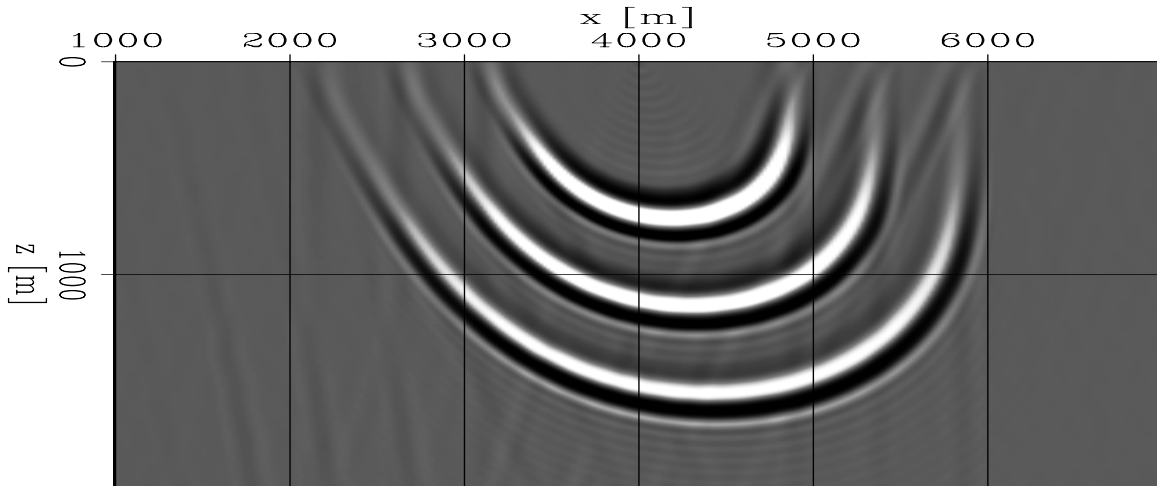


Figure 3: Impulse response of anisotropic phase-shift. `guojian1-phsift` [CR]

IMPULSE RESPONSE TESTS

The performance of an extrapolation operator can be verified by its impulse response. Figures 1-3 are the impulse responses of the qP-wave in the same medium using three different methods. The symmetry axis of the medium is tilted 30° from the vertical direction. The qP- and qSV-wave velocities in the direction parallel to the symmetry axis are 2000 m/s and 1100 m/s, respectively. The anisotropic parameters ε and δ are 0.4 and 0.2, respectively. The impulse location is at 4000 m.

Figure 1 is the impulse response of isotropic phase-shift with an anisotropic correction operator. Figure 2 is the impulse response of isotropic FFD with an anisotropic correction operator. The reference velocity for the FFD is 1500 m/s. We use 39 points for the explicit correction operator in Figures 1 and 2. Since the medium is homogeneous, we can also extrapolate the wavefield with anisotropic phase-shift (equation (5)). Figure 3 is the impulse response of anisotropic phase-shift. Comparing Figures 1, 2 and 3, the impulse response of the isotropic operator with an anisotropic correction operator is the same as that of the anisotropic phase-shift method for propagating angles up to almost 80° . It is different from anisotropic phase-shift for higher angles because the explicit correction operator is not same as the one for anisotropic phase-shift for wavenumbers close to the evanescent area.

CONCLUSION

We describe a new anisotropic wavefield-extrapolation scheme. This new scheme uses an explicit anisotropic correction filter in addition to the normal isotropic extrapolation operator. It can extrapolate wavefields in a laterally varying TI medium with a symmetry axis. It is effective since it uses only the normal isotropic extrapolation operator in isotropic regions. The comparison of impulse responses shows that the new scheme is accurate for angles to

almost 80° in a homogeneous medium. More work is needed to test the scheme on complicated models.

REFERENCES

- Abramowitz, M., and Stegun, I., 1972, Solutions of quartic equations *in* Handbook of Mathematical Functions with Formulas, Graphs, and Mathematical Tables. New York: Dover., 17–18.
- Baumstein, A., and Anderson, J., 2003, Wavefield extrapolation in laterally varying VTI media *in* 73rd Ann. Internat. Mtg. Soc. of Expl. Geophys., 945–948.
- Blacquiere, G., Debye, H. W. J., Wapenaar, C. P. A., and Berkhout, A. J., 1989, 3D table-driven migration: Geophys. Prosp., **37**, 925–958.
- Etgen, J., 2002, Waves, beams and dimensions: an illuminating if incoherent view of the future of migration: 72nd Ann. Internat. Mtg. Soc. of Expl. Geophys., invited presentation.
- Ferguson, R. J., and Margrave, G. F., 1998, Depth migration in TI media by nonstationary phase shift *in* 68th Ann. Internat. Mtg. Soc. of Expl. Geophys., 1831–1834.
- Gazdag, J., 1978, Wave equation migration with the phase-shift method: Geophysics, **43**, 1342–1351.
- Golub, G., and Van Loan, C., 1996 *in* Matrix computation(3rd ed.). Johns Hopkins University Press.
- Hale, D., 1991a, 3-D depth migration via McClellan transformations: Geophysics, **56**, 1778–1785.
- , 1991b, Stable explicit depth extrapolation of seismic wavefields: Geophysics, **56**, 1770–1777.
- Holberg, O., 1988, Towards optimum one-way wave propagation: Geophys. Prosp., **36**, 99–114.
- Huang, L. Y., and Wu, R. S., 1996, Prestack depth migration with acoustic screen propagators *in* 66th Ann. Internat. Mtg. Soc. of Expl. Geophys., 415–418.
- McClellan, J., and Chan, D., 1977, A 2-d fir filter structure derived from the chebychev recursion: IEEE Trans. Circuits Syst., **CAS-24**, 372–378.
- McClellan, J. H., and Parks, T. W., 1972, Equiripple approximation of fan filters: Geophysics, **37**, 573–583.

- Ristow, D., and Ruhl, T., 1994, Fourier finite-difference migration: *Geophysics*, **59**, 1882–1893.
- , 1997, Migration in transversely isotropic media using implicit operators *in* 67th Ann. Internat. Mtg. Soc. of Expl. Geophys., 1699–1702.
- Rousseau, J. H. L., 1997, Depth migration in heterogeneous, transversely isotropic media with the phase-shift-plus-interpolation method *in* 67th Ann. Internat. Mtg. Soc. of Expl. Geophys., 1703–1706.
- Shan, G., and Biondi, B., 2004, Imaging overturned waves by plane-wave migration in tilted coordinates: 74th Ann. Internat. Mtg., Soc. of Expl. Geophys., Expanded Abstracts.
- Stoer, J., and Bulirsch, R., 1992, The development of iterative methods *in* Introduction to numerical analysis (2nd ed.). Springer-Verlag., 261–264.
- Stoffa, P. L., Fokkema, J. T., de Luna Freire, R. M., and Kessinger, W. P., 1990, Split-step Fourier migration: *Geophysics*, **55**, 410–421.
- Thomsen, L., 1986, Weak elastic anisotropy: *Geophysics*, **51**, 1954–1966.
- Thorbecke, J., 1997, Common focus point technology *in* Ph.D. thesis. Delft University of Technology.
- Tsvankin, I., 1996, P-wave signatures and notation for transversely isotropic media: An overview: *Geophysics*, **61**, 467–483.
- Uzcategui, O., 1995, 2-D depth migration in transversely isotropic media using explicit operators: *Geophysics*, **60**, 1819–1829.
- Zhang, J., Verschuur, D. J., and Wapenaar, C. P. A., 2001a, Depth migration of shot records in heterogeneous, transversely isotropic media using optimum explicit operators: *Geophys. Prosp.*, **49**, 287–299.
- Zhang, J., Wapenaar, C., and Verschuur, D., 2001b, 3-D depth migration in VTI media with explicit extrapolation operators *in* 71st Ann. Internat. Mtg. Soc. of Expl. Geophys., 1085–1088.



High-order kernels for Riemannian wavefield extrapolation

*Paul Sava*¹

ABSTRACT

High-order kernels for Riemannian wavefield extrapolation (RWE) are developed and demonstrated by impulse responses for models which are difficult or impossible to handle with Cartesian downward continuation. Those kernels improve the accuracy of extrapolation, particularly for situations when the Riemannian coordinate systems does not match closely the general direction of wave propagation (e.g. triplicating wavefields and migration from topography).

INTRODUCTION

Riemannian wavefield extrapolation (Sava and Fomel, 2003) generalizes solutions to the Helmholtz equation in general Riemannian coordinate systems. The main requirements imposed on the Riemannian coordinate systems are that they maintain orthogonality between the extrapolation coordinate and the other coordinates (2 in 3D, 1 in 2D). In addition, it is desirable that the coordinate system does not triplicate, although numerical methods can stabilize extrapolation even in such situations. Thus, wavefield extrapolation in Riemannian coordinates has the flexibility to be used in many applications where those basic conditions are fulfilled. Cartesian coordinate systems, including tilted coordinates, are special cases of Riemannian coordinate systems. Two straightforward examples of wave propagation in Riemannian coordinates are extrapolation in a coordinate system created by ray tracing in a smooth background velocity (Sava and Fomel, 2003), and extrapolation with a coordinate system created by conformally mapping a given geometry to a regular space, for example migration from topography (Shragge and Sava, 2004).

Coordinate systems created by ray tracing in a background medium often well represent wavefield propagation. In this context, we effectively split wave propagation effects into two parts: one part accounting for the general trend of wave propagation, which is incorporated in the coordinate system, and the other part accounting for the details of wavefield scattering due to rapid velocity variations. If the background medium is close to the real one, the wave-propagation can be properly described with low-order operators. However, if the background medium is far from the true one, the wavefield departs from the general direction of the coordinate system and the low-order extrapolators are not enough for accurate description of wave propagation.

¹email: paul@sep.stanford.edu

For coordinate system describing a geometrical property of the medium (e.g. migration from topography), there is no guarantee that waves propagate in the direction of extrapolation. This situation is similar to that of Cartesian coordinates when waves propagate away from the vertical direction, except that conformal mapping gives us the flexibility to define any coordinates, as required by acquisition. In this case, too, low-order extrapolators are not enough for accurate description of wave propagation.

Therefore, we need to develop higher-order Riemannian wavefield extrapolators in order to handle correctly waves propagating obliquely with the coordinate system. Usually, the high-order extrapolators are implemented as mixed operators, part in the Fourier domain using a reference medium, part in the space domain as a correction from the reference medium. Many methods have been developed for high-order extrapolation in Cartesian coordinates. In this paper, I explore some of those extrapolators in Riemannian coordinates. In particular, I concentrate on high-order finite-differences solutions, and methods from the pseudo-screen family (Huang et al., 1999) and Fourier finite-differences family (Ristow and Ruhl, 1994; Biondi, 2002). In theory, any other high-order extrapolator developed in Cartesian coordinates can have a correspondent in Riemannian coordinates.

In this paper, I implement the finite-differences portion of the high-order extrapolators with implicit methods. Such solutions are accurate and robust, but they face difficulties for 3D implementations because the finite-differences part cannot be solved by fast tridiagonal solvers anymore and require more complex and costlier approaches (Fomel and Claerbout, 1997; Rickett et al., 1998). The problem of 3D wavefield extrapolation is addressed in Cartesian coordinates either by splitting the one-way wave-equation along orthogonal directions (Ristow and Ruhl, 1997), or by explicit numerical solutions (Hale, 1991). Similar approaches can be envisioned for 3D Riemannian extrapolation. The explicit solution seems more appropriate, since splitting is difficult due to the mixed terms of the Riemannian equations. I do not address this subject in this paper, and concentrate on developing higher-order kernels with implicit methods.

RIEMANNIAN WAVEFIELD EXTRAPOLATION

Riemannian wavefield extrapolation (Sava and Fomel, 2003) generalizes solutions to the Helmholtz equation

$$\Delta \mathcal{U} = -\omega^2 s^2 \mathcal{U}, \quad (1)$$

to coordinate systems that are different from simple Cartesian, where extrapolation is performed strictly in the downward direction. In equation (1), s is slowness, ω is temporal frequency, and \mathcal{U} is a monochromatic wave.

The acoustic wave-equation in Riemannian coordinates can be written as:

$$c_{\zeta\zeta} \frac{\partial^2 \mathcal{U}}{\partial \zeta^2} + c_{\xi\xi} \frac{\partial^2 \mathcal{U}}{\partial \xi^2} + c_{\eta\eta} \frac{\partial^2 \mathcal{U}}{\partial \eta^2} + c_{\zeta} \frac{\partial \mathcal{U}}{\partial \zeta} + c_{\xi} \frac{\partial \mathcal{U}}{\partial \xi} + c_{\eta} \frac{\partial \mathcal{U}}{\partial \eta} + c_{\xi\eta} \frac{\partial^2 \mathcal{U}}{\partial \xi \partial \eta} = -(\omega s)^2 \mathcal{U}, \quad (2)$$

where coefficients c_{ij} are functions of the coordinate system and can be computed numerically for any given coordinate system (Sava and Fomel, 2003).

We can simplify the Riemannian wavefield extrapolation method by dropping the first-order terms in equation (2). According to the theory of characteristics for second-order hyperbolic equations (Courant and Hilbert, 1989), these terms affect only the amplitude of the propagating waves. To preserve the kinematics, it is sufficient to keep only the second order terms of equation (2):

$$c_{\zeta\zeta} \frac{\partial^2 \mathcal{U}}{\partial \zeta^2} + c_{\xi\xi} \frac{\partial^2 \mathcal{U}}{\partial \xi^2} + c_{\eta\eta} \frac{\partial^2 \mathcal{U}}{\partial \eta^2} + c_{\xi\eta} \frac{\partial^2 \mathcal{U}}{\partial \xi \partial \eta} = -(\omega s)^2 \mathcal{U}. \quad (3)$$

From equation (3) we can derive the following dispersion relation:

$$-c_{\zeta\zeta} k_\zeta^2 - c_{\xi\xi} k_\xi^2 - c_{\eta\eta} k_\eta^2 - c_{\xi\eta} k_\xi k_\eta = -(\omega s)^2, \quad (4)$$

where k_ζ , k_ξ and k_η are wavenumbers associated with the Riemannian coordinates ζ , ξ and η .

For one-way wavefield extrapolation, we need to solve the quadratic equation (4) for the wavenumber of the extrapolation direction k_ζ , and select the solution with the appropriate sign to extrapolate waves in the desired direction:

$$k_\zeta = \sqrt{\frac{(\omega s)^2}{c_{\zeta\zeta}} - \frac{c_{\xi\xi}}{c_{\zeta\zeta}} k_\xi^2 - \frac{c_{\eta\eta}}{c_{\zeta\zeta}} k_\eta^2 - \frac{c_{\xi\eta}}{c_{\zeta\zeta}} k_\xi k_\eta}. \quad (5)$$

The 2D equivalent of equation (5) takes the form:

$$k_\zeta = \sqrt{\frac{(\omega s)^2}{c_{\zeta\zeta}} - \frac{c_{\xi\xi}}{c_{\zeta\zeta}} k_\xi^2}. \quad (6)$$

In ray coordinates, defined by $\zeta \equiv \tau$ and $\xi \equiv \gamma$, we can re-write equation (6) as

$$k_\tau = \sqrt{(\omega s \alpha)^2 - \left(\frac{\alpha}{J} k_\gamma\right)^2}, \quad (7)$$

where α is velocity and J is geometrical spreading. We can simplify the computations by the notation

$$\begin{cases} a = s\alpha, \\ b = \frac{\alpha}{J}, \end{cases} \quad (8)$$

therefore, equation (7) takes the form

$$k_\tau = \sqrt{(\omega a)^2 - (b k_\gamma)^2}. \quad (9)$$

THEORY

Space-domain solution

The space-domain finite-differences solution to equation (9) is derived based on the square-root expansion, first introduced to Geophysics by Muir (Claerbout, 1985):

$$k_{\tau} \approx \omega a + \omega \frac{v \left(\frac{k_{\gamma}}{\omega} \right)^2}{\mu - \rho \left(\frac{k_{\gamma}}{\omega} \right)^2}, \quad (10)$$

where the coefficients μ , v and ρ take the form:

$$\begin{cases} v = -c_1 a \left(\frac{b}{a} \right)^2, \\ \mu = 1, \\ \rho = c_2 \left(\frac{b}{a} \right)^2. \end{cases} \quad (11)$$

In the special case of Cartesian coordinates, $a = s$ and $b = 1$, equation (10) takes the familiar form

$$k_{\tau} \approx \omega s - \omega \frac{\frac{c_1}{s} \left(\frac{k_{\gamma}}{\omega} \right)^2}{1 - \frac{c_2}{s^2} \left(\frac{k_{\gamma}}{\omega} \right)^2}, \quad (12)$$

where the coefficients c_1 and c_2 take different values for different orders of the Muir expansion: $c_{15} = (c_1, c_2) = (0.50, 0.00)$ for the 15° equation, and $c_{45} = (c_1, c_2) = (0.50, 0.25)$ for the 45° equation.

Mixed-domain solutions

Mixed-domain solutions to the one-way wave equation usually consist of terms computed in the Fourier domain for a reference of the extrapolation medium, followed by a finite-differences correction applied in the space-domain. For equation (9), a generic mixed-domain solution has the form:

$$k_{\tau} \approx k_{\tau 0} + \omega(a - a_0) + \omega \frac{v \left(\frac{k_{\gamma}}{\omega} \right)^2}{\mu - \rho \left(\frac{k_{\gamma}}{\omega} \right)^2}, \quad (13)$$

where a_0 and b_0 are reference values for the medium characterized by the parameters a and b , and the coefficients μ , v and ρ take different forms according to the type of approximation. As for usual Cartesian coordinates, $k_{\tau 0}$ is applied in the Fourier domain, and the other two terms are applied in the space domain. If we limit the space-domain correction to the thin lens term, $\omega(a - a_0)$, we obtain the equivalent of split-step Fourier (SSF) method (Stoffa et al., 1990) in Riemannian coordinates.

Appendix A details the derivations for two types of expansions: pseudo-screen (Huang et al., 1999), and Fourier finite-differences (Ristow and Ruhl, 1994; Biondi, 2002).

- **Pseudo-screen:**

The coefficients for the pseudo-screen solution to equation (13) are

$$\begin{cases} v = a_0 \left[c_1 \left(\frac{a}{a_0} - 1 \right) - \left(\frac{b}{b_0} - 1 \right) \right] \left(\frac{b_0}{a_0} \right)^2, \\ \mu = 1, \\ \rho = 3c_2 \left(\frac{b_0}{a_0} \right)^2, \end{cases} \quad (14)$$

where a_0 and b_0 are reference values for the medium characterized by parameters a and b . In the special case of Cartesian coordinates, $a = s$ and $b = 1$, equation (13) with coefficients equation (14) takes the familiar form

$$k_\tau \approx k_{\tau 0} + \omega \left[1 + \frac{\frac{c_1}{s_0^2} \left(\frac{k_y}{\omega} \right)^2}{1 - \frac{3c_2}{s_0^2} \left(\frac{k_y}{\omega} \right)^2} \right] (s - s_0), \quad (15)$$

where the coefficients c_1 and c_2 take different values for different orders of the finite-differences term: $c_{15} = (c_1, c_2) = (0.50, 0.00)$ and $c_{45} = (c_1, c_2) = (0.50, 0.25)$. When $(c_1, c_2) = (0.00, 0.00)$ we obtain the usual split-step Fourier equation.

- **Fourier finite-differences:**

The coefficients for the Fourier finite-differences solution to equation (13) are

$$\begin{cases} v = \frac{1}{2} \delta_1^2, \\ \mu = \delta_1, \\ \rho = \frac{1}{4} \delta_2, \end{cases} \quad (16)$$

where

$$\begin{cases} \delta_1 = a \left(\frac{b}{a} \right)^2 - a_0 \left(\frac{b_0}{a_0} \right)^2, \\ \delta_2 = a \left(\frac{b}{a} \right)^4 - a_0 \left(\frac{b_0}{a_0} \right)^4. \end{cases} \quad (17)$$

a_0 and b_0 are reference values for the medium characterized by the parameters a and b . In the special case of Cartesian coordinates, $a = s$ and $b = 1$, equation (13) with coefficients equation (16) takes the familiar form:

$$k_\tau \approx k_{\tau 0} + \omega \left[1 + \frac{\frac{c_1}{s s_0} \left(\frac{k_y}{\omega} \right)^2}{1 - c_2 \left(\frac{1}{s^2} + \frac{1}{s s_0} + \frac{1}{s_0^2} \right) \left(\frac{k_y}{\omega} \right)^2} \right] (s - s_0), \quad (18)$$

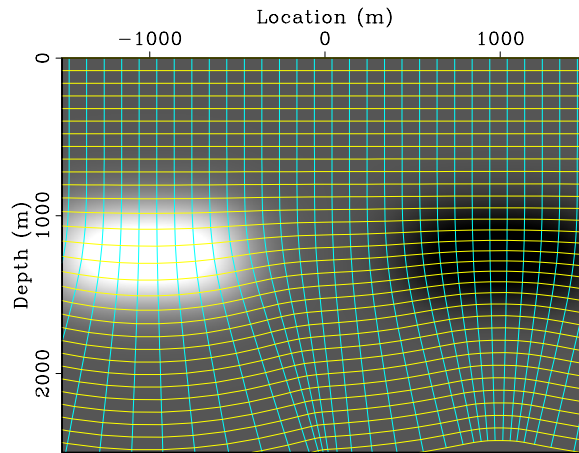
where the coefficients c_1 and c_2 take different values for different orders of the finite-differences term: $c_1 = 0.5, c_2 = 0.0$ for 15° , or $c_1 = 0.5, c_2 = 0.25$ for 45° . When $c_1 = c_2 = 0.0$ we obtain the usual split-step Fourier equation.

EXAMPLES

I illustrate the higher-order RWE extrapolators with impulse responses for two models with increasing levels of complexity.

The first example is based on a model with two smooth velocity anomalies that generate focusing and defocussing of the coordinate system, without triplication. I construct the coordinate system by ray tracing from an incident horizontal plane-wave at the surface. Figure 1 shows the velocity model with the coordinate system overlaid. Figure 2 shows the coordinate system coefficients defined in equation (9).

Figure 1: Velocity map and Riemannian coordinate system.
[paul1-RWEimp0.cos](#) [CR]



The goal of this test model is to illustrate the higher-order extrapolation kernels in a fairly simple coordinate system which is close to a Cartesian basis. The coordinate system is constructed from an incident plane wave, while the data comes from a point source. This setting is almost identical to the case of extrapolation from a point source in Cartesian coordinates, where high-angle² propagation requires high-order kernels. In this case, the Riemannian coordinate system does not match closely the general direction of wave propagation, so higher order kernels are needed. In practice, this situation can be addressed better with synthesized plane-wave data extrapolated in a coordinate system ray traced from an incident plane, and with point source data extrapolated in a coordinate system ray traced from a point source.

Figure 3 shows the velocity model and impulse responses for a point source computed with various extrapolators in ray coordinates (τ and γ). Panel (a) shows the slowness model, panel (b) shows extrapolation with the 15° finite-differences equation, panel (c) shows extrapolation with the 45° finite-differences equation, panel (d) shows extrapolation with the split-step Fourier (SSF) equation, panel (e) shows extrapolation with the pseudo-screen (PSC) equation, and panel (f) shows extrapolation with the Fourier finite-differences (FFD) equation. All plots are displayed in ray coordinates. We can observe that the angular accuracy of the extrapolator improves for the more accurate extrapolators. The finite-differences solutions (panels b and c)

²If the extrapolation axis is time, the meaning of higher angle accuracy is not well defined. We can use this terminology to associate the mathematical meaning of the approximation for the square-root by analogy with the Cartesian equivalents.

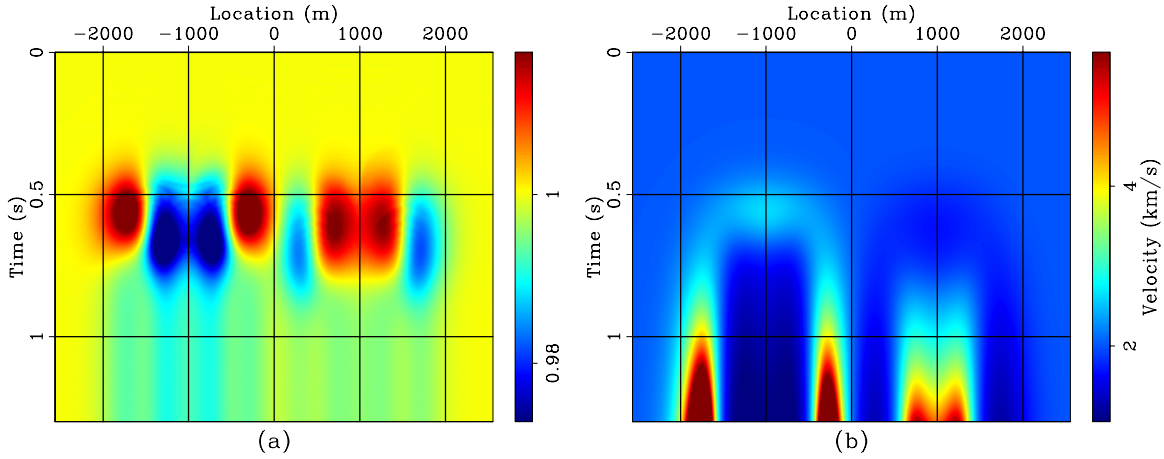


Figure 2: (a) Parameter $a = s\alpha$ in ray coordinates. (b) Parameter $b = \alpha/J$ in ray coordinates.

`paul1-RWEimp0.ab` [CR,M]

show the typical behavior of such solutions for the 15° and 45° equations (e.g. the cardioid for 45°), but in the more general setting of Riemannian extrapolation. The mixed-domain extrapolators (panels d, e, and f) show increased accuracy. The main differences occur at the highest propagation angles, and the most accurate extrapolators of those compared is the equivalent of Fourier finite-differences (panel f).

Figure 4 shows the corresponding plots in Figure 3 mapped in the physical coordinates, except for panel (a) which in this case shows the impulse response for extrapolation in Cartesian coordinates using a Fourier finite-differences extrapolator with a 15° finite-differences term. The overlay is an outline of the extrapolation coordinate system. After re-mapping to the physical space, the comparison of high-angle accuracy for the various extrapolators is more obvious, since it now has the proper physical meaning.

The second example is based on a model with a large lateral gradient which makes an incident plane wave overturn. A small Gaussian anomaly forces the coordinate system to focus slightly, and another large Gaussian anomaly, not used for the coordinate system, forces the propagating wave to triplicate and move at high angles relative to the extrapolation direction. Figure 5 shows the velocity model with the coordinate system overlaid. Figure 6 shows the coordinate system coefficients defined in equation (9).

The goal of this model is to illustrate Riemannian wavefield extrapolation in a situation which cannot be handled correctly by Cartesian extrapolation, no matter how accurate. In this example, an incident plane wave is overturning, thus becoming evanescent for the solution in Cartesian coordinates. Furthermore, the large Gaussian anomaly, Figure 6(a), causes serious wavefield triplication, thus requiring high-order kernels in the Riemannian extrapolator.

Figure 7 shows the velocity model and impulse responses for an incident plane wave computed with various extrapolators in ray coordinates (τ and γ). Panel (a) shows the slowness model, panel (b) shows extrapolation with the 15° finite-differences equation, panel (c) shows extrapolation with the 45° finite-differences equation, panel (d) shows extrapolation with the

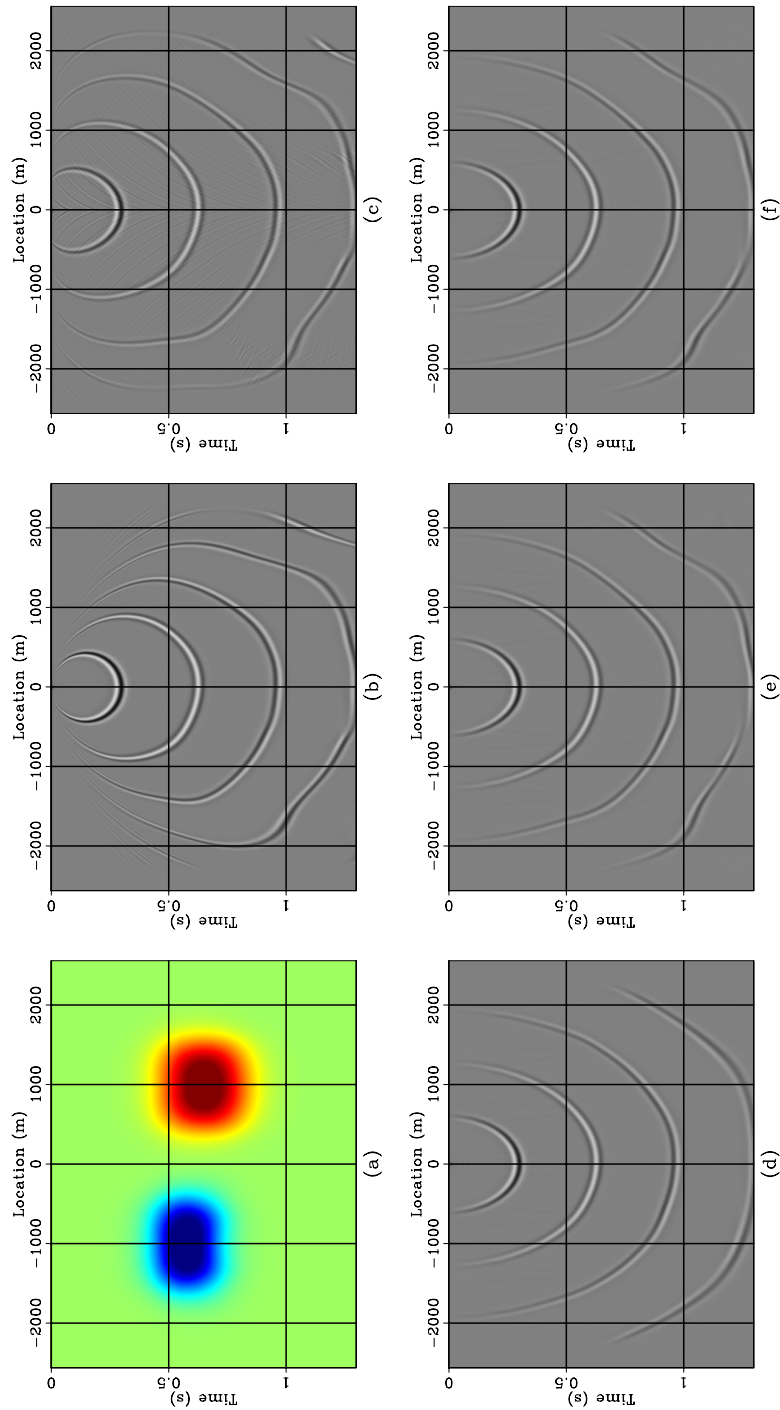


Figure 3: (a) Slowness. (b) Extrapolation with the 15° finite-differences equation. (c) Extrapolation with the 45° finite-differences equation. (d) Extrapolation with the split-step Fourier (SSF) equation. (e) Extrapolation with the pseudo-screen (PSC) equation. (f) Extrapolation with the Fourier finite-differences (FFD) equation. `paul1-RWEimp0.rweimg` [CR,M]

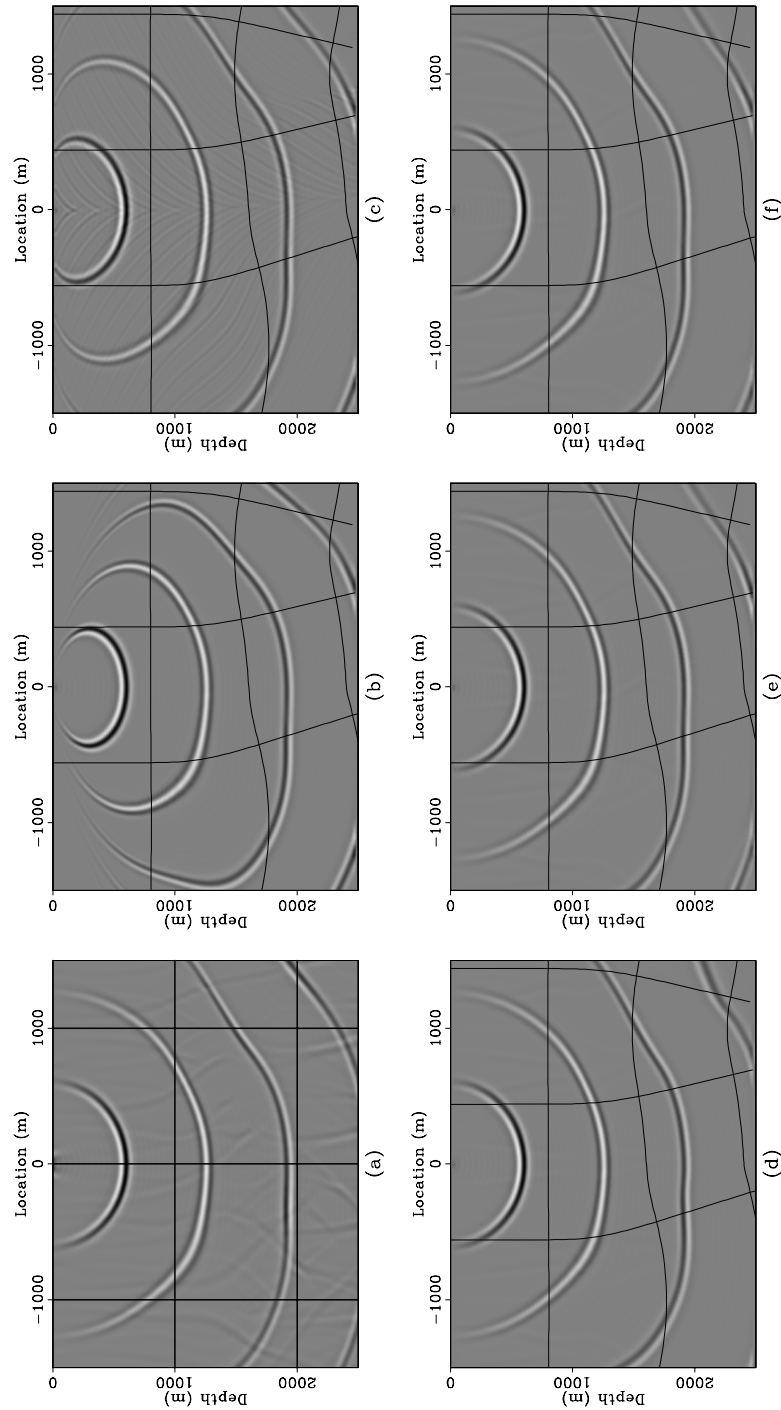
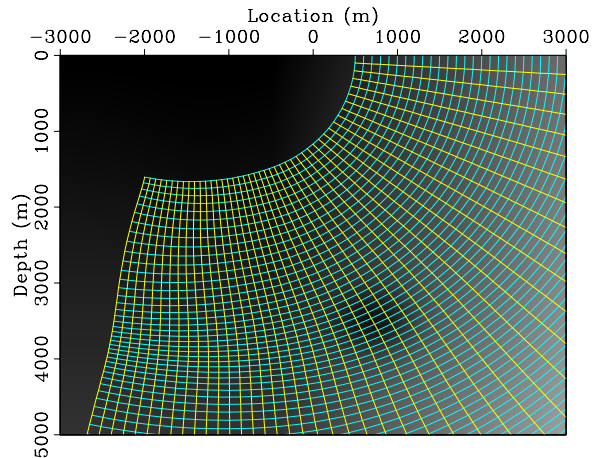


Figure 4: (a) Extrapolation with the Fourier finite-differences (FFD) equation in Cartesian coordinates. (b) Extrapolation with the 15° finite-differences equation. (c) Extrapolation with the 45° finite-differences equation. (d) Extrapolation with the split-step Fourier (SSF) equation. (e) Extrapolation with the pseudo-screen (PSC) equation. (f) Extrapolation with the Fourier finite-differences (FFD) equation. [paul1-RWEimp0.carimg](#) [CR,M]

Figure 5: Velocity map and Riemannian coordinate system.
 paul1-RWEimp1.cos [CR]



split-step Fourier (SSF) equation, panel (e) shows extrapolation with the pseudo-screen (PSC) equation, and panel (f) shows extrapolation with the Fourier finite-differences (FFD) equation. All plots are displayed in ray coordinates. As with the preceding example, we can observe increased angular accuracy as we increase the order of the extrapolator. The equivalent FFD is the most accurate.

As in the preceding example, Figure 4 shows the corresponding plots in Figure 3 mapped in the physical coordinates, except for panel (a) which in this case shows the impulse response for extrapolation in Cartesian coordinates using a Fourier finite-differences extrapolator with a 15° finite-differences term. The overlay is an outline of the extrapolation coordinate system.

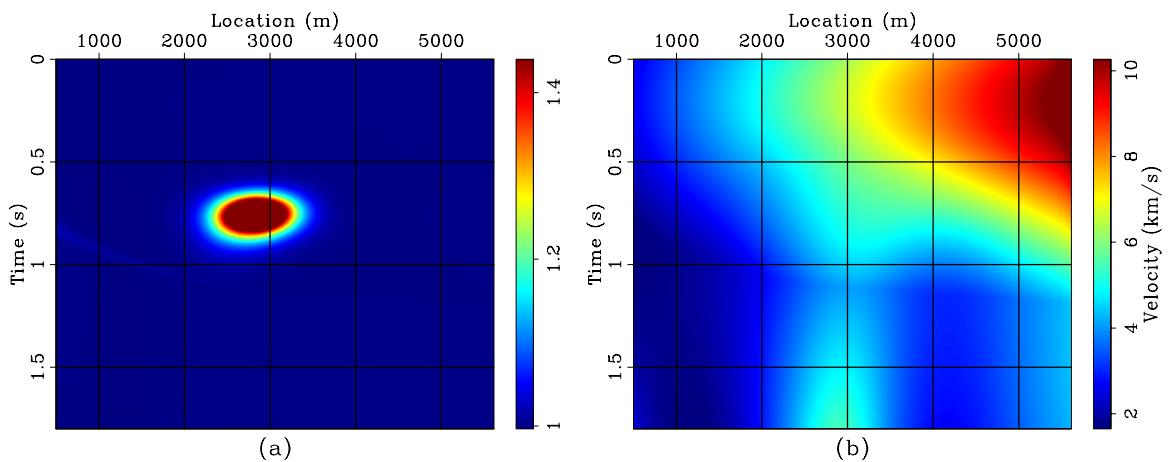


Figure 6: (a) Parameter $a = s\alpha$ in ray coordinates. (b) Parameter $b = \alpha/J$ in ray coordinates.
 paul1-RWEimp1.ab [CR,M]

Panel (a) in Figure 8 clearly shows the failure of the Cartesian extrapolator in propagating waves correctly even up to 90° . All Riemannian extrapolators handle better the overturning waves, including energy that is propagating upward relative to the physical coordinates. As

expected, the higher order kernels are more accurate in describing the triplicating wavefields.

CONCLUSIONS

Higher-order Riemannian wavefield extrapolation is needed when the coordinate system does not closely conform with the general direction of wavefield propagation. This situation occurs, for example, when the coordinate system is created by ray tracing in a medium that is different from the one used for extrapolation, or when the coordinate system is constructed based on some geometrical properties of the acquisition geometry (e.g. migration from topography). Space-domain and mixed-domain finite-difference solutions to Riemannian wavefield extrapolation improve the angular accuracy. 3D solutions can be addressed with explicit finite-differences, although this remains subject for future research.

ACKNOWLEDGMENT

Sergey Fomel contributed to the initial development of the higher-order finite differences kernels for Riemannian wavefield extrapolation.

REFERENCES

- Biondi, B., 2002, Stable wide-angle Fourier finite-difference downward extrapolation of 3-D wavefields: *Geophysics*, **67**, no. 03, 872–882.
- Claerbout, J. F., 1985, *Imaging the Earth's Interior*: Blackwell Scientific Publications.
- Courant, R., and Hilbert, D., 1989, *Methods of mathematical physics*: John Wiley & Sons.
- Fomel, S., and Claerbout, J. F., 1997, Exploring three-dimensional implicit wavefield extrapolation with the helix transform: *SEP-95*, 43–60.
- Hale, D., 1991, Stable explicit depth extrapolation of seismic wavefields: *Geophysics*, **56**, no. 11, 1770–1777.
- Huang, L. Y., Fehler, M. C., and Wu, R. S., 1999, Extended local Born Fourier migration method: *Geophysics*, **64**, no. 5, 1524–1534.
- Rickett, J., Claerbout, J., and Fomel, S., 1998, Implicit 3-D depth migration by wavefield extrapolation with helical boundary conditions: *SEP-97*, 1–12.
- Ristow, D., and Ruhl, T., 1994, Fourier finite-difference migration: *Geophysics*, **59**, no. 12, 1882–1893.
- Ristow, D., and Ruhl, T., 1997, 3-D implicit finite-difference migration by multiway splitting: *Geophysics*, **62**, no. 02, 554–567.

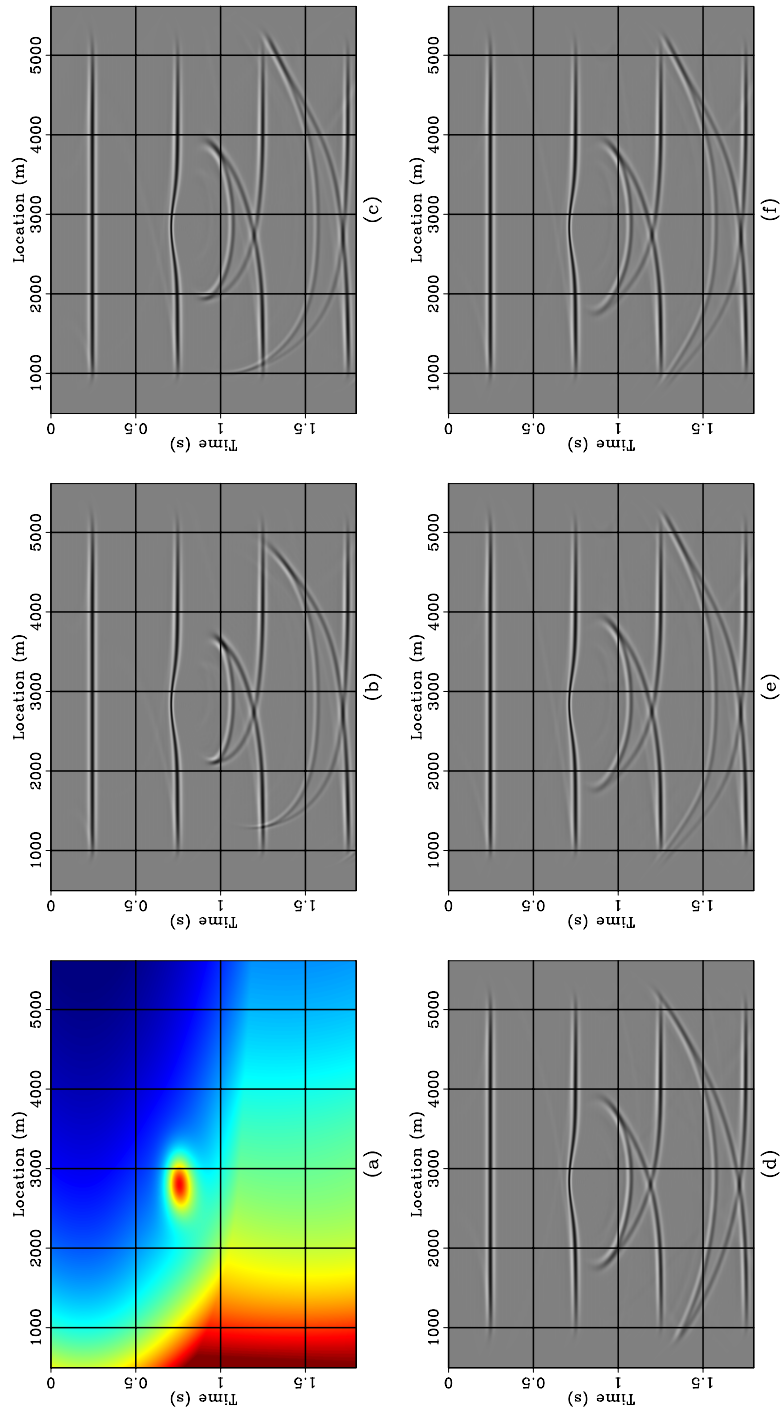


Figure 7: (a) Slowness. (b) Extrapolation with the 15° finite-differences equation. (c) Extrapolation with the 45° finite-differences equation. (d) Extrapolation with the split-step Fourier (SSF) equation. (e) Extrapolation with the pseudo-screen (PSC) equation. (f) Extrapolation with the Fourier finite-differences (FFD) equation. `paul1-RWEimp1.rweimg` [CR,M]

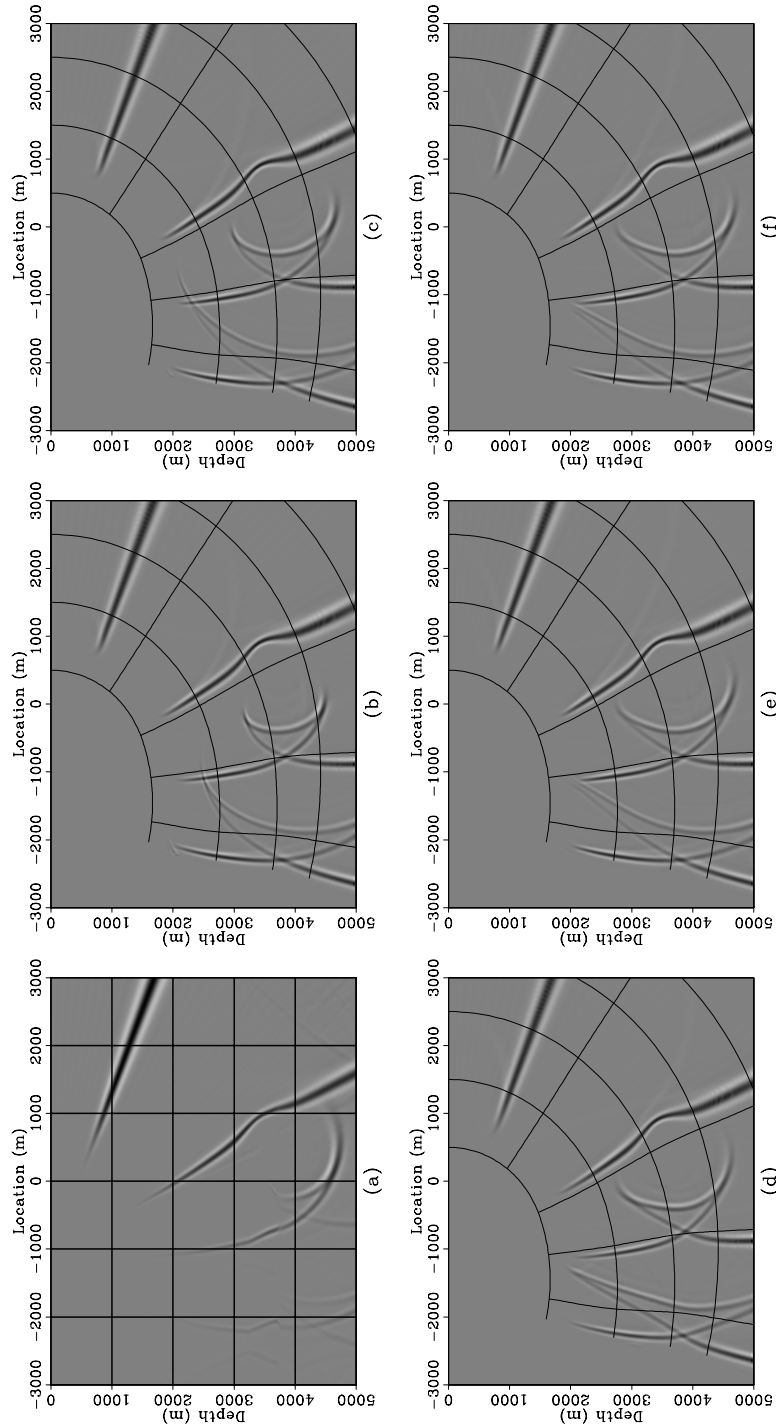


Figure 8: (a) Extrapolation with the Fourier finite-differences (FFD) equation in Cartesian coordinates. (b) Extrapolation with the 15° finite-differences equation. (c) Extrapolation with the 45° finite-differences equation. (d) Extrapolation with the split-step Fourier (SSF) equation. (e) Extrapolation with the pseudo-screen (PSC) equation. (f) Extrapolation with the Fourier finite-differences (FFD) equation. paul1-RWEimp1.carimg [CR,M]

Sava, P., and Fomel, S., 2003, Seismic imaging using Riemannian wavefield extrapolation: SEP-114, 1–30.

Shragge, J., and Sava, P., 2004, Incorporating topography into wave-equation imaging through conformal mapping: SEP-117.

Stoffa, P. L., Fokkema, J. T., de Luna Freire, R. M., and Kessinger, W. P., 1990, Split-step Fourier migration: *Geophysics*, **55**, no. 04, 410–421.

APPENDIX A

SPACE-DOMAIN FINITE-DIFFERENCES

Starting from equation (9), based on the Muir expansion for the square-root (Claerbout, 1985), we can write successively:

$$k_{\tau} = \omega a \sqrt{1 - \left(\frac{b k_y}{a \omega}\right)^2} \quad (\text{A-1})$$

$$\approx \omega a \left[1 - \frac{c_1 \left(\frac{b k_y}{a \omega}\right)^2}{1 - c_2 \left(\frac{b k_y}{a \omega}\right)^2} \right] \quad (\text{A-2})$$

$$\approx \omega a - \omega \frac{c_1 a \left(\frac{b}{a}\right)^2 \left(\frac{k_y}{\omega}\right)^2}{1 - c_2 \left(\frac{b}{a}\right)^2 \left(\frac{k_y}{\omega}\right)^2}. \quad (\text{A-3})$$

If we make the notations

$$\begin{cases} v = -c_1 a \left(\frac{b}{a}\right)^2, \\ \mu = 1, \\ \rho = c_2 \left(\frac{b}{a}\right)^2. \end{cases} \quad (\text{A-4})$$

we obtain the finite-differences solution to the one-way wave equation in Riemannian coordinates:

$$k_{\tau} \approx \omega a + \omega \frac{v \left(\frac{k_y}{\omega}\right)^2}{\mu - \rho \left(\frac{k_y}{\omega}\right)^2}. \quad (\text{A-5})$$

MIXED DOMAIN — PSEUDO-SCREEN

The pseudo-screen solution to equation (9) derives from a first-order expansion of the square-root around a_0 and b_0 which are reference values for the medium characterized by the param-

eters a and b :

$$k_\tau \approx k_{\tau 0} + \left. \frac{\partial k_\tau}{\partial a} \right|_{a_0, b_0} (a - a_0) + \left. \frac{\partial k_\tau}{\partial b} \right|_{a_0, b_0} (b - b_0). \quad (\text{A-6})$$

The partial derivatives relative to a and b , respectively, are:

$$\left. \frac{\partial k_\tau}{\partial a} \right|_{a_0, b_0} = \omega \frac{1}{\sqrt{1 - \left(\frac{b_0 k_\gamma}{a_0 \omega}\right)^2}} \approx \omega \left[1 + \frac{c_1 \left(\frac{b_0 k_\gamma}{a_0 \omega}\right)^2}{1 - 3c_2 \left(\frac{b_0 k_\gamma}{a_0 \omega}\right)^2} \right], \quad (\text{A-7})$$

$$\left. \frac{\partial k_\tau}{\partial b} \right|_{a_0, b_0} = -\omega \frac{b_0}{a_0} \left(\frac{k_\gamma}{\omega}\right)^2 \frac{1}{\sqrt{1 - \left(\frac{b_0 k_\gamma}{a_0 \omega}\right)^2}} \approx -\omega \frac{a_0}{b_0} \left(\frac{b_0 k_\gamma}{a_0 \omega}\right)^2. \quad (\text{A-8})$$

Therefore, the pseudo-screen equation becomes

$$k_\tau \approx k_{\tau 0} + \omega(a - a_0) + \omega \frac{a_0 \left[c_1 \left(\frac{a}{a_0} - 1\right) - \left(\frac{b}{b_0} - 1\right) \right] \left(\frac{b_0}{a_0}\right)^2 \left(\frac{k_\gamma}{\omega}\right)^2}{1 - 3c_2 \left(\frac{b_0}{a_0}\right)^2 \left(\frac{k_\gamma}{\omega}\right)^2}. \quad (\text{A-9})$$

If we make the notations

$$\begin{cases} v = a_0 \left[c_1 \left(\frac{a}{a_0} - 1\right) - \left(\frac{b}{b_0} - 1\right) \right] \left(\frac{b_0}{a_0}\right)^2 \\ \mu = 1 \\ \rho = 3c_2 \left(\frac{b_0}{a_0}\right)^2 \end{cases} \quad (\text{A-10})$$

we obtain the mixed-domain pseudo-screen solution to the one-way wave equation in Riemannian coordinates:

$$k_\tau \approx k_{\tau 0} + \omega(a - a_0) + \omega \frac{v \left(\frac{k_\gamma}{\omega}\right)^2}{\mu - \rho \left(\frac{k_\gamma}{\omega}\right)^2}. \quad (\text{A-11})$$

MIXED DOMAIN — FOURIER FINITE-DIFFERENCES

The pseudo-screen solution to equation (9) derives from a fourth-order expansion of the square-root around (a_0, b_0) and (a, b) :

$$\begin{aligned} k_\tau &\approx \omega a \left[1 + \frac{1}{2} \left(\frac{b k_\gamma}{a \omega}\right)^2 + \frac{1}{8} \left(\frac{b k_\gamma}{a \omega}\right)^4 \right], \\ k_{\tau 0} &\approx \omega a_0 \left[1 + \frac{1}{2} \left(\frac{b_0 k_\gamma}{a_0 \omega}\right)^2 + \frac{1}{8} \left(\frac{b_0 k_\gamma}{a_0 \omega}\right)^4 \right]. \end{aligned} \quad (\text{A-12})$$

If we subtract equations (A-12), we obtain:

$$k_\tau \approx k_{\tau 0} + \omega(a - a_0) + \frac{1}{2}\omega \left[a \left(\frac{b}{a} \right)^2 - a_0 \left(\frac{b_0}{a_0} \right)^2 \right] \left(\frac{k_\gamma}{\omega} \right)^2 + \frac{1}{8}\omega \left[a \left(\frac{b}{a} \right)^4 - a_0 \left(\frac{b_0}{a_0} \right)^4 \right] \left(\frac{k_\gamma}{\omega} \right)^4. \quad (\text{A-13})$$

We can make the notations

$$\delta_1 = a \left(\frac{b}{a} \right)^2 - a_0 \left(\frac{b_0}{a_0} \right)^2, \quad (\text{A-14})$$

$$\delta_2 = a \left(\frac{b}{a} \right)^4 - a_0 \left(\frac{b_0}{a_0} \right)^4, \quad (\text{A-15})$$

therefore equation (A-13) becomes

$$k_\tau = k_{\tau 0} + \omega(a - a_0) + \frac{1}{2}\omega\delta_1 \left(\frac{k_\gamma}{\omega} \right)^2 + \frac{1}{8}\omega\delta_2 \left(\frac{k_\gamma}{\omega} \right)^4. \quad (\text{A-16})$$

With the approximation

$$\frac{1}{2}\delta_1 u^2 + \frac{1}{8}\delta_2 u^4 \approx \frac{\frac{1}{2}\delta_1^2 u^2}{\delta_1 - \frac{1}{4}\delta_2 u^2}, \quad (\text{A-17})$$

we can write

$$k_\tau = k_{\tau 0} + \omega(a - a_0) + \omega \frac{\frac{1}{2}\delta_1^2 \left(\frac{k_\gamma}{\omega} \right)^2}{\delta_1 - \frac{1}{4}\delta_2 \left(\frac{k_\gamma}{\omega} \right)^2}. \quad (\text{A-18})$$

If we make the notations

$$\begin{cases} v = \frac{1}{2}\delta_1^2, \\ \mu = \delta_1, \\ \rho = \frac{1}{4}\delta_2, \end{cases} \quad (\text{A-19})$$

we obtain the mixed-domain Fourier finite-differences solution to the one-way wave equation in Riemannian coordinates:

$$k_\tau \approx k_{\tau 0} + \omega(a - a_0) + \omega \frac{v \left(\frac{k_\gamma}{\omega} \right)^2}{\mu - \rho \left(\frac{k_\gamma}{\omega} \right)^2}. \quad (\text{A-20})$$

Incorporating topography into wave-equation imaging through conformal mapping

Jeff Shragge and Paul Sava¹

ABSTRACT

Conformal mapping is a technique used widely in applied physics and engineering fields to facilitate numerical solution of boundary value problems involving solution domains characterized by complex geometry. The predominant reason for applying a conformal mapping procedure is to transform an irregular solution domain to one of symmetric geometry. The conformal map transform has the property that the angle between neighboring arc segments is (locally) conserved under the mapping. Accordingly, in the context of wave-equation imaging under topography, conformal mapping can transform an irregular, topographically-influenced solution domain to a regular computational mesh. In this paper, we demonstrate that the use of the conformal mapping transform coupled with Riemannian wavefield extrapolation generates an orthogonal coordinate system and the governing wavefield continuation equation required for wave-equation migration directly from a topographic surface. We illustrate the potential of this approach by migrating a 2-D prestack data set acquired on a geologic model of thrust belt.

INTRODUCTION

Migration of seismic land data acquired on topography presents a significant imaging challenge. One technique used to correct for the deleterious effects of topography in a more accurate fashion than simple statics corrections is to include a wavefield datuming step in the processing flow (Berryhill, 1979). Usually, this step propagates wavefields down to a common subsurface depth level. However, the presence of strong lateral velocity contrast directly beneath the surface can generate significant wavefield triplication that leads to non-optimal datuming results, especially if Kirchhoff-based methods are used. Therefore, a migration workflow that includes an upward or downward wavefield continuation processing step should produce better imaging results.

However, in practice wavefield continuation is seldom applied directly to data sets acquired on topography without significant preprocessing. The predominant challenge is that the metric of source and geophone arrays seldom conform to a regular computational mesh. Rather, due to instrument cabling, geophone arrays are more likely to uniformly sample the topographic surface. Two common solutions to this problem are either to employ a migration

¹email: jeff@sep.stanford.edu,paul@sep.stanford.edu

procedure involving wavefield injection (Jiao et al., 2004), or to perform an upward-datuming prior to migration (Bevc, 1997). Migration by wavefield injection commences at the global topographic maximum where the data recorded at this station are injected into the wavefield. The wavefield is then continued downward and data are injected into the wavefield whenever the extrapolation step reaches the height of the topography. Two drawbacks of this approach are that data need to be regularized beforehand to a uniform grid usually through interpolation, and that the additional number of fine-scale extrapolation steps significantly increase cost. Upward wavefield datuming or “flooding the topography” procedures are employed to generate a regular wavefield above the highest point. This processing step can be done successfully with Kirchhoff or other migration operators. One downside of this approach is, again, the increased preprocessing cost. In general, although these methods produce good results, a significant amount of data preprocessing is required to render Cartesian-based wave-equation migration approaches applicable and, as a result, data fidelity may be compromised.

In this paper, we argue that many of the difficulties with state-of-the-art migration from topography technology could be precluded by abandoning the Cartesian coordinate system for one conformal with the topographic surface. To find such a method, we observe that wave-equation imaging is a specific example of a boundary value problem (BVP) that has a solution domain defined by a polygonal boundary. (Images are the superposition of the monochromatic solutions to a number of BVPs of different frequency.) This observation motivates us to examine the results of other applied fields that routinely solve BVPs, such as aerospace and mechanical engineering.

One method routinely employed to help solve BVPs is conformal mapping. This procedure defines how to transform the physical solution domain to a more symmetric canonical domain through mapping in the complex plane (Kythe, 1998). Relating this concept to wave-equation imaging from topography, we suggest using conformal mapping to transform the topographically-influenced physical domain to a canonical domain characterized by a rectangular computational grid. We term this new orthogonal calculation mesh a “topographic” coordinate system. Moreover, the forward and inverse conformal map transforms are also used in defining the wavefield extrapolation equations appropriate for the canonical domain. Consequently, we are both able to perform wavefield extrapolation and to apply the imaging condition in the topographic coordinate domain. The final image is generated by mapping the topographic coordinate image to the physical domain using the inverse conformal mapping transform.

We begin the paper with an overview of conformal mapping illustrated by some simple examples. We then review Riemannian wavefield extrapolation (Sava and Fomel, 2004) and the steps required to generate appropriate wavefield extrapolation equations. Prestack migration results are presented for a data set acquired over a 2-D geological model characterized by severe elevation relief, strong near-surface velocity contrast, and complicated folding and faulting. The paper concludes with a discussion on the relative merits and drawbacks of the proposed approach.

CONFORMAL MAPPING

Conformal mapping is a topic of wide-spread interest in the field of applied complex analysis. Generally, this subject deals with the manner in which point sets are mapped between two different analytic domains in the complex plane. In this paper, we refer only to domains that are simply- (i.e. not multiply) connected. A mapping between complex planes may be thought of as a rule relating how a field of points defined on a domain in the z -plane, $z = x + iy$, maps to the w -plane, $w = u(x, y) + iv(x, y)$, according to a mapping function, $w = f(z)$ (see the example in Figure 1). If for each point in the z -plane domain there corresponds a unique number in the w -plane, then the mapping function is analytic. In addition, if for each point in the w -plane there corresponds precisely one point in the z -plane, then the mapping is one-to-one and the transformation is invertible. The Cauchy-Riemann equations (Nehari, 1975) are the necessary and sufficient conditions for function $f(z)$ to be analytic in a domain of interest.

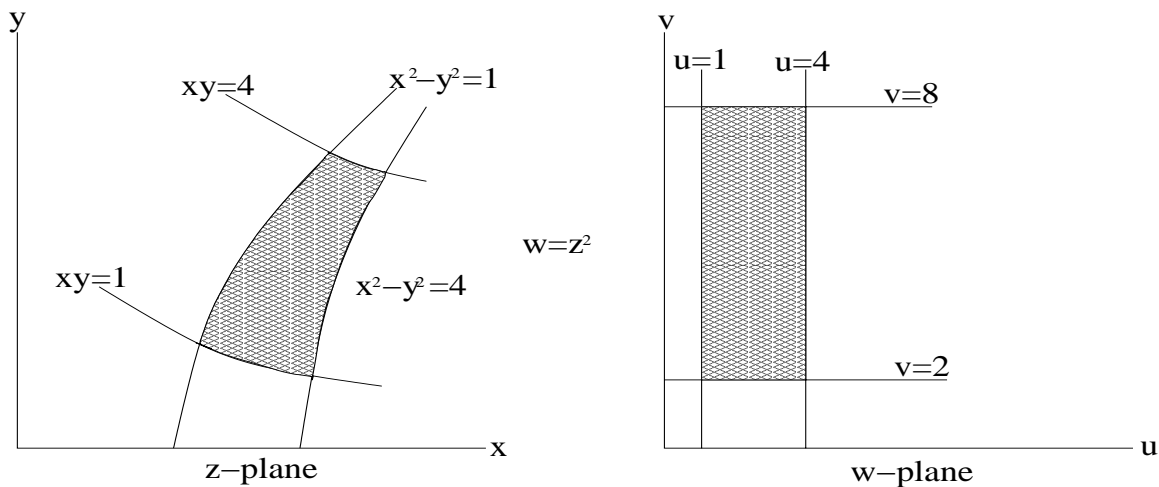


Figure 1: An example of a conformal mapping between the z -plane, $z = x + iy$, and the w -plane, $w(z) = u(x, y) + iv(x, y)$, according to mapping function $w = z^2$. In this example, the shaded region in the z -plane maps to the shaded region in the w -plane. Coordinates (u, v) are given by $(x^2 - y^2, 2xy)$. Lines in the w -plane: $u = 1$, $u = 4$, $v = 2$, and $v = 8$, map to the following lines in the z -plane: $x^2 - y^2 = 1$, $x^2 - y^2 = 4$, $xy = 1$. Note also that orthogonality of line intersections in the w -plane are preserved in the z -plane. [jeff1-map1](#) [NR]

A conformal map is distinguishable from other mappings between complex planes by characteristic properties. Most important to this discussion is the following property:

Conservation of Angle: A conformal mapping of two continuous arcs that locally form an angle α_0 in the z -plane will generate two continuous arcs separated by the same local angle α_0 in the w -plane.

Figure 1 illustrates the property that grid lines orthogonal in the w -plane are orthogonal in the z -plane under a conformal map. By extension, non-Cartesian orthogonal coordinate systems

can be created in the z -plane (or conversely in the w -plane) by a conformal mapping of a rectangular coordinate system in the w -plane (z -plane).

The first major developments in the theory of conformal mapping originated with the mapping theorem of Riemann (1851), who proved the existence of a unique analytic mapping between any two simply-connected, analytic domains:

Riemann Mapping Theorem: Let D be a simply-connected region. Then there exists a bijective conformal map $f : D \rightarrow U$, where U is the open unit disk. By extension, if G is another simply-connected domain, there exists a mapping $g : G \rightarrow U$. Hence, there exists a composite mapping operation, $f \cdot g^{-1} : D \rightarrow G$, between two arbitrary simply-connected domains.

Figure 2 illustrates the Riemann mapping theorem between three domains pertinent to the current discussion. Figure 3 presents an example of a conformal mapping between a square and unit circle (the mapping g in Figure 2).

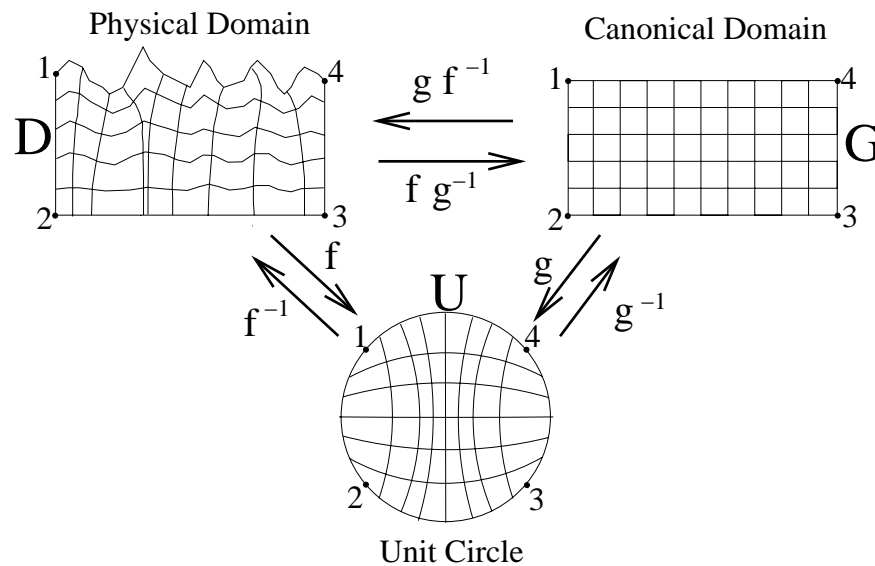


Figure 2: Illustration of the Riemann Mapping Theorem between a physical domain with an undulating upper surface, the unit circle, and a rectangular canonical domain. In this example, a forward mapping function, f , exists between the physical domain and the unit circle and, because the mapping is one-to-one, an inverse mapping f^{-1} also exists. Forward and inverse mapping functions (g and g^{-1}) also exist between the rectilinear domain and the unit circle. Hence, the composition of functions $f \cdot g^{-1}$ denotes a mapping between the physical and canonical domains, while the inverse mapping is given by $g \cdot f^{-1}$. The mapping locations of points labeled 1 through 4 are specified to ensure that the sides in the physical domain correspond to the sides in the canonical domain. jeff1-Riemap [NR]

We will use the Riemann mapping theorem to transform the topographic domain to a rectangular computational mesh. Assisting us is an extensive catalog of conformal maps between

common geometrical domains. Pertinent to the current discussion are the conformal maps between the unit circle (UC) and the upper half plane (UHP), $f : UC \rightarrow UHP$ and its inverse $f^{-1} : UC \leftarrow UHP$,

$$\begin{aligned} f : z &\rightarrow \frac{z-i}{z+i}, \\ f^{-1} : i \frac{1+z}{1-z} &\leftarrow z, \end{aligned} \quad (1)$$

and the mapping between the UHP and a rectangle with sides of arbitrary length, $g : UHP \rightarrow Rect$, and its inverse $g^{-1} : UHP \leftarrow Rect$,

$$\begin{aligned} g : w(k) &= \int_0^z \frac{d\zeta}{\sqrt{1-\zeta^2}\sqrt{1-k^2\zeta^2}} \\ g^{-1} : &sn(w;k), \end{aligned} \quad (2)$$

where g is an elliptic integral of the first kind, k is a function of the ratio of the length of the two sides, and $sn(w;k)$ is a Jacobian elliptic function (Nehari, 1975). Appendix A discusses a method for computing conformal map transforms between arbitrary polygons and the UHP .

Figure 3: Conformal mapping between a square coordinate system and the unit circle. jeff1-confexamp
[NR]

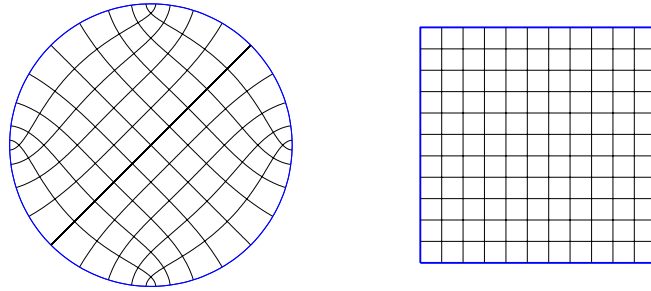


Table 1 outlines a work flow to generate a topographic coordinate system through conformal mapping. The first step is to define the enclosure of the physical domain where the topographic surface defines the upper boundary. We create the lower boundary by mirroring the topography at twice the maximum extrapolation depth. The side boundaries are defined by straight lines that join the top and bottom segments. We denote the border points z_{topo}^{bnd} , where subscript *topo* and superscript *bnd* refer to topography and boundary points, respectively. The four corner points of the physical domain are also specified. The next two steps involve calculating the forward and inverse mapping functions, f and f^{-1} , between the topographic surface and the unit circle. The fourth step is to generate a rectilinear boundary and to define its four corner points. We denote this boundary z_{rect}^{bnd} , where subscript *rect* refers to rectangle. The next two steps involve calculating forward and inverse mappings functions, g and g^{-1} , between the boundary of the rectangle and the unit circle.

To discern where in the canonical domain to form the coordinate system grid, we need to find the mapping of the topography boundary points on the rectangular domain boundary. This is accomplished by calculating the image of the boundary points under composite mapping operations, $z_{im}^{bnd} = g^{-1} \cdot f(z_{topo}^{bnd})$. A rectangular grid is then set up at the image points to create computational grid, z_{rect}^{cs} , where superscripts *cs* denote coordinate system.

Table 1. Work flow to calculate topographic coordinates with conformal mapping.

Step	Description	Notation
1	Define physical domain boundary and 4 corner points	z_{topo}^{bnd}
2	Calculate mapping $f : Topo \rightarrow UHP \rightarrow UC$	$w_{topo}^{bnd} = f(z_{topo}^{bnd})$
3	Calculate mapping $f^{-1} : UC \rightarrow UHP \rightarrow Topo$	$z_{topo}^{bnd} = f^{-1}(w_{topo}^{bnd})$
4	Define canonical domain border and 4 corner points	z_{rect}^{bnd}
5	Calculate mapping $g : Rect \rightarrow UHP \rightarrow UC$	$w_{rect}^{bnd} = g(z_{rect}^{bnd})$
6	Calculate mapping $g^{-1} : UC \rightarrow UHP \rightarrow Rect$	$z_{rect}^{bnd} = g^{-1}(w_{rect}^{bnd})$
7	Find image of topography in the rectangle	$z_{im}^{bnd} = g^{-1}(f(z_{topo}^{bnd}))$
8	Construct rectilinear grid using z_{im}^{bnd} (z_{topo}^{bnd})	z_{rect}^{cs}
9	Map grid z_{rect}^{cs} to physical domain	$z_{topo}^{cs} = f^{-1}(g(z_{rect}^{cs}))$

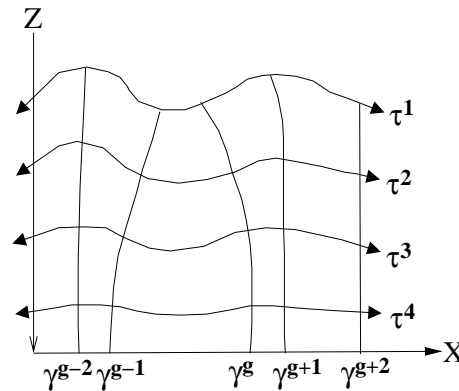
The final step is to map the rectilinear coordinate system, z_{rect}^{cs} , from the canonical domain back to the topographic coordinates under composite mapping operation, $z_{topo}^{cs} = f^{-1} \cdot g(z_{rect}^{cs})$. Point set z_{topo}^{cs} defines a coordinate system appropriate for performing wavefield continuation directly from topography at the acquisition locations. The next section details how this point set is used to generate the appropriate extrapolation equations.

RIEMANNIAN WAVEFIELD EXTRAPOLATION

Performing wavefield extrapolation on topographic computational meshes computed through conformal mapping requires parameterizing the acoustic wave-equation by a set of variables that describe the coordinate system. In 2-D, we denote these variables the extrapolation direction, τ , (analogous to depth in Cartesian wavefield extrapolation), and the direction orthogonal, γ (analogous to horizontal offset in Cartesian wavefield extrapolation). Variables τ and γ are related to the topographic coordinate system point set through $(\tau, \gamma) = (\Re(z_{topo}^{cs}), \Im(z_{topo}^{cs}))$. Figure 4 presents a sketch of the topographic coordinate system geometry.

Figure 4: Cartoon illustrating the topography coordinate system. Variable $\tau = \tau(x, z)$ is the extrapolation direction and parameter τ^l may be considered a topographic “front”. Variable $\gamma = \gamma(x, z)$ is the coordinate across the extrapolation step at a constant τ step, and parameter γ^s may be considered a topographic “ray”.

jeff1-topocoord [NR]



The 2-D acoustic wave-equation for wavefield, \mathcal{U} , at frequency, ω , governing propagation in topographic coordinates is (Sava and Fomel, 2004),

$$\frac{1}{\alpha J} \left[\frac{\partial}{\partial \tau} \left(\frac{J}{\alpha} \frac{\partial \mathcal{U}}{\partial \tau} \right) + \frac{\partial}{\partial \gamma} \left(\frac{\alpha}{J} \frac{\partial \mathcal{U}}{\partial \gamma} \right) \right] = -\omega^2 s^2 \mathcal{U}, \quad (3)$$

where s is the slowness of the medium, α a distance scaling factor in the extrapolation direction τ , and J a Jacobian of transformation of coordinate γ (analogous to a geometrical ray spreading factor). Parameters α and J are defined by,

$$\begin{aligned}\alpha &= \left[\frac{\partial x}{\partial \tau} \frac{\partial x}{\partial \tau} + \frac{\partial z}{\partial \tau} \frac{\partial z}{\partial \tau} \right]^{\frac{1}{2}}, \\ J &= \left[\frac{\partial x}{\partial \gamma} \frac{\partial x}{\partial \gamma} + \frac{\partial z}{\partial \gamma} \frac{\partial z}{\partial \gamma} \right]^{\frac{1}{2}},\end{aligned}\quad (4)$$

where x and z are the coordinates of the underlying Cartesian basis. Note that parameters α and J are solely components of the coordinate system and are independent of the extrapolated wavefield values.

Analogous to wavefield continuation on a Cartesian mesh, a dispersion relation must be specified that forms the basis for all derived extrapolation operators in a topographic coordinate system. The relation being sought is the wavenumber along the extrapolation direction, k_τ . Following Sava and Fomel (2004), the partial derivative operators in (3) are expanded out to generate a second-order partial differential equation with non-zero cross derivatives. Fourier-domain wavenumbers are then substituted for the partial differential operators acting on wavefield, \mathcal{U} , and the quadratic formula is applied to yield the expression for k_τ ,

$$k_\tau = \frac{i\alpha}{2J} \frac{\partial}{\partial \tau} \left(\frac{J}{\alpha} \right) \pm \left[\omega^2 s^2 \alpha^2 - \left[\frac{\alpha}{2J} \frac{\partial}{\partial \tau} \left(\frac{J}{\alpha} \right) \right]^2 + \frac{i\alpha}{J} \frac{\partial}{\partial \gamma} \left(\frac{\alpha}{J} \right) k_\gamma - \frac{\alpha^2}{J^2} k_\gamma^2 \right]^{\frac{1}{2}}. \quad (5)$$

One relatively straightforward way to apply wavenumber k_τ in an extrapolation scheme is to develop the topographic coordinate system equivalent to a phase-screen extrapolation operator (Sava, 2004). In the following example, we treat solely the kinematic, one-way propagation of recorded wavefields. This asymptotic approximation leads us to drop the first order partial differential terms in (5),

$$k_\tau = \pm \sqrt{a^2 \omega^2 - b^2 k_\gamma^2}, \quad (6)$$

where $a = s\alpha$ and $b = \alpha/J$. The expansion of k_τ about reference parameters a_0 and b_0 is,

$$k_\tau \approx k_{\tau 0} + \frac{\partial k_\tau}{\partial a} \Big|_{a_0, b_0} (a - a_0) + \frac{\partial k_\tau}{\partial b} \Big|_{a_0, b_0} (b - b_0), \quad (7)$$

where subscript 0 denotes reference. Partial derivatives with respect to parameters a and b are,

$$\begin{aligned}\frac{\partial k_\tau}{\partial a} \Big|_{a_0, b_0} &= \omega \frac{1}{\sqrt{1 - \left(\frac{b_0 k_\gamma}{\omega a_0} \right)^2}} \approx \omega \left[1 + \frac{c_1 \left(\frac{b_0 k_\gamma}{\omega a_0} \right)^2}{1 - 3c_2 \left(\frac{b_0 k_\gamma}{\omega a_0} \right)^2} \right], \\ \frac{\partial k_\tau}{\partial b} \Big|_{a_0, b_0} &= -\omega \frac{b_0}{a_0} \left(\frac{k_\gamma}{\omega} \right)^2 \frac{1}{\sqrt{1 - \left(\frac{b_0 k_\gamma}{\omega a_0} \right)^2}} \approx -\omega \frac{b_0}{a_0} \left(\frac{k_\gamma}{\omega} \right)^2,\end{aligned}\quad (8)$$

where the square root function in the denominator has been expanded using a Padé approximation. The choice of numerical constants $c_1 = \frac{1}{2}$ and $c_2 = 0$ yields a 15° finite-difference

term. Thus, the phase-screen approximation for extrapolation wavenumber, k_τ , is,

$$k_\tau \approx k_{\tau 0} + \omega(a - a_0) + \omega \frac{\left[c_1 \left(\frac{a_0}{b_0} \right)^2 (a - a_0) - \frac{b_0}{a_0} (b - b_0) \right] \left(\frac{k_y}{\omega} \right)^2}{1 - 3c_2 \left(\frac{b_0}{a_0} \right)^2 \left(\frac{k_y}{\omega} \right)^2}. \quad (9)$$

This expression can be generalized to include multiple reference media through a phase-shift plus interpolation (PSPI) approach (Gazdag and Sguazzero, 1984) over the two parameters; however, this extension is not treated here. The approximation for wavenumber, k_τ , given in (9) is used in a conventional wavefield extrapolation scheme that extends the recorded wavefield away from the acquisition surface to the required subsurface locations. This involves solving a one-way wave-equation which, in discrete extrapolation steps of $\Delta\tau$, requires a recursive computation of the following:

$$\mathcal{U}(\tau + \Delta\tau, \gamma, \omega) = \mathcal{U}(\tau, \gamma, \omega) e^{ik_\tau \Delta\tau}. \quad (10)$$

Our prestack migration example is computed using a shot profile migration code. This involves extrapolating the source and receiver wavefields, \mathcal{S} and \mathcal{R} , independently using,

$$\begin{aligned} \mathcal{S}_{\tau+\Delta\tau} &= \mathcal{S}_\tau e^{-ik_\tau \Delta\tau}, \\ \mathcal{R}_{\tau+\Delta\tau} &= \mathcal{R}_\tau e^{ik_\tau \Delta\tau}, \end{aligned} \quad (11)$$

and applying an imaging condition at each extrapolation level to generate image, $\mathcal{I}(\tau, \gamma)$,

$$\mathcal{I}(\tau, \gamma) = \sum_i \sum_w \mathcal{S}(\tau, \gamma, \omega; \mathbf{s}_i) \overline{\mathcal{R}(\tau, \gamma, \omega; \mathbf{s}_i)}, \quad (12)$$

where the line over the receiver wavefield indicates complex conjugate. Image $\mathcal{I}(\tau, \gamma)$ is then mapped to a Cartesian coordinate system using sinc-based interpolation operators in the neighborhood of each mapped point to generate the final image, $\mathcal{I}(x, z)$.

NUMERICAL EXAMPLES

We test the combined conformal mapping and Riemannian wavefield extrapolation approach on a synthetic dataset computed on a rugged topographic surface. The geological model is a merger of common geologic features from the Canadian Foothills in northeastern British Columbia, Canada. The velocity model, shown in Figure 5, consists of steep thrust fault planes and complex folds typical of a mountainous thrust region. The topographic boundary of interest is demarcated by the velocity model discontinuity nearest to the surface. The total relief of the Earth's surface in this model is approximately 1600 m. Also note that the complex near-surface velocity structure should present a significant imaging challenge (Gray and Marfurt, 1995).

Figure 6 shows the result of using conformal mapping to construct a coordinate system that incorporates the topography shown in Figure 5. One important observation is that topography

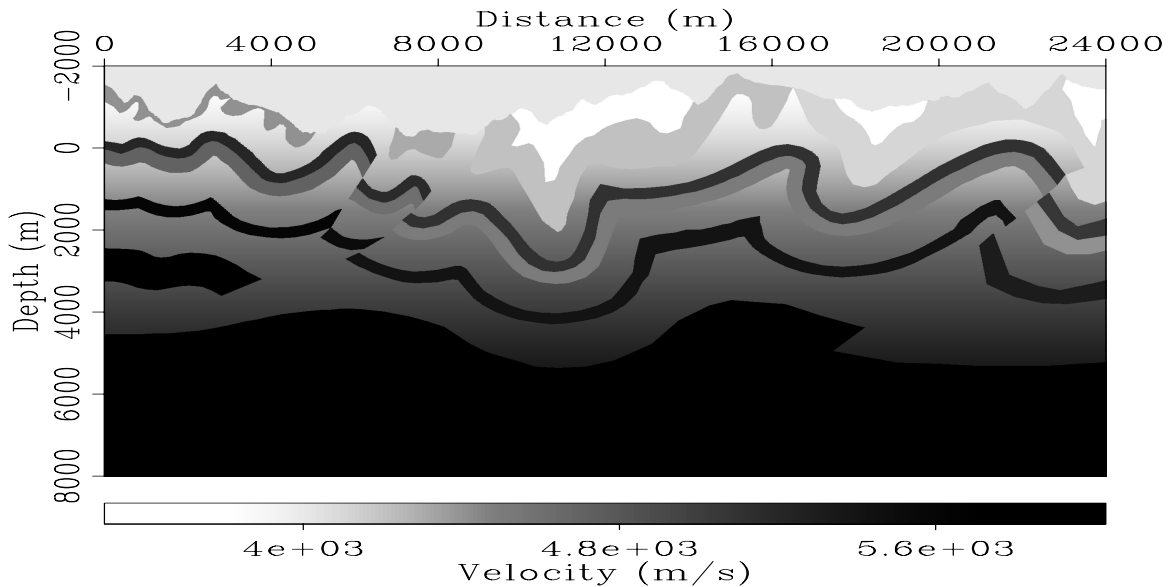


Figure 5: Foothills velocity model constructed from composite 2-D geologic model from northeastern British Columbia, Canada. Total elevation relief is approximately 1600 m. The topographic boundary of interest is demarcated by the velocity model discontinuity nearest to the surface. `jeff1-Foothills.vel` [ER]

causes focusing of the coordinate system. In particular, the coordinate system compresses under local topographic maxima, and expands beneath local topographic minima. This suggests that Jacobian spreading factor, J , in (3) will be strongly dependent on the local radius of curvature of the topographic surface. However, as the topographic fronts move farther from the surface, the topographic influence diminishes and the fronts move toward becoming a flat datum. (Hence, this approach could be used for wavefield datuming.)

A prestack wave-equation imaging test was conducted using a synthetic data set generated by an acoustic, 2-D, finite-difference code through the model shown in Figure 5. The data set is comprised of 278 shot gathers with a split-spread geophone geometry where absolute offsets range between 15 m and 3600 m. Geophone and source spacing are 15 m and 90 m, respectively. Data were generated on a regular Cartesian mesh. Thus, we interpolated the data to fit on a grid uniform along the topographic surface. Data fidelity may have been lowered by this processing step; however, we emphasize that this step is normally of modest importance since field data likely are nearly uniformly-spaced on the topographic surface.

A sample shot record at horizontal location 14040 m is shown in Figure 7. Note that the relief causes non-linear moveout of the direct arrival, and a substantial amount of topographic scattering as illustrated by the horizontal banding across the section. No preprocessing of the sections was done to remove these two potential noise sources, and the resulting image is contaminated accordingly.

A preliminary prestack migration image is presented in Figure 8. The majority of reflectors are well positioned; however, diffractions and discontinuous reflectors exist at locations

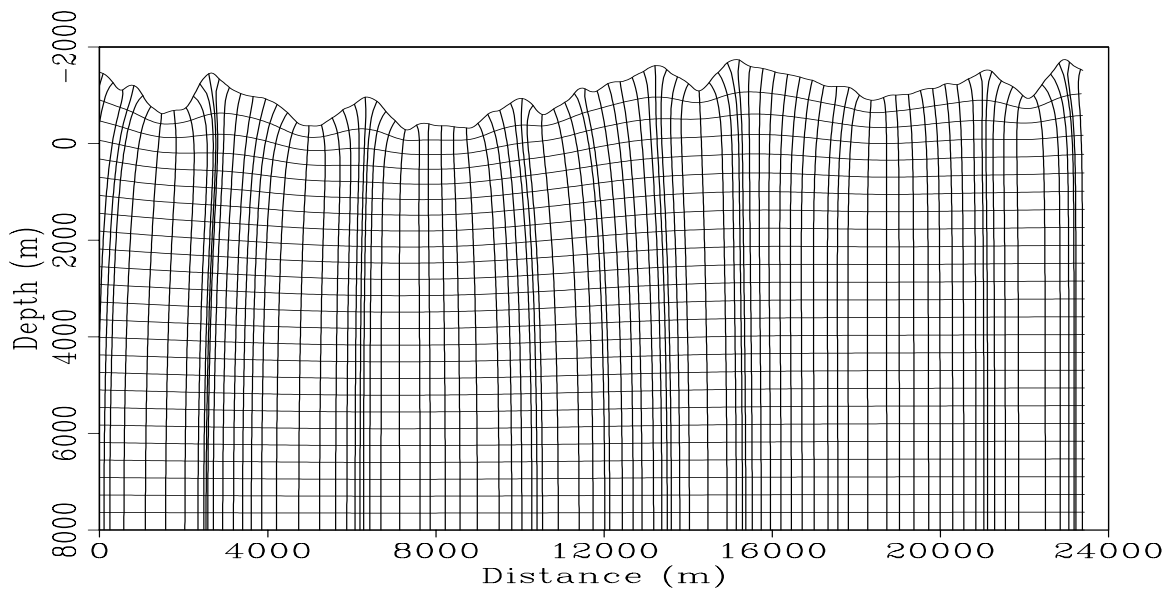


Figure 6: Topographic coordinate system constructed using conformal mapping. Note the compression of the rays under topographic maxima, and their extension under topographic minima. The influence of topography on the coordinate system diminishes farther from the surface. `jeff1-Foothills.coords` [ER]

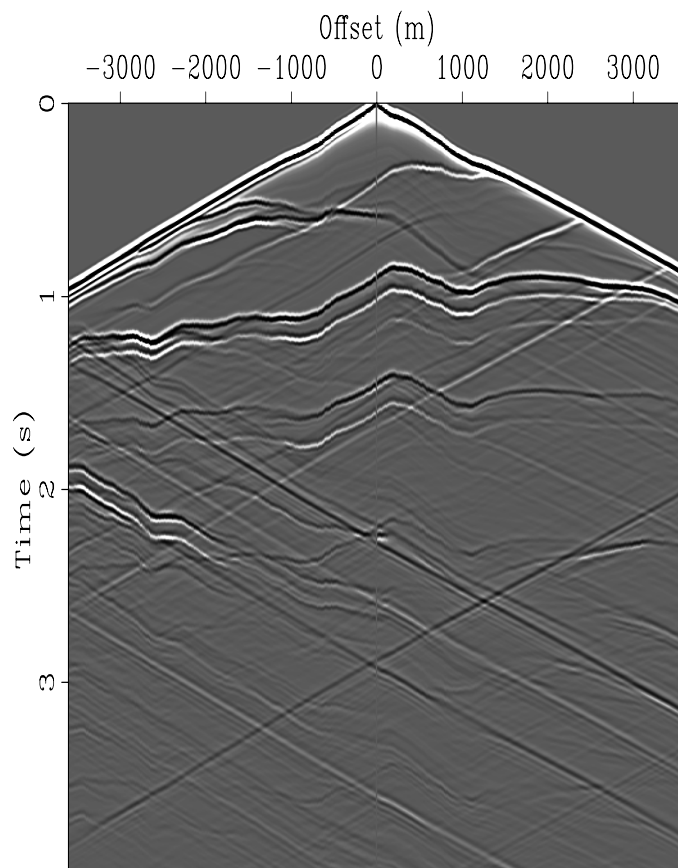


Figure 7: Shot record from source station 14040 m that shows the influence of topography. Note the non-linear moveout of the direct arrivals, and the significant amount of topographic scattering typified by horizontal streaking across the section. `jeff1-singleshot` [ER]

directly beneath topographic minima and maxima. Although these anomalies may be caused by the data regularization procedure, they more likely arise from limitations imposed by the phase-screen approximation.

Also present are vertical streaks of higher (lower) amplitude directly under local topographic minima (maxima). We attribute these anomalous amplitudes to a combination of: i) the simplicity of the weighing function used in the interpolation of the image between the topographic and Cartesian coordinate systems; and ii) our non-consideration of the dynamic terms in (6). Geological structure poorly imaged or absent include sections of the steeply-dipping fold belt, which is probably due to limitations imposed by both the limited angular bandwidth of the phase-screen approximation, and our use of only one reference medium.

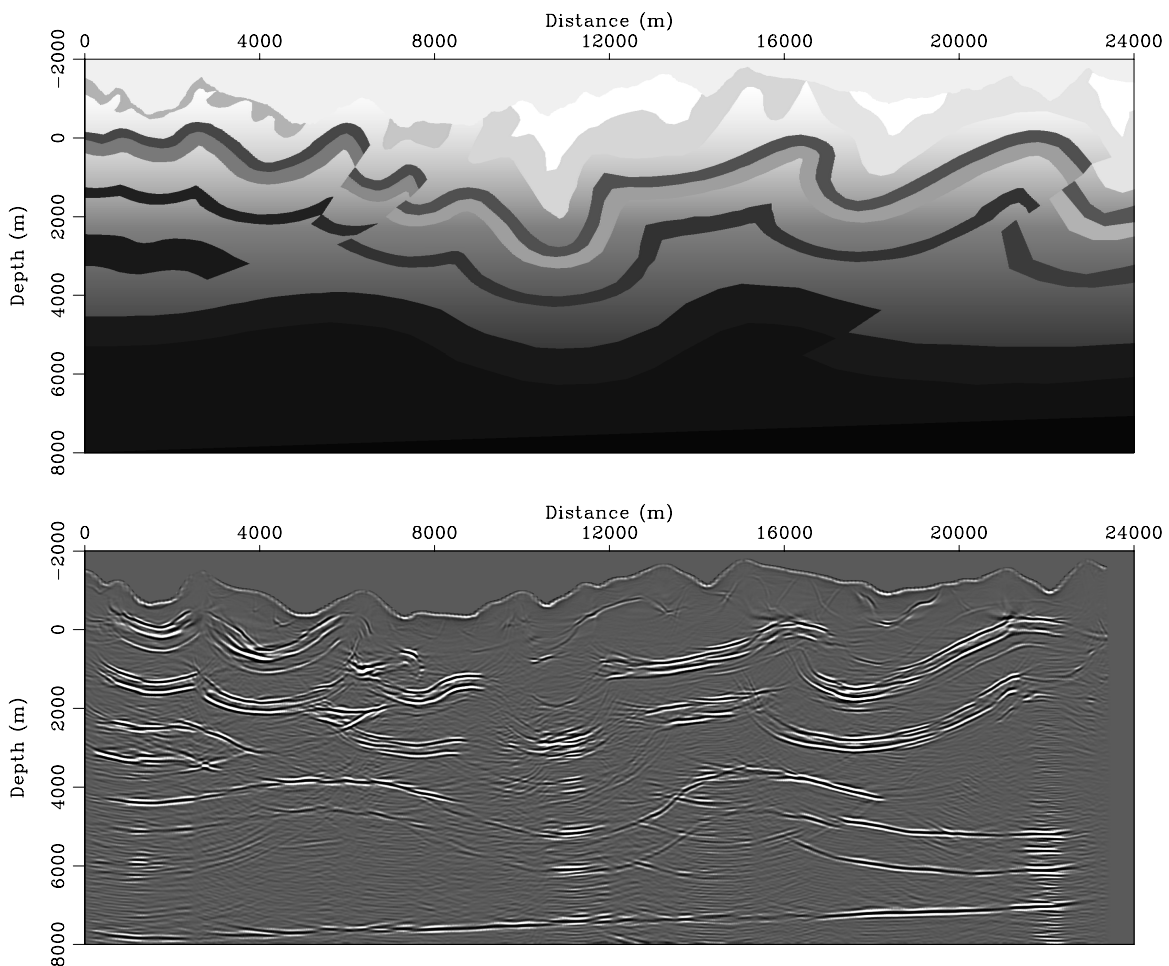


Figure 8: Top: Foothills thrust model velocity model. Bottom: The preliminary prestack migration image using Riemannian wavefield extrapolation on a coordinate system generated through conformal mapping. [jeff1-prestackimage](#) [ER]

DISCUSSION AND FUTURE WORK

The issues below are important for improving the quality of wave-equation migration directly from topography images. In some cases, we discuss ideas not yet implemented, while in others we speculate on directions of future research.

Muting direct arrivals: We did not mute out the direct arrivals from the shot gathers, which probably introduced artifacts. In principle, a first-arrival mute is fairly easy to implement; however, their non-linear moveout requires introducing more complicated muting functions. In the future, we will eliminate this source of image contamination.

Using improved mapping weighting functions: We speculate that amplitudes could become more uniform along the reflectors through the use of a better weighting function. The image is currently interpolated to the Cartesian domain using sinc-function operators, where the image points are weighted by the mapping fold. A better weighting function should include the Jacobian of the transformation between the two coordinate systems.

Including dynamic propagation terms: We have incorporated only the second-order partial differential terms in the phase-screen approximation for extrapolation direction wavenumber, k_τ . Including the remaining two dynamic terms should lead to reflectors of more uniform intensity, since these terms contribute to wavefield amplitudes.

Incorporating multiple reference media: The above image was generated using one reference medium (i.e., we performed Taylor expansions about a_0 and b_0). However, in practice many reference media (e.g., velocities) are often used to generate images through the PSPI approach. Noting that the variability of coordinate spacing is significant (and functions a and b thereby), we surmise that the incorporation of multiple reference media is likely necessary to eliminate existing kinematic errors and to improve diffraction focusing.

Implementing a separate wavefield datuming step: By extension, we have shown that this procedure works as a datuming procedure. For example, a coordinate system generated by conformal mapping could be used in an upward continuation scheme to establish the wavefield at a uniform level above topography. Standard Cartesian migration technology could then be applied directly to migrate the datumed wavefield.

CONCLUSIONS

Performing wave-equation migration directly from topographic surfaces is achievable with a minimum of preprocessing in topographic coordinate systems. We show that conformal mapping generates the required topographic coordinate systems, and that the conformal map transform determines the appropriate wavefield extrapolation equations. We also conclude that multiple reference media are likely needed to image under complicated topography, which is consistent with wavefield extrapolation practice in a Cartesian coordinate system.

By extension, we show that upward datuming on a coordinate system generated through conformal mapping transformation could work as a pre-imaging processing step. Moreover, upward datuming could be more effective than downward migration direct from topography, since a constant velocity function would likely improve the range over which the phase-screen approximation is accurate. Standard Cartesian-based migration technology could then be used to downward continue the upward datumed wavefields.

ACKNOWLEDGMENTS

We acknowledge BP for providing the data set used in the prestack migration example, and would like to thank Bee Bednar and Biondo Biondi for helpful discussions.

REFERENCES

- Berryhill, J., 1979, Wave-equation datuming: *Geophysics*, **44**, 1329–1344.
- Bevc, D., 1997, Floodint the topography: Wave-equation datuming of land data with rugged acquisition topography: *Geophysics*, **62**, 1558–1569.
- Gazdag, J., and Sguazzero, P., 1984, Migration of seismic data by phase-shift plus interpolation: *Geophysics*, **69**, 124–131.
- Gray, S., and Marfurt, K., 1995, Migration from topography: Improving the near-surface image: *J. Can. Soc. Expl. Geophys.*, **31**, 18–24.
- Jiao, J., Trickett, S., and Link, B., 2004, Wave-equation migration of land data: 2004 CSEG Convention, CSEG, CSEG Abstracts.
- Kythe, P., 1998, *Computational conformal mapping*: Birkhäuser, Boston, MA.
- Nehari, Z., 1975, *Conformal mapping*: Dover Publications Inc., New York.
- Riemann, B., 1851, Grundlagen für eine allgemeine Theorie der Funktionen einer veränderlichen komplexen grösse (1851) in collected works: Dover Publications Inc, New York.
- Sava, P., and Fomel, S., 2004, Seismic imaging using Riemannian wavefield extrapolation: submitted to *Geophysics*.
- Sava, P., 2004, High-order kernels for Riemannian wavefield extrapolation: SEP-117.

APPENDIX A

This appendix discusses the conformal mapping between polygons of arbitrary shape and the upper half plane. Assisting us in this transformation is an important conformal map transformation, termed Schwarz-Christoffel mapping, that facilitates solution of a class of BVPs with polygonal boundaries. Figure A-1 illustrates the transformation and also illustrates the basic nomenclature.

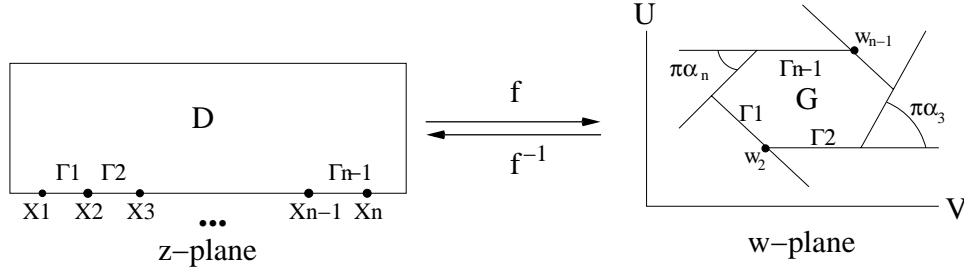


Figure A-1: Schematic of the Schwarz-Christoffel transformation between a polygonal domain in the w -plane and the upper half plane (UHP), $D = z : \Im(z) > 0$, in the z -plane. This transformation maps line segments Γ_i that lie on the $y = 0$ line in the z -plane to the line segments Γ_i that define the polygonal boundary of the w -plane according to mapping rule f . Exterior angles, $\pi\alpha_i$, are used in the transformation formula, and are defined by $|\alpha_i| > 1$ and $\sum_{i=1}^n \alpha_n = 2$. Points x_i in the z -plane are mapped to points w_i in the w -plane. jeff1-sctran [NR]

The formula for calculating the transformation is,

$$w = f(z) = A + B \int_{z_0}^z \prod_{i=1}^n (\zeta - x_i)^{-\alpha_i} d\zeta, \quad (\text{A-1})$$

where A and B are constants that determine the size and position of the polygon Γ , and α_i denotes the exterior angle (see Figure A-1). Constants A and B are computed after defining the mapping of 3 points (i.e., known points z_0). The integration is carried out along any path in the domain D that connects known point z_0 and the point in question z .

The inverse Schwarz-Christoffel transformation is given by,

$$z = f(w) = C_0 + C \int_{w_0}^w \prod_{i=1}^n (\zeta - w_i)^{-\mu_i} d\zeta, \quad (\text{A-2})$$

where μ_i are the interior angles, and integration is carried out along any path that connects known mapping point w_0 with the point in question w .

In numerical applications of Schwarz-Christoffel mapping, it is necessary to determine numerically the $(2n+2)$ parameters (i.e. all α_i , x_i and A , B) that appear in equations (A-1) and (A-2). In conformal mapping literature, this problem is termed the 'parameter problem'

(Kythe, 1998). The numerical solution to this problem requires selecting 3 points of the x -axis that map to 3 preassigned points in the u -axis (i.e. p_1 , p_2 and p_3). This allows for equation (A-1) to be segmented into the Schwarz-Christoffel integrals,

$$\begin{aligned} I_1 &= \int_{p_1}^{p_2} (\zeta - p_1)^{-\alpha_1} (\zeta - p_2)^{-\alpha_2} (\zeta - p_3)^{-\alpha_3} \dots (\zeta - p_{n-1})^{-\alpha_{n-1}} (\zeta - p_n)^{-\alpha_n} d\zeta \\ I_2 &= \int_{p_2}^{x_3} (\zeta - p_1)^{-\alpha_1} (\zeta - p_2)^{-\alpha_2} (\zeta - p_3)^{-\alpha_3} \dots (\zeta - p_{n-1})^{-\alpha_{n-1}} (\zeta - p_n)^{-\alpha_n} d\zeta \\ &\vdots \\ I_{n-2} &= \int_{x_{n-2}}^{x_{n-1}} (\zeta - p_1)^{-\alpha_1} (\zeta - p_2)^{-\alpha_2} (\zeta - p_3)^{-\alpha_3} \dots (\zeta - p_{n-1})^{-\alpha_{n-1}} (\zeta - p_n)^{-\alpha_n} d\zeta \end{aligned} \quad (\text{A-3})$$

Fortunately, the ratio of any two sides of the mapped polygon is independent of scale factors A and B . This allows the parameter problem to be written as the following series of equations:

$$I_j(x_3, x_4, \dots, x_{n-1}) = \lambda_j I_1(x_3, x_4, \dots, x_{n-1}), \quad j = 2, 3, \dots, n-2, \quad (\text{A-4})$$

where

$$\lambda_j = \frac{|w_{j+1} - w_j|}{|w_2 - w_1|} \quad j = 3, 4, \dots, n-2. \quad (\text{A-5})$$

A solution to the Schwarz-Christoffel integrals begins by expanding the series of equations (A-5) in a first order Taylor power series about initial guesses, $x_i^{(0)}$, of the true values, \tilde{x}_i . This leads to a system of equations that may be solved using Newton's method:

$$I_j^{(0)} + \sum_{v=3}^{n-1} h_v^{(1)} \frac{\partial I_j^{(0)}}{\partial x_v} = \lambda_j \left[I_1^{(0)} + \sum_{v=3}^{n-1} h_v^{(1)} \frac{\partial I_1^{(0)}}{\partial x_v} \right], \quad j = 2, \dots, n-2, \quad (\text{A-6})$$

where h_v , the correction factors that are being solved for, are applied to yield the next estimate of the vertex corners,

$$x_v^{(0)} = x_v^{(0)} + h_v^{(1)}. \quad (\text{A-7})$$

This process is repeated using n^{th} iterative updates of $h_v^{(n)}$ until the desired tolerance is reached. Finally, the Schwarz-Christoffel integrals are improper because the integrand of each integral becomes unbounded at the two points of integration. Kythe (1998) discusses using the Kantorovich method to regularize these integrals.

Regularized inversion for imaging: Effect on the data space

Marie L. Clapp¹

ABSTRACT

Imaging in areas of complex subsurfaces is difficult due to poor illumination. This poor illumination is partially caused by seismic energy being directed outside of the survey bounds. Imaging in areas with poor illumination can be improved by using Regularized Inversion with model Preconditioning (RIP). RIP helps compensate for poor illumination by regularizing amplitudes in the image. By compensating for the lost energy, RIP in essence expands the data space.

INTRODUCTION

Subsurface imaging in complex areas, particularly around salt, is plagued by poor illumination. This poor illumination is caused by seismic energy being lost due to such processes as evanescence, mode conversion, or being directed outside of the recording geometry. In this paper, I am concerned with the seismic energy that is directed outside the bounds of the seismic survey by the complex structures. This energy can be thought of as lost data.

One method for compensating for poor illumination is Regularized Inversion with model Preconditioning (RIP). RIP uses a migration operator and a regularization operator in a least-squares inversion. RIP regularizes the image of the subsurface in a way that is consistent with the recorded data. Since it is trying to compensate for the illumination problems, it is filling in parts of the image that correspond to the energy that left the surface bounds. It is as if RIP is recovering the lost data.

In this paper, I will first explain the theory for regularized inversion with model preconditioning. I will discuss how energy that leaves the survey area affects the inversion process. I will show that by expanding the data space and introducing a weighting operator that accounts for the actual recording geometry, we can account for much of the energy that escapes the survey bounds.

BASIC THEORY

My inversion scheme is based on the downward continuation migration explained by Prucha et al. (1999a). To summarize, this migration is carried out by downward continuing the wavefield

¹email: marie@sep.Stanford.EDU

in frequency space, slant stacking at each depth, and extracting the image at zero time. The result is an image in depth (z), common reflection point (CRP), and offset ray parameter (p_h) space. Offset ray parameter is related to the reflection angle (θ) and the dip angle of the reflector (ϕ) in 2-D as:

$$\frac{\partial t}{\partial h} = p_h = \frac{2 \sin \theta \cos \phi}{V(z, \text{CRP})}. \quad (1)$$

In complex areas, the image produced by downward continuation migration will suffer from poor illumination. To compensate for this, I use the migration as an operator in a least-squares inversion. The inversion procedure used in this paper can be expressed as fitting goals as follows:

$$\begin{aligned} \mathbf{0} &\approx \mathbf{Lm} - \mathbf{d} \\ \mathbf{0} &\approx \epsilon \mathbf{Am}. \end{aligned} \quad (2)$$

The first equation is the “data fitting goal,” meaning that it is responsible for making a model that is consistent with the data. The second equation is the “model styling goal,” meaning that it allows us to impose some idea of what the model should look like using the regularization operator \mathbf{A} . The model styling goal also helps to prevent a divergent result.

In the data fitting goal, \mathbf{d} is the input data and \mathbf{m} is the image obtained through inversion. \mathbf{L} is a linear operator, in this case it is the adjoint of the angle-domain wave-equation migration scheme summarized above and explained thoroughly by Prucha et al. (1999b). In the model styling goal, \mathbf{A} is a regularization operator and ϵ controls the strength of the regularization.

Unfortunately, the inversion process described by fitting goals (2) can take many iterations to produce a satisfactory result. I can reduce the necessary number of iterations by making the problem a preconditioned one. I use the preconditioning transformation $\mathbf{m} = \mathbf{A}^{-1}\mathbf{p}$ (Fomel et al., 1997; Fomel and Claerbout, 2003) to give us these fitting goals:

$$\begin{aligned} \mathbf{0} &\approx \mathbf{LA}^{-1}\mathbf{p} - \mathbf{d} \\ \mathbf{0} &\approx \epsilon \mathbf{p}. \end{aligned} \quad (3)$$

\mathbf{A}^{-1} is obtained by mapping the multi-dimensional regularization operator \mathbf{A} to helical space and applying polynomial division (Claerbout, 1998). I call this minimization scheme Regularized Inversion with model Preconditioning (RIP).

The question now is what the regularization operator \mathbf{A} is. In this paper, I will use two different regularization schemes. The first, which I call geophysical regularization, acts horizontally along the offset ray parameter axis. Rather than using the derivative operator used by Kuehl and Sacchi (2001) or the steering filter used by Prucha et al. (2000), I have created a symmetrical filter by cascading two steering filters that are mirror images of each other. The other regularization scheme that will be demonstrated in this paper is called geological regularization. This operator acts along user-specified dips in the CRP-depth plane. It is a steering filter constructed from the dips of picked reflectors.

LOST SEISMIC ENERGY AND THE FITTING GOALS

In a perfect world, we would have perfect data and the data fitting goal would allow us to construct a perfect model of the subsurface without needing any regularization. However, we never have perfect data. It is always corrupted by noise and the acquisition geometry is always a compromise between cost and what would provide sufficient data to image the subsurface. The latter is a particularly bad problem in areas of complex subsurface. Subsurface volumes with high velocity contrasts, such as salt bodies or even the simple low velocity lens model seen in Figure 1, are difficult to image at least partially due to seismic energy being directed outside of the limited survey area. The rays in Figure 1 show how seismic energy that is reflected at the flat reflector is affected by the low velocity lens. The maximum offset used in this paper is 4000 m, so the energy that is redirected by the lens will not be recorded. If we look at the synthetic data generated for this model (left panel of Figure 2), we can see the bounds of the survey cutting off the recorded events. The energy that leaves the survey bounds causes the migration result (right panel of Figure 2) to have holes in the common image gathers (CIGs).

Figure 2 indicates that we need to reconsider our fitting goals. Our model is incomplete because we are missing data. If we include the data that leaves the survey (\mathbf{d}_L), our fitting goals become:

$$\begin{aligned} \mathbf{0} &\approx \mathbf{L}\mathbf{A}^{-1}\mathbf{p} - \begin{bmatrix} \mathbf{d} \\ \mathbf{d}_L \end{bmatrix} \\ \mathbf{0} &\approx \epsilon\mathbf{p}. \end{aligned} \quad (4)$$

Initially, \mathbf{d}_L is set to zero, since by definition we haven't recorded it. However, as we perform conjugate-gradient iterations of the fitting goals, regularizing the model with each iteration, we are filling in the parts of the model that correspond to \mathbf{d}_L and thereby reconstructing some version of \mathbf{d}_L .

In practice, RIP includes \mathbf{d}_L by padding the original data space with zero traces. However, since we are doing conjugate-gradient iterations, it is important to mask out the padded traces during each iteration. Otherwise the "recovered" \mathbf{d}_L would exist in the data residual space and confuse the minimization. Defining

$$\mathbf{d}_{\text{pad}} = \begin{bmatrix} \mathbf{d} \\ \mathbf{d}_L \end{bmatrix} \quad (5)$$

and including the weighting operator \mathbf{W} , the fitting goals become:

$$\begin{aligned} \mathbf{0} &\approx \mathbf{W}(\mathbf{L}\mathbf{A}^{-1}\mathbf{p} - \mathbf{d}_{\text{pad}}) \\ \mathbf{0} &\approx \epsilon\mathbf{p}. \end{aligned} \quad (6)$$

Figure 1: Velocity model with a flat reflector under a low velocity lens. The maximum offset used for this experiment is 4000 m, so some of the rays representing seismic energy are directed outside of the survey bounds. Synthetic provided by Bill Symes and The Rice Inversion Project. [marie1-symesray](#) [CR]

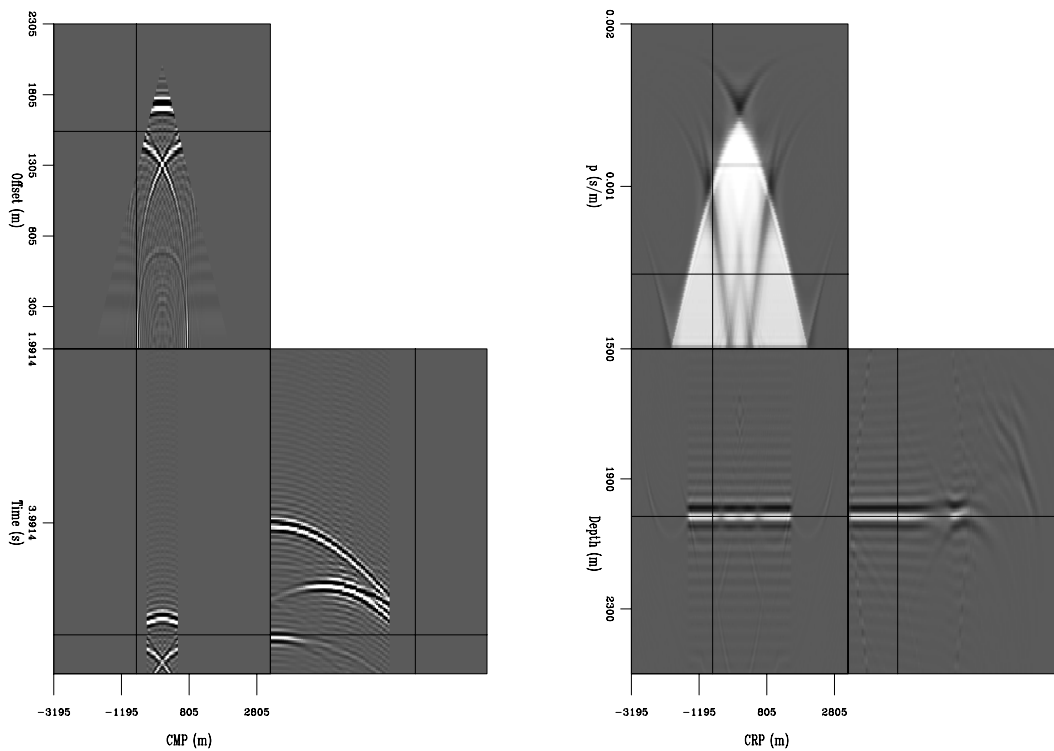
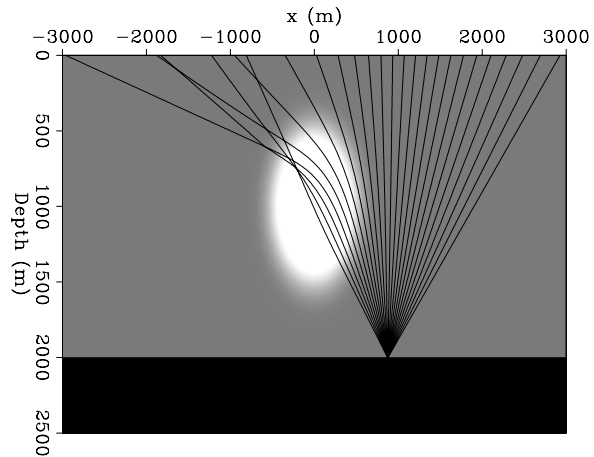


Figure 2: Left: The recorded data displayed as a flattened cube. The top panel is a time slice, the lower left is a common offset section and the lower right is a CMP gather. The triangular shape seen in the time slice is caused by the limited survey geometry. Right: The migration result. The top panel is a depth slice, lower left is a common offset ray parameter section, and lower right is a CIG. Note the holes caused by illumination problems in the reflector.

[marie1-dat.mig](#) [CR]

EFFECT ON THE DATA SPACE

To see how RIP affects the data space, I first ran 3 iterations of RIP with geophysical regularization. The resulting image (right panel of Figure 3) shows that the shadow zones are beginning to fill in. The data space corresponding to this model (left panel of Figure 3) shows that we now have energy extending outside of the original data (left panel of Figure 2). This “recovered” data has lower amplitude than the recorded data, but theory suggests that with more iterations it would become similar in amplitude.

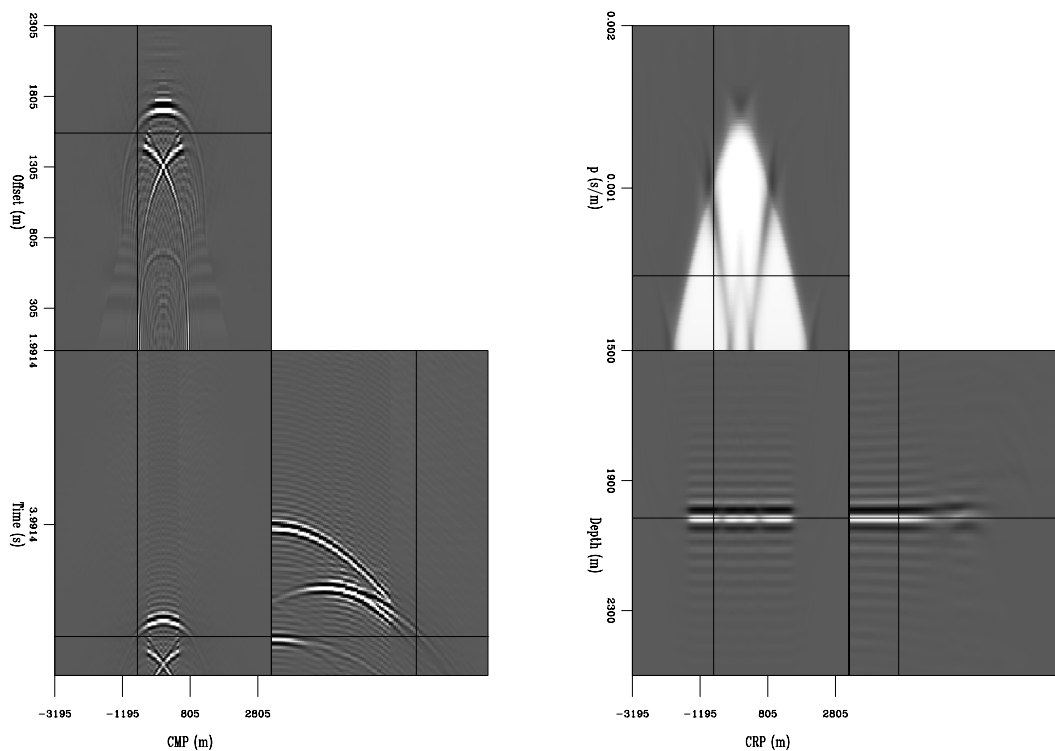


Figure 3: Left: Data space after 3 iterations of geophysical RIP. Right: RIP result after 3 iterations. `marie1-datex.3it1eps` [CR]

I also ran 3 iterations of RIP with geological regularization. This result (right panel of Figure 4) shows that the shadow zones are almost completely gone. The corresponding data space (left panel of Figure 4) has extended events with almost the same amplitude as the original data. The similarity in amplitude after only 3 iterations is due to the use of regularization along p_h and in the CRP-depth plane. In cases where the reflectors used to create the steering filter are easily interpreted, as for this simple example, geological regularization will provide a better image faster than geophysical regularization.

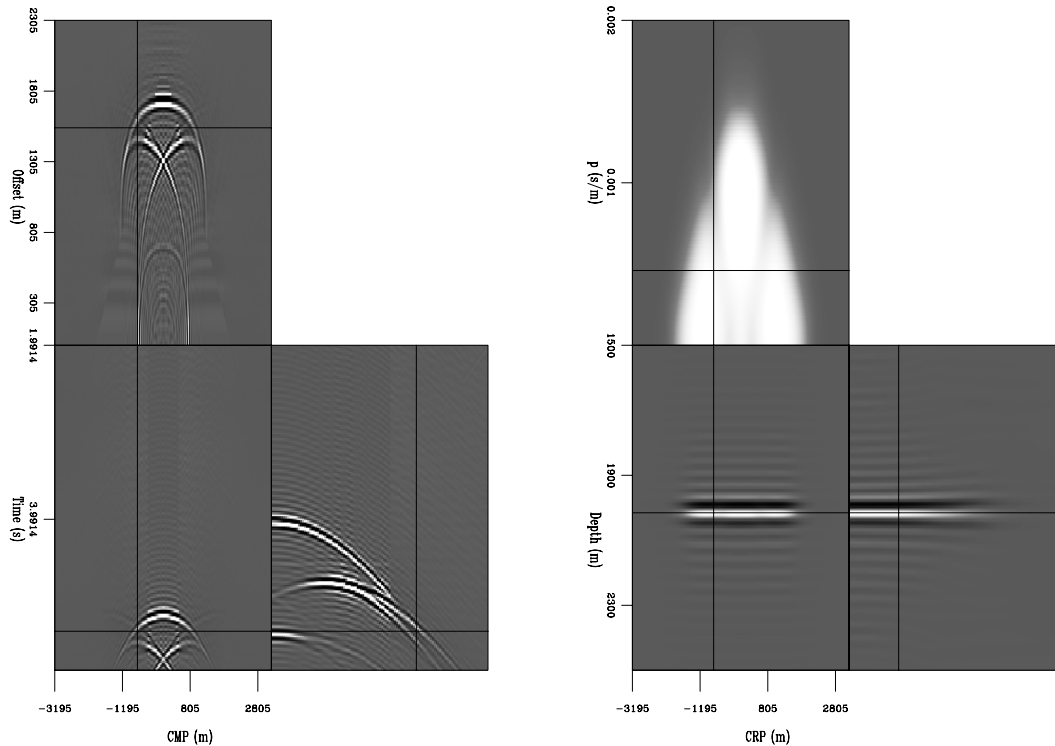


Figure 4: Left: Data space after 3 iterations of geological RIP. Right: RIP result after 3 iterations. `marie1-datex.2d.3it1eps` [CR]

CONCLUSIONS

Regularized Inversion with model Preconditioning (RIP) helps to compensate for poor illumination. RIP produces images with more consistent amplitudes in shadow zones. This partially corresponds to energy that has left the survey area. I have demonstrated that RIP, both with geophysical and geological regularization, essentially expands the data space to recover that lost energy.

ACKNOWLEDGMENTS

I would like to thank Bill Symes and The Rice Inversion Project for the synthetic dataset used in my experiments.

REFERENCES

Claerbout, J., 1998, Multidimensional recursive filters via a helix: *Geophysics*, **63**, no. 05, 1532–1541.

- Fomel, S., and Claerbout, J., 2003, Multidimensional recursive filter preconditioning in geophysical estimation problems: *Geophysics*, **68**, no. 2, 577–588.
- Fomel, S., Clapp, R., and Claerbout, J., 1997, Missing data interpolation by recursive filter preconditioning: *SEP-95*, 15–25.
- Kuehl, H., and Sacchi, M., 2001, Generalized least-squares dsr migration using a common angle imaging condition: 71st Ann. Internat. Meeting, Soc. Expl. Geophysics, Expanded Abstracts, 1025–1028.
- Prucha, M., Biondi, B., and Symes, W., 1999a, Angle-domain common image gathers by wave-equation migration: 69th Ann. Internat. Meeting, Soc. Expl. Geophysics, Expanded Abstracts, 824–827.
- Prucha, M. L., Biondi, B. L., and Symes, W. W., 1999b, Angle-domain common image gathers by wave-equation migration: *SEP-100*, 101–112.
- Prucha, M. L., Clapp, R. G., and Biondi, B., 2000, Seismic image regularization in the reflection angle domain: *SEP-103*, 109–119.



Bound constrained optimization: Application to the dip estimation problem

*Antoine Guitton*¹

ABSTRACT

A bound constrained optimization algorithm called L-BFGS-B is presented. It combines a trust region method with a quasi-Newton update of the Hessian and a line-search. This algorithm is tested on the non-linear dip estimation problem. Results show that the optimization algorithm converges effectively toward a model with bounds. Furthermore, bounds improve the estimated dips where plane-waves with different slopes overlap (e.g., with aliased data). When no constraints are applied, the algorithm is of comparable speed to a conjugate gradient solver.

INTRODUCTION

Most geophysical inverse problems require, explicitly or implicitly, that the final model is within a range of acceptable values. For instance, densities should always be positives, P-waves velocity should be greater than S-waves velocity, etc. These bounds, or constraints, on the final model are called simple bounds. Many different techniques have been developed by the optimization community to solve inverse problems with simple bounds. What makes these methods attractive is their cost and ease of use.

Among the variety of bound constrained methods, the L-BFGS-B technique (Zhu et al., 1997) is very appealing. The L-BFGS-B method is an extension of the well-known, quasi-Newton, limited-memory BFGS technique (Broyden, 1969; Fletcher, 1970; Goldfarb, 1970; Shanno, 1970; Nocedal, 1980; Liu and Nocedal, 1989) that can impose simple bounds on the model parameters. L-BFGS-B (Limited-memory BFGS with Bounds) incorporates a trust region method with update of the Hessian (or second derivative) and a line search. There are three main reasons why L-BFGS-B is chosen for this task. First, the L-BFGS method has been already successfully applied on different geophysical optimization problems such as minimization of the Huber norm (Guitton and Symes, 2003) or multiple attenuation with sparse radon transforms (Sava and Guitton, 2003). Second, the memory requirements and the computation costs for L-BFGS-B are limited. Finally, the user interface is very simple, making its implementation within existing code very simple.

In this paper, the L-BFGS-B method is presented with a few algorithmic details. These details include the gradient projection technique and the trust region method. Both elements

¹email: antoine@sep.stanford.edu

are blended inside the L-BFGS-B algorithm to insure that the estimated models are within a desired range of values. As an illustration, L-BFGS-B is tested on the dip estimation problem as formulated by Fomel (2002). L-BFGS-B is an improvement over the conventional conjugate gradient approach because it allows the incorporation of simple bound constraints on the dipoles. Several examples illustrate the dip estimation results.

OPTIMIZATION

In this section, the basic ideas behind bound constrained optimization algorithms are presented. Then the L-BFGS-B method is succinctly described.

The problem

The goal of the proposed algorithm is to find a vector of model parameters \mathbf{x} such that we minimize (Kelley, 1999)

$$\min f(\mathbf{x}) \text{ subject to } \mathbf{x} \in \Omega, \quad (1)$$

where

$$\mathbf{x} \in \Omega = \{\mathbf{x} \in \mathbb{R}^N \mid l_i \leq x_i \leq u_i\}, \quad (2)$$

with l_i and u_i being the lower and upper bounds for the model x_i , respectively. In this case, l_i and u_i are called simple bounds. They can be different for each point of the model space. The model vector that obeys equation (1) is called \mathbf{x}^* .

The sets of indices i for which the i th constraint are active/inactive are called the active/inactive sets $A(x)/I(x)$. Most of the algorithms used to solve bound constrained problems first identify $A(x)$ and then solve the minimization problem for the free variables of $I(x)$.

Gradient Projection Algorithm

Identifying $A(x)$ is a minimization problem in itself. An effective way to find $A(x)$ is by using the gradient projection method (Kelley, 1999). First, define P as the projection onto Ω of \mathbf{x} such that for each x_i we have

$$P(x_i) = \begin{cases} l_i & \text{if } x_i \leq l_i, \\ x_i & \text{if } l_i \leq x_i \leq u_i, \\ u_i & \text{if } x_i \geq u_i. \end{cases} \quad (3)$$

From this definition, one can modify the classical steepest descent algorithm by projecting it onto the feasible region as follows:

$$\mathbf{x}_{k+1} = P(\mathbf{x}_k - \lambda \mathbf{g}_k), \quad (4)$$

where k is the iteration number, \mathbf{g}_k is the gradient of $f(\mathbf{x})$ at iteration k and λ is the step-length given by a line search scheme. Given the current position \mathbf{x}_k , finding the local minimizer is relatively straightforward. The important property of the projection algorithm is that the active set after many iterations is the same as the active set of the solution vector \mathbf{x}^* . Then, the exact solution of the projected gradient is not needed and only an approximate one is. Then, the inactive set can be optimized for the unconstrained variables, the bounded variables being held fixed. The unconstrained problem can be solved by any method for unconstrained optimization. The method in this paper is based on a trust region method that incorporates two important variations: first, line searches are used; second, the Hessian of the objective function (or second derivative) is approximated with BFGS matrices.

Trust region methods

Trust region methods are widely popular for solving problems where the Hessian has regions of negative curvatures (Kelley, 1999). The basic idea behind these methods is to fit the objective function locally with a quadratic model near a point \mathbf{x}_k :

$$m(\mathbf{x}) = f(\mathbf{x}_k) + \mathbf{g}_k^T(\mathbf{x} - \mathbf{x}_k) + (\mathbf{x} - \mathbf{x}_k)^T \mathbf{B}_k (\mathbf{x} - \mathbf{x}_k)/2, \quad (5)$$

where $()^T$ is the transpose and \mathbf{B}_k is the Hessian of $f(\mathbf{x})$ at iteration k . The goal is to find an \mathbf{x} that minimizes $m(\mathbf{x})$ such that

$$\|\mathbf{x} - \mathbf{x}_k\| \leq \Delta, \quad (6)$$

where Δ is the trust region radius. Once a local minimizer is found, either the step is accepted, or the radius Δ is changed, or both. Termination criterion end the process. In the most simple case, an update of \mathbf{x}_k is obtained by minimizing the projected steepest descent onto the quadratic area

$$\Phi(\lambda) = m(\mathbf{x}_k - \lambda \mathbf{g}_k), \quad (7)$$

with

$$\|\mathbf{x}_k - \lambda \mathbf{g}_k\| \leq \Delta.$$

This update is also called the Cauchy point. This technique resembles quite closely the projection gradient algorithm to find the active set $A(\mathbf{x})$. It is then not surprising that many algorithms for bound constrained optimization are either completely or partially based on trust region methods.

The algorithm used in this paper does not involve any trust region radii, but line search algorithms instead. Yet, this algorithm keeps the concept of fitting the objective function locally with a quadratic form in equation (5) to find the minimum of $f(\mathbf{x})$ in equation (1).

The L-BFGS-B algorithm

The L-BFGS-B algorithm is an extension of the L-BFGS algorithm to handle simple bounds on the model (Zhu et al., 1997). The L-BFGS algorithm is a very efficient algorithm for solving large scale problems. L-BFGS-B borrows ideas from the trust region methods while keeping the L-BFGS update of the Hessian and line search algorithms. Methods based completely on the trust region techniques exist and are freely available. Among them, the program SBMIN from the LANCELOT package² (written in Fortran 77) is very popular (Conn et al., 1992). The original L-BFGS-B is freely available in Fortran 77 from the Northwestern University webpage³.

The L-BFGS-B works as follows for one iteration:

1. Find an approximation of the Cauchy point for

$$\Phi(\lambda) = m(\mathbf{x}(\lambda)) = m(P(\mathbf{x}_k - \lambda \mathbf{g}_k)), \quad (8)$$

with $m(\mathbf{x})$ being the quadratic form in equation (5). Identify $A(\mathbf{x})$ and $I(\mathbf{x})$.

2. Minimize the quadratic form in equation (5) for the unconstrained variables. This step gives a search direction.
3. Perform a line search along the new search direction to find the minimum of $f(\mathbf{x})$.
4. Update the Hessian with the L-BFGS method (Nocedal, 1980) and check if convergence is obtained.

In a “pure” trust region method, step (3) is replaced by tests assessing the success of the update by measuring the difference between the quadratic form and the true objective function at the update. In addition, the radius Δ is also examined.

The L-BFGS-B algorithm is affordable for very large problems. The memory requirement is roughly $(12 + 2m)N$ where m is the number of BFGS updates kept in memory and N the size of the model space. In practice, $m = 5$ is a typical choice. Per iteration, the number of multiplications range from $4mN + N$ when no constraints are applied to m^2N when all variables are bounded. The program offers the freedom to have different bounds for different points of the model space. In addition, some points can be constrained while others are not.

There are three different stopping criteria for the L-BFGS-B algorithm. First the program stops when the maximum number of iterations is reached. Or, the program stops when the decrease of the objective function becomes small enough. Or, the program stops when the norm of the projected gradient (in a ℓ^∞ sense) is small enough.

Now for the bells and whistles, tests indicate that the L-BGFS-B algorithm ran in single precision with no constraints is not quite twice as slow as a conjugate gradient solver per

²<http://www.cse.clrc.ac.uk/nag/lancelot/lancelot.shtml>

³<http://www.ece.northwestern.edu/nocedal/lbfgsb.html>

iteration. This result is quite remarkable when considering that L-BFGS-B works for any type of non-linear (or linear) problem with line searches. In addition, the number of iterations needed to convergence is almost identical for both L-BFGS-B and the conjugate gradient solver. In the next section, the L-BFGS-B algorithm is utilized to estimate local dips from seismic data.

APPLICATION TO THE DIP ESTIMATION PROBLEM

The goal of dip estimation is to find a local stepout, σ , that destroys the local plane wave such that,

$$0 \approx \frac{\partial u}{\partial h} + \sigma \frac{\partial u}{\partial \tau}, \quad (9)$$

where u is the wavefield at time τ and offset h . For all gathers, we evaluate the slope σ with a method based on high-order plane-wave destructor filters (Fomel, 2002). With the Z transform notation, Fomel (2002) shows that there is a 2-D filter

$$C_n(Z_t, Z_h) = B_n(Z_t^{-1}) - Z_h B_n(Z_t), \quad (10)$$

with

$$B_n(Z_t) = \sum_{k=-n/2}^{n/2} a_k(\sigma^{n-1}) Z_t^k, \quad (11)$$

that annihilates the local plane wave. The number of coefficients for the filter B_n is n . The filter coefficients $a_k(\sigma^{n-1})$ are functions of σ^{n-1} as detailed in equations (9) and (10) of Fomel (2002). For instance, if $n = 3$, we have

$$\begin{aligned} a_{-1}(\sigma^2) &= \frac{(1-\sigma)(2-\sigma)}{12}, \\ a_0(\sigma^2) &= \frac{(2+\sigma)(2-\sigma)}{6}, \\ a_1(\sigma^2) &= \frac{(1+\sigma)(2+\sigma)}{12}. \end{aligned} \quad (12)$$

In equation (10), σ is unknown and is estimated with a non-linear solver.

Inversion

Fomel (2002) shows that a possible solution to the slope estimation problem is obtained by minimizing the non-linear function

$$f(\sigma) = \|\mathbf{C}(\sigma)\mathbf{d}\|^2, \quad (13)$$

where $\mathbf{C}(\sigma)$ is the operator convolving the data with the 2-D filter $C_n(Z_t, Z_h)$ and \mathbf{d} is the known data. Fomel (2002) proposes iterating with a Gauss-Newton algorithm:

$$\sigma_{k+1} = \sigma_k - (\mathbf{C}(\sigma_k)' \mathbf{d} \mathbf{C}(\sigma_k)' \mathbf{d})^{-1} \mathbf{C}(\sigma_k)' \mathbf{d} \mathbf{C}(\sigma_k) \mathbf{d}, \quad (14)$$

where the step is estimated with a conjugate gradient method. One problem with this approach is that it converges well only if we are close enough to the true solution. Another problem stems from the fact that no line search in the gradient direction is implemented. Therefore, this method might oscillate close to the solution.

To make the dip estimation more robust and also to incorporate the possibility to bound-constrain the dips, the L-BFGS-B method is used instead of the Gauss-Newton approach. For the L-BFGS-B method, similar to BFGS, we need to estimate the function and its gradient. Incorporating a regularization operator \mathbf{R} that penalizes differences between adjacent dip values, the objective function becomes

$$f(\sigma) = \frac{1}{2} (\|\mathbf{C}(\sigma) \mathbf{d}\|^2 + \epsilon^2 \|\mathbf{R} \sigma\|^2) \quad (15)$$

and the gradient is

$$\mathbf{g}(\sigma) = \mathbf{C}(\sigma)' \mathbf{d} \mathbf{C}(\sigma) \mathbf{d} + \epsilon^2 \mathbf{R}' \mathbf{R} \sigma. \quad (16)$$

The dips can be then estimated reliably. In the next section, the L-BFGS-B method is illustrated on different examples. These examples illustrate that the bound constrained optimization improves the dip values when events with different local slopes overlap.

EXAMPLES

This section presents several examples of the dip estimation problem with bound constraints. All of these examples were computed with double precision arithmetic. For most of these examples the program stopped because the objective function was not decreasing enough, thus indicating that a possible minimum was found.

Figures 1 to 6 show in (a) the input data, in (b) the estimated dips with L-BFGS-B and no constraints, in (c) the estimated positive dips and in (d), the estimated negative dips. The same clip is applied for all the color plots within each Figure. Warm colors represent positive dips whereas cold colors represent negative dips. Figures 1 and 2 illustrate that the dip estimation program with bounds work as expected, but they do not represent real challenges where, for example, multiple events with different slopes overlap.

Figure 3 shows how the bounds can improve the local dip values. In Figure 3a, when no bounds are used, a clear cut difference between positive and negative dips is visible. Applying bounds in Figures 3b and 3c, the dip estimation program is able to locate the dips of interest when aliasing is present.

On a CMP gather in Figure 4a, two lines cross at a location where the dips should be positive. If no bounds are applied, Figure 4b shows that negative dips are found instead.

Applying bounds in Figure 4c, strong positive dips are now recovered. We are able to estimate positive dips beyond aliasing, thus improving on the existing program. Similar conclusions can be made on Figure 5.

It might happen that we cannot separate dips as easily as we could in Figures 3, 4 and 5. For example, Figure 6 displays some earthquake data from Professor Peter Shearer for which positive and negative dips do not clearly separate (see, for instance, where the two black lines cross). The problem here stems from the fact that the event with negative dips (in blue) is much stronger than the overlapping event with positive dips at this location.

Finally, Figure 7 shows a dip decomposition of the data in Figure 5a. This illustrates the ability to select a small range of dips that goes beyond the simple positive/negative constraints of the preceding examples.

CONCLUSION

L-BFGS-B is an algorithm that solves non-linear problems by imposing some constraints on the model. This program incorporates concepts from trust region methods plus BFGS matrices and line searches. Per iteration, this program requires roughly $O(N)$ computations, N being the size of the model space. Used with single precision arithmetic and no bounds, this program is not quite twice as slow as conjugate gradient. Therefore, L-BFGS-B can be used for solving many non-linear geophysical problems.

As an illustration, the bound constrained optimization code was employed to estimate local dips from seismic data. These examples show that the bounds were effectively working and that this method was converging toward acceptable solutions. In addition, this technique clearly improves on the existing method without bounds by discarding non-physical dip values at locations where aliasing is present. Flattening (Lomask, 2003) could greatly benefit from this improvement.

In geophysics, the number of applications for this type of solver could be quite large. An obvious choice is velocity estimation. For instance, Dix inversion might benefit from the possibility of constraining the estimated interval velocities to a reasonable range.

ACKNOWLEDGMENTS

I would like to thank Jesse Lomask for his suggestions on this paper.

REFERENCES

- Broyden, C. G., 1969, A new double-rank minimization algorithm: AMS Notices, **16**, 670.
- Conn, A. R., Gould, N. I. M., and Toint, P. L., 1992, LANCELOT: A Fortran package for large-

- scale nonlinear optimization (Release A): Springer Series in Computational Mathematics 17.
- Fletcher, R., 1970, A new approach to variable metric methods: *Comput. J.*, **13**, 317–322.
- Fomel, S., 2002, Applications of plane-wave destruction filters: *Geophysics*, **67**, no. 06, 1946–1960.
- Goldfarb, D., 1970, A family of variable metric methods derived by variational means: *Math. Comp.*, **24**, 23–26.
- Guitton, A., and Symes, W., 2003, Robust inversion of seismic data using the Huber norm: *Geophysics*, **68**, no. 4, 1310–1319.
- Kelley, C. T., 1999, *Iterative methods for optimization: SIAM in applied mathematics*.
- Liu, D. C., and Nocedal, J., 1989, On the limited memory BFGS method for large scale optimization: *Mathematical Programming*, **45**, 503–528.
- Lomask, J., 2003, Flattening 3D seismic cubes without picking: *Soc. of Expl. Geophys.*, 73rd Ann. Internat. Mtg., 1402–1405.
- Nocedal, J., 1980, Updating quasi-Newton matrices with limited storage: *Mathematics of Computation*, **95**, 339–353.
- Sava, P., and Guitton, A., 2003, Multiple attenuation in the image space: *Soc. of Expl. Geophys.*, 73rd Ann. Internat. Mtg., 1933–1936.
- Shanno, D. F., 1970, Conditioning of quasi-Newton methods for function minimization: *Math. Comp.*, **24**, 647–657.
- Zhu, H., Byrd, R. H., and Nocedal, J., 1997, Algorithm 778: L-BFGS-B, FORTRAN routines for large scale bound constrained optimization: *ACM Transactions on Mathematical Software*, **23**, 550–560.

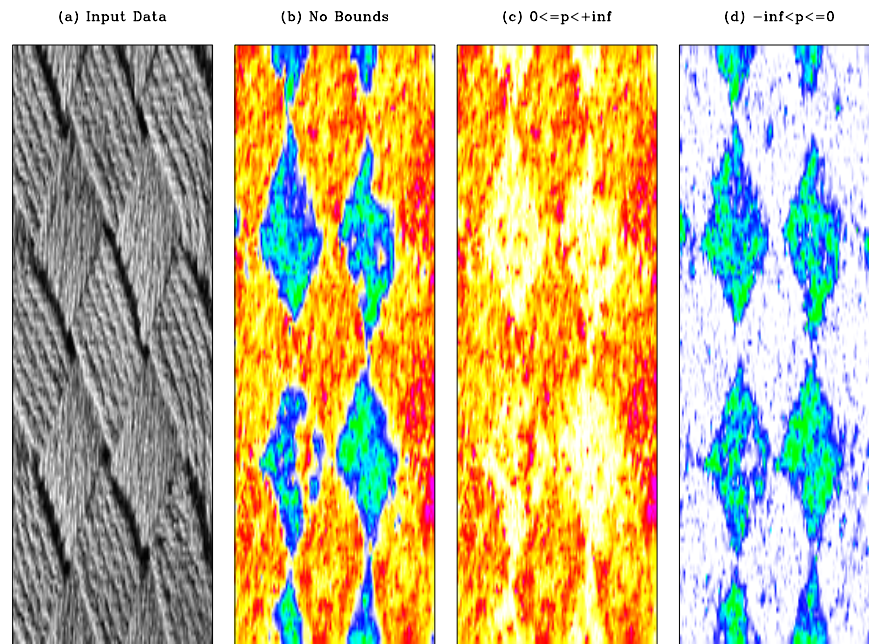


Figure 1: (a) Input data. (b) Estimated dips with L-BFGS-B without bound constraints. (c) Estimated positive dips only. (d) Estimated negative dips only. antoine1-fabricposneg [ER]

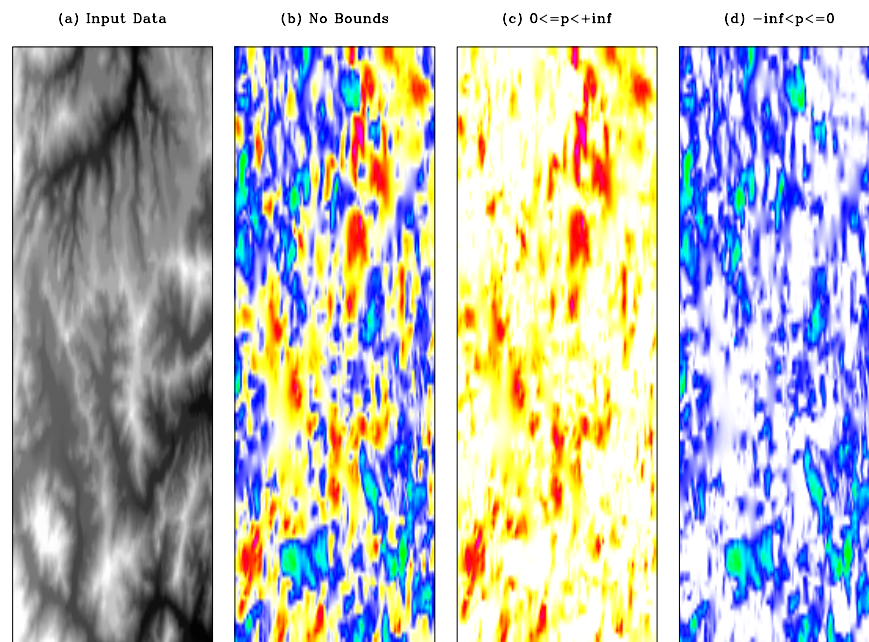


Figure 2: (a) Input data. This topographic map comes from the bay area. (b) Estimated dips with L-BFGS-B without bound constraints. (c) Estimated positive dips only. (d) Estimated negative dips only. antoine1-sfbayposneg [ER]

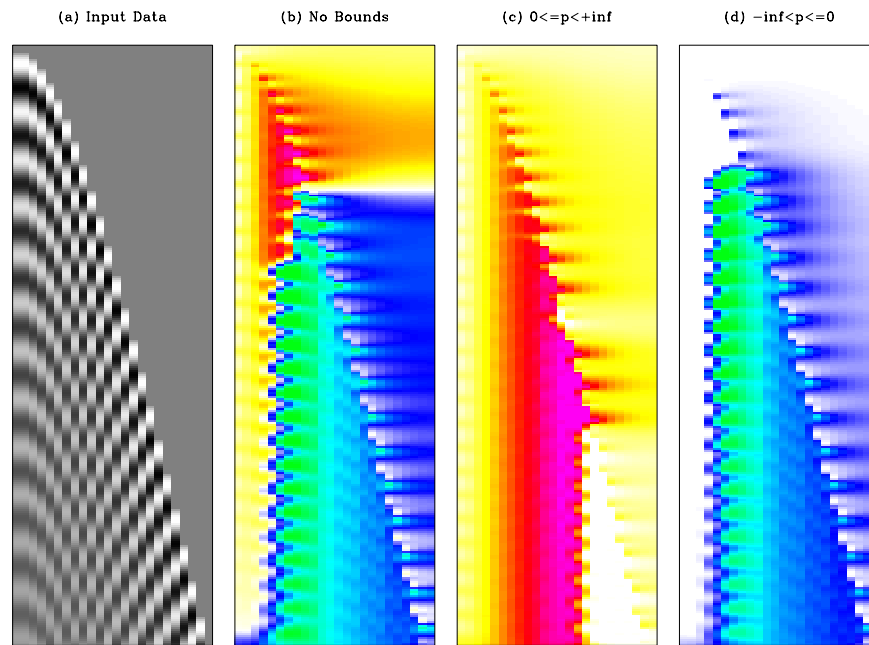


Figure 3: (a) Input data. (b) Estimated dips with L-BFGS-B without bound constraints. (c) Estimated positive dips only. (d) Estimated negative dips only. Positive and negative dips are found beyond aliasing. `antoine1-aliasposneg` [ER]

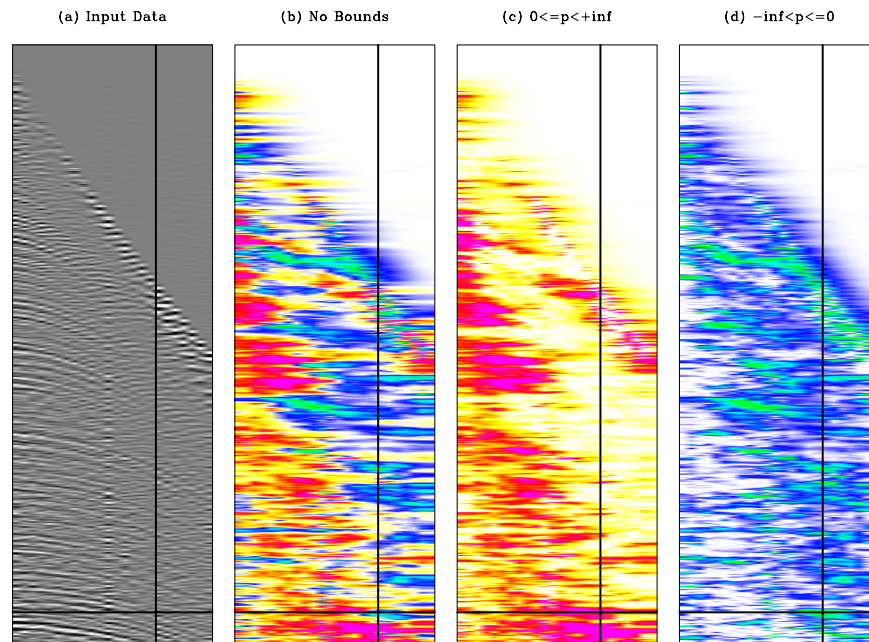


Figure 4: (a) Input data. The lines cross at a location where the dips should be positive. (b) Estimated dips with L-BFGS-B without bound constraints. Negative dips are actually found at the crossing of the lines. (c) Estimated positive dips only. The bound constrained optimization is capable of identifying the true positive dips. (d) Estimated negative dips only. `antoine1-dipposneg` [ER]

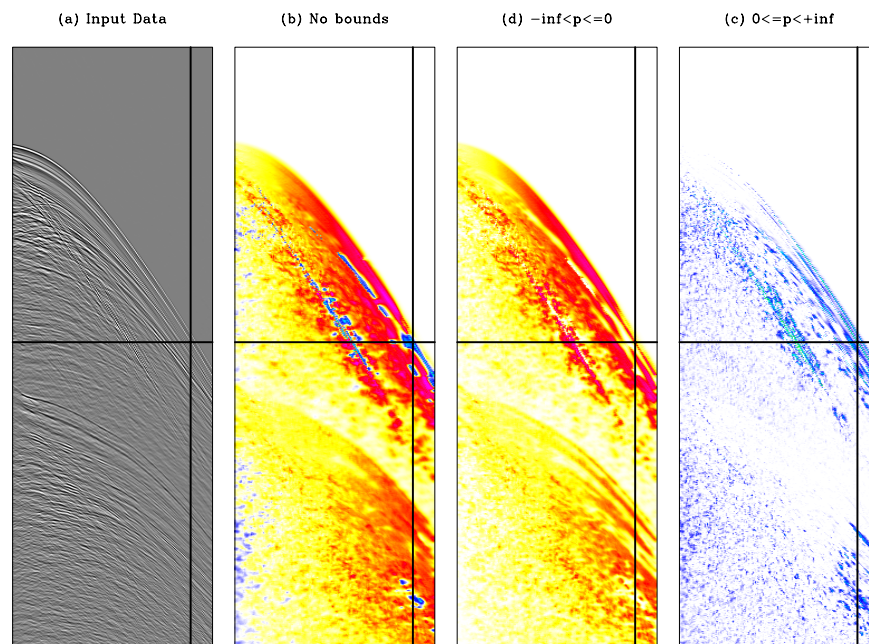


Figure 5: (a) Input data. (b) Estimated dips with L-BFGS-B without bound constraints. At the cross, negative dips are given although only positive dips should be found. (c) Estimated positive dips only. Positive dips are recovered everywhere. (d) Estimated negative dips only.

antoine1-gmdip [ER]

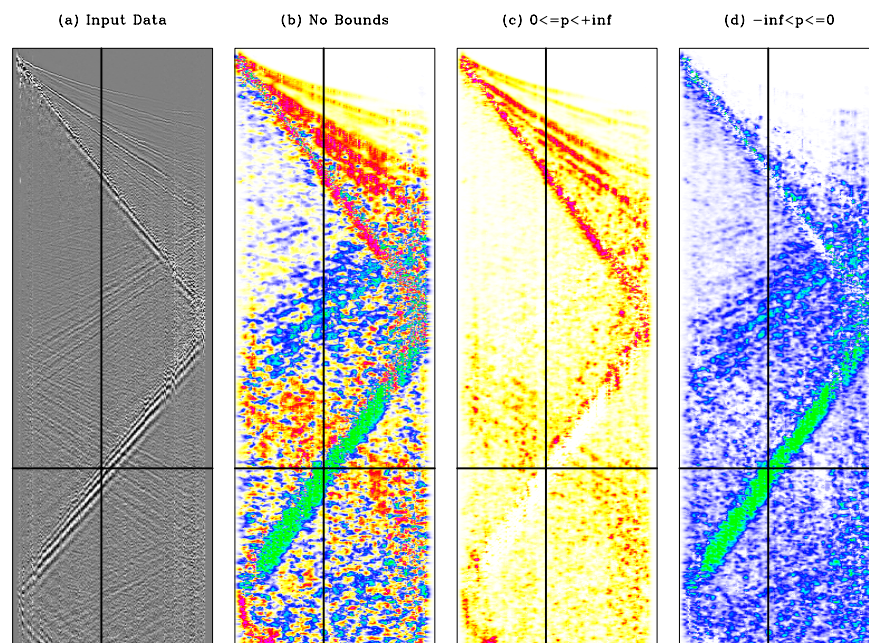


Figure 6: (a) Input data. The cross shows a location where two events overlap. (b) Estimated dips with L-BFGS-B without bound constraints. (c) Estimated positive dips only. At the cross, no positive dips are estimated because the overlapping event that goes in the other direction is too strong. (d) Estimated negative dips only.

antoine1-idaposneg [ER]

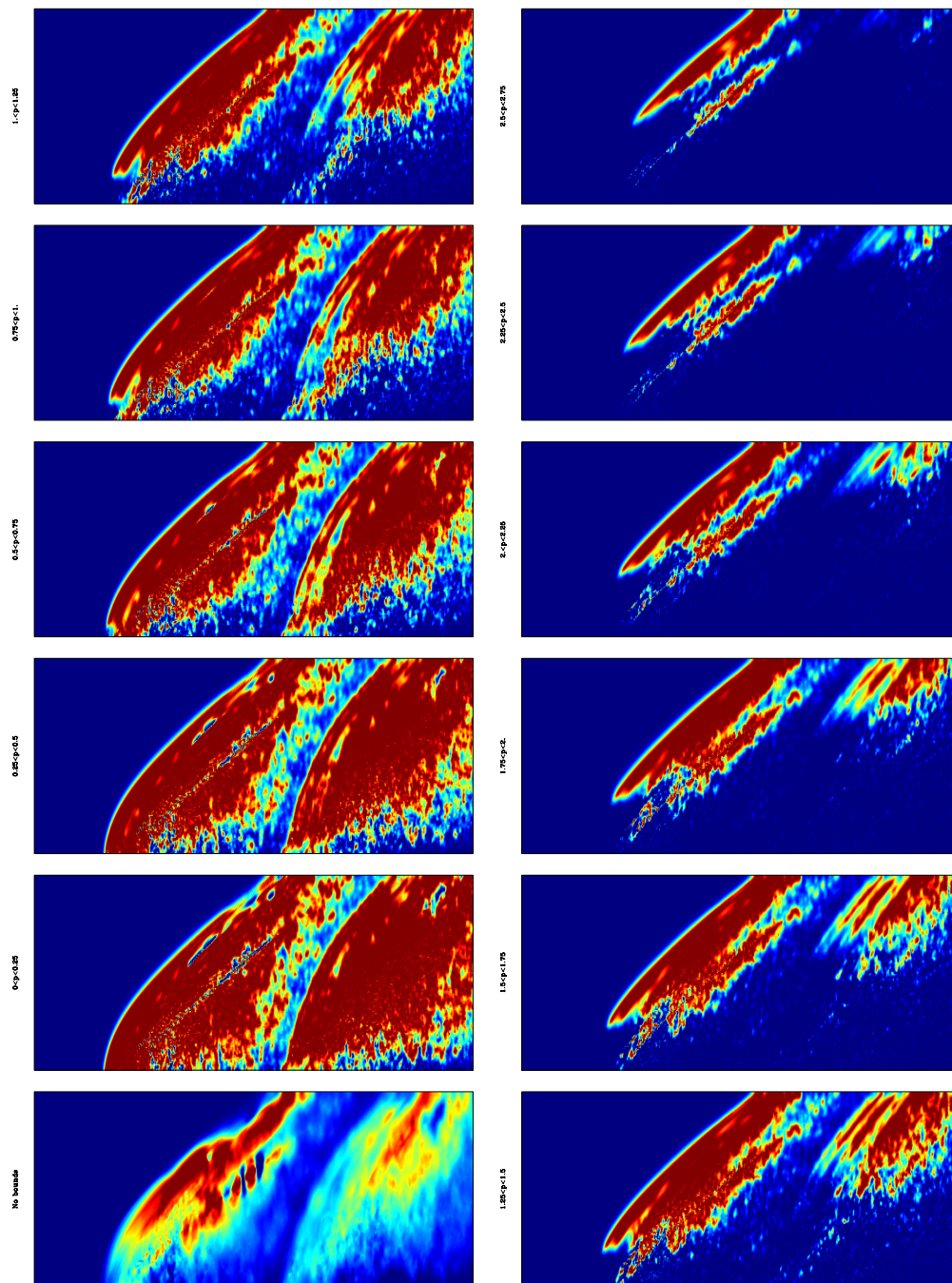


Figure 7: The first panel on the top left corner shows the dips without the bounds. Then, from left to right, top to bottom, the range of dip increases by 0.25 between each panel, starting at $0 \leq \sigma \leq 0.25$ and finishing at $2.5 \leq \sigma \leq 2.75$. The lower and upper clip values are equal to the bounds for each panel. `antoine1-gmdecomp` [ER,M]

Target-oriented computation of the wave-equation imaging Hessian

Alejandro A. Valenciano and Biondo Biondi¹

ABSTRACT

A target-oriented strategy can be applied to explicitly compute the wave-equation imaging Hessian. This approach allows us to study the characteristics of the Hessian for different acquisition and subsurface geometries (low illumination, faults, etc.). Results on the Sigsbee and the Marmousi model show that in complex areas, a diagonal approximation of the Hessian might be insufficient to obtain the correct position and amplitudes of the reflectors.

INTRODUCTION

Seismic imaging (migration) operators are non-unitary (Claerbout, 1992) because they depend on: (1) the seismic experiment acquisition geometry (Nemeth et al., 1999; Duquet and Marfurt, 1999; Ronen and Liner, 2000), (2) the complex subsurface geometry (Prucha et al., 2000; Kuehl and Sacchi, 2001) and (3), the bandlimited characteristics of the seismic data (Chavent and Plessix, 1999). Often, they produce images with reflectors correctly positioned but with biased amplitudes.

Attempts to solve this problem have used the power of geophysical inverse theory (Tarantola, 1987), which compensates for the experimental deficiencies (acquisition geometry, obstacles, etc.) by weighting the migration result with the inverse of the Hessian. The main difficulty with this approach is the explicit calculation of the inverse of the Hessian. However, in most of the situations, the direct computation of its inverse for the entire model space is practically unfeasible.

Three different paths have been followed to practically approximate the inverse of the Hessian. The first approach approximates the Hessian as a diagonal matrix (Chavent and Plessix, 1999; Rickett, 2003), which makes its inversion trivial. The second approach makes use of iterative algorithms like conjugate-gradient (Nemeth et al., 1999; Duquet and Marfurt, 1999; Ronen and Liner, 2000; Prucha et al., 2000; Kuehl and Sacchi, 2001) to implicitly calculate the inverse of the Hessian. The third approach (Guitton, 2004) approximates the inverse of the Hessian with a bank of nonstationary matching filters.

Since accurate imaging of reflectors is more important at the reservoir level, we propose

¹**email:** valencia@sep.stanford.edu, biondo@sep.stanford.edu

calculating the Hessian in a target-oriented fashion. This can be done in practice, since the new dimensions of the Hessian (in the target region alone) are smaller than the dimensions of the whole image. By knowing the characteristics of the exact Hessian, an educated choice can be made regarding how to approximate its inverse.

In this paper, we first discuss how the target-oriented Hessian can be calculated from pre-computed Green functions. We also show three numerical examples of target-oriented computed Hessians, the first in a constant velocity model, the second in the Sigsbee model (to study the effects of poor illumination in the Hessian), and the third in the Marmousi model.

LINEAR LEAST-SQUARES INVERSION

Tarantola (1987) formalizes the geophysical inverse problem by giving a theoretical approach to compensate for the experiment's deficiencies (acquisition geometry, obstacles, etc.), while being consistent with the acquired data. His approach can be summarized as follows: given a linear modeling operator \mathbf{L} to compute synthetic data \mathbf{d} ,

$$\mathbf{d} = \mathbf{L}\mathbf{m}, \quad (1)$$

where \mathbf{m} is a reflectivity model, and given the recorded data \mathbf{d}_{obs} , a quadratic cost function

$$S(\mathbf{m}) = \|\mathbf{d} - \mathbf{d}_{obs}\|^2 = \|\mathbf{L}\mathbf{m} - \mathbf{d}_{obs}\|^2 \quad (2)$$

is formed. The model of the earth $\hat{\mathbf{m}}$ that minimize $S(\mathbf{m})$ is given by

$$\hat{\mathbf{m}} = (\mathbf{L}'\mathbf{L})^{-1}\mathbf{L}'\mathbf{d}_{obs} = \mathbf{H}^{-1}\mathbf{L}'\mathbf{d}_{obs}, \quad (3)$$

where \mathbf{L}' is the adjoint of the linear operator \mathbf{L} , and $\mathbf{H} = \mathbf{L}'\mathbf{L}$ is the Hessian of $S(\mathbf{m})$.

The main difficulty with this approach is that the explicit calculation of inverse of the Hessian for the entire model space is practically unfeasible. That is why iterative algorithms like conjugate-gradient have been used to implicitly calculate the inverse of the Hessian (Nemeth et al., 1999; Duquet and Marfurt, 1999; Ronen and Liner, 2000; Prucha et al., 2000; Kuehl and Sacchi, 2001).

In the case of wave-equation migration or inversion, the operator \mathbf{L} is expensive to apply. Thus, applying this operator and its transpose iteratively is sometimes prohibitive. Among other factors, the computational cost is proportional to the number of depth steps the wave-fields need to be propagated (Audebert, 1994), and the number of iterations.

TARGET-ORIENTED HESSIAN

Since accurate imaging of reflectors is more important in the neighborhood of the reservoir, it makes sense to apply a target-oriented strategy to reduce the number of depth steps. A way to achieve this objective is to write the modeling operator \mathbf{L} in a target-oriented fashion and explicitly compute the Hessian.

In general, the synthetic data for one frequency, a shot positioned at $\mathbf{x}_s = (0, x_s, y_s)$ and a receiver positioned at $\mathbf{x}_r = (0, x_r, y_r)$ can be given by a linear operator \mathbf{L} acting on the full model space $\mathbf{m}(\mathbf{x})$ with $\mathbf{x} = (z, x, y)$ ($\mathbf{x} = (z, x)$ in $2D$) as

$$\mathbf{d}(\mathbf{x}_s, \mathbf{x}_r; \omega) = \mathbf{L}\mathbf{m}(\mathbf{x}) = \sum_{\mathbf{x}} \mathbf{G}(\mathbf{x}, \mathbf{x}_s; \omega) \mathbf{G}(\mathbf{x}, \mathbf{x}_r; \omega) \mathbf{m}(\mathbf{x}), \quad (4)$$

where $\mathbf{G}(\mathbf{x}, \mathbf{x}_s; \omega)$ and $\mathbf{G}(\mathbf{x}, \mathbf{x}_r; \omega)$ are the Green functions from the shot position \mathbf{x}_s and the receiver position \mathbf{x}_r to a point in the model space \mathbf{x} .

In equation (4), two important properties have been used (Ehinger et al., 1996): first, the Green functions are computed by means of the one-way wave equation, and second, the extrapolation is performed by using the adequate paraxial wave equations (flux conservation) (Bamberger et al., 1988).

The quadratic cost function is

$$S(\mathbf{m}) = \sum_{\omega} \sum_{\mathbf{x}_s} \sum_{\mathbf{x}_r} \|\mathbf{d} - \mathbf{d}_{obs}\|^2 = \sum_{\omega} \sum_{\mathbf{x}_s} \sum_{\mathbf{x}_r} [\mathbf{d}(\mathbf{x}_s, \mathbf{x}_r; \omega) - \mathbf{d}_{obs}]' [\mathbf{d}(\mathbf{x}_s, \mathbf{x}_r; \omega) - \mathbf{d}_{obs}], \quad (5)$$

and its second derivative with respect to the model parameters $\mathbf{m}(\mathbf{x})$ and $\mathbf{m}(\mathbf{y})$ is the Hessian

$$\mathbf{H}(\mathbf{x}, \mathbf{y}) = \frac{\partial^2 S(\mathbf{m})}{\partial \mathbf{m}(\mathbf{x}) \partial \mathbf{m}(\mathbf{y})} = \sum_{\omega} \sum_{\mathbf{x}_s} \sum_{\mathbf{x}_r} \left[\frac{\partial \mathbf{d}(\mathbf{x}_s, \mathbf{x}_r; \omega)}{\partial \mathbf{m}(\mathbf{x})} \right]' \left[\frac{\partial \mathbf{d}(\mathbf{x}_s, \mathbf{x}_r; \omega)}{\partial \mathbf{m}(\mathbf{y})} \right] \quad (6)$$

$$\mathbf{H}(\mathbf{x}, \mathbf{y}) = \sum_{\omega} \sum_{\mathbf{x}_s} \mathbf{G}'(\mathbf{x}, \mathbf{x}_s; \omega) \mathbf{G}(\mathbf{y}, \mathbf{x}_s; \omega) \sum_{\mathbf{x}_r} \mathbf{G}'(\mathbf{x}, \mathbf{x}_r; \omega) \mathbf{G}(\mathbf{y}, \mathbf{x}_r; \omega). \quad (7)$$

Notice that to compute $\mathbf{H}(\mathbf{x}, \mathbf{y})$ in equation (7), only the precomputed Green functions at model points \mathbf{x} and \mathbf{y} are needed. Thus, the size of the problem can be considerably reduced by storing the Green functions only at the target location \mathbf{x}_T . Then equation (7) reduces to

$$\mathbf{H}(\mathbf{x}_T, \mathbf{y}_T) = \sum_{\omega} \sum_{\mathbf{x}_s} \mathbf{G}'(\mathbf{x}_T, \mathbf{x}_s; \omega) \mathbf{G}(\mathbf{y}_T, \mathbf{x}_s; \omega) \sum_{\mathbf{x}_r} \mathbf{G}'(\mathbf{x}_T, \mathbf{x}_r; \omega) \mathbf{G}(\mathbf{y}_T, \mathbf{x}_r; \omega), \quad (8)$$

where the Hessian is computed only at the target location.

In the next section we show three numerical examples of Hessians estimated with the proposed target-oriented approach.

NUMERICAL EXAMPLES

In this section we show three numerical examples of target-oriented computed Hessians. The first Hessian is estimated in a constant velocity model, the second in the Sigsbee model (to study the effects of poor illumination in the Hessian), and the third in the Marmousi model (to study the effect of faults in the Hessian).

Constant-velocity model

It is possible to explicitly compute the Hessian for small models, or if a target-oriented strategy is followed. We created a synthetic data set assuming a land-type acquisition geometry: the shots were positioned every 25 m from $x = -0.8$ km to $x = 0.8$ km, keeping fixed receivers from $x = -0.8$ km to $x = 0.8$ km. Figures 1a and 1b show the Hessian matrix of the constant-velocity model. Notice the banded nature of the matrix (Figure 1b), with most of the energy in the main diagonal (Chavent and Plessix, 1999). At the extremes of the diagonal the amplitudes become dimmer (Figure 1a) indicating points of lower illumination at the extremes of the acquisition.

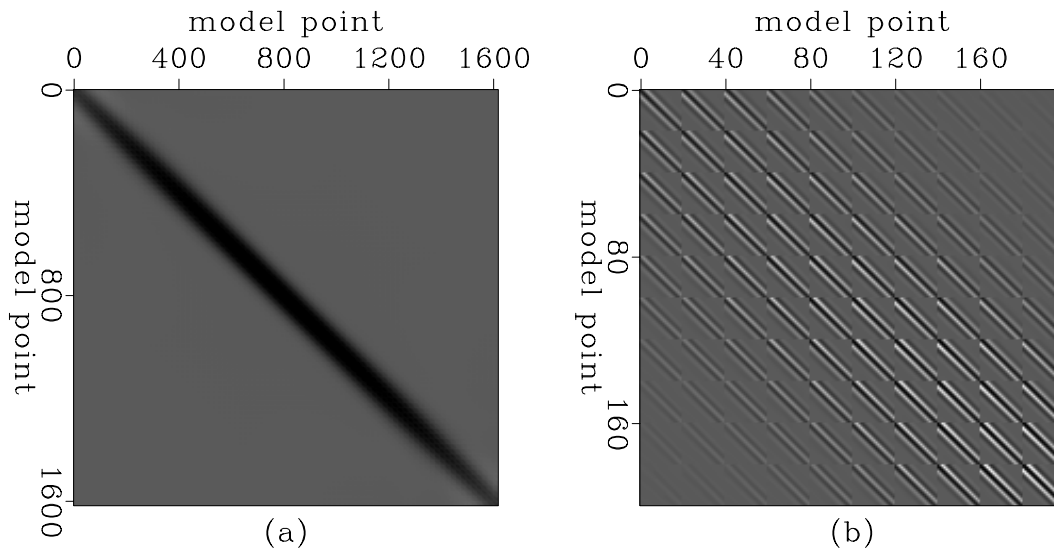


Figure 1: (a) Hessian matrix of the constant-velocity model, and, (b) close-up of Figure 1a.

`alejandro1-hmatrix_const` [CR]

For a fixed point \mathbf{x} , each line of the Hessian $\mathbf{H}(\mathbf{x}, \mathbf{y})$ can be mapped to a grid the size of the model space. Figures 2 and 3 show the Hessian and the envelope of the Hessian at four different fixed points. The Hessian (Figure 2) has phase information that can make it difficult to interpret in complex subsurface geometries (see Sigsbee and Marmousi model case), therefore we based our analysis looking at the envelope of the Hessian, (Figure 3), which shows clearly the main features of interest.

Figure 3a shows point 1, with coordinates $\mathbf{x} = (0.2, 0)$ (at the center of the acquisition). Notice the size of the ellipse and the orientation of the principal semi-axis perpendicular to the x axis. Figure 3b shows point 2, with coordinates $\mathbf{x} = (0.8, 0)$. Notice that the ellipse is bigger than the ellipse corresponding to point 1 (the size of the ellipse depends on the depth and background velocity (Chavent and Plessix, 1999)), and also that the orientation of the principal semi-axis is perpendicular to the x axis. Figures 3c and 3d show points 3 and 4, with coordinates $\mathbf{x} = (0.2, -0.6)$ and $\mathbf{x} = (0.2, 0.6)$, respectively (opposite sides of the center of the acquisition). Notice the size of the ellipses are the same, but the orientation of the principal semi-axes are tilted in opposite directions. The energy of the ellipses become dimmer than the

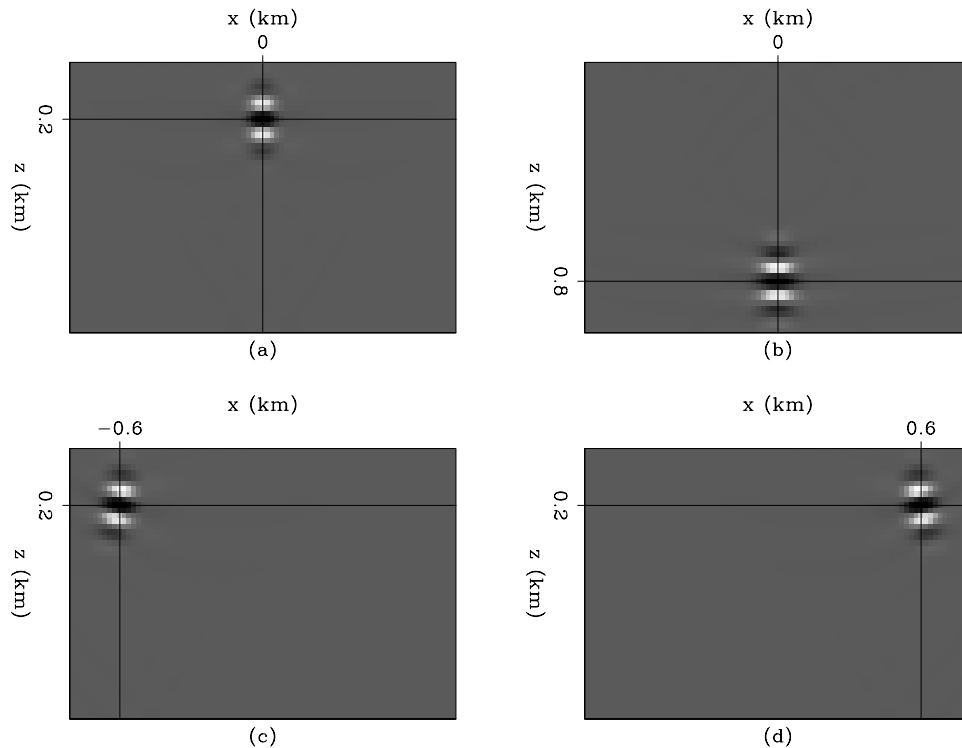


Figure 2: Hessian of the constant-velocity model, (a) point 1, (b) point 2, (c) point 3, and (d) point 4. `alejandrol-hessian_phase_const` [CR]

one in the center, indicating that these points have lower illumination.

Sigsbee model

The Sigsbee data set was modeled by simulating the geological setting found on the Sigsbee escarpment in the deep-water Gulf of Mexico. The model exhibits the illumination problems due to the complex salt shape, with a rugose salt top (Figure 4) found in this area. We choose a target zone (indicated with the "target" box in Figure 4) to see the effects of illumination on the Hessian close to the salt.

Figures 5a and 5b show the Hessian matrix for the Sigsbee model. Notice the banded nature of the matrix (Figure 5b), with most of the energy on the main diagonal (Figure 5a). As opposed to the case with the constant-velocity, the energy decreases considerably in some areas of the diagonal due to illumination problems caused by the salt body. But, similar to the constant velocity case, amplitudes become dimmer at the extremes of the diagonal due to the acquisition geometry.

We fixed seven points, all of them at the same depth, to see the corresponding lines of the Hessian. Figures 6 and 7 show the Hessian and the envelope of the Hessian, respectively. The envelope of the Hessian (Figure 7) shows clearly the main features of interest.

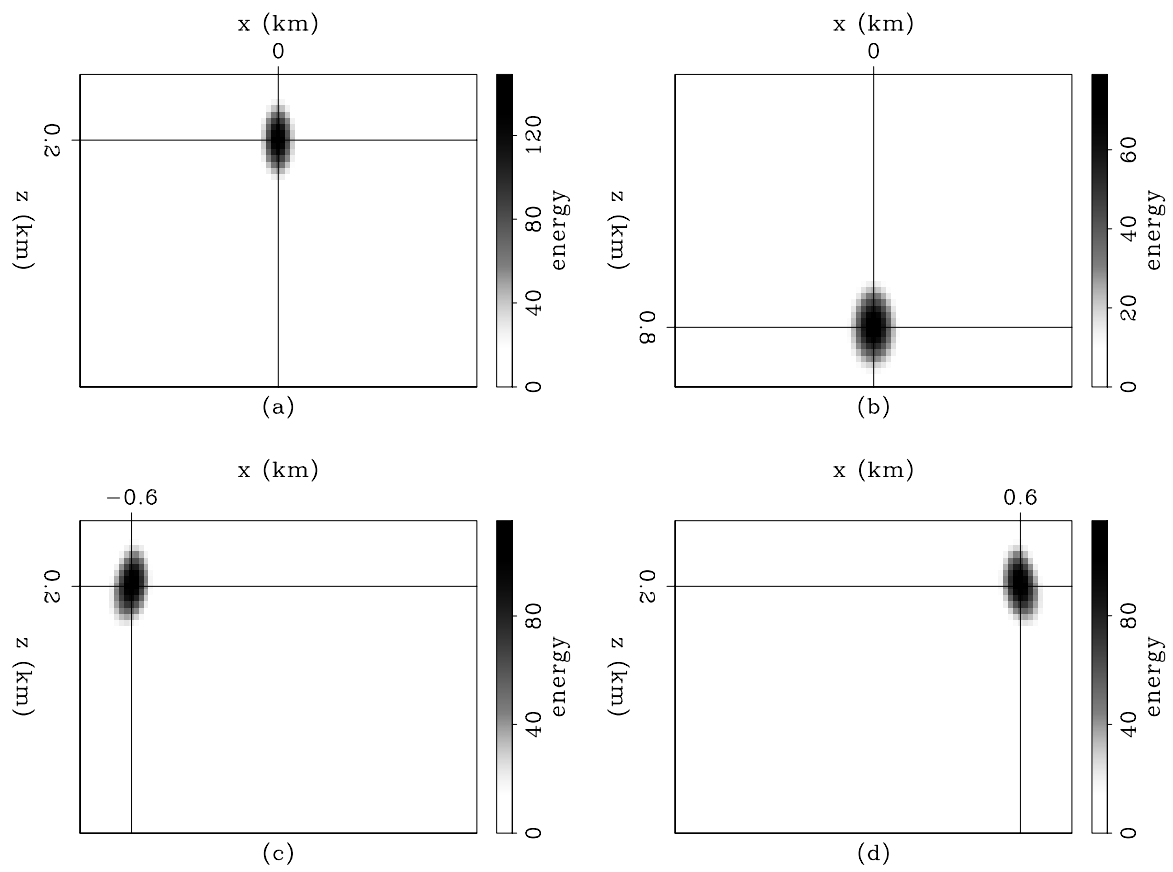


Figure 3: Envelope of the Hessian of the constant-velocity model, (a) point 1, (b) point 2, (c) point 3, and (d) point 4. `alejandrol-hessian_const` [CR]

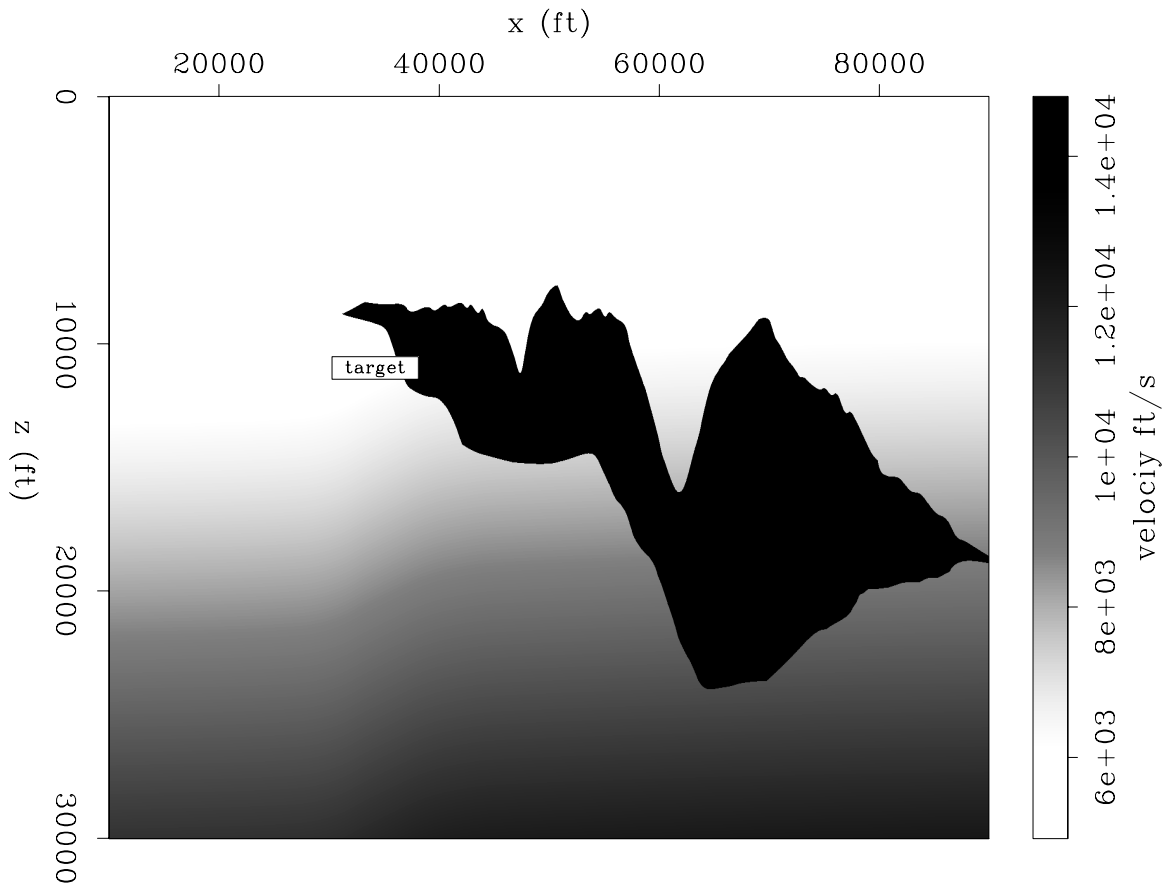


Figure 4: Sigsbee velocity model, target zone indicated with the "target" box. `alejandrol-Sis_vel` [ER]

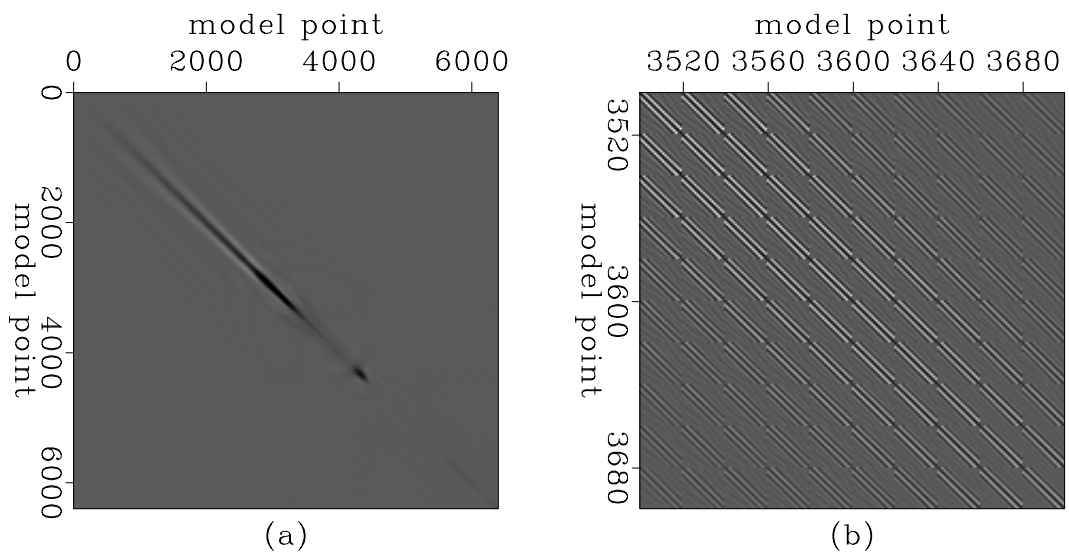


Figure 5: Hessian matrix of the Sigsbee velocity model. `alejandrol-hmatrix_Sis` [CR]

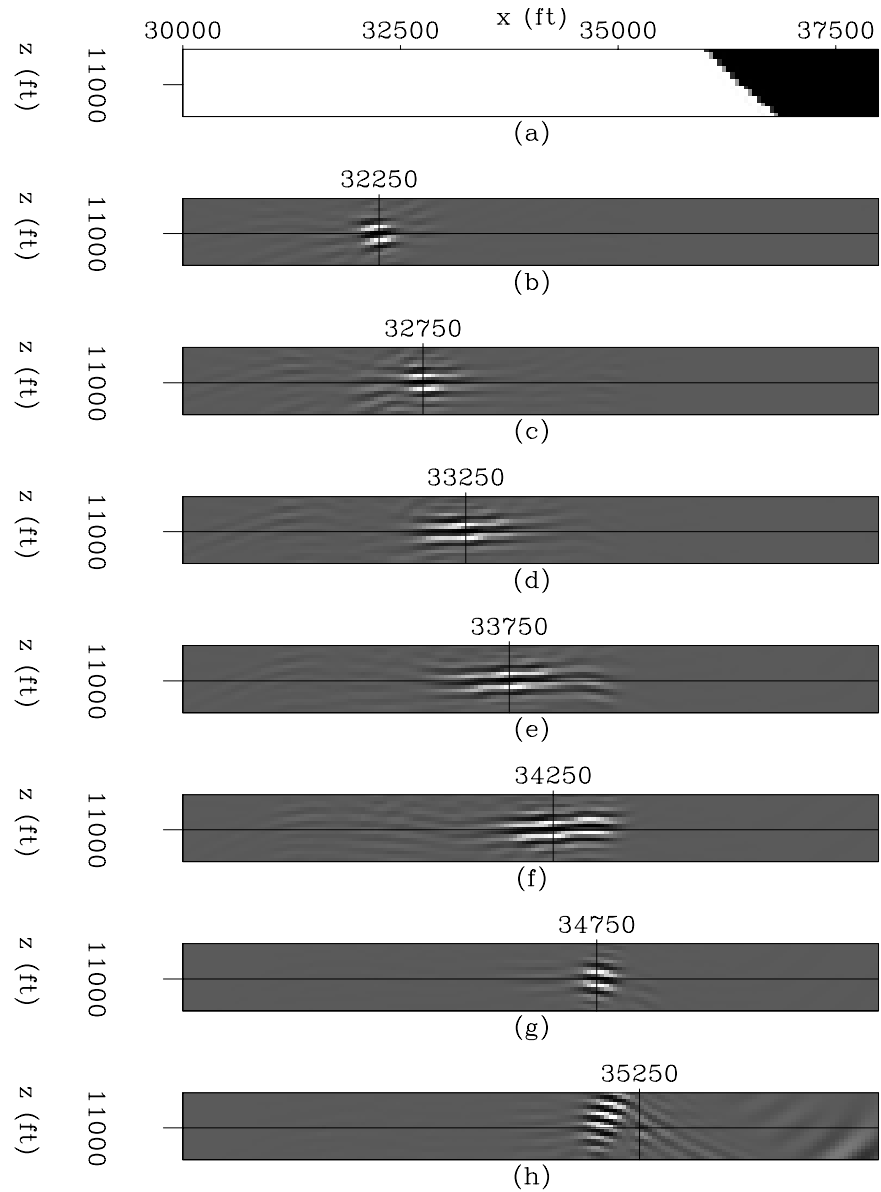


Figure 6: Hessian of the constant-velocity model, (a) Close-up of the Sigsbee velocity model (salt body to the right and sediments to the left), (b) point 1, (c) point 2, (d) point 3, (e) point 4, (f) point 5, (g) point 6, and (h) point 7. [alejandrol-hessian_phase_Sis](#) [CR]

Figure 7a shows a close-up of the velocity model in the area where the target-oriented Hessian was computed (salt body to the right and sediments to the left). Figure 7b shows point 1, with coordinates $\mathbf{x} = (11000, 32250)$; since this point in the model is well illuminated, the resulting ellipse looks similar to the constant-velocity ellipses. Figures 7c-7f show points 2 to 5, with coordinates $\mathbf{x} = (11000, 32750)$, $\mathbf{x} = (11000, 33250)$, $\mathbf{x} = (11000, 33750)$, and $\mathbf{x} = (11000, 34250)$, respectively. As the points enter a shadow zone, the ellipses lose energy and splits. A diagonal matrix approximation of the Hessian would not be appropriate to describe this behavior, since there is considerable energy away from the point where the ellipse should be centered. Figure 7g shows point 6, with coordinates $\mathbf{x} = (11000, 34750)$; out of the shadow zone, the ellipse gains energy.

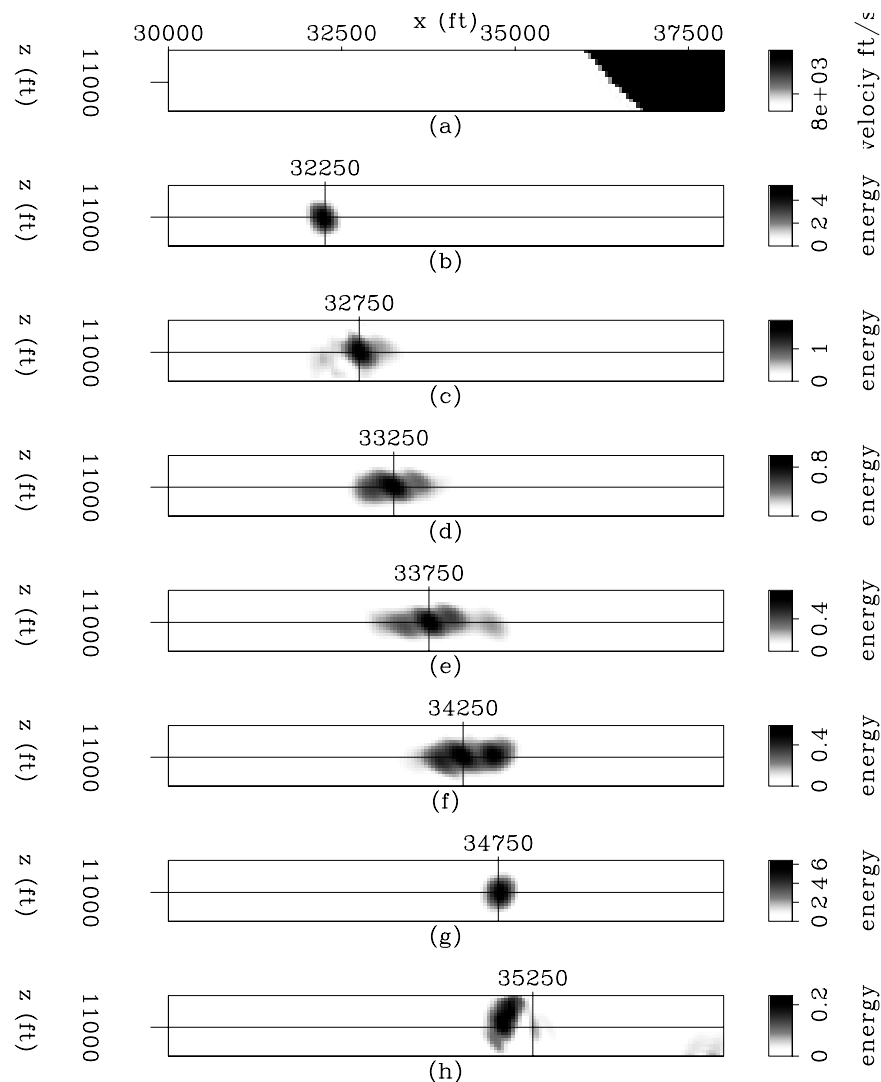


Figure 7: Envelope of the Hessian of the constant-velocity model, (a) Close-up of the Sigsbee velocity model (salt body to the right and sediments to the left), (b) point 1, (c) point 2, (d) point 3, (e) point 4, (f) point 5, (g) point 6, and (h) point 7. [alejandrol-hessian_Sis](#) [CR]

Finally, Figure 7h shows point 7, with coordinates $\mathbf{x} = (11000, 35250)$. As the point gets

closer to the salt boundary it enters a new shadow zone. This point behaves differently, the Hessian not only losses energy but the ellipse center is away from where it should be. This behavior might suggest that not enough reference velocities were used in the split-step computation of the Green functions. Or more fundamentally, that the physics of wave propagation is not well modeled by the acoustic one-way wave-equation close to the salt. This subject deserves more attention in the future.

Marmousi model

The Marmousi synthetic data set (Bourgeois et al., 1991) was first released as a blind test for velocity estimation. It has become a popular testbed for migration algorithms. Its structural style is dominated by growth faults, which arise from salt creep and give rise to the complicated velocity structure in the upper part of the model (Figure 8). We choose a target zone (indicated with the "target" box in Figure 8) to see the effects of the faults on the Hessian.

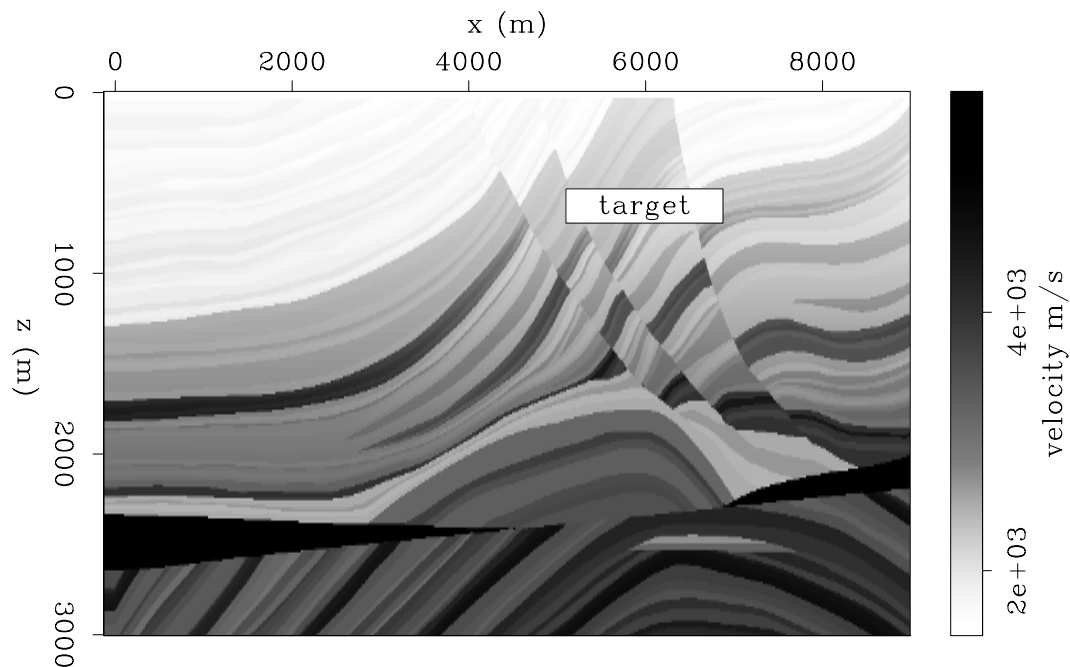


Figure 8: Marmousi velocity model. `alejandro1-Marm_vel` [ER]

Figures 9a and 9b show the Hessian matrix of the Marmousi model. Notice the banded nature of the matrix (Figure 9b), with most of the energy in the main diagonal (Figure 9a). There are changes of the energy in the diagonal, but not as strong as for the Sigsbee model case.

We fixed four points to see the lines of the Hessian corresponding to different geological features in the model. Figures 10 and 11 show the Hessian and the envelope of the Hessian, respectively. The envelope of the Hessian (Figure 11) shows clearly the main features of interest.

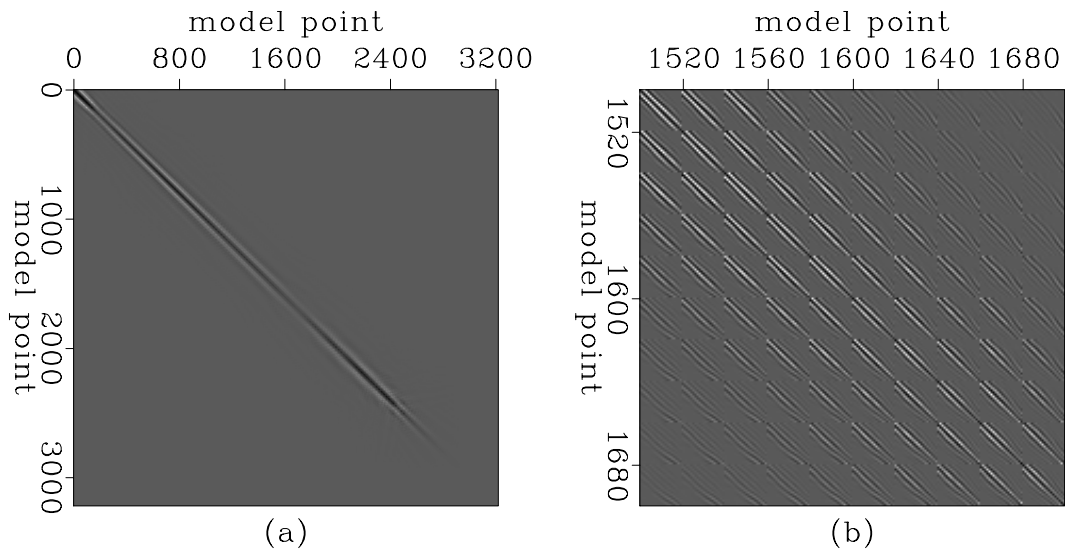


Figure 9: Hessian matrix of the Marmousi model. `alejandrol-hmatrix_marm` [CR]

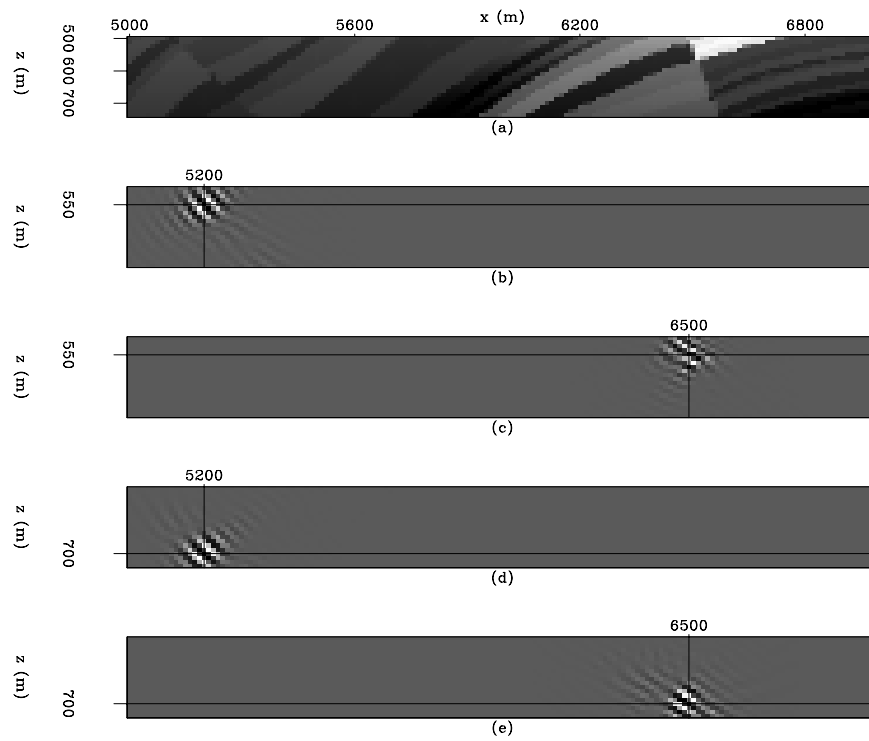


Figure 10: Hessian of the Marmousi model, (a) Close-up of the Marmousi velocity model, (b) point 1, (c) point 2, (d) point 3, and (e) point 4. `alejandrol-hessian_phase_marm` [CR]

Figure 11a shows a close-up of the velocity model in the area where the target-oriented Hessian was computed. Figure 11b shows point 1, with coordinates $\mathbf{x} = (550, 5200)$. Since this point in the model is well illuminated, the resulting ellipse looks similar to the constant-velocity ellipses. Figure 7c shows point 2, with coordinates $\mathbf{x} = (550, 6500)$. Notice that this point is close to a fault, producing a distortion to the ellipse shape. Figure 11d shows point 3, with coordinates $\mathbf{x} = (700, 5200)$; as with point 1, the ellipse is not distorted. Finally, Figure 7e shows point 4, with coordinates $\mathbf{x} = (700, 6500)$. This point is also close to the fault, but the velocity contrast across the fault is smaller, producing less distortion than in the point 3 case.

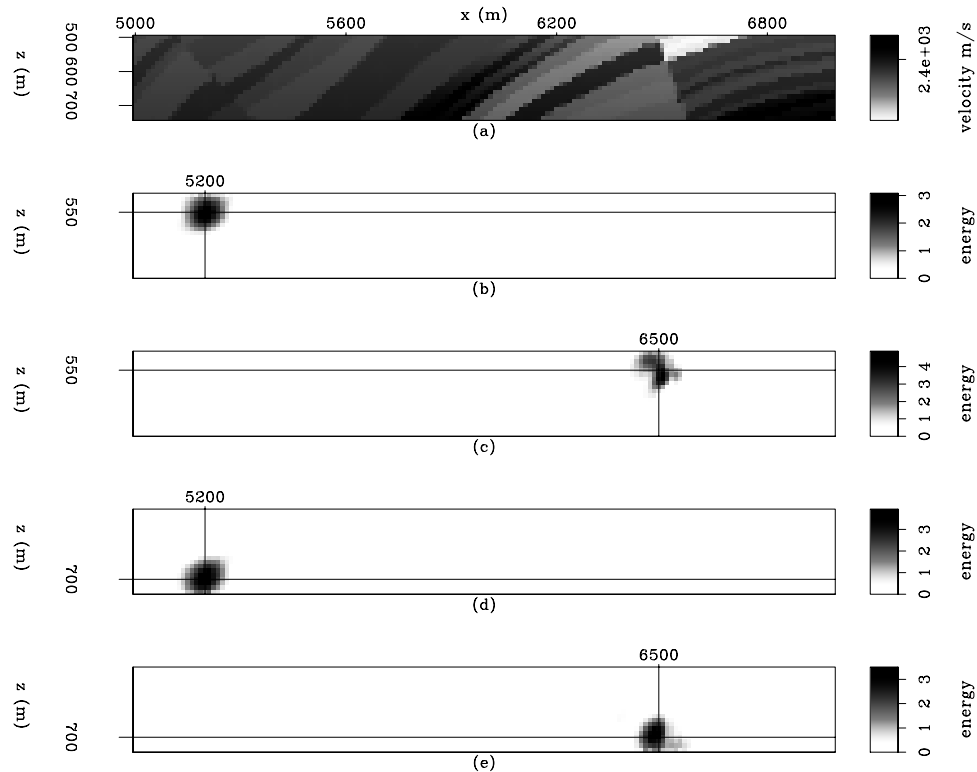


Figure 11: Envelope of the Hessian of the Marmousi model, (a) Close-up of the Marmousi velocity model, (b) point 1, (c) point 2, (d) point 3, and (e) point 4. `alejandrol-hessian_marm` [CR]

CONCLUSIONS

Since accurate imaging of reflections is more important in the neighborhood of the reservoir, a target-oriented strategy can be applied to explicitly compute the inversion Hessian. This allows us to study the characteristics of the Hessian in different acquisition geometries and subsurface situations (low illumination, faults, etc.) and will make possible the design of a strategy to approximate its inverse.

Results on the Sigsbee model show that inside the shadow zones, the Hessian ellipses split

and reduce their energy. Something different happened close to faults, as can be seen in the Marmousi model. There, the Hessian ellipses are distorted but do not split. The latest results suggest that in complex areas the usual diagonal-matrix approximation of the Hessian might be insufficient to obtain the correct position and amplitude of the reflectors.

ACKNOWLEDGMENTS

We would like to thank SMAART JV for the Sigsbee dataset used in our experiments.

REFERENCES

- Audebert, F., 1994, 3-D prestack depth migration: Why Kirchhoff?: SEP-80, 191–208.
- Bamberger, A., Engquist, B., Halpern, L., and Joly, P., 1988, Paraxial approximation in heterogeneous media: SIAM J. Appl. Math., 48, 98–128.
- Bourgeois, A., Bourget, M., Lailly, P., Poulet, M., Ricarte, P., and Versteeg, R., 1991, Marmousi, model and data: Proceedings of 1990 EAEG workshop on practical aspects of seismic data inversion.
- Chavent, G., and Plessix, R. E., 1999, An optimal true-amplitude least-squares prestack depth-migration operator: Geophysics, 64, no. 2, 508–515.
- Claerbout, J. F., 1992, Earth soundings analysis, processing versus inversion: Blackwell Scientific Publications.
- Duquet, B., and Marfurt, K. J., 1999, Filtering coherent noise during prestack depth migration: Geophysics, 64, no. 4, 1054–1066.
- Ehinger, A., Lailly, P., and Marfurt, K. J., 1996, Green's function implementation of common-offset wave-equation migration: Geophysics, 61, no. 06, 1813–1821.
- Guitton, A., 2004, Amplitude and kinematic corrections of migrated images for nonunitary imaging operators: Geophysics, 69, no. 04, 1017–1024.
- Kuehl, H., and Sacchi, M., 2001, Generalized least-squares DSR migration using a common angle imaging condition: Soc. of Expl. Geophys., 71st Ann. Internat. Mtg, 1025–1028.
- Nemeth, T., Wu, C., and Schuster, G. T., 1999, Least-squares migration of incomplete reflection data: Geophysics, 64, no. 1, 208–221.
- Prucha, M. L., Clapp, R. G., and Biondi, B., 2000, Seismic image regularization in the reflection angle domain: SEP-103, 109–119.
- Rickett, J. E., 2003, Illumination-based normalization for wave-equation depth migration: Geophysics, 68, no. 04, 1371–1379.

Ronen, S., and Liner, C. L., 2000, Least-squares DMO and migration: *Geophysics*, **65**, no. 5, 1364–1371.

Tarantola, A., 1987, *Inverse problem theory*: Elsevier.

Short Note

Velocity uncertainty: Non-linearity and the starting guess

Robert G. Clapp¹

INTRODUCTION

The last few years have seen a significant increase in research assessing risk. Several papers deal with assessing risk from a geostatistical framework (Shanor et al., 2002; Gambus-Ordaz et al., 2002). The general methodology is to create equi-probable models based on simplified covariance descriptions and probability functions. Each point is visited in turn and a value selected based on *a priori* probability distribution, surrounding point value, and the covariance description.

In previous work I showed how we accomplish something similar in a global inversion problem. As long as a decorrelator exists (such as a regularization operator that is an inverse noise covariance operator) adding random noise into the residual space will create equi-probable models (Clapp, 2001a). This methodology can be applied to tomography in two distinct ways. If random noise is added to components in the residual vector corresponding to the regularization operator, we produce models that have not only correct covariance but also a reasonable variance. These models add fine layered features that standard tomography can not resolve. From realization to realization these features change in shape and amplitude. They do not effect the kinematics of the final image, but do have an effect on the amplitudes (Clapp, 2003a).

The second choice, adding noise to the portion of the residual vector corresponding to the data fitting goal, does have a more significant effect on the velocity and the final image (Clapp, 2004). Adding noise in this space corresponds to selecting an alternate set of data points. These new data points aren't simply random perturbations from the original model. In the case of tomography, they are similar to not selecting the maximum amplitude of a move-out measure, but a trend of lower or higher move-out. The added complexity is that the migration velocity analysis problem is not linear. We routinely will do several non-linear iterations to come up with the final answer. How to best deal with this non-linearity is unclear.

In this paper I take a slightly different tact from the one taken Clapp (2004). I perform four iterations of non-linear tomography. In the first two iterations I create five equi-probable realizations for the move-out functions. For the last two iterations I choose the minimum-energy

¹email: bob@sep.stanford.edu

move-out function. The resulting twenty-five models provide an interesting and instructive measure of the uncertainty involved in standard migration velocity analysis and its effect on final image.

REVIEW

In inversion we try to estimate some model \mathbf{m} given some data \mathbf{d} and an operator \mathbf{L} that maps between the quantities. If our problem is poorly constrained, we can employ Tikhonov regularization (Tikhonov and Arsenin, 1977), adding a roughening operator \mathbf{A} to our objective function Q . To balance the two components of the objective function we introduce a twiddle parameter ϵ and end up with

$$Q(\mathbf{m}) = \|\mathbf{d} - \mathbf{Lm}\|^2 + \epsilon^2 \|\mathbf{Am}\|^2. \quad (1)$$

The two terms in our objective function serve different purposes. The first deals with *data fitting* and the second *model styling*. We can write the minimization in a slightly different form in terms of two *fitting goals*,

$$\begin{aligned} \mathbf{0} &\approx \mathbf{r}_{\text{data}} = \mathbf{d} - \mathbf{Lm} \\ \mathbf{0} &\approx \mathbf{r}_{\text{model}} = \epsilon \mathbf{Am}, \end{aligned} \quad (2)$$

where $\mathbf{0}$ is a vector of zeros, \mathbf{r}_{data} is the data residual vector, and $\mathbf{r}_{\text{model}}$ is the model. Our regularization operator, at best, usually only accounts for second order statistics, producing a model that is often unrealistic. In previous papers (Clapp, 2000, 2001a) I showed how by adding Gaussian random noise to the $\mathbf{r}_{\text{model}}$ we can add variance to our models and give the a more realistic texture.

If we decorrelate our data residual vector by adding an inverse noise covariance operator \mathbf{N} ,

$$\begin{aligned} \mathbf{0} &\approx \mathbf{r}_{\text{data}} = \mathbf{N}(\mathbf{d} - \mathbf{Lm}) \\ \mathbf{0} &\approx \mathbf{r}_{\text{model}} = \epsilon \mathbf{Am}, \end{aligned} \quad (3)$$

we can account for uncertainty in our data (Clapp, 2001b). This is similar, but not the same as, using stochastic simulation (Isaaks and Srivastava, 1989a,b) to create several different datasets. The two most notable differences are that we can handle much more spatially variant and complex covariance descriptions and we have the effect of a model styling goal in our inversion.

Tomography

In order to use this methodology our tomography problem has to be set up in a similar fashion to that of fitting goals (3). This isn't necessarily straight forward. Our first problem is that tomography is a non-linear process. The standard approach in ray-based tomography is to linearize around an initial slowness model \mathbf{s}_0 . Our linearized tomography operator \mathbf{T}_0 is formed

by rays traced through the background slowness. We then write a linear relation between the change in slowness $\Delta \mathbf{s}$ and the change in travel-time $\Delta \mathbf{t}$.

When doing migration velocity analysis in the depth domain, we are not dealing with travel-times but instead move-out as a function of some parameter (offset or azimuth) (Stork, 1992). Biondi and Symes (2003) showed how for angle domain migration there is a link between travel-time error dt , local dip ϕ , the local slowness s depth of the reflection z , the reflection angle θ , and scaling γ of the background slowness model. This relation can be written in terms of an operator \mathbf{D} which maps from $1. - \gamma$ to $\Delta \mathbf{t}$ and whose elements are

$$D(\theta, \phi, z, s) = \frac{zs \sin(\theta)^2}{\cos(\phi) * (\cos(\theta)^2 - \sin(\theta)^2)}. \quad (4)$$

For our regularization operator we can use a steering filter (Clapp et al., 1997; Clapp, 2001a) oriented along reflector dips. Our basic linearized fitting goals become

$$\begin{aligned} \mathbf{0} &\approx \mathbf{r}_{\text{data}} = \mathbf{D}\gamma - \mathbf{T}_0\Delta \mathbf{s} \\ \mathbf{0} &\approx \mathbf{r}_{\text{model}} = \epsilon \mathbf{A}(\mathbf{s}_0 + \Delta \mathbf{s}). \end{aligned} \quad (5)$$

The added term in our regularization fitting goal $\mathbf{A}\mathbf{s}_0$ is due to the fact that we want to smooth *slowness* not *change in slowness*. Clapp (2003a) and Chen and Clapp (2002) showed that adding noise to $\mathbf{r}_{\text{model}}$ produced velocity models with what looked like thin layers that had little effect on image kinematics but noticeable effects on amplitudes.

We run into problems when we want to explore the effect of adding noise to \mathbf{r}_{data} . Our γ values, and therefore our data fitting error exist in some irregular space (potentially consistent angle sampling, but irregular in space). This makes making an effective noise covariance operator difficult.

Multiple realization methodology

Clapp (2004) suggested breaking up the tomography problem into two portions: creating several realizations of γ maps and using them as input to the tomography problem. Estimating the **gamma** field is in itself difficult. The standard approach is to calculate semblance over a range of move-out values. The move-out at given point is then the maximum semblance at the location. To reduce noise, the semblance field is often smoothed. This is still far from in ideal solution. We are constantly fighting a battle between selecting local minima (not enough smoothing) and missing important move-out features (too much smoothing).

In Clapp (2004) the various γ maps were created by selecting a smooth set of random number and converting them into γ values based on a normal score transform (Isaaks and Srivastava, 1989a). This approach was somewhat successful, but suffered from the fact that we don't, and effectively can't scan over an infinite set of move-outs. Therefore our distribution function is misleading. Methods to correct for the limited range proved *ad hoc*.

Instead I am going to start from the approach outlined in Clapp (2003b). My goal is to estimate a smooth set of semblance values $\mathbf{g}_{\text{smooth}}$. I begin by selecting the maximum

semblance at each point \mathbf{g}_{\max} . I solve the simple minimization problem

$$\begin{aligned} \mathbf{0} &\approx \mathbf{r}_{\text{data}} = \mathbf{W}_{\mathbf{g}}(\mathbf{g}_{\max} - \mathbf{g}_{\text{smooth}}) \\ \mathbf{0} &\approx \mathbf{r}_{\text{model}} = \epsilon \mathbf{A} \mathbf{g}_{\text{smooth}}, \end{aligned} \quad (6)$$

where \mathbf{A} is again a steering filter, and $\mathbf{W}_{\mathbf{g}}$ is a function of the semblance value at each location. After estimating $\mathbf{g}_{\text{smooth}}$ I select the maximum within a range around $\mathbf{g}_{\text{smooth}}$ to form a new \mathbf{g}_{\max} , and repeat the estimation. At each iteration, the window I search around and the amount of smoothing (ϵ) decreases. To create a series of models I introduce random noise into \mathbf{r}_{data} scaled by the variance in the semblance at each location. With different sets of random noise I get different realistic models.

EXAMPLE

Clapp (2004) took nine different realizations of a single linearization of a complex synthetic model (Figure 1). There were several problems with this approach. The most significant problem was that a single non-linear iteration, was far from sufficient. After one iteration, we still have significant move-out that another non-linear iteration of tomography has a chance of using. When doing multiple non-linear iterations we have two choices to make at each iteration. First, should we use the minimum energy model (no random perturbation) or introduce random perturbations? Second, if we are adding random perturbations, how many models should we create at each non-linear iteration?

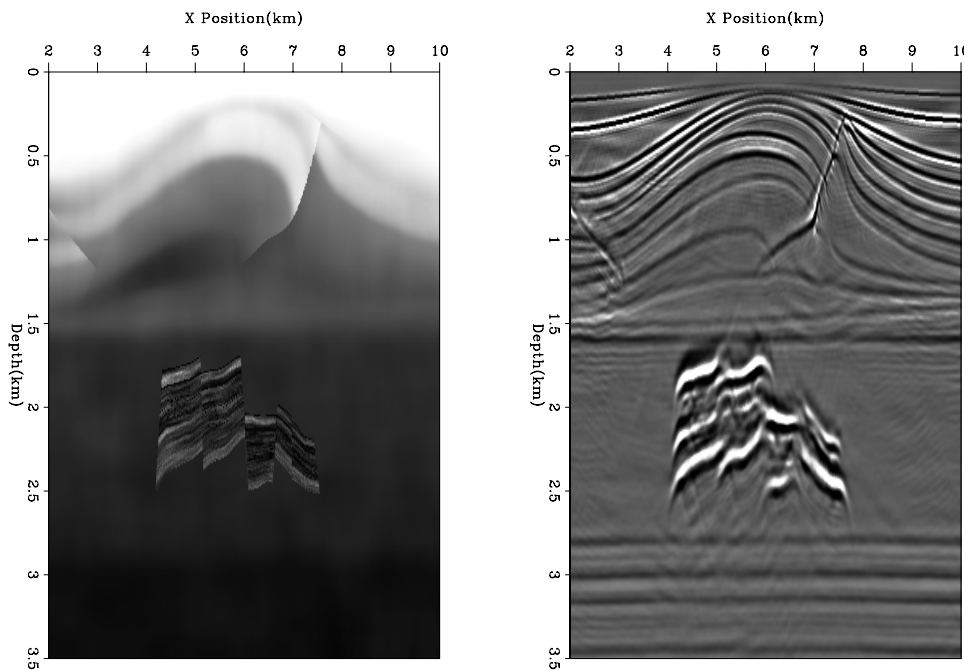


Figure 1: The left panels shows the velocity model used as input to the finite difference scheme used to create the data. The right panel is the resulting migrating the data with the correct velocity. The fine structure seen below 1.6km is the *reservoir*. `bob3-model` [ER,M]

For this experiment I decided to create five random perturbed models in the first non-linear iteration. From these five models I generated twenty five models during the second non-linear iteration. I then used these twenty-five models in a conventional migration velocity updating scheme. This gives some measure on the effect of the starting guess on the final solution. Each of the twenty-five models were equally reasonable points from which start a tomographic loop. The difference between the final images gives me some measure of the uncertainty in this updating scheme.

The left panel of Figure 2 shows my starting guess for the velocity problem. The right panel shows the resulting image. The velocity was created by applying a strong smoother to the correct velocity field then scaling the resulting model by .9. Figure 3 shows the results after one non-linear iteration. The top panel are the five realizations of γ . The center panels are the resulting five velocity models, and the bottom five panels are the migrated images using these velocity models. The anticline trend is in all of the realizations but we still see significant differences in how the velocity estimate deals with the listric fault.

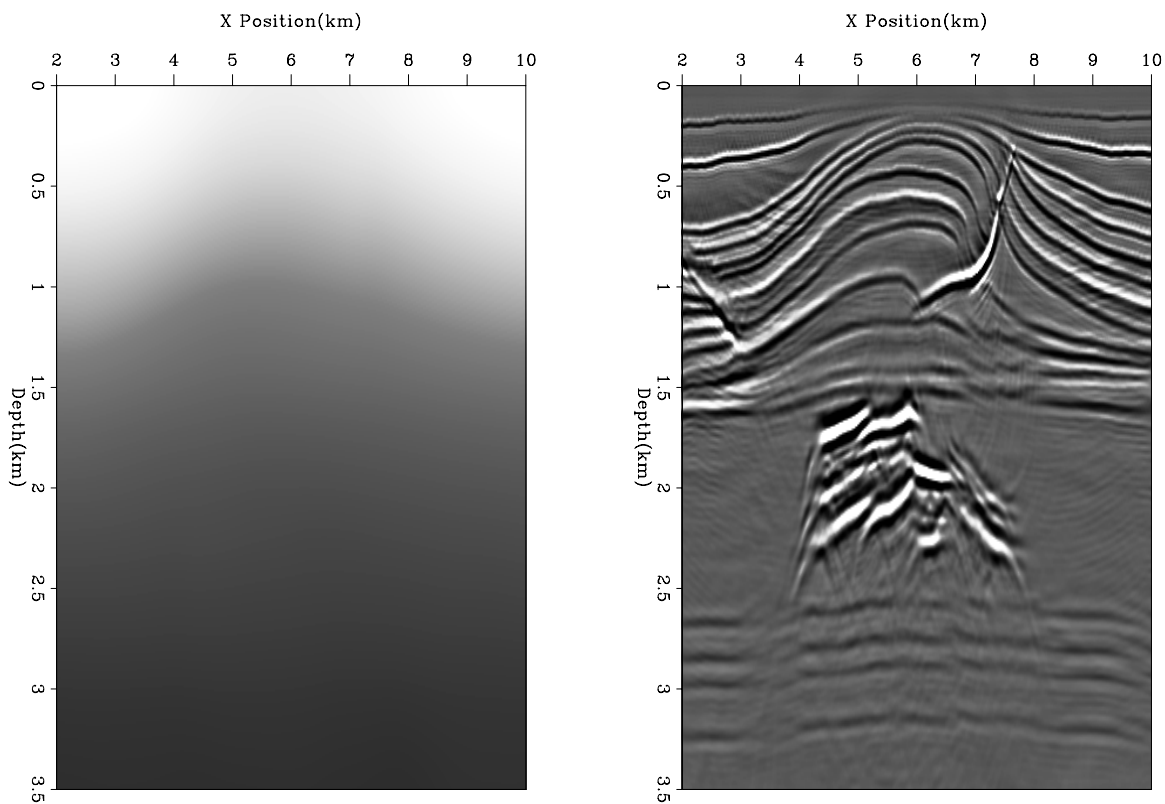


Figure 2: The left panel shows the initial velocity model. The right panel the resulting migration. `bob3-iter0` [CR,M]

After four iterations, now with twenty-five different models, the differences are more dramatic. Figure 4 show the twenty-five different gamma panels. We see an overall reduction in the amount move-out (closer to gray), but the realizations still have significantly different character. The twenty-five velocity models (Figure 5) also show significant variation, especially as we go deeper in the model. After four iterations we see significant differences in

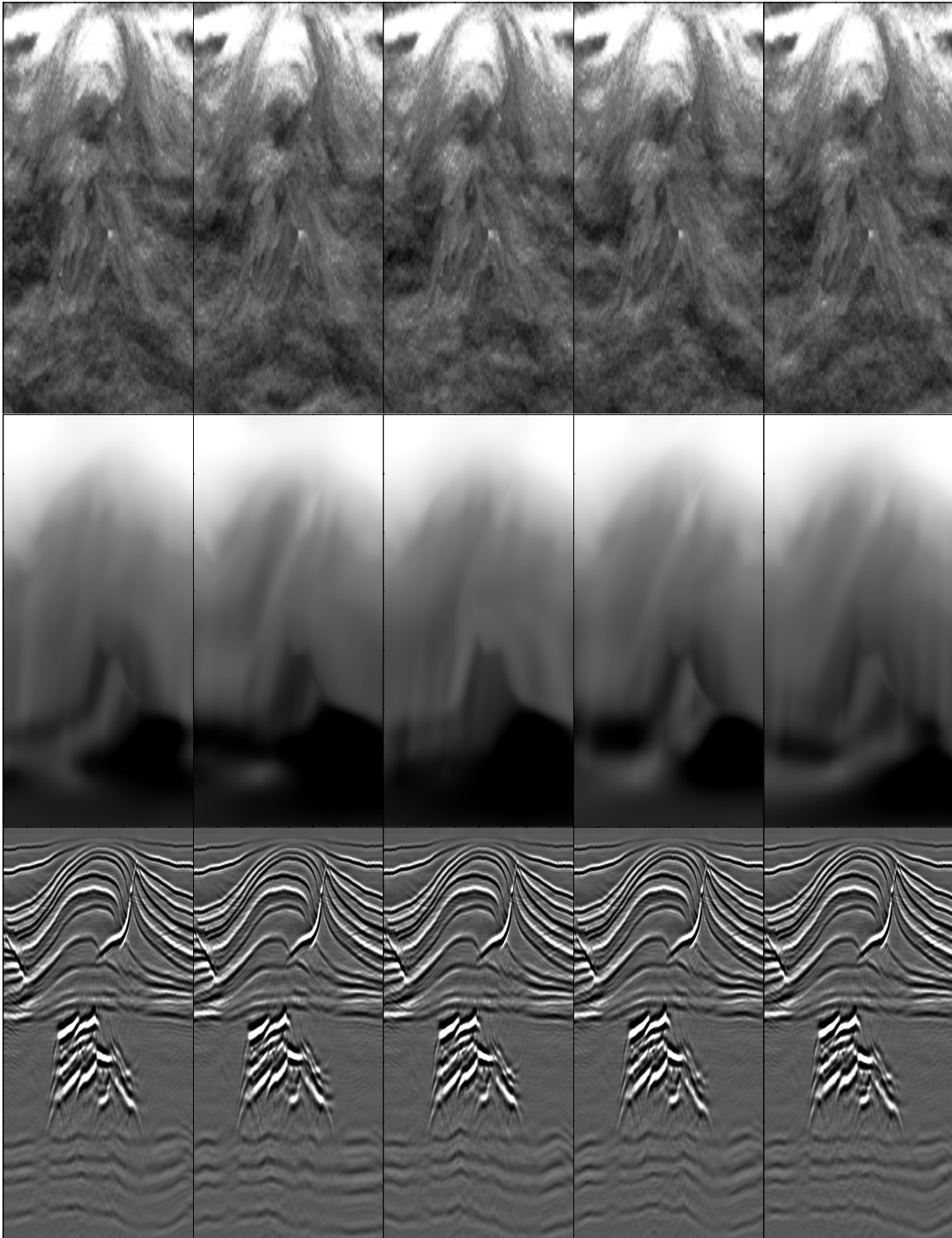


Figure 3: The top panel are the five realizations of γ . The center panels are the resulting five velocity models, and the bottom five panels are the migrated images using these velocity models. `bob3-iter1` [CR,M]

the images (Figure 4). In most of the models we have focused the anticline structure, but the images have significant variation below. The basement reflectors are discontinuous in many of the models.

CONCLUSION

Multiple reasonable starting points for migration velocity analysis are generated by adding uncertainty to the moveout analysis procedure. It is demonstrated on a complex synthetic that these different starting points can have large effect on the final velocity model and the resulting image.

REFERENCES

- Biondi, B., and Symes, W., 2003, Angle-domain common-image gathers for migration velocity analysis by wavefield-continuation imaging: SEP-**113**, 177–210.
- Chen, W., and Clapp, R., 2002, Exploring the relationship between uncertainty of wave attributes and rock information: SEP-**112**, 259–268.
- Clapp, R. G., Fomel, S., and Claerbout, J., 1997, Solution steering with space-variant filters: SEP-**95**, 27–42.
- Clapp, R., 2000, Multiple realizations using standard inversion techniques: SEP-**105**, 67–78.
- Clapp, R. G., 2001a, Geologically constrained migration velocity analysis: Ph.D. thesis, Stanford University.
- Clapp, R. G., 2001b, Multiple realizations: Model variance and data uncertainty: SEP-**108**, 147–158.
- Clapp, R. G., 2003a, Multiple realizations and data variance: Successes and failures: SEP-**113**, 231–246.
- Clapp, R. G., 2003b, Semblance picking: SEP-**113**, 323–330.
- Clapp, R. G., 2004, Velocity uncertainty in tomography: SEP-**115**, 233–248.
- Gambus-Ordaz, M., Torres-Verdin, C., and Schile, C., 2002, High-resolution geostatistical inversion of a seismic data set acquired in a gulf of Mexico gas reservoir, *in* 72nd Ann. Internat. Mtg Soc. of Expl. Geophys., 1785–1788.
- Isaaks, E. H., and Srivastava, R. M., 1989a, An Introduction to Applied Geostatistics: Oxford University Press.
- Isaaks, E. H., and Srivastava, R. M., 1989b, An introduction to applied geostatistics: Oxford University Press, New York, Nork.



Figure 4: The twenty-five gamma panels after the third non-linear iteration. Note how we are overall closer to 1.0 (gray), but we still see differences in the various panels. `bob3-iter3_g`
[CR]

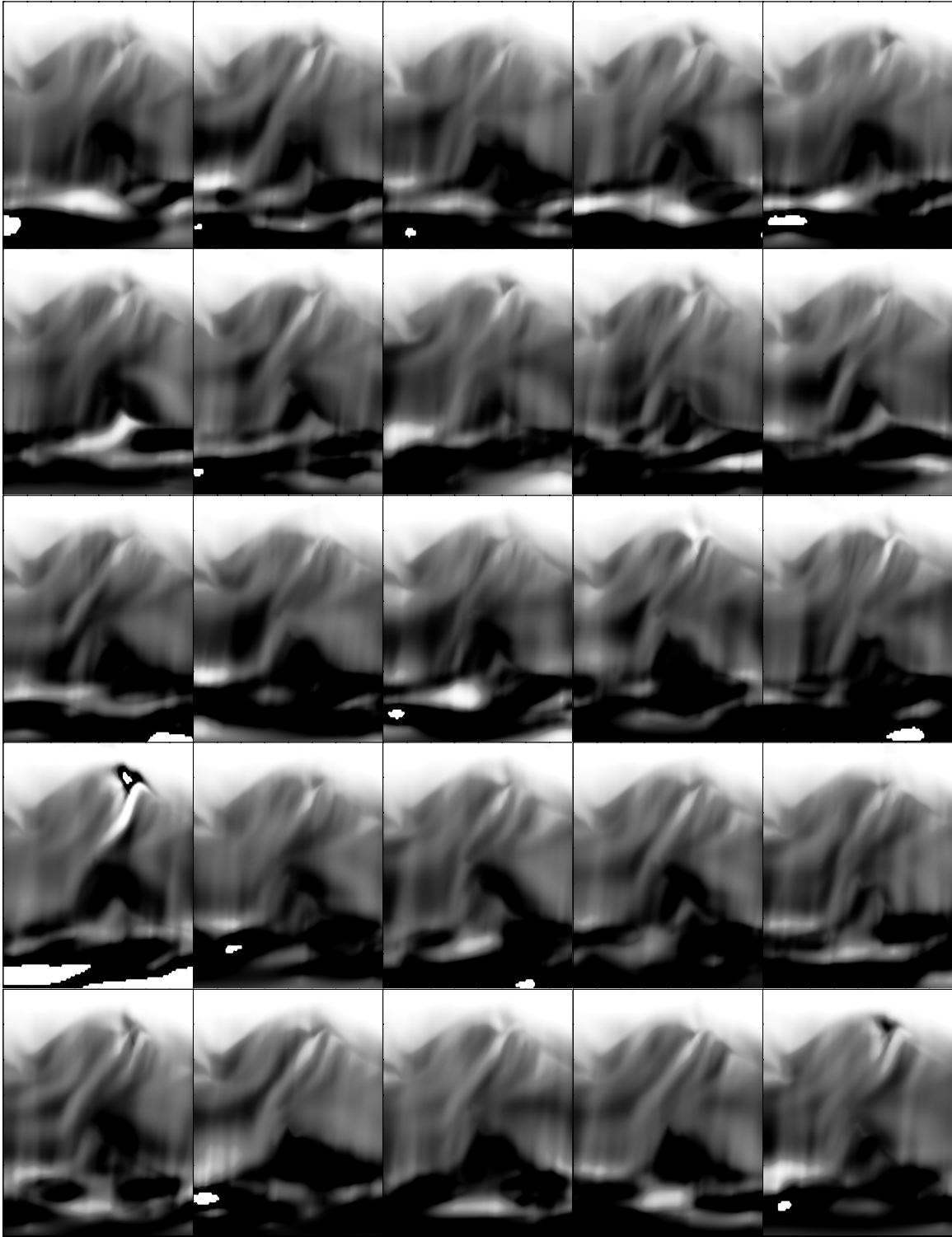


Figure 5: The final twenty-five velocity models. `bob3-iter4_v` [CR,M]

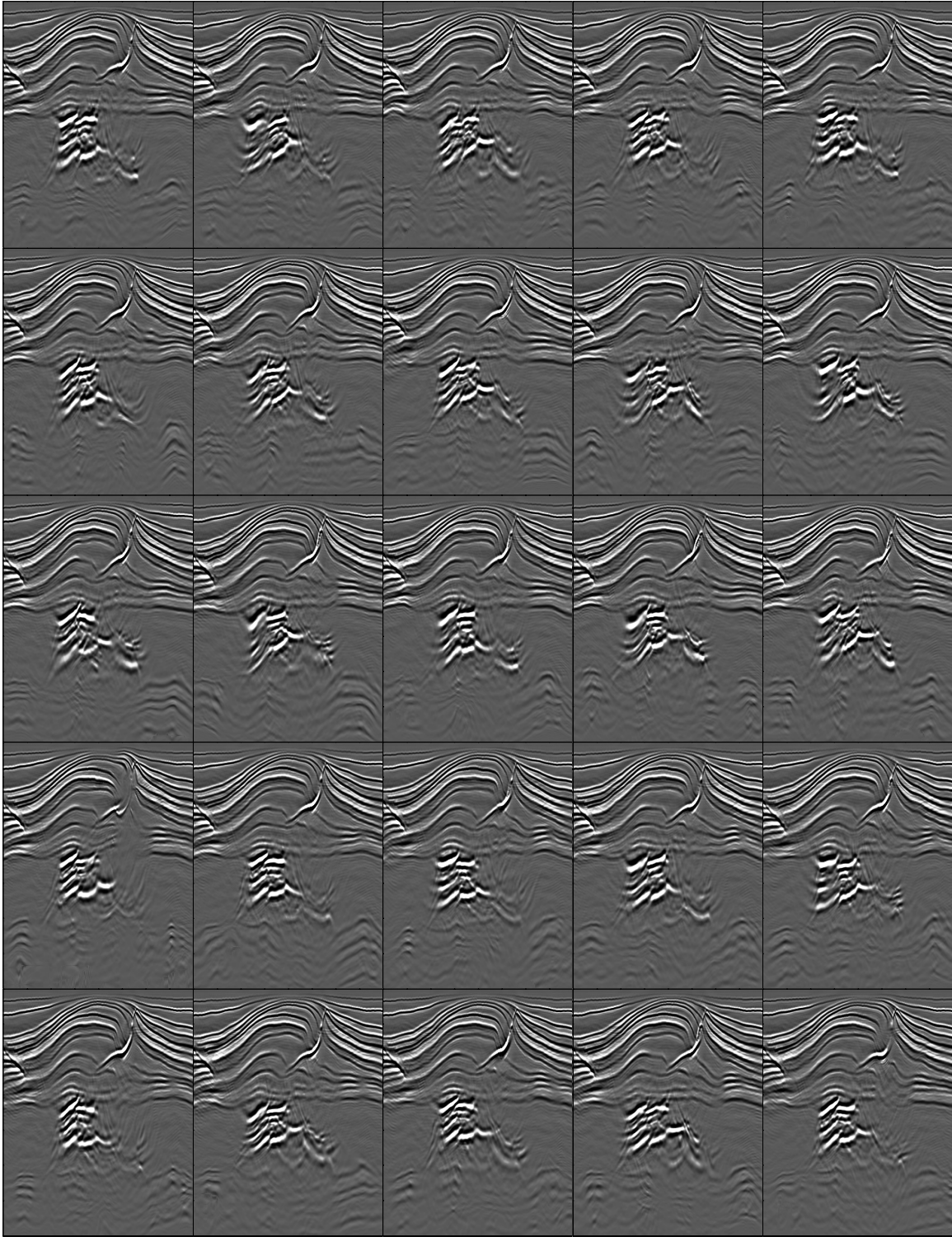


Figure 6: The twenty-five different images. Note the differences, especially in the reservoir.

`bob3-iter4_i` [CR]

- Shanor, G., Rawanchaikul, M., Sams, M., Muggli, R., Tiley, G., and Ghulam, J., 2002, From seismic to simulator through geostatistical modelling and inversion: Makarem gas accumulation, sultanate of oman: *First Break*, **20**, no. 02, 110–115.
- Stork, C., 1992, Reflection tomography in the postmigrated domain: *Geophysics*, **57**, no. 5, 680–692.
- Tikhonov, A. N., and Arsenin, V. Y., 1977, *Solution of ill-posed problems*: John Wiley and Sons.



Short Note

The effect of model covariance description on global seismology tomography problems

Robert G. Clapp and Charles K. Wilson¹

INTRODUCTION

Global seismology tomography faces a different set of problems than those faced in typical oil exploration tomography projects. Energy travels at significantly wider range of angles in global seismology and the velocity-depth ambiguity of reflection based seismology is not present. On the other hand, global seismologists have orders of magnitude less data. In addition, this data usually has a much lower signal to noise ratio than in the typical oil industry project.

The result is that both types of tomography operators have a large null space. In global seismology, this problem is usually addressed by limiting the number of model components, either through some type of global harmonic parameterization or simply larger grid cells. Another approach is to introduce an inverse model covariance operator as a regularization operator into the inversion scheme. This regularization operator can be a non-stationary operator that introduce a desired, or hypothesized, structure to the velocity model (Clapp, 2001).

In this paper we apply a series of non-stationary regularization operators, a steering filter (Clapp, 2001), to a global seismology tomography problem. We show how these filters can produce a more aesthetic pleasing image that still fits the data, and we hypothesize they can be used to help evaluate different model hypotheses.

DATA

The data is from an array laid out across the Colorado-Wyoming border. The array is composed of 30 seismometers laid out in line in a semi-straight line with approximate spacing of 2.6 km. The data consists of a series of arrival times from known station locations, at known dips and arrival directions (back azimuths). The left panel of Figure 1 shows an initial velocity model with the stations marked with an '*'. The right panel of Figure 1 shows the distribution, in terms of azimuth and angle, of the earthquakes used in this experiment.

¹email: bob@sep.stanford.edu

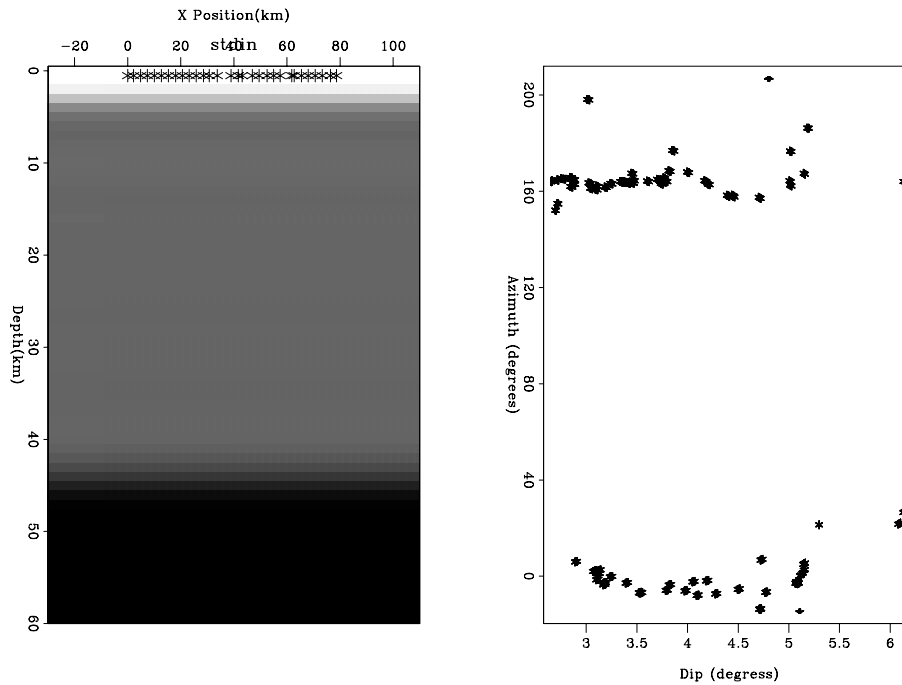
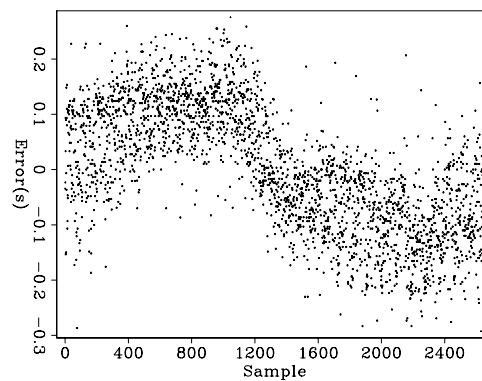


Figure 1: The left panel shows an initial velocity model with the recording stations marked with an ‘*’. The right panel shows the distribution, in terms of azimuth (compared to receiver line) and dip, of the earthquakes used in this experiment. The large change at 43 km is the Moho. `bob4-initial` [ER,M]

A linear trend is removed from the arrival times for each event (earthquake). The subtraction of the trend is meant to account for the varying source directions (earthquake position compared to the array). The trend removed arrival times generally form the data Δt for the global tomography problem. Figure 2 shows these arrivals with the trend removed. Note the general shape in the times.

Figure 2: The arrival times with a linear trend removed. Note the pattern in the arrival times. `bob4-dt` [ER]



TOMOGRAPHY

We linearize the tomography problem around an initial slowness model \mathbf{s}_0 . Rays are traced through the model based on the recorded arrival direction. The length of the ray segments through each model cell form the basis of the tomography operator \mathbf{T}_0 . Figure 3 show the rays forming \mathbf{T}_0 overlying the initial velocity model. Note that we have decent angular coverage.

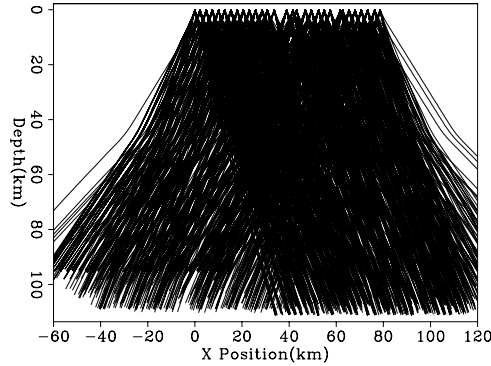


Figure 3: The rays forming \mathbf{T}_0 overlying the initial velocity model.

`bob4-rays` [ER]

For this experiment we are limiting ourselves to a 2-D earth model. As shown in Figure 1, our selected set of earthquakes are approximately oriented along the receiver line. For this experiment we assume constant velocity out of plane. We do 2-D ray tracing and then correct all lengths by

$$l_{\text{new}} = \frac{l_{\text{old}}}{\|\cos(\phi)\|}, \quad (1)$$

where l_{old} is the old ray length, l_{new} is the updated ray length and ϕ is the azimuth direction of the earthquake.

Each arrival time also has a variance associated with it. The inverse of these variances form a noise covariance operator \mathbf{W}_0 for the inversion. We invert for the change in slowness $\Delta\mathbf{s}$ by minimizing the fitting goal,

$$\mathbf{0} \approx \mathbf{W}_0(\Delta\mathbf{t} - \mathbf{T}_0\Delta\mathbf{s}). \quad (2)$$

Regularization

Our velocity model is sampled in 1km in both depth and x position. Our total number of model points is approximately seven times our number of data points. As a result our model is significantly underdetermined. There are several ways to deal with the problem. One solution would be to decrease the number of grid points by sampling differently (coarser regular sampling or some type of irregular sampling). We can improve the situation by back propagating along fatter rays or we can add some type of regularization operator. Potentially the most interesting, and the one chosen for this paper is to add a regularization operator.

The typical choice for a regularization operator is an isotropic roughner. This will tend to fill undetermined portions of the model with isotropic blobs. In many cases this is unrealistic.

Generally velocity follows structure and our structure is laid down as a series of layers that are later deformed by tectonic processes. A better choice for our regularization operator is something that tends to create features that follow structure. Clapp (2001) showed that this can improve the velocity estimate for oil exploration targets. Our regularization operator becomes a *steering filter*, a non-stationary filter which tends to smooth along some predefined dip map. In this case we used three reflectors to build the dip map from: the surface, a basement reflector, and the Moho. We measure the dip along each reflector and then interpolate between them. Figure 4 shows the dip field overlain by the reflectors.

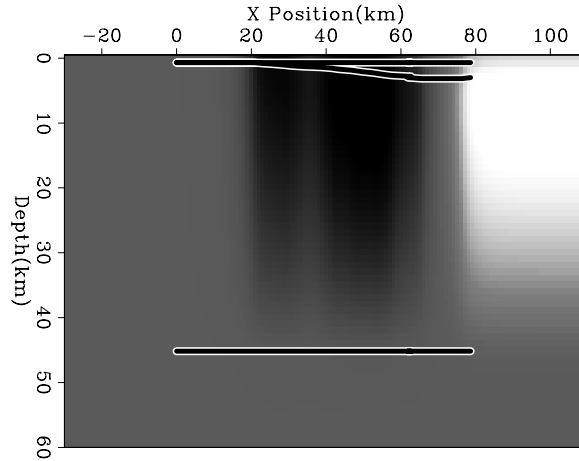


Figure 4: The dip field and reflectors used to construct the steering filter operator. The upward dip on the right edge is due to continuing the dip present at the edge of the reflectors.

bob4-dips [ER]

We want to smooth the slowness model, not the change in slowness that we are inverting for. As a result our regularization fitting goal becomes

$$\mathbf{0} \approx \mathbf{A}(\mathbf{s}_0 + \Delta\mathbf{s}), \quad (3)$$

where \mathbf{s}_0 is the initial slowness and \mathbf{A} is our steering filter. This problem converges quite slowly. As a result we precondition the model using the inverse of our regularization operator (Claerbout, 1999). Our final set of fitting goals become

$$\begin{aligned} \Delta\mathbf{t} &\approx \mathbf{T}_0\mathbf{A}^{-1}\mathbf{p} \\ \mathbf{0} &\approx \epsilon\mathbf{p}, \end{aligned} \quad (4)$$

where \mathbf{p} is the preconditioned variable and ϵ is a twiddle parameter controlling the amount of smoothing. Figure 5 shows the resulting change in velocity and the updated velocity model. Note how the basin structure that has now appears in the model.

RELINERIZATION

As mentioned above tomography is actually a non-linear problem. We can potentially achieve a better result by relinearization around our updated slowness model. We can write our updated travel times in terms of non-linear iteration i ,

$$\Delta\mathbf{t}_i = \Delta\mathbf{t} - \mathbf{T}_i(\mathbf{s}_i - \mathbf{s}_0). \quad (5)$$

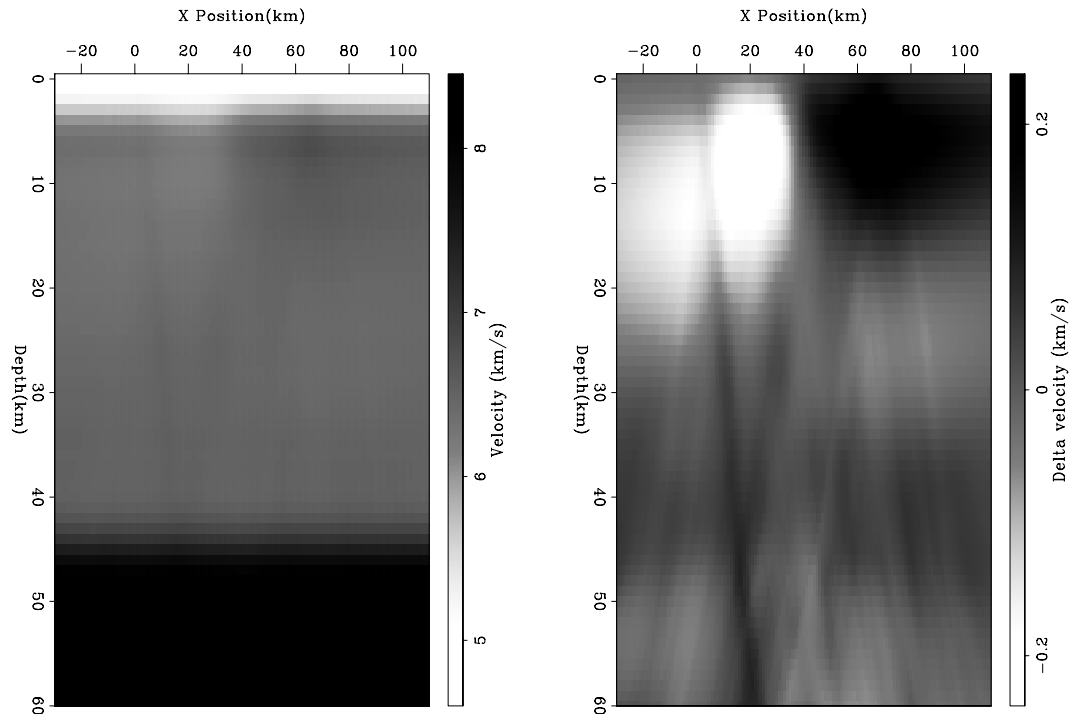


Figure 5: The left panel shows the updated velocity model. The right panel is the change in velocity resulting from 120 iterations of fitting goals (4). `bob4-vel1` [ER]

We performed two more non-linear iterations of tomography. The right panel of Figure 6 shows our updated ray field. The ray field shows moderate changes from the initial field (left panel of Figure 6). After two additional non-linear iterations we get a moderately changed velocity model, shown in the left panel of Figure 6. The overall reduction in the RMS travel-time error is about 80%, with the majority coming on the first iteration.

FUTURE WORK

There are several avenues for future research. One obvious step is to solve for a 3-D velocity model. This would require significantly more events and stations than are available in this experiment. Second, the subtraction of the best fit plane wave from the arrival times is less than optimal. In areas of complex velocity this could introduce significant travel-time errors that would be difficult to correct.

The most interesting future research direction is to use the steering filters to test different geologic hypotheses. The difference in the reduction in the travel time errors and the location of large values in the regularization portion of the residual vector would both be good indicators of model suitability.

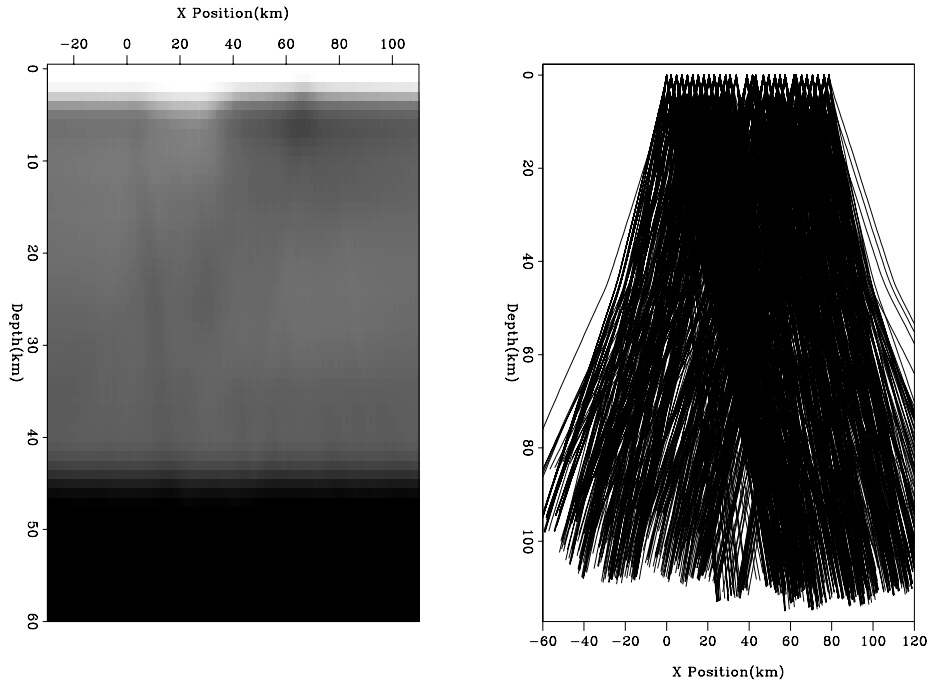


Figure 6: The final set of rays (right) and the final velocity model (left) after three non-linear iterations of tomography. Note how many of the feature seen in Figure 5 have become more defined. `bob4-final` [ER]

CONCLUSION

We apply a non-stationary filter, a *steering filter*, to a deep crustal tomography problem. We show that the updated velocity model shows more consistency with our geologic model than typically is found. We hypothesize that steering filters could be an effective tool in evaluating different geologic model in global seismologic tomography problems.

REFERENCES

- Claerbout, J., 1999, Geophysical estimation by example: Environmental soundings image enhancement: Stanford Exploration Project, <http://sepwww.stanford.edu/sep/prof/>.
- Clapp, R. G., 2001, Geologically constrained migration velocity analysis: Ph.D. thesis, Stanford University.

The influence of multiples and imaging approximations on focusing-effect AVA detection and removal

*Ioan Vlad*¹

ABSTRACT

Focusing-effect AVA (FEAVA) consists of anomalous amplitudes due to transmission effects. In multiple-free synthetic datasets, whether simple or complex, the focusing is removed by migration with the correct velocity and an operator adjoint to that used in modeling. In multiple-affected synthetic datasets, migration with the correct velocity but with an operator less accurate than that used in modeling is only partially successful in removing FEAVA. There are numerical experiments which can distinguish whether this is due to the presence of multiples, to lack of imaging operator accuracy, or to lack of imaging-modeling adjointness.

INTRODUCTION

While propagating through velocity lenses, seismic wavefields focus and defocus, causing variations in recorded amplitudes. In the case of lateral velocity variations of a large spatial extent, reflected energy is redirected outside the survey aperture, causing illumination problems. Small lenses, producing small traveltime anomalies but rather visible amplitude focusing (Focusing-Effect AVA), do not bring about loss of information, making the recovery of velocity information from amplitudes and traveltimes feasible in principle.

Vlad and Biondi (2002) and Vlad (2002) show that Wave-Equation Migration Velocity Analysis (Biondi and Sava, 1999) is a highly suitable method for finding the FEAVA-causing velocity lenses. Vlad et al. (2003) show that for a simple synthetic dataset under optimal conditions, this method generates velocity models which eliminate FEAVA through migration with an operator of the same accuracy as the one used for modeling. Vlad (2004) also demonstrates a FEAVA detector on the same synthetic dataset.

Simple controlled experiments, however, are only the first step in the testing of scientific hypotheses. In this paper I advance by testing the previously proposed methods on a significantly more complex synthetic dataset. I examine the behavior of FEAVA in the data domain and in the image domain, in a setting with and without heavy internal multiples contamination, in an image migrated just with the background velocity trend and with the correct velocity model (one and eight reference velocities), with high offset sampling and with sparse offset sampling. In particular, the purposes of the study are: 1. Determining the robustness of

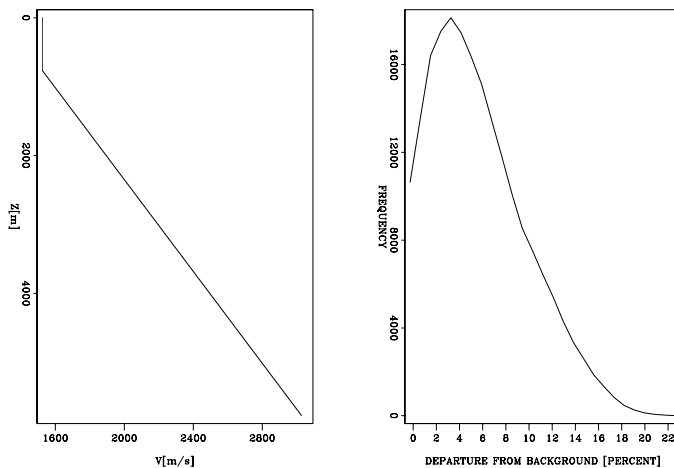
¹email: nick@sep.stanford.edu

FEAVA detection with respect to multiples and imaging approximations; 2. Probing the degree of amplitude accuracy needed by a migration operator in order to eliminate FEAVA from the image; 3. Finding to what extent internal multiples can interfere with FEAVA removal through migration.

EXPERIMENT SETUP

The numerical experiment uses a highly realistic velocity model composed of stratigraphically plausible succession of reflectors superimposed over a linearly increasing background velocity. Figure 1 displays some properties of the velocity model. The velocity variations are

Figure 1: **Left:** Background velocity; **Right:** Histogram of velocity deviation from the background, in percentages, for a random number of samples in a certain region of the model. `nick1-velomod` [CR]



sufficiently abrupt to cause massive multiple internal reflections when modeled with a two-way propagation algorithm. Figure 2 shows both multiple-free data created with a one-way algorithm (split-step with three reference velocities) and multiple-affected data² created with a finite-difference algorithm. Vertical streaks of high-amplitude focusing are visible, especially in the multiple-free panel.

FEAVA IN THE IMAGE DOMAIN

In the absence of multiples

The top panel of Figure 3 displays the result of migrating the multiple-free data with the background velocity shown in the left panel of Figure 1. High-amplitude vertical streaks mark the presence of FEAVA. The FEAVA detector (Vlad, 2004) works by measuring the departure of AVA from the Shuey (1985) model. The output of the detector (bottom panel of Figure 3) highlights the AVA much more clearly than the stack. Migrating with the adjoint of the modeling operator (split-step, three reference velocities) eliminates the FEAVA from the image (Figure 4).

²courtesy of ChevronTexaco Corp.

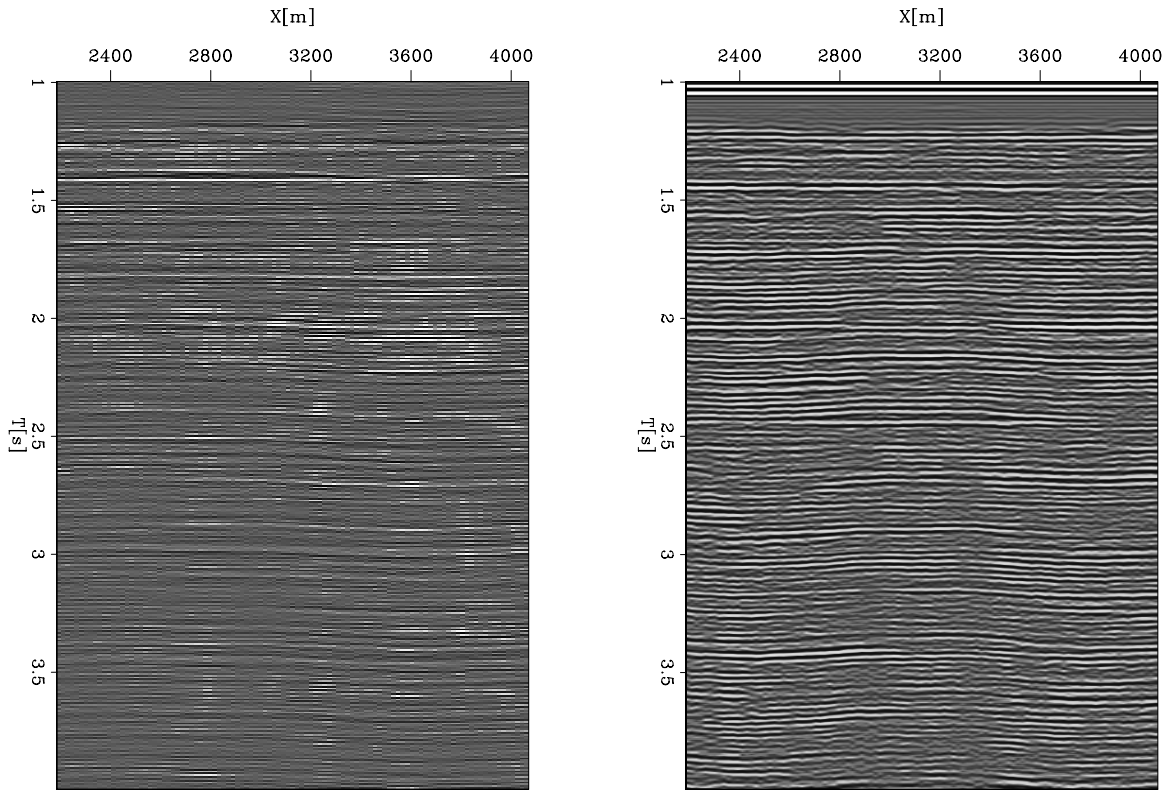


Figure 2: Zero-offset data. **Left:** without multiples; **Right:** with multiples. `nick1-zoff` [CR]

In the presence of multiples

High contrasts between layers in the velocity model cause a very large number of multiples to be generated. The result of migrating this multiple-affected dataset with the background trend from the left panel of Figure 1 is shown in the upper panels of Figure 5. FEAVA is indicated by a vertical path of high energy in the middle of the image and is clearly outlined by the FEAVA detector. Non-focused multiples depart from Shuey's approximation too, but the resulting FEAVA detector output is one order of magnitude smaller than that caused by actual focusing. The lower panels of Figure 5 show the results of migrating with the correct velocity model, albeit with a single reference velocity. The focusing is no longer visible in the image. The focusing-caused FEAVA detector output has fallen significantly, to the level of power of surrounding multiples. The two FEAVA outputs are displayed in the same intensity scale.

FEAVA was clearly reduced by migration, but not entirely eliminated. One natural question is whether significantly increasing the number of reference velocities in migration will improve the outcome. However, a migration with eight reference velocities which produced the upper panels of Figure 6, show that this is not the case for this type of stratigraphic play. The improvements are incremental, visible only by electronically displaying the two pictures in an animated sequence.

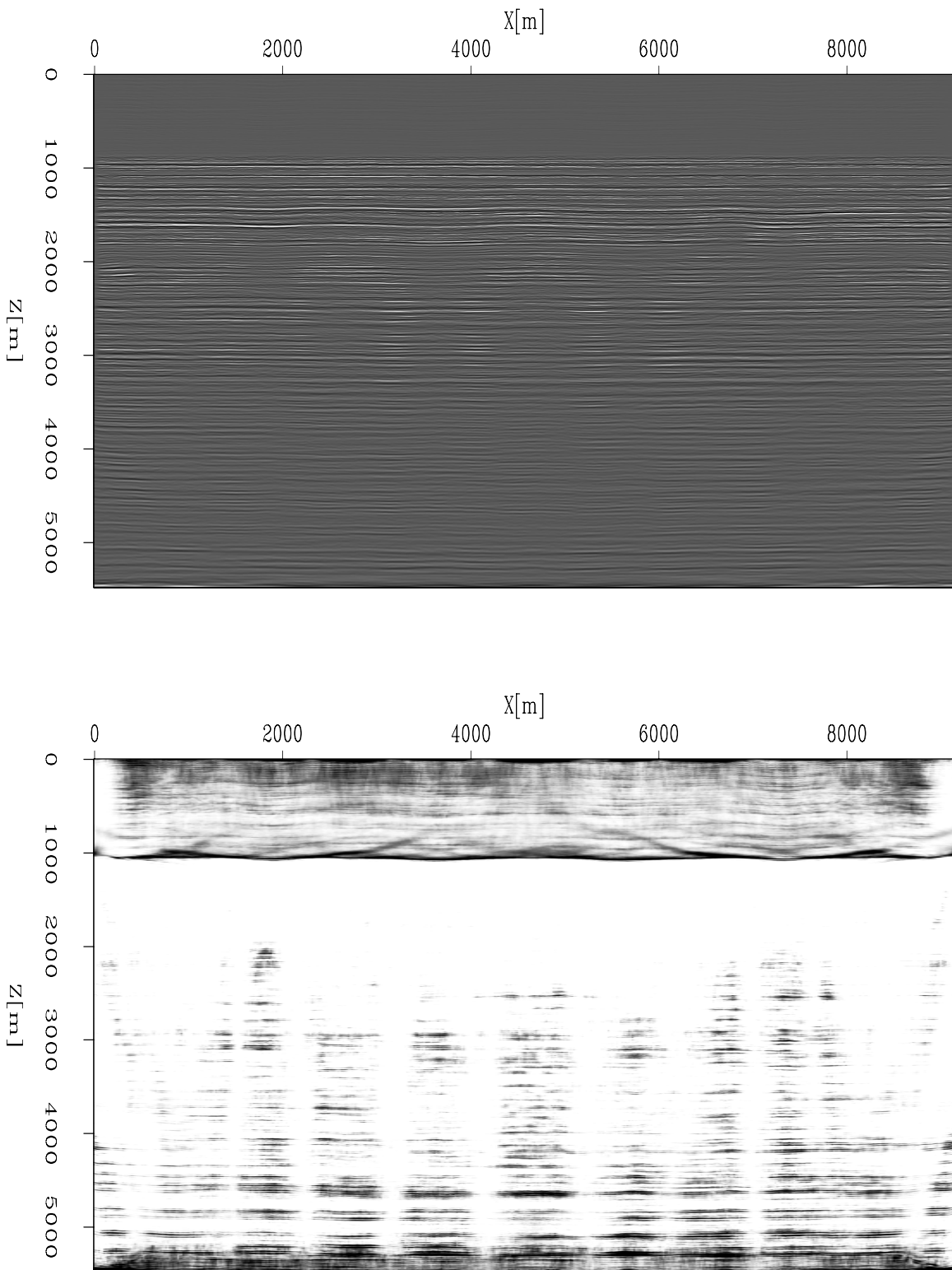


Figure 3: FEAVA is present after migrating the multiple-free data with the background velocity. **Top:** as higher-amplitude streaks in the stack (barely visible); **Bottom:** after applying the FEAVA detector. `nick1-com_nomult_imag` [CR]

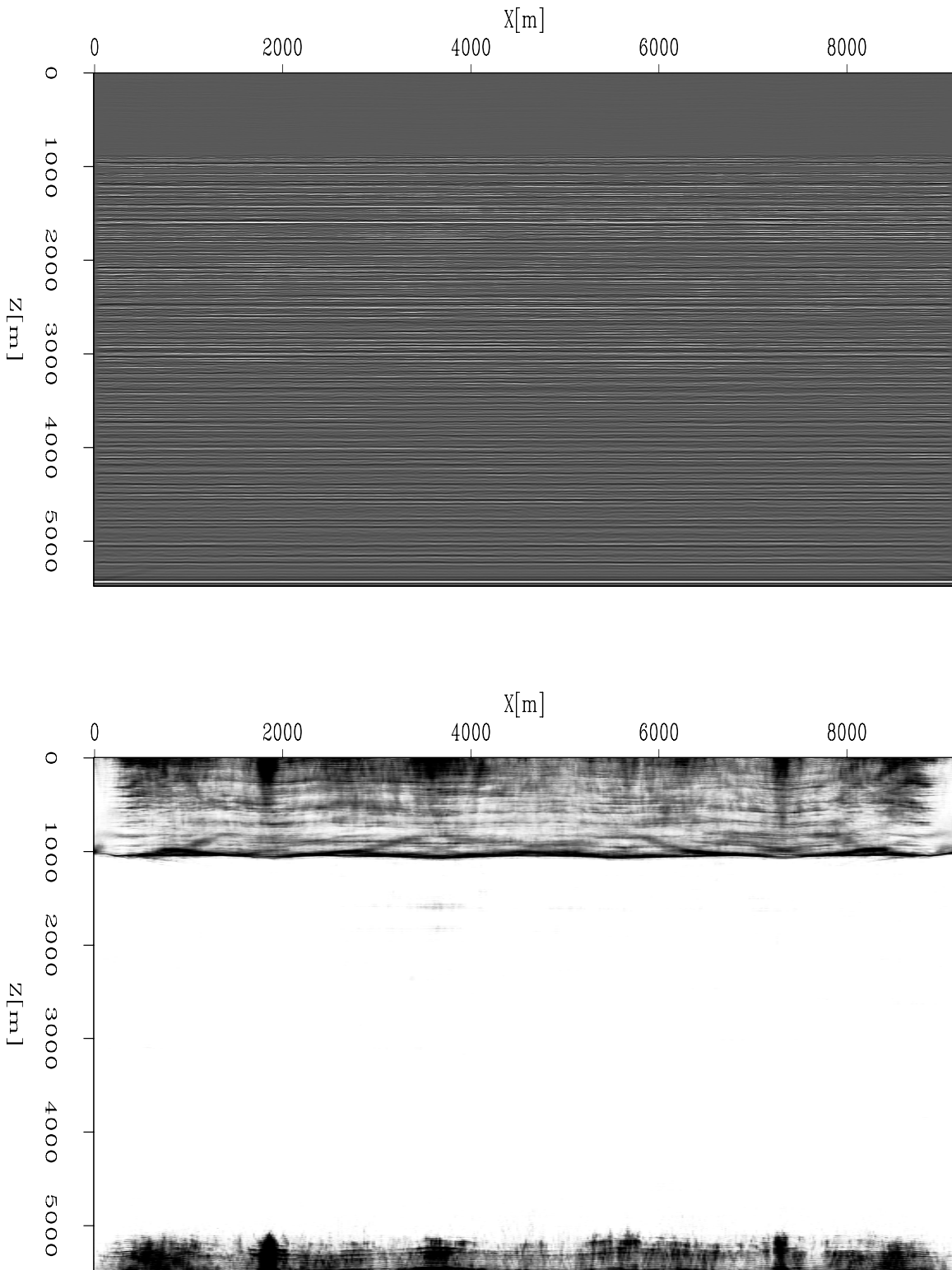


Figure 4: FEAVA disappears after migrating the multiple-free data with the correct velocity and the exact adjoint of the modeling operator. **Top:** Stack. **Bottom:** after applying the FEAVA detector. Compare with lower panel of Figure 3 `nick1-com_nomult_imaC` [CR]

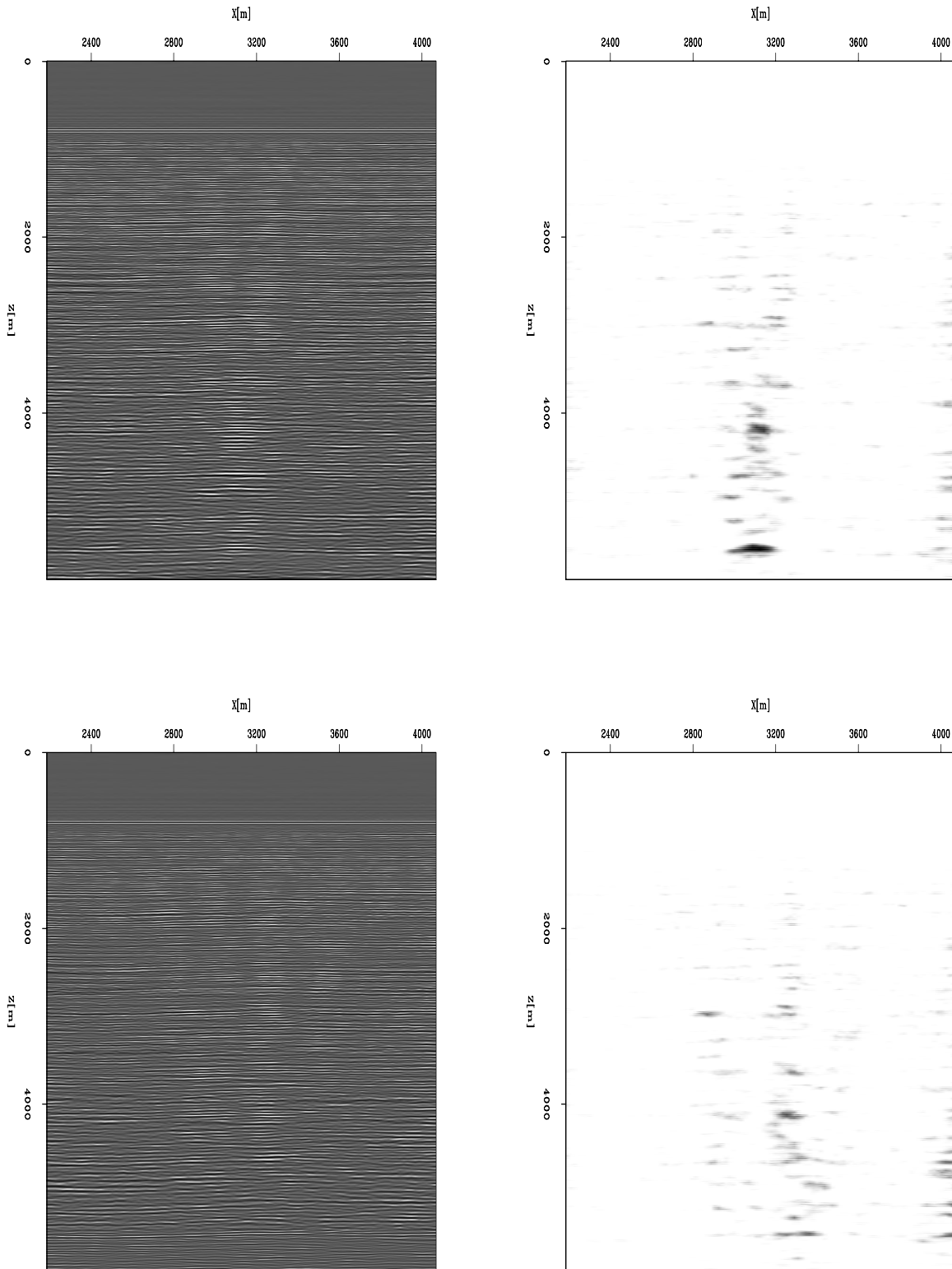


Figure 5: **Top-left:** image produced with the linear background velocity trend; **Top-right:** output of FEAVA detection applied after linear background velocity migration; **Bottom-left:** image produced with the correct velocity (split-step kernel with one reference velocity); **Bottom-right:** output of FEAVA detection applied after split-step migration with the correct model, one reference velocity. FEAVA detector outputs in the same color scale, for comparison.

`nick1-bg-refvel1` [CR]

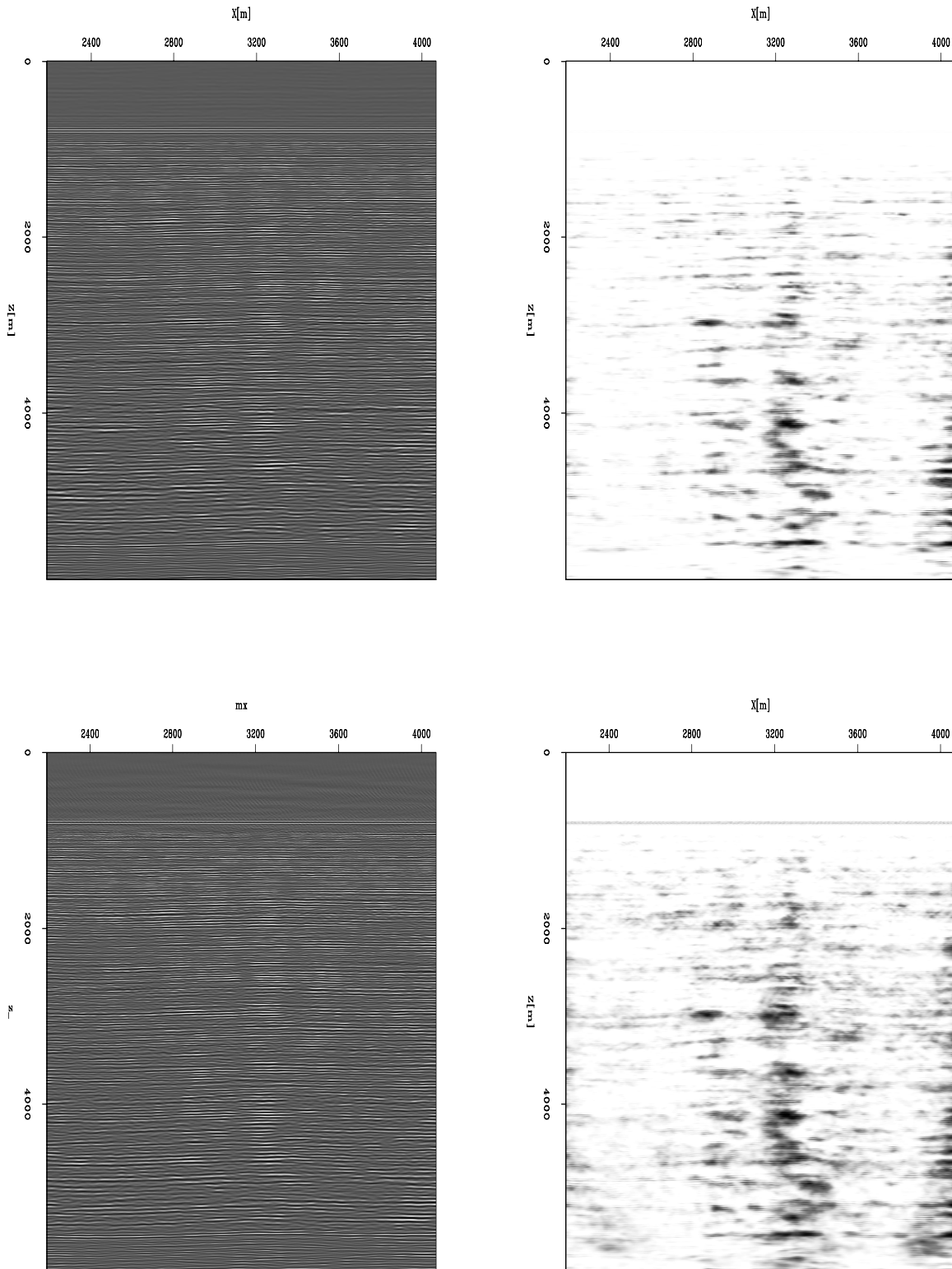


Figure 6: **Top-left:** image produced with the correct velocity (split-step kernel, eight reference velocities); **Top-right:** output of FEAVA detection applied after migration with the correct velocity (eight reference velocities); **Bottom-left:** image produced with the correct velocity (split-step kernel with one reference velocity) on dense data; **Bottom-right:** output of FEAVA detection applied after split-step migration with the correct model, one reference velocity on dense data. For detail enhancement, FEAVA detector outputs are not in the same color scale.

Another potential limitation stems from the fact that, due to the combination of depth/offset sampling (Sava and Biondi, 2001), the range of angles into which offsets can be reliably transformed was limited to 15° , while the FEAVO detector works up to 30° . Would energy from greater angles improve the situation? The bottom panels of Figure 6 are produced with an offset sampling four times smaller than before, resulting in reliable transformations from offset to angle up to 45° . This does not bring improvements either. On the contrary, multiples, highly curved at large angles, create more noise in the FEAVA detector output. The extra smoothness comes from having decreased the midpoint sampling by a factor of four.

CONCLUSIONS

Lateral velocity deviations as small as three percent from the background can cause visible focusing. The FEAVA detector performs well both in the presence and in the absence of multiples. FEAVA removal by migration works when the migration operator is the adjoint of the modeling one and when no multiples are present. When internal multiples are present and imaging is performed with an algorithm of a lower order than the one used for modeling, FEAVA is removed only partially by migration. This is most likely caused by multiples not being defocused by a migration with the velocity of the primary reflections, regardless of the order of the algorithm. To verify this conjecture, one would need to model with an amplitude-preserving two-way algorithm two similarly complex datasets – one multiple-free and one multiple-affected, and then migrate each of them with the operator adjoint to the one used in modeling. If the conjecture is true, FEAVA will be removed completely from the multiple-free dataset, but only partially from the multiple-affected one. I also conjecture that, for a synthetic dataset, FEAVA removal is possible if the algorithm used for migration has the same accuracy or greater than the one used for modeling, and that exact adjointness of migration and modeling operators is not important. To verify this I will need to image with a higher-order algorithm a multiple-free dataset generated with a lower-order algorithm. I plan to verify these assertions in the near future.

ACKNOWLEDGMENTS

I thank Joseph Stefani, James Rickett, Fred Herkenhoff, and other people from the Chevron-Texaco research group in San Ramon for the velocity model, for the finite-difference synthetic dataset and for meaningful discussions. I thank Biondo Biondi for useful suggestions and Paul Sava and Marie Clapp for lending me computer time.

REFERENCES

- Biondi, B., and Sava, P., 1999, Wave-equation migration velocity analysis: SEP-100, 11–34.
- Sava, P., and Biondi, B., 2001, Amplitude-preserved wave-equation migration: SEP-108, 1–26.

Shuey, R. T., 1985, A simplification of the Zoeppritz equations: *Geophysics*, **50**, no. 4, 609–614.

Vlad, I., and Biondi, B., 2002, Velocity estimation for seismic data exhibiting focusing-effect AVO: SEP-**111**, 107–123.

Vlad, I., Biondi, B., and Sava, P., 2003, Velocity estimation for seismic data exhibiting focusing-effect AVO (Part 3): SEP-**114**, 101–109.

Vlad, I., 2002, Velocity estimation for seismic data exhibiting focusing-effect AVO (Part 2): SEP-**112**, 47–64.

Vlad, I., 2004, Velocity estimation for seismic data exhibiting focusing-effect AVO (Part 4): SEP-**115**, 265–272.

Short Note

An educated guess on the V_p/V_s ratio

Daniel A. Rosales¹

INTRODUCTION

Data processing of converted waves generally yields estimated values for both P velocity and S velocity in the area of study. These values are usually seen in the form of two parameters: 1) the multiplication of both velocity fields, and 2) the ratio of both velocity fields. Traditionally the ratio of the P and S velocities, which is known as the γ value, is the result of an extensive combined analysis on the PS data and the single P-mode data. Knowledge of γ is important not only for seismic processing but also for rock property estimation. Traditionally, γ is estimated through a combined processing of the PS data and the PP data, as described by Thomsen (1998) and Audebert et al. (1999).

In this note, I present an analytical procedure to estimate an initial value of γ that depends only on the most basic processing scheme, the NMO stacking process. Several authors have discussed the stacking process for converted waves (Tessmer and Behle, 1988; Castle, 1988; Iverson et al., 1989; Huub Den Rooijen, 1991). Tessmer and Behle (1988) apply conventional NMO to converted waves where the RMS stacking velocity is designated as the *converted-wave* velocity. This NMO procedure uses a hyperbolic approximation of the moveout equation; so, there is not a satisfactory correction of the moveout.

I introduce a non-hyperbolic moveout equation that characterizes converted waves. This moveout equation consists of three main terms. The third term depends on the γ function giving us an equation to estimate an approximately constant value of γ , directly from the PS data alone.

THEORY: NON-HYPERBOLIC MOVEOUT

The main characteristic of converted-wave data is their non-hyperbolic moveout. However, for certain offset/depth ratios, it is possible to approximate the non-hyperbolic moveout as a hyperbola (Tessmer and Behle, 1988).

Tessmer and Behle (1988) extend the work of Taner and Koehler (1969) for converted waves. They apply a second-order approximation to the moveout equation to converted-wave

¹email: daniel@sep.stanford.edu

data. In such cases the stacking velocity corresponds to the product of both P and S velocities known as converted-wave velocity.

Castle (1988) presents the third-order-approximation coefficient terms for the converted-wave moveout equation. In this note, I simplify this term and present it as a function of γ alone.

Equation (1) is the expanded traveltime function of reflected PP or SS data presented by Taner and Koehler (1969):

$$t^2 = c_1 + c_2x^2 + c_3x^4, \quad (1)$$

where x represents full offset, $c_1 = b_1^2$, $c_2 = \frac{b_1}{b_2}$, and $c_3 = \frac{b_2^2 - b_1b_3}{4b_2^4}$, with

$$b_m = \sum_{k=1}^n z_k (\alpha_k^{2m-3} + \beta_k^{2m-3}), \quad (2)$$

where k indicates the stratigraphic layers present in the model. Here and hereafter, α_k and β_k respectively denote the P velocity and the S velocity for the k^{th} -layer. Tessmer and Behle (1988) show that

$$c_1 = \left(\sum_{k=1}^n z_k \left(\frac{1}{\alpha_k} + \frac{1}{\beta_k} \right) \right)^2 = t_0^2, \quad (3)$$

and

$$c_2 = \frac{\sum_{k=1}^n z_k \left(\frac{1}{\alpha_k} + \frac{1}{\beta_k} \right)}{\sum_{k=1}^n z_k (\alpha_k + \beta_k)} = \frac{1}{v_{rms}^2}, \quad (4)$$

where $v_{rms}^2 = \alpha_{rms} \cdot \beta_{rms}$, this is only true when γ is constant. The formal definition for c_3 is as follows (Castle, 1988):

$$c_3 = \frac{(\sum_{k=1}^n z_k (\alpha_k + \beta_k))^2 - \sum_{k=1}^n z_k \left(\frac{1}{\alpha_k} + \frac{1}{\beta_k} \right) \cdot \sum_{k=1}^n z_k (\alpha_k^3 + \beta_k^3)}{4 \left(\sum_{k=1}^n z_k (\alpha_k + \beta_k) \right)^4}. \quad (5)$$

For one layer, equation (5) simplifies to

$$c_3 = \frac{z^2 \left[(\alpha + \beta)^2 - \left(\frac{1}{\alpha} + \frac{1}{\beta} \right) (\alpha^3 + \beta^3) \right]}{4z^4 (\alpha + \beta)^4}, \quad (6)$$

which reduces to

$$c_3 = \frac{2\alpha\beta - \frac{\alpha^3}{\beta} - \frac{\beta^3}{\alpha}}{4z^2(\alpha + \beta)^4}. \quad (7)$$

Now, the simple trick I use to make an educated guess for γ with PS data alone is to consider [from the results of c_1 and c_2 , equations (3) and (4)] that $\alpha_{rms}^2 = v_{rms}^2 \gamma$ and $\beta_{rms}^2 = v_{rms}^2 \gamma^{-1}$,

remember that γ is approximately constant in all layers. With these assumptions, equation (5) simplifies to

$$c_3 = \frac{2 - (\gamma^2 + \gamma^{-2})}{4t_0^2 v_{rms}^4 (\gamma^{1/2} + \gamma^{-1/2})^4}. \quad (8)$$

Introducing the final results for c_1 , c_2 and c_3 into equation (1), I obtain an equation to perform non-hyperbolic moveout for PS data that is dependent on only two parameters: 1) the multiplication of the P and S velocities, or the converted wave *rms* velocity (v_{rms}), and 2) the Vp/Vs ratio (γ). It is also important to note that this equation is valid for a constant Poisson's ratio in all layers. With these simplifications and equations, it is possible to obtain an approximate value of γ using PS data alone.

$$t^2 = t_0^2 + \frac{x^2}{v_{rms}^2} + \frac{x^4}{t_0^2 v_{rms}^4} \left[\frac{2 - (\gamma^2 + \gamma^{-2})}{4 (\gamma^{1/2} + \gamma^{-1/2})^4} \right] \quad (9)$$

Equation (9) is the central result of this paper. It is possible to note that the moveout equation is more than a hyperbolic relation, since it involves a third term. Another important characteristic of equation (9) is that it depends only on two parameters: 1) the converted-waves *rms* velocity, and 2) the Vp/Vs ratio. This important characteristic will allow us to invert for a value of γ . It is also important to note that the sensitivity of equation (9) to γ probably is not too high, since the third term of the equation also depends on the offset-depth ratio.

It is important to note that for the specific case of $\alpha = \beta$ (this never happens in practice), i.e., no converted waves, the value of γ equals 1, and equation (9) reduces to the conventional normal moveout equation. This is also a result of the one layer assumption.

NUMERICAL EXAMPLES

Figure 1 presents a simple flat-layer model. Figures 2 and 3 show the result of modeling the two-way travel time with the conventional normal moveout equation, and with the non-hyperbolic moveout equation, using an initial velocity of 1100 m/s, a velocity gradient of 125 s⁻¹ and a constant value of $\gamma = 2$.

Both results (Figures 2 and 3) present a hyperbolic moveout at near offset or small offset-to-depth ratio. This result resembles the well known theoretical presentation of Tessmer and Behle (1988). However, the non-hyperbolic moveout is dominant for large offsets and shallow depths, as can be observed in Figure 2.

I also apply the non-hyperbolic moveout equation to a PS CMP gather from the Alba dataset acquired on the Alba oil field in the North sea. The data set is a multicomponent 3-D Ocean Bottom Seismic experiment. Figure 4 shows the original CMP gather before (left), after (center) non-hyperbolic moveout, and after traditional hyperbolic moveout (right). I use

Figure 1: Reflectivity model.
 daniel2-mod5 [ER]

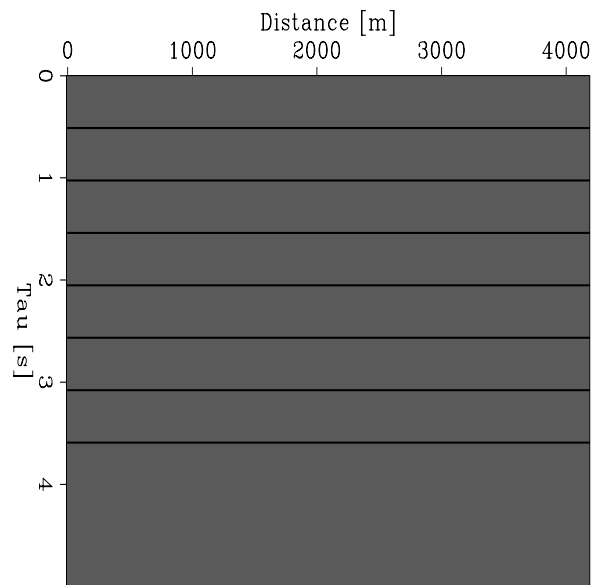
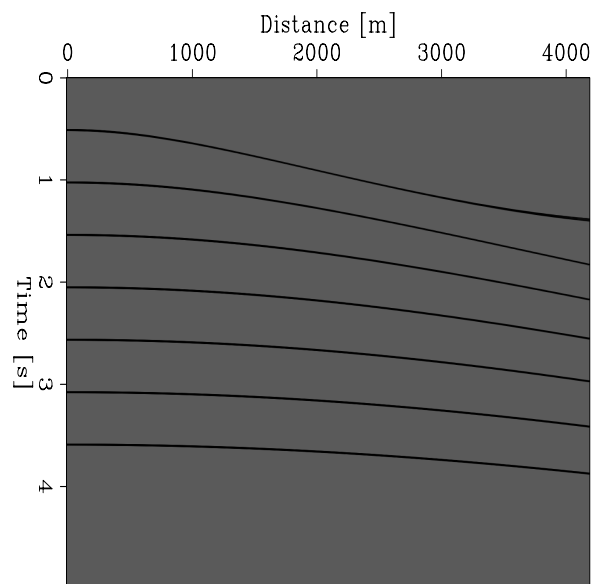


Figure 2: Modeled data, using the non-hyperbolic equation with a constant value of $\gamma = 2$.
 daniel2-mod5NMO [ER,M]



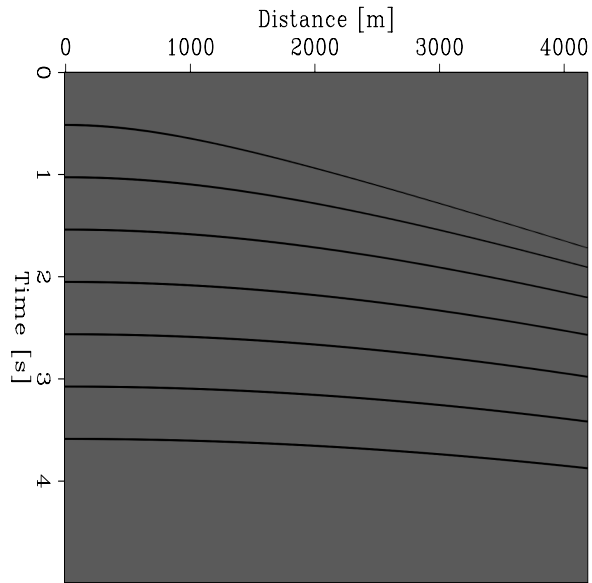


Figure 3: Modeled data, using the the traditional hyperbolic equation.
daniel2-mod5NMO1 [ER,M]

an initial velocity value of 1100 m/s, and a velocity gradient of 125 s^{-1} and a constant $\gamma = 2.0$. Note that even though the events are not totally corrected, the non-hyperbolic correction gives a better result for shallow events at large offsets. These events are flatter after the non-hyperbolic moveout correction than with the hyperbolic moveout correction.

CONCLUSIONS AND FUTURE WORK

The non-hyperbolic equation introduced here is an approximation; therefore, I suggest it should be used only as a way to obtain an initial constant value for the V_p/V_s ratio. This ratio should be optimized later, using for example an iterative velocity-analysis technique with wave-equation migration velocity analysis.

A future goal is to produce a γ -scan technique, similar to a velocity scan, to obtain the best γ value. This final value will probably be a key element for more advanced velocity analysis techniques.

Also, with the definition of a direct and more appropriate formulation for the PS travel time with both P and S velocities, one tentative future step is to generate an inversion scheme to estimate both P and S velocities from a single PS section.

REFERENCES

- Audebert, F., Granger, P. Y., and Herrenschmidt, A., 1999, CCP-Scan technique: true common conversion point sorting and converted wave velocity analysis solved by PP and PS Pre-Stack Depth Migration: 69th Annual Internat. Mtg., Society Of Exploration Geophysicists, Expanded Abstracts, 1186–1189.

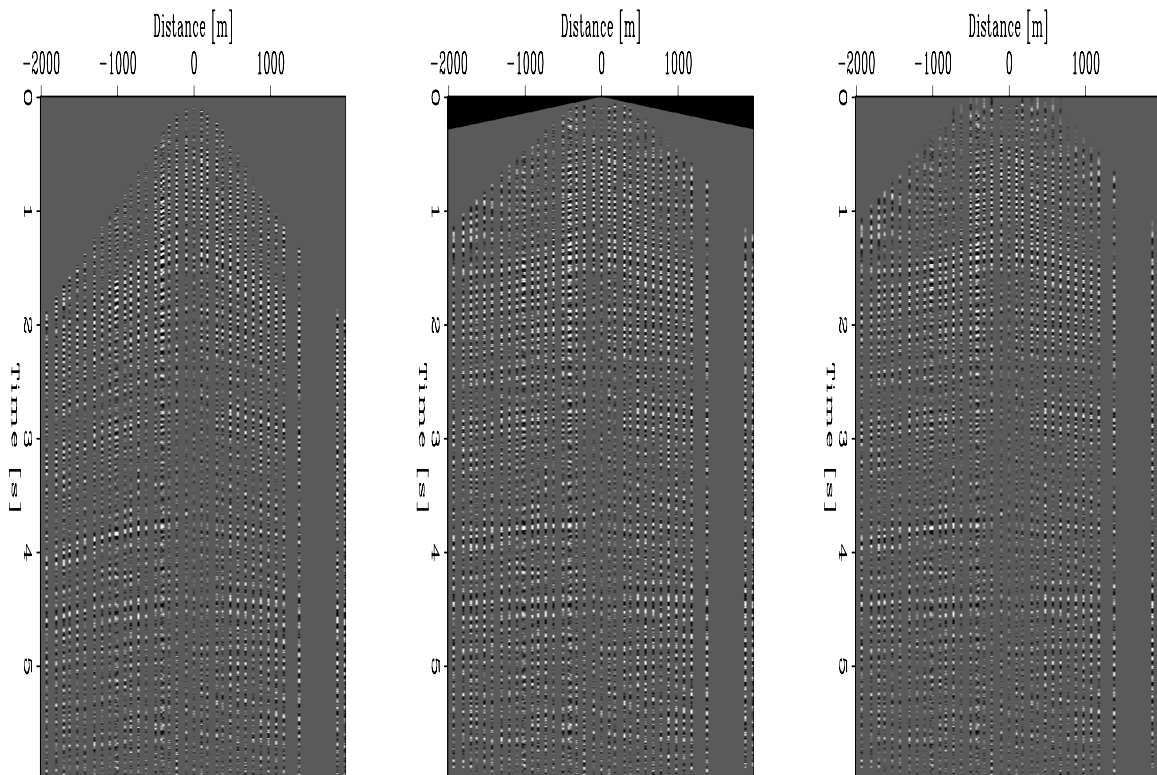
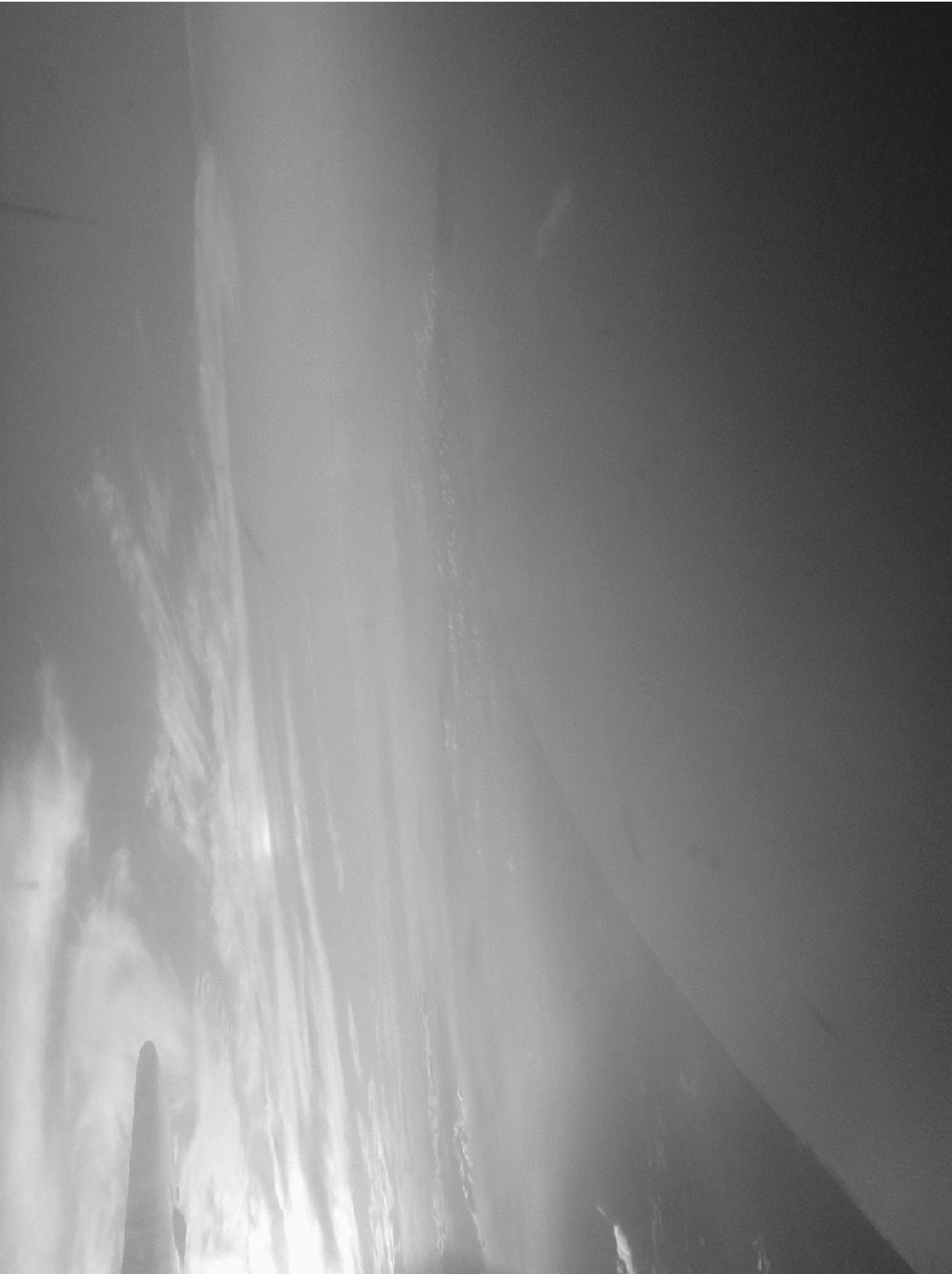


Figure 4: PS CMP gather from the Alba dataset, original gather (left), after non-hyperbolic moveout (center), and after traditional hyperbolic moveout (right). I performed non-hyperbolic moveout and traditional moveout both with an initial velocity of 1100 m/s, a velocity gradient of 125 s^{-1} with $\gamma = 2.0$ for the non-hyperbolic case. `daniel2-cmp_comp` [ER,M]

- Castle, R. J., 1988, Shifted hyperbolas and normal moveout: 58th Annual Internat. Mtg., Society Of Exploration Geophysicists, Expanded Abstracts, 894–896.
- Huub Den Rooijen, P. G. M., 1991, Stacking of P-SV seismic reflection data using dip moveout: *Geophysical Prospecting*, **39**, no. 4, 585–598.
- Iverson, W. P., Fahmy, B. A., and Smithson, S. B., 1989, VpVs from mode-converted P-SV reflections: *Geophysics*, **54**, no. 7, 843–852.
- Taner, M. T., and Koehler, F., 1969, Velocity spectra digital computer derivation and applications of velocity functions: *Geophysics*, **34**, no. 7, 859–881.
- Tessmer, G., and Behle, A., 1988, Common reflection point data-stacking technique for converted waves: *Geophysical Prospecting*, **36**, no. 5, 671–688.
- Thomsen, L., 1998, Converted wave reflection seismology over anisotropic, inhomogeneous media.: 68th Annual Internat. Mtg., Society Of Exploration Geophysicists, Expanded Abstracts, 2048–2051.



Multiple suppression in the image space: A Mahogany field example

Daniel A. Rosales and Paul Sava¹

ABSTRACT

Stolt residual migration (SRM) is an effective technique for image processing after migration. It allows us to reconstruct an image corresponding to a velocity different from the original migration velocity. Furthermore, multiple attenuation in the image space (MAIS) is a powerful technique for seismic data processing after migration. Combining these two techniques makes it possible to remove multiples in the image space without accurately knowing the velocity model. The PZ section of the Mahogany field serves as a field data example to demonstrate the advantage of this combined methodology.

INTRODUCTION

Separating multiples from primaries has been a long-standing problem in exploration geophysics. Multiple reflections often destructively interfere with the primary reflections of interest (Foster and Mosher, 1992). Marine data often exhibits strong multiple-reflection problems. However, Ocean Bottom Seismic (OBS) data presents an ideal acquisition setting for removing the receiver ghost by PZ summation (Barr and Sanders, 1989; Soubaras, 1996). However, the PZ summation does not remove all the multiples, and further processing is required.

This paper combines two post-imaging processing techniques: 1) Stolt Residual Migration (SRM) (Sava, 1999, 2000), and 2) Multiple Attenuation in the Image Space (MAIS) (Sava and Guitton, 2003). Integrating these two processing techniques in one process leads to a way of eliminating multiple reflections in areas with unresolved velocity problems. Stolt Residual Migration is used in the prestack domain to obtain an image focused with a different velocity model.

Sava and Guitton (2003) discuss multiple suppression in the image space (i.e., after migration) as an alternative technique to multiple suppression in the data space (i.e., before any imaging operation). Their main assumption is that after migration with the correct velocity model, primaries are flat in angle-domain common-image gathers, while multiples present a residual curvature; therefore, primaries and multiples can be separated using the Radon transform (Foster and Mosher, 1992). However, if we yet do not have the correct velocity model, the primaries and multiples may present a similar residual moveout in the angle domain, and

¹email: daniel@sep.stanford.edu, paul@sep.stanford.edu

they will not be distinguishable by their curvatures using the Radon transform.

The problem we address in this paper is how to discern between primaries and multiples in the image space if the events have similar curvatures. We present a real data example, the Mahogany field, a 2-D OBS data set in the Gulf of Mexico.

METHODOLOGY

The methodology introduced in this paper targets those multiples that are not easily removed with known techniques, for example when stacking normal-moveout corrected seismic gathers does not eliminate all multiples (Foster and Mosher, 1992). In a previous report, Sava and Guitton (2003) introduce a technique to remove multiples after imaging. Their technique consists of applying the Radon analysis in the depth-angle domain instead of the standard Radon analysis done in the offset-time domain. Their main assumption is that primaries and multiples migrated with the correct velocity model for the primaries and transformed into angle domain common image gathers, map to distinctive angles, where primaries are flat and multiples present a residual curvature. Finally, the angle gathers are mapped into the Radon domain, where the multiples can be suppressed.

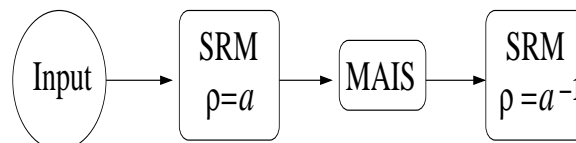
A potential issue with the previous methodology is the coupled problem of velocity analysis and multiple suppression. It is difficult to obtain an accurate velocity model when multiples are present. Moreover, the previous methodology relies on an accurate velocity model in order to suppress the multiples.

This paper proposes a solution for solving this problem. Our methodology combines two post-migration processing techniques. The first one, SRM, produces an intermediate image with a new velocity information given, by the ratio (ρ) between the original migration velocity and the new migration velocity; therefore, SRM induces a curvature change between primaries and multiples if ρ is significantly different than 1. The second technique, MAIS, separates the primaries and multiples into two different groups, based on their distinctive curvature induced by SRM. This allows us to model the multiples and suppress them from the final section.

Figure 1 shows the basic flow chart to eliminate multiples in the image space. The input data are our best result after processing in the data space, and after prestack migration with our best velocity model at this stage. Such processing may vary and depends on the data set under study. The next step is to perform SRM with a velocity ratio high enough to produce a difference in curvature between the primaries and the multiples (e.g., $\rho = 1.25$). The difference in curvature yields to the application of the Radon transform in the angle domain to eliminate multiples (Sava and Guitton, 2003). Finally, we apply SRM with a ratio that should be the inverse of the ratio applied before (e.g., $\rho = 0.8$).

Figure 1: Flowchart for multiple suppression in the image space with no flat events in the angle domain.

[daniel1-flow](#) [NR]



APPLICATION

The Mahogany field, located in the Gulf of Mexico, is dominated by a salt body structure. One of the data set acquired on this area consists on a 2-D Ocean Bottom Seismic (OBS) multicomponent line. Rosales and Guitton (2004) present the steps involved in the PZ summation that results in the P component section that is now under study. The PZ summation was successful in eliminating the receiver ghost; however, other surface-related multiples, like the source pegleg, are still present after the combination.

The remaining multiples are a problem when performing any migration-velocity-analysis technique. Therefore, we apply the methodology discussed in the previous section to eliminate the remaining multiples. Figure 2 shows three characteristic angle-domain common-image gathers, after three processes: the PZ summation described in Rosales and Guitton (2004), the downward continuation of the sources to the receiver label, and the migration with the velocity model presented in Rosales and Guitton (2004).

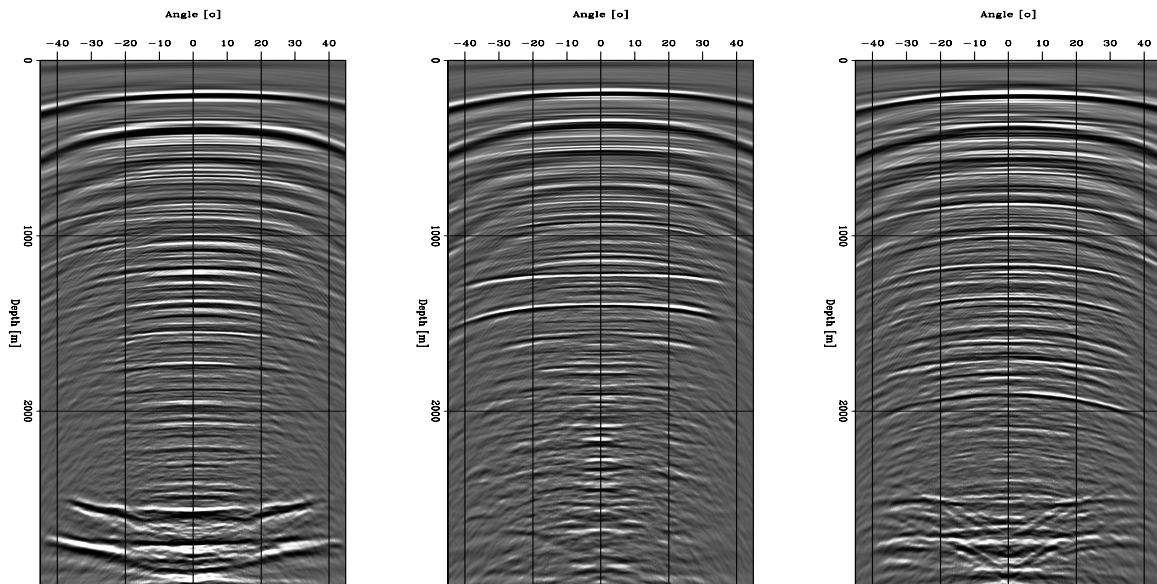


Figure 2: ADCIGS after PZ summation at three different locations. daniel1-adcigs [CR,M]

It is possible to observe a similar residual curvature for both primaries and multiples. Additionally, at this stage the primaries and multiples present a very similar moveout, since the migration velocity is still not perfect. Any migration-velocity-analysis technique done with this data will be biased with the multiple reflections still present. Additionally, Figure 3 presents the same ADCIGS as in Figure 2 but after Radon transform in the angle domain is not easy to distinguish between primaries and multiples; therefore, another process is required.

A residual curvature process will help to separate primaries and multiples in the Radon domain. The advantage of using residual migration (as discussed on the methodology) over residual moveout is that residual migration reduces the effects of image-point dispersal between events imaged at the same physical location but with different aperture angle (Biondi, 2004). Performing SRM with a value of ρ different than 1 (e.g., $\rho = 2.0$) produces a distinct

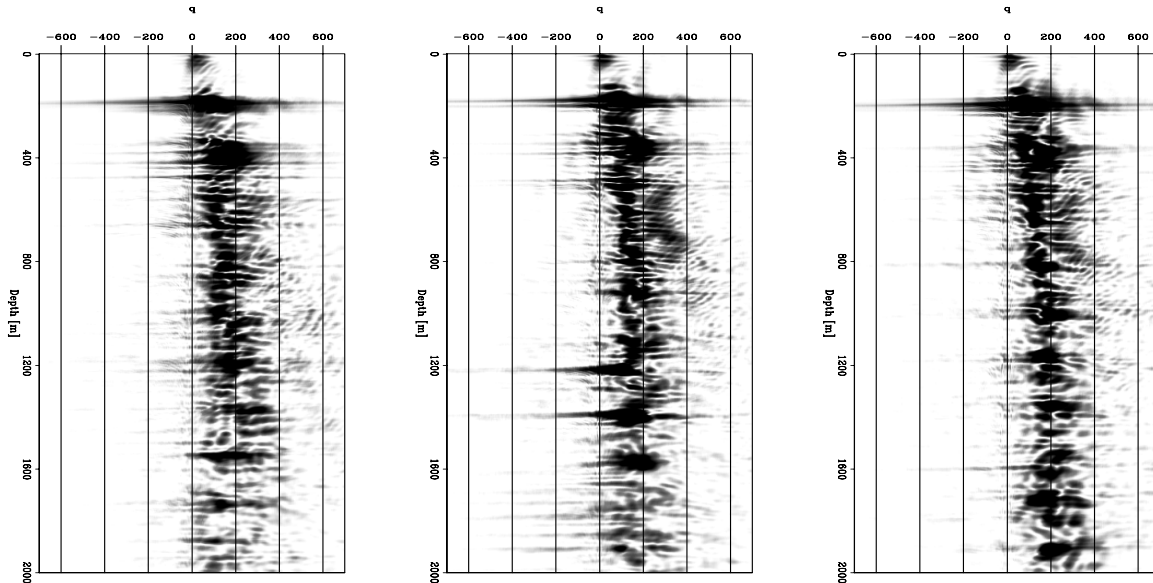


Figure 3: ADCIGs in the Radon domain, before any residual curvature process. [daniel1-adcigs.art](#) [CR]

difference between the residual moveouts of the primaries and multiples. Figure 4 shows the same ADCIGs as in Figure 2 after SRM with $\rho = 2.0$. It is now easy to distinguish between primaries and multiples through their distinctive curvatures.

Applying the Radon transform splits the image into two different curvatures; therefore, it is possible to distinguish between primaries (positive curvature) and multiples (negative curvature); additionally, it is possible to apply principles and techniques similar to those discussed by Sava and Guitton (2003) or Alvarez et al. (2004). Figure 5 shows the ADCIGs in the Radon domain. After SRM is possible to distinguish between primaries and multiples, compare the results on Figures 5 and 3. Figure 6 presents the result after eliminating the multiples and applying SRM with a ρ value of $\rho = 0.75$; this result shows a satisfactory elimination of multiples.

CONCLUSIONS AND FUTURE WORK

We have introduced a technique that addresses an important problem in seismic processing: the elimination of multiples in the image space with a not-yet-perfect initial velocity model. The combination of SRM and MAIS yields a procedure that can safely clean multiples from the data before performing any migration-velocity-analysis technique.

This technique yielded satisfactory results when applied to a 2-D line of the Mahogany field. The multiples were separated and eliminated from the primaries in the image domain, while our velocity analysis model was still incorrect.

Because both SRM and MAIS work separately on 3-D data, this technique might be useful

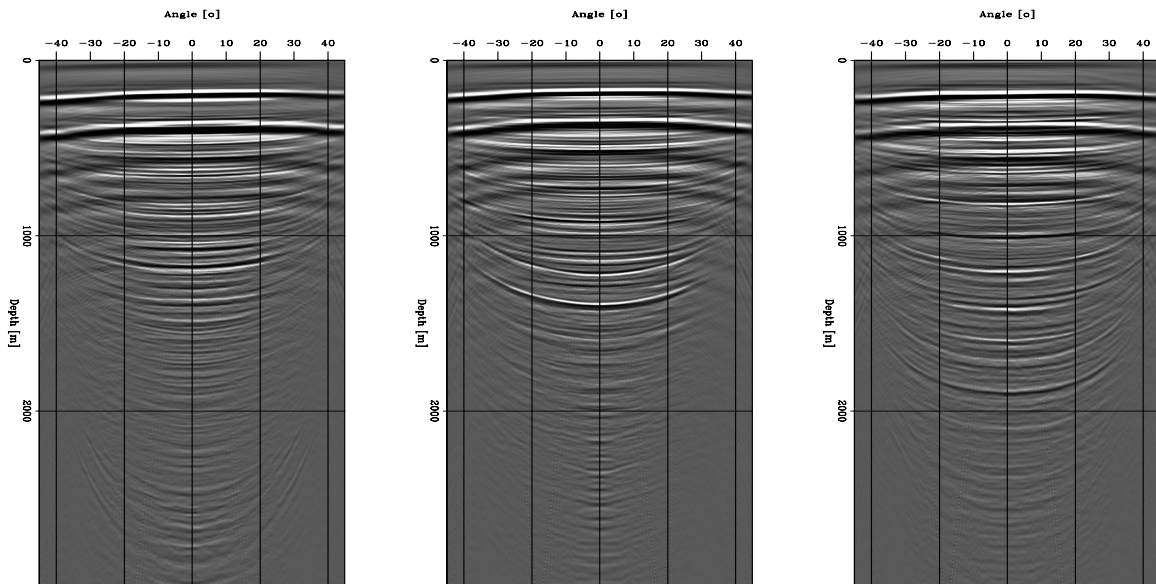


Figure 4: ADCIGs after SRM with $\rho = 2.0$. `daniel1-adcigs.srm` [CR,M]

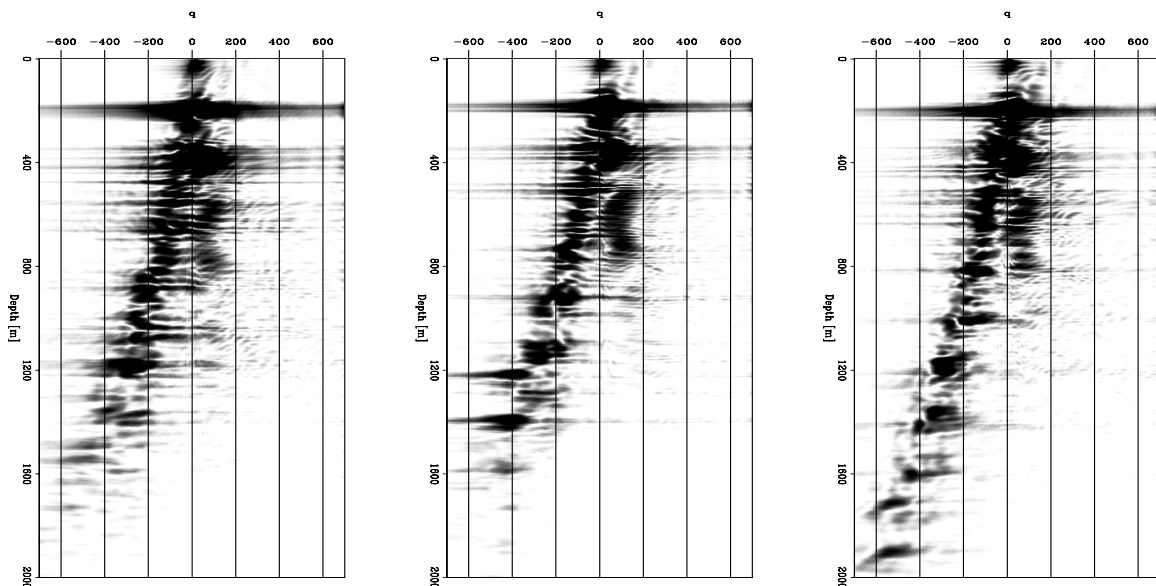


Figure 5: ADCIGs after SRM in the Radon domain. Compare with the ADCIGs in Figure 3 and note how multiples and primaries are split into two different trends.

`daniel1-adcigs.srm.art` [CR,M]

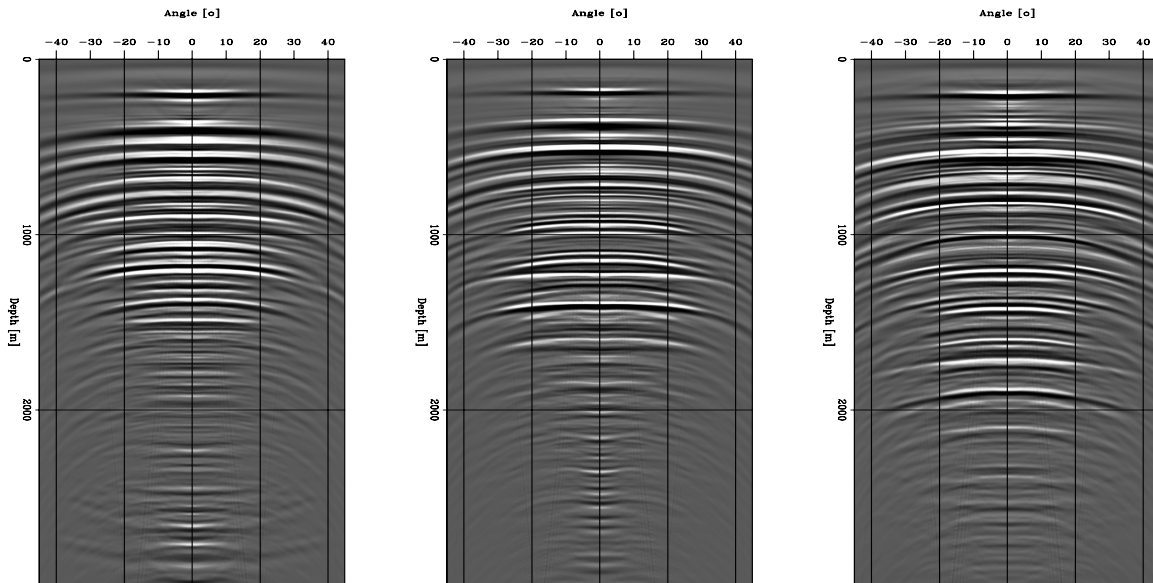


Figure 6: ADCIGS after multiple suppression. daniel1-adcigs.srm.art.isrm [CR,M]

in 3-D for eliminating multiples in the image space, in parallel with estimating a suitable migration velocity model.

ACKNOWLEDGMENTS

We thank Antoine Guitton for his useful comments and for providing his angle-domain Radon transform algorithm for the separation of multiples and primaries.

REFERENCES

- Alvarez, G., Biondi, B., and Guitton, A., 2004, Attenuation of diffracted multiples with an apex-shifted tangent-squared radon transform in image space: *SEP-115*, 139–152.
- Barr, F. J., and Sanders, J. L., 1989, Attenuation of water-column reverberations using pressure and velocity detectors in a water-bottom cable: 59th Ann. Internat. Meeting, Soc. Expl. Geophys., Expanded Abstracts, 653–656.
- Biondi, B., 2004, 3-D Seismic Imaging: Class notes, <http://sepwww.stanford.edu/sep/biondo/Lectures>.
- Foster, D. J., and Mosher, C. C., 1992, Suppression of multiple reflections using the Radon transform.: *Geophysics*, **57**, 386–395.
- Rosales, D. A., and Guitton, A., 2004, Ocean-bottom hydrophone and geophone coupling: *SEP-115*, 57–70.

Sava, P., and Guitton, A., 2003, Multiple attenuation in the image space: SEP-**113**, 31–44.

Sava, P., 1999, Short note—on Stolt prestack residual migration: SEP-**100**, 151–158.

Sava, P., 2000, Variable-velocity prestack Stolt residual migration with application to a North Sea dataset: SEP-**103**, 147–157.

Soubaras, R., 1996, Ocean bottom hydrophone and geophone processing: 66th Ann. Internat. Meeting, Soc. Expl. Geophys., Expanded Abstracts, 24–27.



Short Note

Analytical traveltimes for arbitrary multiples in constant velocity

Chris Liner and Ioan Vlad¹

INTRODUCTION

Levin and Shah (1977) compute analytical traveltimes for internal multiples generated by a single-CMP seismic survey over a 2-D, two-layer, constant-velocity Earth. Their expression treats the specific case of a single reflection from the bottom of the second layer, preceded and followed by a number of bounces inside the first layer. To obtain the traveltimes, they use the method of images, computing successive images of the source through successive reflections towards the receivers, then computing an image of the receiver through the last reflector. The traveltime is obtained by dividing the distance between the two images to the wavespeed. This way they obtain an analytical traveltime along the pegleg ray that joins the given source and receiver positions only as a function of the respective positions, without the need to take the ray parameter into account.

We extend this procedure to an Earth model with an arbitrary number of layers and an arbitrary sequence of internal bounces between the respective layers. The Earth model is still 2-D, constant-velocity, and with linear interfaces defining constant-density layers. The computations are also done individually for each CMP. The ultimate goal of this study is to assist in the computation of amplitudes for pegleg multiples. This will be used in further studies to isolate the geologic settings in which pegleg multiples are strong enough to cause errors in the interpretation.

PROBLEM SETUP

Let us assume that reflecting interface i is given through two points belonging to it, A and B . Since traveltimes are computed independently for each CMP, we use a coordinate system with the origin in the midpoint between source and receiver (both located at the surface). In this CMP-centric coordinate system, interface i can be expressed as

$$z = x \tan \theta_i + \frac{d_i}{\cos \theta_i}, \quad (1)$$

¹email: cll@utulsa.edu, ivlad@stanford.edu

where θ_i is the dip of the interface:

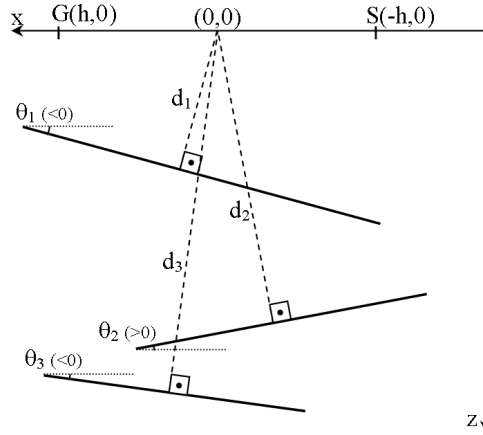
$$\tan \theta_i = \frac{z_b - z_a}{x_b - x_a} \quad (2)$$

and d_i is the distance from the CMP point to the interface:

$$d_i = z_a \cos \theta - x_a \sin \theta. \quad (3)$$

Figure 1 shows a three-interface example. Similar to Levin and Shah (1977), we use the

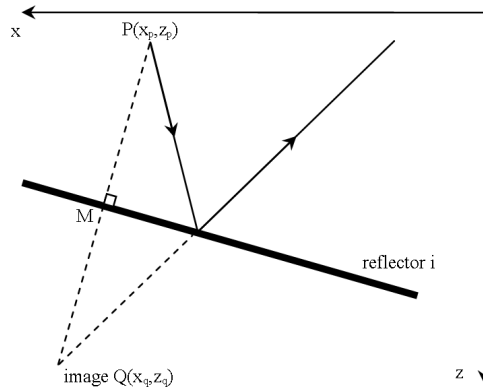
Figure 1: Three interface reflectivity model for illustrating the meaning of the notations d_i and θ_i . Notice the sign convention for angles. `nick2-peglegmodel` [NR]



method of images to compute traveltimes. Let us denote with $Q(x_q, z_q)$ the image of point $P(x_p, z_p)$ through reflector i (see Figure 2). Through simple analytical geometry we find that

$$\underbrace{\begin{bmatrix} x_q \\ z_q \end{bmatrix}}_{\mathbf{q}} = \underbrace{\begin{bmatrix} \cos 2\theta_i & \sin 2\theta_i \\ \sin 2\theta_i & -\cos 2\theta_i \end{bmatrix}}_{\mathbf{A}(2\theta_i)} \underbrace{\begin{bmatrix} x_p \\ z_p \end{bmatrix}}_{\mathbf{p}} + \underbrace{\begin{bmatrix} -2d_i \sin \theta_i \\ 2d_i \cos \theta_i \end{bmatrix}}_{\mathbf{b}(\theta_i)}. \quad (4)$$

Figure 2: Image point concept illustration. `nick2-imex` [NR]



CASCADING IMAGE-CONSTRUCTION OPERATIONS

In order to compute the position of the image after a cascade of several image-construction operations, we first need to define the cascade sequence c as the ordered sequence of interface

numbers at which we will consider that a reflection occurs. We define the source as $S(-h, 0)$ and the receiver as $G(0, h)$, as shown in Figure 1. Because both S and G are at the surface, any sort of multiple event will be reflected more than once by the same interface. Therefore, the mapping of the counting index i of the cascading sequence onto the values c_i of the cascading sequence is therefore surjective, but not injective. To be able to work with indices in an efficient manner, we describe the geometry of the problem through the sequences

$$\phi_i = \theta_{c_i} \quad (5)$$

and

$$l_i = d_{c_i} \quad (6)$$

which incorporate information both on the geometry of the interfaces and on the order of the cascade, and for which the index numbering starts with the value 1. The subscripts for q will also denote the counting index for the image reflection cascade. The first reflection operation can be written as

$$\mathbf{q}_1 = \mathbf{A}(2\phi_i) p + \mathbf{b}(\phi_i). \quad (7)$$

Then,

$$\mathbf{q}_2 = \mathbf{A}(2\phi_j) \mathbf{q}_1 + \mathbf{b}(\phi_j) \quad (8)$$

$$= \mathbf{A}(2\phi_j) \mathbf{A}(2\phi_i) p + \mathbf{A}(2\phi_j) \mathbf{b}(\phi_i) + \mathbf{b}(\phi_j), \quad (9)$$

$$\mathbf{q}_3 = \mathbf{A}(2\phi_k) \mathbf{q}_2 + \mathbf{b}(\phi_k) \quad (10)$$

$$= \mathbf{A}(2\phi_k) \mathbf{A}(2\phi_j) \mathbf{A}(2\phi_i) p + \mathbf{A}(2\phi_k) \mathbf{A}(2\phi_j) \mathbf{b}(\phi_i) + \mathbf{A}(2\phi_k) \mathbf{b}(\phi_j) + \mathbf{b}(\phi_k), \quad (11)$$

and so on. Let us denote the counterclockwise rotation matrix with

$$\mathbf{R}(\alpha) = \begin{bmatrix} \cos \alpha & -\sin \alpha \\ \sin \alpha & \cos \alpha \end{bmatrix}. \quad (12)$$

Both \mathbf{A} and \mathbf{R} are involutory matrices. It can be easily verified that:

$$\mathbf{A}(\alpha) \mathbf{A}(\beta) = \mathbf{R}(\alpha - \beta) \quad (13)$$

$$\mathbf{R}(\alpha) \mathbf{R}(\beta) = \mathbf{R}(\alpha + \beta) \quad (14)$$

$$\mathbf{A}(\alpha) \mathbf{R}(\beta) = \mathbf{A}(\alpha - \beta) \quad (15)$$

$$\mathbf{R}(\alpha) \mathbf{A}(\beta) = \mathbf{A}(\alpha + \beta) \quad (16)$$

Chains of \mathbf{A} operators can be written as a single operator:

$$\mathbf{A}(\beta) \mathbf{A}(\gamma) \mathbf{A}(\delta) = \mathbf{A}(\beta) \mathbf{R}(\gamma - \delta) = \mathbf{A}(\beta - \gamma + \delta), \quad (17)$$

$$\mathbf{A}(\alpha)\mathbf{A}(\beta)\mathbf{A}(\gamma)\mathbf{A}(\delta) = \mathbf{A}(\alpha)\mathbf{A}(\beta - \gamma + \delta) = \mathbf{R}(\alpha - \beta + \gamma - \delta), \quad (18)$$

According to (15), we can write any \mathbf{A} as

$$\mathbf{A}(\alpha) = \begin{bmatrix} 1 & 0 \\ 0 & -1 \end{bmatrix} \mathbf{R}(-\alpha), \quad (19)$$

so the product of any number k of \mathbf{A} operators can be written as

$$\prod_{i=1}^k \mathbf{A}(\alpha_i) = \begin{bmatrix} 1 & 0 \\ 0 & (-1)^k \end{bmatrix} \mathbf{R}\left(\sum_{i=1}^k (-1)^{i+k-1} \alpha_i\right). \quad (20)$$

To use these properties for constructing cascades of image reflections, we must replace the set α_i with the *inverse* succession of the dips of the reflecting interfaces, multiplied by two according to the definition of \mathbf{A} in (4):

$$\alpha_i = 2\phi_{k-i+1}, \quad (21)$$

where $i = 1 \dots k$. The reverse “chronological” order is a consequence of the operators in the chain being matrices that multiply the previous image coordinate vector from the left, as exemplified by (8) and (10). The result of the succession of image-building operations can be written as

$$\mathbf{q}_n = \sum_{j=0}^n \begin{bmatrix} 1 & 0 \\ 0 & (-1)^j \end{bmatrix} \mathbf{R}\left(2\sum_{i=1}^j (-1)^{i+j-1} \phi_{j-i+1}\right) \mathbf{b}(\phi_{n-j}), \quad (22)$$

where we define a nonphysical quantity $\phi_0 = -\frac{\pi}{2}$ and we also define $\mathbf{b}(\phi_0)$ as the coordinates vector of the initial point in the cascade of reflections. We also consider that the summation index increases in increments of 1 and that summation operators return zero when the upper summation limit is smaller than the lower summation limit. Under the assumption that the starting point of the cascade is at the surface, and by denoting *half* of its x coordinate with l_0 , we can write all \mathbf{b} vectors using rotations:

$$\mathbf{b}(\phi_i) = 2l_i \begin{bmatrix} -\sin \phi_i \\ \cos \phi_i \end{bmatrix} = 2l_i \mathbf{R}(\phi_i) \begin{bmatrix} 0 \\ 1 \end{bmatrix} = 2l_i \mathbf{R}\left(\phi_i + \frac{\pi}{2}\right) \begin{bmatrix} 1 \\ 0 \end{bmatrix}. \quad (23)$$

Substituting this into (22),

$$\mathbf{q}_n = 2 \sum_{j=0}^n l_{n-j} \begin{bmatrix} 1 & 0 \\ 0 & (-1)^j \end{bmatrix} \mathbf{R}\left(\phi_{n-j} + \frac{\pi}{2} + 2\sum_{i=1}^j (-1)^{i+j-1} \phi_{j-i+1}\right) \begin{bmatrix} 1 \\ 0 \end{bmatrix}, \quad (24)$$

These particular choices of l_0 and ϕ_0 , together with the assumption of a surface starting point, ensure that (23) is consistent for the starting point of the cascading operations too. After a few algebraic manipulations, we obtain

$$\mathbf{q}_n = 2 \sum_{j=0}^n l_{n-j} \begin{bmatrix} -\sin \beta_j \\ (-1)^j \cos \beta_j \end{bmatrix}, \quad (25)$$

where

$$\beta_j = \phi_{n-j} + 2\sum_{i=1}^j (-1)^{i+j-1} \phi_{j-i+1}. \quad (26)$$

COMPUTING THE TRAVELTIME: THE THEORY

Let us denote by n a value smaller 1 less than the total number of bounces of the wave in the earth. Let us pretend “not to know” that the horizontal coordinates of S and G are $-h$ and h , respectively, and denote them with s and g instead, since we will later need a more general expression that can be differentiated with respect to these variables. We start by generating the sequences ϕ_i and l_i , according to (5) and (6), and keeping in mind the nonphysical preprendix $\phi_0 = -\frac{\pi}{2}$.

Using the fact that n is always even because the total number of bounces inside the earth is always odd, and substituting into (25), we find the image cascaded through n reflection operations from the source to be

$$\mathbf{q}_n^S = s \begin{bmatrix} -\sin \beta_n \\ \cos \beta_n \end{bmatrix} + 2 \sum_{j=0}^{n-1} l_{n-j} \begin{bmatrix} -\sin \beta_j \\ (-1)^j \cos \beta_j \end{bmatrix}. \quad (27)$$

The receiver image is obtained from a single reflection operation, through the last reflecting interface:

$$\mathbf{q}_1^G = g \begin{bmatrix} \cos 2\phi_{n+1} \\ \sin 2\phi_{n+1} \end{bmatrix} + 2l_{n+1} \begin{bmatrix} -\sin \phi_{n+1} \\ \cos \phi_{n+1} \end{bmatrix}. \quad (28)$$

The travelttime is the distance between \mathbf{q}_n^S and \mathbf{q}_1^G divided by the velocity. This distance will be computed as the magnitude of the vector $\mathbf{q}_n^S - \mathbf{q}_1^G$. By making the notations

$$\mathbf{u}_1 = \frac{2}{v} \left\{ \sum_{j=0}^{n-1} l_{n-j} \begin{bmatrix} -\sin \beta_j \\ (-1)^j \cos \beta_j \end{bmatrix} + l_{n+1} \begin{bmatrix} \sin \phi_{n+1} \\ -\cos \phi_{n+1} \end{bmatrix} \right\}, \quad (29)$$

$$\mathbf{u}_2 = \frac{1}{v} \begin{bmatrix} -\sin \beta_n \\ \cos \beta_n \end{bmatrix}, \quad (30)$$

$$\mathbf{u}_3 = -\frac{1}{v} \begin{bmatrix} \cos 2\phi_{n+1} \\ \sin 2\phi_{n+1} \end{bmatrix}, \quad (31)$$

we can write:

$$t = |\mathbf{u}_1 + s\mathbf{u}_2 + g\mathbf{u}_3|. \quad (32)$$

In particular, for $s = -h$ and $g = h$ and

$$\mathbf{u}_4 = \mathbf{u}_2 - \mathbf{u}_3 = \frac{1}{v} \begin{bmatrix} \sin(-\beta_n) + \cos 2\phi_{n+1} \\ \cos(-\beta_n) + \sin 2\phi_{n+1} \end{bmatrix}, \quad (33)$$

the travelttime can be written as

$$t = |\mathbf{u}_1 - h\mathbf{u}_4|. \quad (34)$$

This vector magnitude can be computed using scalar products:

$$t = \sqrt{[\mathbf{u}_1 - h\mathbf{u}_4] \cdot [\mathbf{u}_1 - h\mathbf{u}_4]} \quad (35)$$

or it can be written as

$$t^2 = \mathbf{u}_4 \cdot \mathbf{u}_4 \left(h - \frac{\mathbf{u}_1 \cdot \mathbf{u}_4}{\mathbf{u}_4 \cdot \mathbf{u}_4} \right)^2 + \mathbf{u}_1 \cdot \mathbf{u}_1 - \frac{(\mathbf{u}_1 \cdot \mathbf{u}_4)^2}{\mathbf{u}_4 \cdot \mathbf{u}_4}, \quad (36)$$

which is the equation of a hyperbola with the apex at

$$h_{apex} = \frac{\mathbf{u}_1 \cdot \mathbf{u}_4}{\mathbf{u}_4 \cdot \mathbf{u}_4}, \quad (37)$$

$$t_{apex} = \sqrt{\mathbf{u}_1 \cdot \mathbf{u}_1 - \frac{(\mathbf{u}_1 \cdot \mathbf{u}_4)^2}{\mathbf{u}_4 \cdot \mathbf{u}_4}}. \quad (38)$$

COMPUTING THE TRAVELTIME: AN EXAMPLE

We will illustrate the theory presented above using the multiple reflection event S1010201G (the zeros denote the Earth surface). For this event, $n = 6$, 1 less than the total number of bounces in the earth. The first step is generating sequences ϕ_i and l_i , according to (5) and (6):

$$\{\phi_1, \phi_2, \phi_3, \phi_4, \phi_5, \phi_6, \phi_7\} = \{\theta_1, \theta_0, \theta_1, \theta_0, \theta_2, \theta_0, \theta_1\} \quad (39)$$

and

$$\{l_1, l_2, l_3, l_4, l_5, l_6, l_7\} = \{d_1, d_0, d_1, d_0, d_2, d_0, d_1\} \quad (40)$$

We prepend $\phi_0 = -\frac{\pi}{2}$ to the sequence of angles, then we compute the β sequence:

$$\beta_0 = \phi_6 \quad (41)$$

$$\beta_1 = \phi_5 - 2\phi_1 \quad (42)$$

$$\beta_2 = \phi_4 - 2\phi_1 + 2\phi_2 \quad (43)$$

$$\beta_3 = \phi_3 - 2\phi_1 + 2\phi_2 - 2\phi_3 \quad (44)$$

$$\beta_4 = \phi_2 - 2\phi_1 + 2\phi_2 - 2\phi_3 + 2\phi_4 \quad (45)$$

$$\beta_5 = \phi_1 - 2\phi_1 + 2\phi_2 - 2\phi_3 + 2\phi_4 - 2\phi_5 \quad (46)$$

$$\beta_6 = \phi_0 - 2\phi_1 + 2\phi_2 - 2\phi_3 + 2\phi_4 - 2\phi_5 + 2\phi_6 \quad (47)$$

It may be useful to notice the regularities in signs and indices. The summation and trigonometric operators in (25) and (26) can be written in matrix form to verify the correctness of their numerical implementation. We then compute the auxiliary vectors given by (29) and (33):

$$\mathbf{u}_1 = \frac{2}{v}l_5 \begin{bmatrix} -\sin \beta_1 \\ -\cos \beta_1 \end{bmatrix} + \frac{2}{v}l_4 \begin{bmatrix} -\sin \beta_2 \\ +\cos \beta_2 \end{bmatrix} + \frac{2}{v}l_3 \begin{bmatrix} -\sin \beta_3 \\ -\cos \beta_3 \end{bmatrix} + \frac{2}{v}l_2 \begin{bmatrix} -\sin \beta_4 \\ +\cos \beta_4 \end{bmatrix} + \frac{2}{v}l_1 \begin{bmatrix} -\sin \beta_5 \\ -\cos \beta_5 \end{bmatrix} + \frac{2}{v}l_7 \begin{bmatrix} \sin \phi_7 \\ -\cos \phi_7 \end{bmatrix}, \quad (48)$$

$$\mathbf{u}_4 = \frac{1}{v} \begin{bmatrix} \sin(-\beta_6) + \cos 2\phi_7 \\ \cos(-\beta_6) + \sin 2\phi_7 \end{bmatrix}, \quad (49)$$

For our very particular case in which some of the bounces are with the surface ($d_0 = 0, \theta_0 = 0$),

$$\mathbf{u}_1 = \frac{2}{v} d_1 \begin{bmatrix} +\sin 3\theta_1 + \sin(3\theta_1 + 2\theta_2) + \sin \theta_1 \\ -\cos 3\theta_1 - \cos(3\theta_1 + 2\theta_2) - \cos \theta_1 \end{bmatrix} + \frac{2}{v} d_2 \begin{bmatrix} +\sin(2\theta_1 - \theta_2) \\ -\cos(2\theta_1 - \theta_2) \end{bmatrix}, \quad (50)$$

$$\mathbf{u}_4 = \frac{2}{v} \cos(3\theta_1 + \theta_2) \begin{bmatrix} \cos(\theta_1 + \theta_2) \\ -\sin(\theta_1 + \theta_2) \end{bmatrix}, \quad (51)$$

and the traveltime for each offset h can now be computed by plugging these vectors directly into (35). By performing trigonometric operations, we may find that the expression for the distance is the same as that in Equation (A-14) of Levin and Shah (1977).

ANGLES OF DEPARTURE AND ARRIVAL

The previous sections presented a method to compute the traveltime from a given source point to a given receiver point. Using the image point reflection method has eschewed the need for traditional ray tracing. However, in order to estimate the effect of the acquisition arrays on the amplitudes, or to graphically display the raypaths, we need to compute the angles of departure of the rays from the source and of arrival to the receiver.

Shah (1973) shows that if we denote with α_s the smallest angle between the raypath departing from the source and the vertical, with α_g the similarly defined arrival angle, with s the coordinate of the source and with g the coordinate of the receiver, the two angles can be found from the relations:

$$\frac{\sin \alpha_s}{v} = \frac{\partial t}{\partial s}, \quad (52)$$

$$\frac{\sin \alpha_g}{v} = \frac{\partial t}{\partial g}. \quad (53)$$

Writing (32) as

$$t^2 = \mathbf{u}_1 \cdot \mathbf{u}_1 + s^2 \mathbf{u}_2 \cdot \mathbf{u}_2 + g^2 \mathbf{u}_3 \cdot \mathbf{u}_3 + 2s \mathbf{u}_1 \cdot \mathbf{u}_2 + 2g \mathbf{u}_1 \cdot \mathbf{u}_3 + 2sg \mathbf{u}_2 \cdot \mathbf{u}_3, \quad (54)$$

we obtain

$$\frac{\partial t}{\partial s} = \frac{1}{t} \mathbf{u}_2 \cdot (\mathbf{u}_1 + \mathbf{u}_2 + g \mathbf{u}_3), \quad (55)$$

$$\frac{\partial t}{\partial g} = \frac{1}{t} \mathbf{u}_3 \cdot (\mathbf{u}_1 + s \mathbf{u}_2 + \mathbf{u}_3). \quad (56)$$

Replacing now s with $-h$ and g with h , the angles are given by:

$$\sin \alpha_s = \frac{v}{t} \mathbf{u}_2 \cdot (\mathbf{u}_1 + \mathbf{u}_2 + h \mathbf{u}_3), \quad (57)$$

$$\sin \alpha_g = \frac{v}{t} \mathbf{u}_3 \cdot (\mathbf{u}_1 - h \mathbf{u}_2 + \mathbf{u}_3), \quad (58)$$

where t is computed as a function of h as given by (35).

CONCLUSION

We have derived a formula which describes the traveltimes of internal or surface-related multiples of any order, reflected between any number of layers in a constant-velocity medium. We have also derived an analytical formula for their angles of departure from the source and arrival for the receiver. The low computational cost of this algorithm makes it highly suitable for an analytical-stochastic estimation of the strength of internal multiples in various geological settings, with the ultimate purpose of identifying classes of settings in which internal multiples are likely to be a problem. We plan to perform this work in the near future.

REFERENCES

- Levin, F. K., and Shah, P. M., 1977, Peg-leg multiples and dipping reflectors: *Geophysics*, **42**, no. 5, 957–981.
- Shah, P. M., 1973, Use of wavefront curvature to relate seismic data with subsurface parameters: *Geophysics*, **38**, no. 5, 812–825.

Estimating a 2D stationary PEF on sparse data

Jesse Lomask¹

ABSTRACT

A stationary 2D PEF and missing data are simultaneously estimated on sparse data where the 2D PEF is never fully on known data. This PEF is estimated using non-linear conjugate gradients. A weight is applied to the residual to use only fitting equations where a prescribed minimum number of the PEF coefficients are on known data. The minimum parameter is then reduced and a new 2D PEF is estimated using the previous PEF as a starting solution. This process is repeated and the 2D PEF is gradually built up. This method is tested on the Madagascar satellite data. Using increasingly sparse data, the sparse 2D PEF compares favorably to the 2D PEF estimated on the dense data even when 67 percent of the data is unknown.

INTRODUCTION

Prediction error filters (PEFs) are commonly used to interpolate data. This is typically carried out in a two step process. First the PEFs are estimated on areas where all of the filter coefficients land on known data. Then the PEFs are used to fill in the missing data. However, sometimes the data is so sparse that PEFs estimated on entirely known data do not adequately capture the nature of the data. In Curry (2003), a multi-scale approach estimates a non-stationary PEF on sparse data. This requires that the gaps in the data range continuously in size. If the data has only a few scales of gaps then this multi-scale approach fails.

I present an approach to estimate a stationary PEF on sparse data using non-linear conjugate gradients (Claerbout, 1999) where both the filter and the missing data are estimated simultaneously. I add a weight to use only fitting equations where a prescribed minimum number of filter coefficients are on known data. Then, I reduce the minimum number of filter coefficients and solve again. I repeat this bootstrapping process until all of the data is used. A variant of this method was first suggested by Jon Claerbout and described in Lomask (2002). In this paper, this method proves capable of estimating a 2D PEF on datasets where the known data occurs systematically as in the Madagascar satellite data (Ecker and Berlioux, 1995; Lomask, 1998, 2002; Curry, 2004b) or possibly the data used in Curry (2004a). If the data is not too radically non-stationary, this stationary PEF can, in principle, be used as a starting solution for tackling the non-stationary problem.

In the following paper, I first present the methodology for estimating the stationary PEF

¹email: lomask@sep.stanford.edu

on sparse data. Then I illustrate its effectiveness on the Madagascar satellite data.

METHODOLOGY

Equation (1) is taken from Chapter 6. of Claerbout (1999).

$$\mathbf{0} \approx \begin{bmatrix} \mathbf{AJ} & \mathbf{YK} \end{bmatrix} \begin{bmatrix} \Delta \mathbf{y} \\ \Delta \mathbf{a} \end{bmatrix} + \bar{\mathbf{r}}. \quad (1)$$

This fitting goal estimates both missing data and a filter simultaneously. \mathbf{A} and \mathbf{Y} are the convolutional matrix algebraic notations for the filter and the data, respectively. $\Delta \mathbf{a}$ and $\Delta \mathbf{y}$ are perturbation vectors for the filter and the data. The free-mask matrix for missing data is denoted \mathbf{J} and that for the PEF is \mathbf{K} . The original residual is defined as $\bar{\mathbf{r}} = \mathbf{Ay}$.

Next, a diagonal weight matrix \mathbf{W} can be applied to the residual as:

$$\mathbf{0} \approx \mathbf{W} \left[\begin{bmatrix} \mathbf{AJ} & \mathbf{YK} \end{bmatrix} \begin{bmatrix} \Delta \mathbf{y} \\ \Delta \mathbf{a} \end{bmatrix} + \bar{\mathbf{r}} \right]. \quad (2)$$

This weight is used to remove any fitting equations in which the filter has fewer than a specified number of coefficients on known data. The number of coefficients that are on known data at each point in the model can be thought of as the coefficient fold. The range of coefficient fold values is broken up into several steps. Equation (2) is first solved using fitting equations with coefficient fold greater than the highest step. Then the resulting PEF and missing data are used as the initial solution for the next step. This is repeated and the 2D PEF is gradually built up.

Within the solver, the following equations are iterated over (Claerbout, 1999):

$$\mathbf{r} \leftarrow \mathbf{WAy} \quad (3)$$

$$\begin{bmatrix} \Delta \mathbf{y} \\ \Delta \mathbf{a} \end{bmatrix} \leftarrow \begin{bmatrix} \mathbf{J}'\mathbf{A}' \\ \mathbf{K}'\mathbf{Y}' \end{bmatrix} \mathbf{W}'\mathbf{r} \quad (4)$$

$$\Delta \mathbf{r} \leftarrow \mathbf{W} \begin{bmatrix} \mathbf{AJ} & \mathbf{YK} \end{bmatrix} \begin{bmatrix} \Delta \mathbf{y} \\ \Delta \mathbf{a} \end{bmatrix} \quad (5)$$

$$\mathbf{y} \leftarrow \text{cgstep}(\mathbf{y}, \Delta \mathbf{y}) \quad (6)$$

$$\mathbf{a} \leftarrow \text{cgstep}(\mathbf{a}, \Delta \mathbf{a}) \quad (7)$$

Balancing the unknown data and the filter

When solving an inversion problem, it can be useful to look at the residual for a couple of reasons. The first is to see that it is white. The second reason, important in the case of regularized inversion, is to see that the fitting goals have been properly balanced.

In equation (2), we are finding both a filter and missing data at the same time. If the solver focuses entirely on finding the filter, it will not change the missing data and create a filter that is estimated on incorrect data. On the other hand, if the solver focuses entirely on missing data, it does not change the filter and creates incorrect interpolation results.

I found it useful to inspect movies of the gradient to balance the data and filter. Since the individual residuals of $\mathbf{WAJ}\Delta\mathbf{y}$ and $\mathbf{WYK}\Delta\mathbf{a}$ are summed, it does not make sense to look at the total residual to see how well the filter and missing data are balanced. Alternatively, the individual residuals could be looked at before they are summed. However, I found it useful to make movies of each step in the solver of the gradient, equation (4).

By observing the relative sizes of the perturbation of the filter and missing data in movies of the gradient, the two can be easily balanced by scaling the input data, $\alpha\mathbf{y}$. Conceptually, it may sound better to implement a model weight to balance the filter and the data, but I got better results by merely scaling the input data.

TEST RESULTS

I tested this method on the Madagascar satellite data set with increasingly sparse missing data. I found that this method estimated a 2D PEF that is comparable to a 2D PEF estimated on dense data when the sparse data was 67 percent unknown. For input data that was more sparse than that, the method failed.

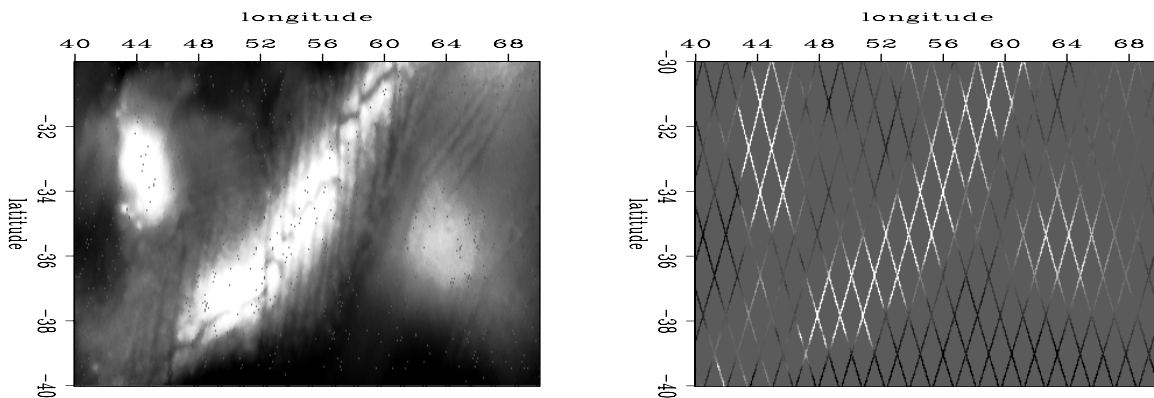


Figure 1: Left is the dense data in the overlapping region. Right is the sparse data.

`jesse1-dense_sparse` [ER]

The data consists of two overlapping datasets. One is densely sampled and one is sparsely sampled. I chose to work in the overlapping region. On the left side of Figure 1 is the dense data in the southern half of the Madagascar data. The right of the figure is the sparse data overlapping the dense data.

Figure 2 is the dense data after its few empty bins have been filled with a laplacian. The right side has been roughened with the helical derivative.

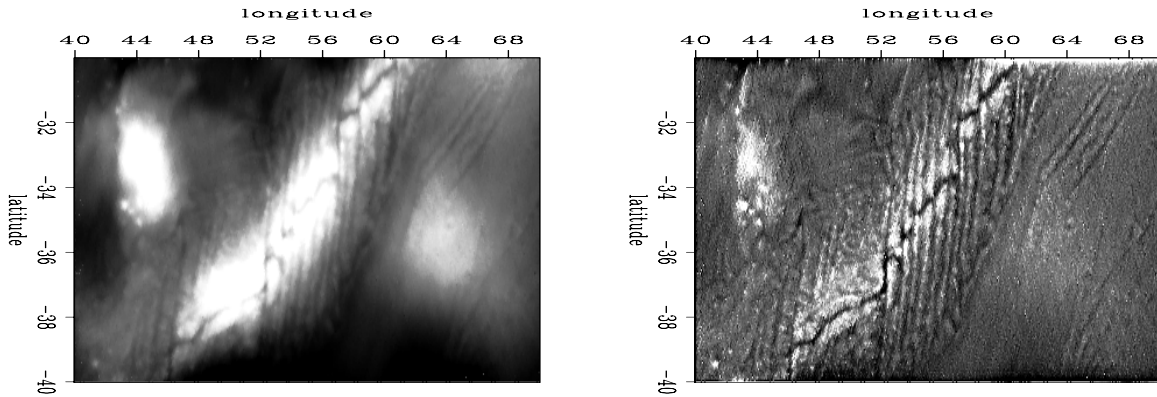


Figure 2: Left is the dense data with it few empty bins filled with a laplacian. Right is the same data roughened with the helical derivative. `jesse1-dense_fill` [ER]



Figure 3: Left is the impulse response of the inverse full 2D PEF estimated on southern dense region after the few remaining bins have been filled using a 2D gradient as regularization. Right is the impulse response of the inverse helical derivative. This is the starting solution for the sparse 2D PEF estimation. `jesse1-comp_imp` [ER]

I began with the densely sampled data and gradually threw away data. As I threw out data, I compared the impulse response of the inverse 10 by 10 PEF estimated on the dense data to the impulse response of the inverse PEF estimated using the approach described in the paper. The left side of Figure 3 is the impulse response wrapped on the helix of the inverse PEF estimated on the dense data in Figure 2. Notice that it has a similar character to data it is trying to emulate. This is the result that the sparse 2D PEF is hoping to achieve.

For nonlinear problems, the initial solution is extremely important. Thus far, I have used only the helical derivative (Claerbout, 1999). In the future, other starting solutions may improve the results, such as the solution used in Curry (2004b). In the right side of Figure 3, is the impulse response of the inverse helical derivative.

Figure 4: This is the map to be interpolated. The tracks have been made thicker therefore it is less sparse than the original sparse tracks. `jesse1-data_mask.4.wide` [ER]

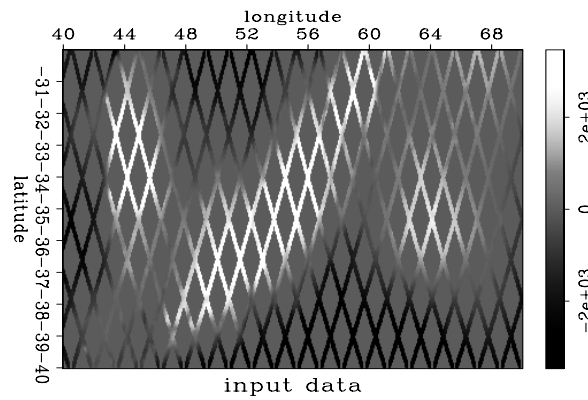


Figure 4 shows thicker tracks than the original sparse data shown on the right side of Figure 1. This has 2.6 times as many non-zero values as the original sparse data.

Figure 5: A coefficient fold map for the tracks in Figure 4 with a 10 by 10 filter. The value indicates the number of coefficients of the filter that are on known data at each location in the model. `jesse1-coef_fold.4.wide` [ER]

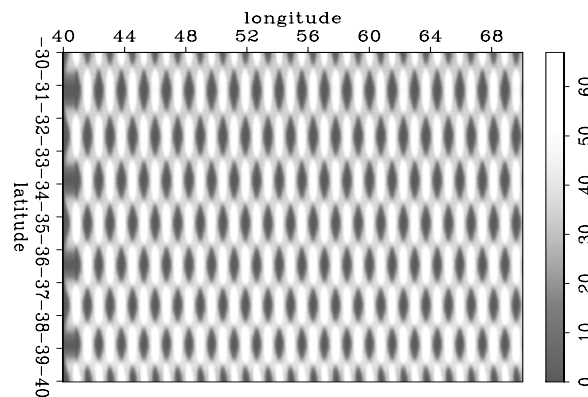
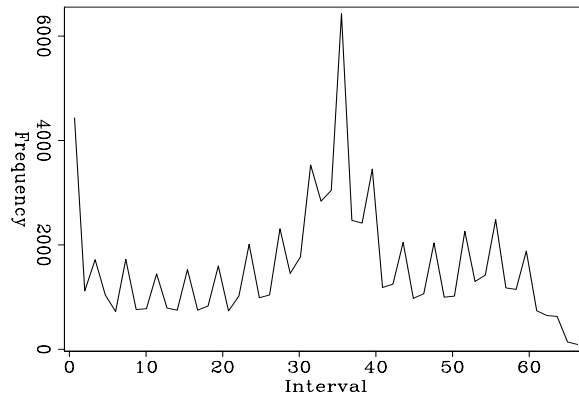


Figure 5 shows the coefficient fold map for a 10 by 10 filter on the sparse data in Figure 4. The number of coefficients that are on known data at each point in the model can be thought of as the coefficient fold. A coefficient fold map can easily be created by packing the filter with all ones and setting the known data in the model to ones and the unknown to data to zeros. The output of the convolution is a coefficient fold map.

In Figure 6 is a histogram of the convolution map in Figure 5. For this 10 by 10 PEF, there are 98 coefficients. It can be seen in the histogram that the maximum coefficient fold is approximately 67. This means that at those locations 31 filter coefficients are on unknown data.

Figure 6: A histogram of the values in the coefficient fold map in Figure 5. Notice that most of the filter locations have about 33 out of about 98 coefficients on known data. The areas with the highest (50-65) are located where the tracks cross. jesse1-histo.4 [ER]



Also, most of the filter locations have about 33 coefficients on known data, 65 coefficients on unknown data. In this case, I set the first minimum fold parameter to 60, solved for the filter and missing data. Then set the minimum fold parameter to 50 and repeated until all of the data was used.

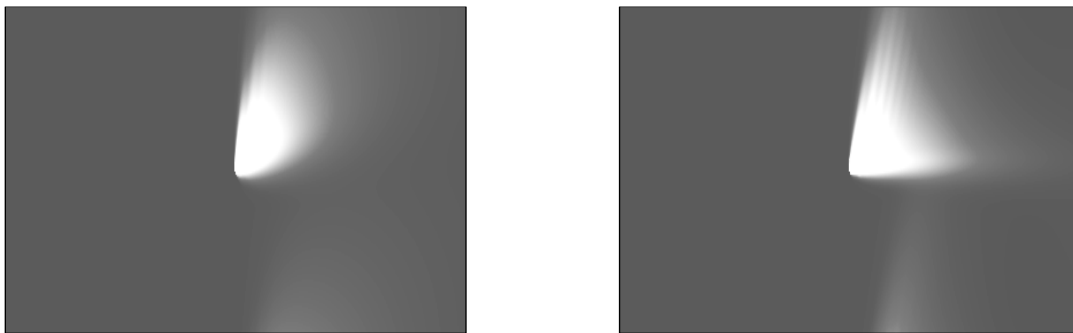


Figure 7: Left is the impulse response of the inverse 2D PEF estimated on the dense data in left of Figure 2. Right is the impulse response of the inverse 2D PEF estimated on the sparse tracks in Figure 4. jesse1-comp_imp2.4 [ER]

Figure 7 compares the impulse responses of the inverse PEF of the full 2D PEF on the left to the 2D PEF estimated on the sparse tracks from Figure 4 on the right. Although they are not exactly the same, they are similar. The sail shape possibly results from the PEF's ability to capture the narrow ridges trending almost north and the entire submerged mountain range trending west and its inability to capture the central spreading ridge trending northeast.

Another comparison to evaluate the quality of the result is to inspect the filled data. Figure 8 is the sparse tracks in Figure 4 filled with the full 2D PEF estimated on the dense data. Figure 9 is the sparse tracks in Figure 4 filled with the 2D PEF estimated on the sparse tracks themselves. In general, this method adequately fills the missing data, only showing some weakness in capturing the main spreading ridge feature.

If the data is too sparse, this method fails. Estimating a PEF on the original sparse tracks on the right side of Figure 1 illustrates this. First, we recalculate a new coefficient fold map shown in Figure 10. Analysis of the histogram in Figure 11 reveals that this data is indeed

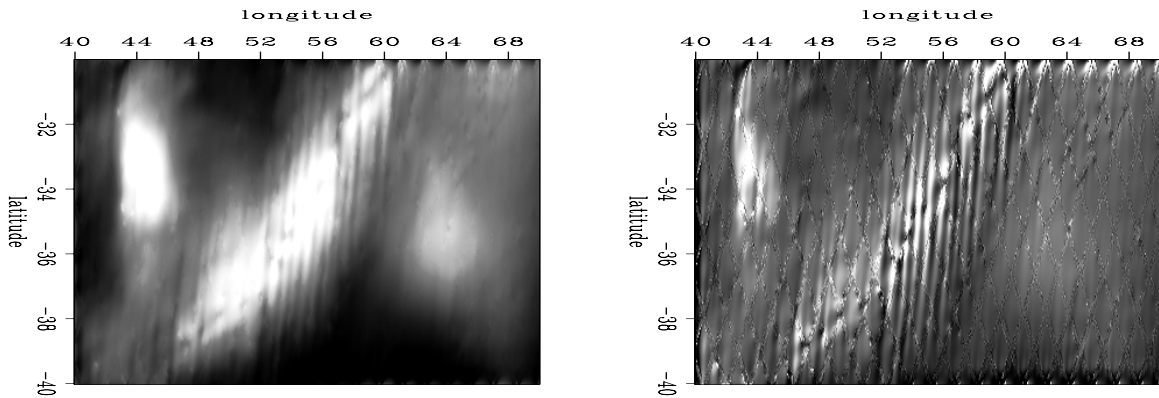


Figure 8: Left is the result of filling the sparse tracks in Figure 4 with a full 2D PEF estimated on the dense data in left side of Figure 2. Right is roughened with the helical derivative. `jesse1-hel.2d.4.fill` [ER,M]

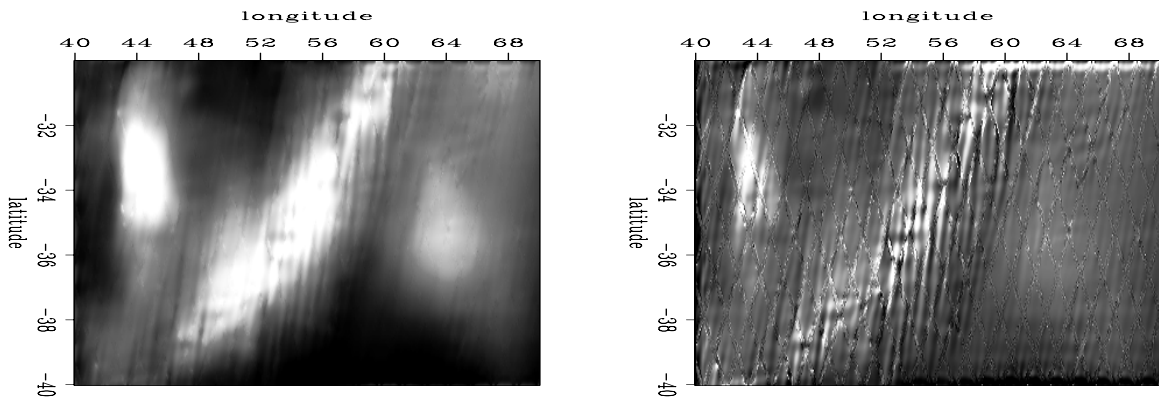


Figure 9: Left is the result of estimating a sparse 2D PEF on the sparse tracks in Figure 4 and filling in the same data. Right is roughened with the helical derivative. Notice the similarity to Figure 8. `jesse1-recursive_pef.4.fill` [ER,M]

Figure 10: A coefficient fold map for the sparse tracks with a 10 by 10 filter. The value indicates the number of coefficients of the filter that are on known data at each location in the model. `jesse1-coef_fold` [ER]

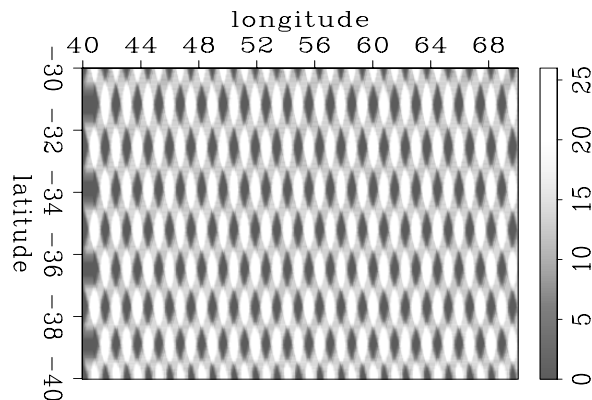


Figure 11: A histogram of the values in the coefficient fold map in Figure 10. Notice that most of the filter locations have about 13 out of about 98 coefficients on known data.

`jesse1-histo.1` [ER]

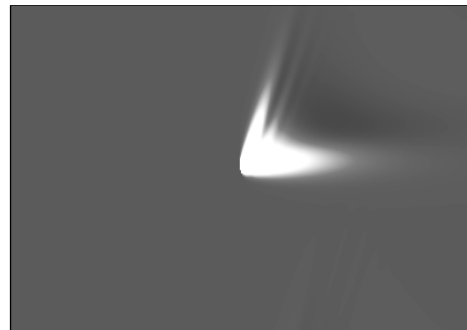
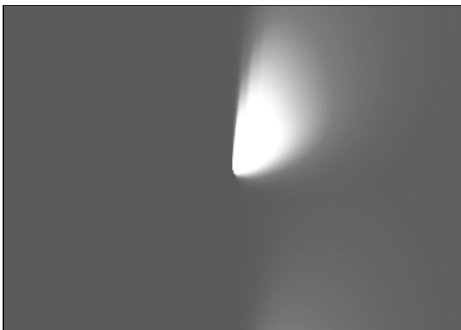
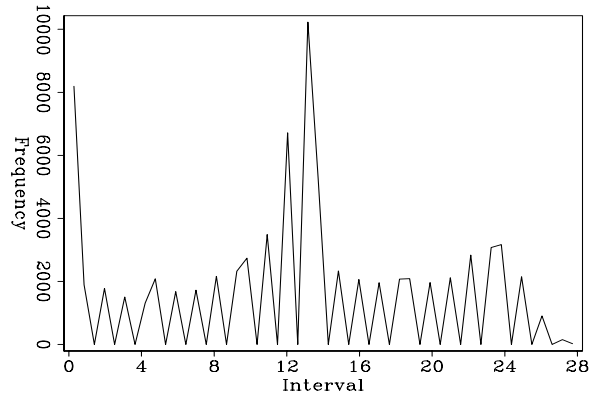


Figure 12: Left is the impulse response of the inverse 2D PEF estimated on the dense data in left of Figure 2. Right is the impulse response of the inverse 2D PEF estimated on the sparse tracks in the right of Figure 1. The two impulse responses are noticeably different.

`jesse1-comp_imp2.1` [ER]

very sparse. Then, Figure 12 compares the impulse responses. The sparse 2D PEF on the right does a very poor job of matching the desired response on the left. Comparison of the filled results in Figures 13 and 14 further demonstrate the sparse 2D PEF inability to capture much of the high frequencies.

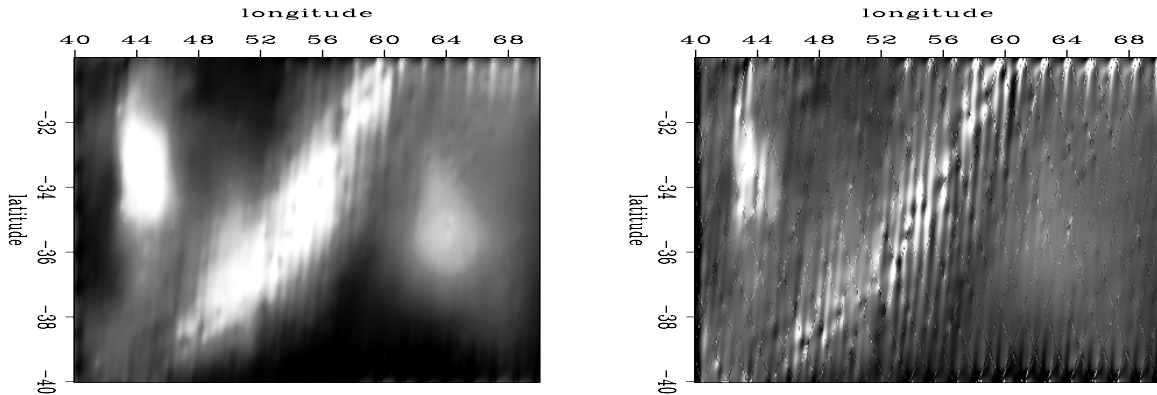


Figure 13: Left is the result of filling the sparse tracks in the right of Figure 1 with a full 2D PEF estimated on the dense data in left side of Figure 2. Right is roughened with the helical derivative. `jesse1-hel.2d.1.fill` [ER,M]

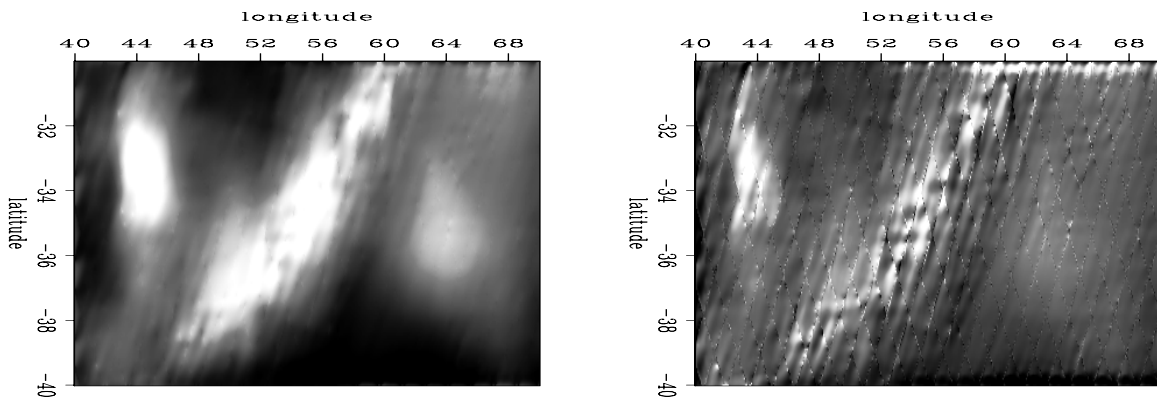


Figure 14: Left is the result of estimating a sparse 2D PEF on the sparse tracks in the right Figure 1. Right is roughened with the helical derivative. Unfortunately, it is not able to capture the higher frequency nature of the data as captured by the full 2D PEF result shown in Figure 13. `jesse1-recursive_pef.1.fill` [ER,M]

FUTURE WORK

There are still several ways of improving this method to be investigated. For instance, we could start with a smaller PEF and gradually increase its size, iteratively recalculating a new 2D PEF in a similar bootstrapping approach. Also, it would be prudent to come up with a good way of finding the data scale to balance the filter and the missing data. This would probably

depend on the relative size of the data and filter. Lastly, for this technique to be useful on seismic data, it has to be able solve the non-stationary problem. We could possibly use this stationary PEF as a starting guess for non-stationary problem. Using code adapted from Clapp (2000), a non-stationary PEF is estimated on the dense data and used to fill in the sparse data in Figure 15. Although this figure was created using the dense data, it illustrates what we hope to achieve with a non-stationary PEF estimated on sparse data tracks.

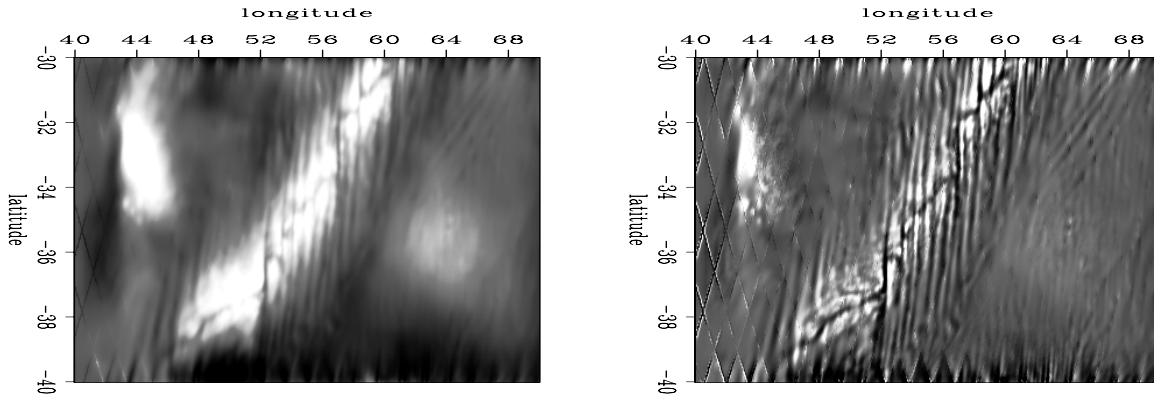


Figure 15: The result of filling the sparse tracks in the Right of Figure 1 with a non-stationary 2D PEF estimated on the dense data in Figure 2. `jesse1-non_station.fill` [ER,M]

CONCLUSION

The 2D PEF estimated on sparse data compares favorably to the 2D PEF estimated on the dense data in some cases. For the Madagascar data set, when the unknown data exceeds 67 percent, this method fails. However, up to that point, this method is able to estimate a 2D PEF when conventional estimation techniques would certainly fail.

ACKNOWLEDGMENTS

I would like to thank Antoine Guitton, Paul Sava, Alejandro Valenciano, and Bill Curry for useful suggestions.

REFERENCES

- Claerbout, J., 1999, Geophysical estimation by example: Environmental soundings image enhancement: Stanford Exploration Project, <http://sepwww.stanford.edu/sep/prof/>.
- Clapp, R. G., 2000, Regularizing tomography with non-stationary filters: SEP-103, 47-60.
- Curry, W., 2003, More fitting equations for PEF estimation on sparse data: SEP-114, 171-176.

Curry, W., 2004a, Midpoint-offset vs. source-receiver coordinates for PEF-based interpolation: SEP-117.

Curry, W., 2004b, Regularizing madagascar: Pefs from the data space?: SEP-115, 347-356.

Ecker, C., and Berlioux, A., 1995, Flying over the ocean southeast of Madagascar: SEP-84, 295-306.

Lomask, J., 1998, Madagascar revisited: A missing data problem: SEP-97, 207-216.

Lomask, J., 2002, Madagascar satellite data: An inversion test case: SEP-111, 337-349.

Midpoint-offset vs. source-receiver coordinates for PEF-based interpolation

William Curry¹

ABSTRACT

There are two obvious choices of coordinates to use when interpolating seismic data: cmp-offset and source-receiver. A multi-scale prediction-error filter (PEF) based interpolation works well on both sets of coordinates for a 2D prestack land dataset, although the cmp-offset coordinates appear to be preferable. By using reciprocity in source-receiver space, a pair of 2D PEFs may interpolate the data with more efficiency and practical applicability to 3D data.

INTRODUCTION

Interpolation of reflection seismic data is performed in many different ways, including kinematically (Chemingui, 1999; Fomel, 2001; Biondi and Vlad, 2001), with high-resolution radon-based methods (Sacchi and Ulrych, 1995; Trad et al., 2002; Trad, 2003), with Fourier-domain methods (Schonewille, 2000; Zwartjes and Hindriks, 2001; Liu, 2004), and with prediction-error filter (PEF) based methods (Spitz, 1991; Claerbout, 1999; Crawley, 2000).

PEF-based methods can now deal with irregularly-sampled data (Curry and Brown, 2001; Curry, 2002), where multiple rescaled copies of the data are used to estimate a non-stationary PEF. This multi-scale methodology has been shown to work on sparse synthetic data.

I use the multi-scale method on a prestack 2D land dataset from Colombia. The data suffers from many missing shots but the receiver coverage is relatively uniform, meaning that in source-receiver coordinates only one axis is poorly-sampled. In cmp-offset coordinates the coverage is not uniform in either the cmp or the offset axes. The multi-scale PEF estimation should be robust to this problem, however.

I test the interpolation with non-stationary, multi-scale PEFs in both source-receiver as well as cmp-absolute offset coordinates. In source-receiver coordinates, additional traces predicted by reciprocity are added, so that the known data looks like a grid of crossing tracks. The crossing tracks are quite reminiscent of the Madagascar interpolation problem (Ecker and Berlioux, 1995; Lomask, 1998, 2002; Curry, 2004; Lomask, 2004). I also propose a method using two orthogonal 2D non-stationary single-scale PEFs, based largely on a proposed method for the Madagascar problem (Curry, 2004).

¹email: bill@sep.stanford.edu

BACKGROUND

Prediction-error filter (PEF) based interpolation can be cast as a two stage linear least-squares process (Claerbout, 1999), where a PEF is first estimated on the known data. Then, the output of convolution of the newly-found PEF with the desired model is minimized while fixing the known data. The first stage of the process can be described mathematically by

$$\mathbf{W}(\mathbf{DKf} + \mathbf{d}) \approx \mathbf{0}, \quad (1)$$

where the known data (\mathbf{d}) is convolved (\mathbf{D}) with a PEF with unknown coefficients (\mathbf{f}), except for the first, which is constrained by \mathbf{K} to be 1. If there are areas where the filter is being convolved with unknown data, those areas are weighted to 0 by a diagonal weight \mathbf{W} . The second stage can be described by

$$\begin{aligned} \mathbf{L}_{\text{data}}\mathbf{m} &= \mathbf{d} \\ \mathbf{Fm} &\approx \mathbf{0}. \end{aligned} \quad (2)$$

In the second fitting goal, \mathbf{L} is a selector matrix that is 1 where there is a data point and 0 where there isn't, \mathbf{m} is the interpolated output, \mathbf{d} is once again the known data, and \mathbf{F} represents convolution with the newly-found PEF.

In the case of a non-stationary PEF, where the filter varies with position, a second fitting goal has to be added to the first stage of the interpolation process, so that the now much greater number of filter coefficients becomes adequately constrained. This fitting goal can be expressed as

$$\mathbf{Af} \approx \mathbf{0}, \quad (3)$$

where \mathbf{A} is a regularization operator (typically a Laplacian) that operates spatially over each filter coefficient separately, and \mathbf{f} is the non-stationary PEF. Fitting goal (1) is written identically for the non-stationary case, but each of the operators present (as well as the filter) are now non-stationary. A full description of what the matrices for non-stationary PEFs look like is given in SEP-113 (Guitton, 2003).

Typically, when interpolating data that are regularly-sampled, the filter is interlaced so that the filter skips over the missing traces, which allows a filter to be estimated (Crawley, 2000). Once the filter has been estimated, the interlacing of the filter is undone for the second stage of the interpolation process.

When the data are not regularly-sampled, the interlacing approach usually fails. In this case, a multi-scale approach can be used where a non-stationary PEF can be estimated on multiple regridded copies of the original data (Curry and Brown, 2001; Curry, 2002, 2003). This can be expressed as

$$\mathbf{W} \left(\begin{bmatrix} \mathbf{D}_0 \\ \mathbf{D}_1 \\ \mathbf{D}_2 \\ \dots \\ \mathbf{D}_n \end{bmatrix} \mathbf{K}\mathbf{P}\mathbf{f} + \begin{bmatrix} \mathbf{d}_0 \\ \mathbf{d}_1 \\ \mathbf{d}_2 \\ \dots \\ \mathbf{d}_n \end{bmatrix} \right) \approx \mathbf{0}. \quad (4)$$

Here, the different scales of data \mathbf{D}_i are generated by the normalized adjoint of linear interpolation, which takes points from a fine grid and sprays them into the coarser grid, then normalizes by the fold. The weight \mathbf{W} is now a diagonal weight for all scales of data, while the introduction of a sub-sampling operator \mathbf{P} subsamples the non-stationary filter so that the spatial size of the filter will match the size of the rescaled data.

Another possible approach is to use a pair of non-stationary 2D PEFs which are estimated independently from the original unscaled data using fitting goals (1) and (3) in two different directions. Once these two PEFs have been estimated, they could be used in tandem to interpolate missing data by (Claerbout, 1999; Curry, 2004):

$$\begin{aligned} \mathbf{L}_{\text{data}}\mathbf{m} &\approx \mathbf{d} \\ \epsilon_x \mathbf{F}_x \mathbf{m} &\approx \mathbf{0} \\ \epsilon_y \mathbf{F}_y \mathbf{m} &\approx \mathbf{0}, \end{aligned} \quad (5)$$

where \mathbf{F}_x and \mathbf{F}_y are 2D non-stationary PEFs (compared to the typically-3D PEF shown before in fitting goal 2), \mathbf{L}_{data} selects known data points, \mathbf{d} is still the known data and \mathbf{m} the unknown model. Unlike the multi-scale approach, this method requires that the data are evenly-sampled along tracks oriented in two different directions.

EXAMPLE

The data set used in this paper is a 2D land dataset from Colombia. There are approximately 300 shots with a nominal spacing of 50 m, 350 receivers in a split-spread with a spacing of 25 m, and a time sampling of 4 ms. A fold diagram of the acquisition is shown in Figure 1. As seen in the figure, there is almost no irregularity in the receiver positions, excluding the lack of very near offsets. However, the source positions in the survey are quite irregular, as shown by the gaps in the vertical axis.

When examining the spatial distribution of the data in cmp and offset coordinates (Figure 2), the irregularity of the source positions can be seen in both the cmp and offset positions. In Figure 2, the data are shown in cmp and absolute offset coordinates, as the sign of the offset of a trace is unimportant if reciprocity is assumed. The receiver cables that appear as horizontal lines in Figure 1 now appear as diagonal lines in cmp-absolute offset space. However, since this is split-spread land data, the negative offsets appear as diagonal lines running orthogonal to the positive offsets, with the 'reflecting point' of this line occurring at zero absolute offset.

The orthogonal tracks caused by the split-spread acquisition are very reminiscent of the crossing tracks shown in the Madagascar satellite dataset (Ecker and Berlioux, 1995). It is possible that methods being developed for this data would also be applicable to split-spread land data. When looking at the spatial distribution of this land data in source-receiver coordinates and by adding a second set of traces predicted by reciprocity, two sets of crossing horizontal and vertical lines can be observed, shown in Figure 3.

A window was selected from both the cmp-absolute offset and the source-receiver cube, that was $200 \times 100 \times 100$ both for both display and computational concerns. The two cubes

Figure 1: A map of source and receiver positions. Receivers are well-sampled, as shown in the horizontal axis. The source sampling is irregular, as seen in the vertical axis..

`bill1-sg-fold` [ER]

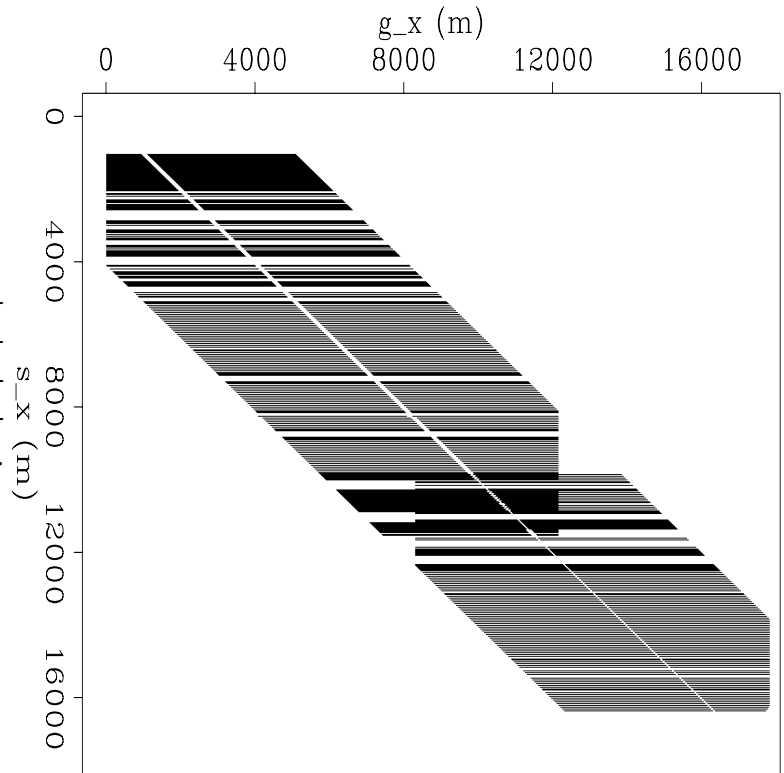
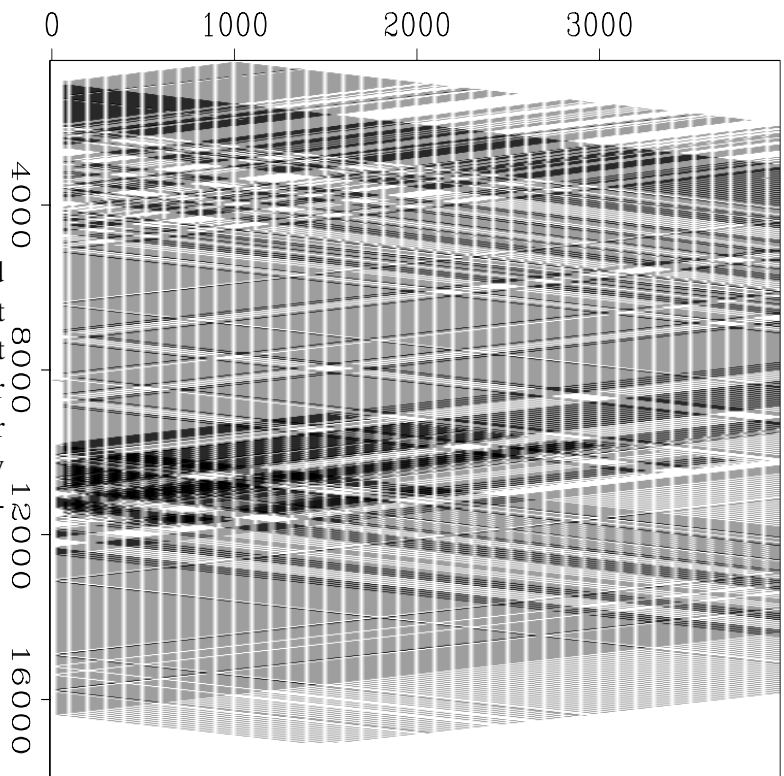


Figure 2: A map of midpoint and absolute offset positions. The split spread is shown by the two different orientations of a receiver line, one for the positive offsets and another for the negative offsets. The irregularity in sources leads to gaps in both directions.

`bill1-co-fold` [ER]



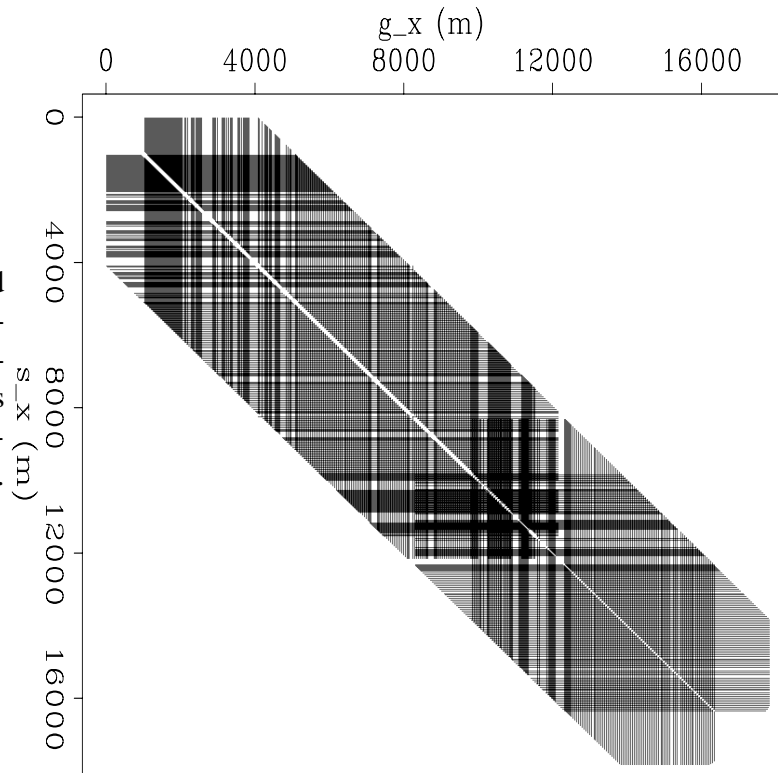


Figure 3: A map of source and receiver positions, including a second set of traces predicted by reciprocity. This second set intersects with the first set because both positive and negative offsets are present.

`bill1-sg-rec-fold` [ER]

are somewhat co-located, and contain small as well as large gaps. In both domains a 3D non-stationary $10 \times 3 \times 3$ coefficient PEF was estimated with 5 scales of data. The filter had micropatches (Crawley, 2000) of size $5 \times 5 \times 5$, Laplacian regularization with an identical ϵ , and 100 iterations of a conjugate-gradient solver were used to estimate the PEFs.

For the second stage of the interpolation (after the PEF has been estimated), fitting goals (2) were solved in each domains with 100 iterations of a conjugate-gradient solver.

The results from the `cmp-absolute` offset domain interpolation are shown in Figure 4. The interpolation is quite successful. While in the common offset section there does not appear to be that many discernible features to interpolate, the `cmp` gather has multiple simultaneous dips (some steep) that are interpolated correctly, as well as a range of gap sizes.

The results of the interpolation in source-receiver coordinates are shown in Figure 5. In this domain, absent sources appear as empty boxes within the data cube, whereas the same holes are roughly diamond-shaped in `cmp-absolute` offset space. The interpolated results are acceptable, but are not as impressive as those in `cmp-absolute` offset space. This could be because of the distribution of the data, and the fact that the square-shaped holes would lead to coarser scales of data dominating the estimation in source-receiver coordinates compared to `cmp-absolute` offset coordinates.

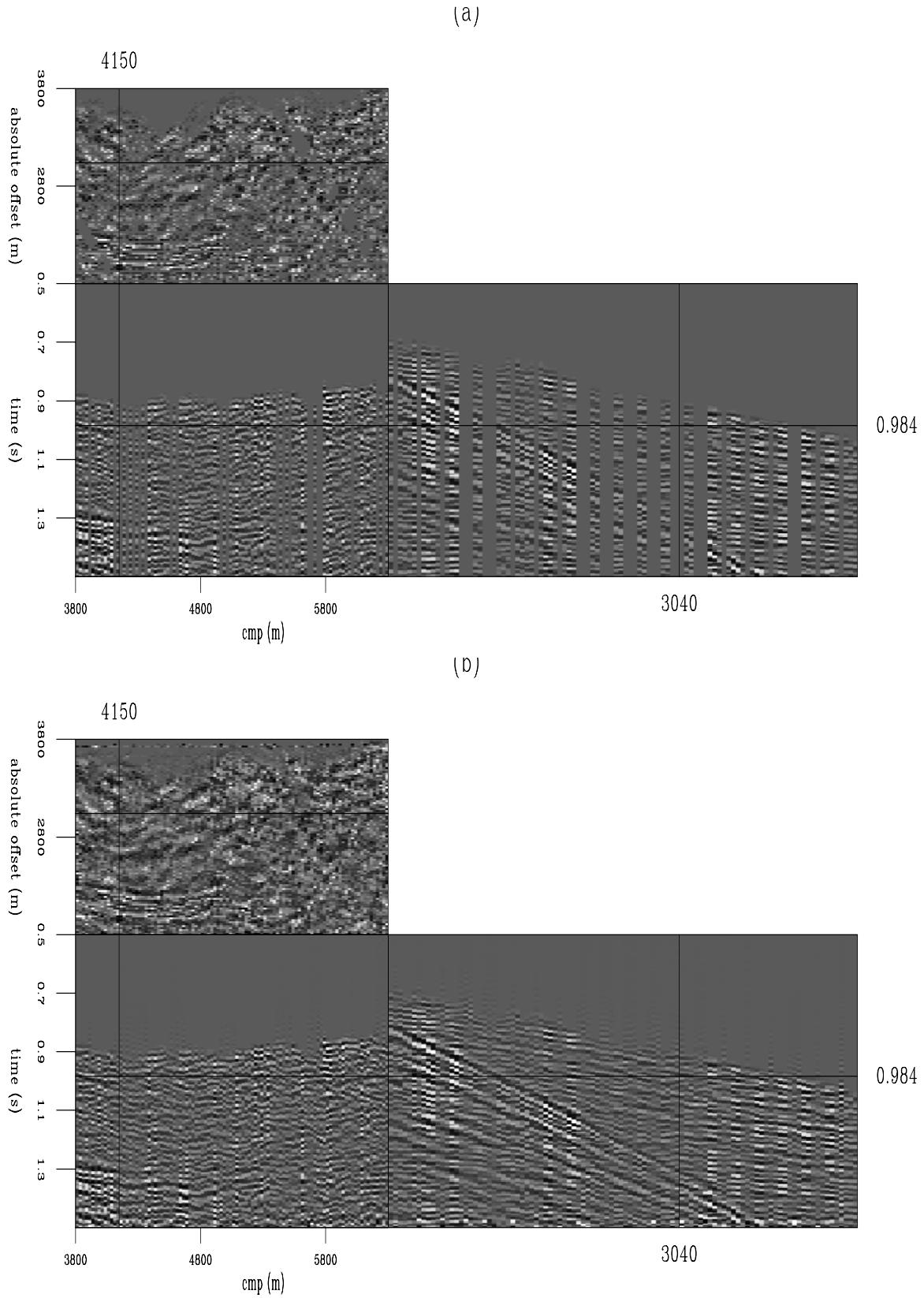


Figure 4: Interpolation in cmp-absolute offset coordinates, (a): Original data, (b): Interpolated data. `bill1-cmp-interp` [CR,M]

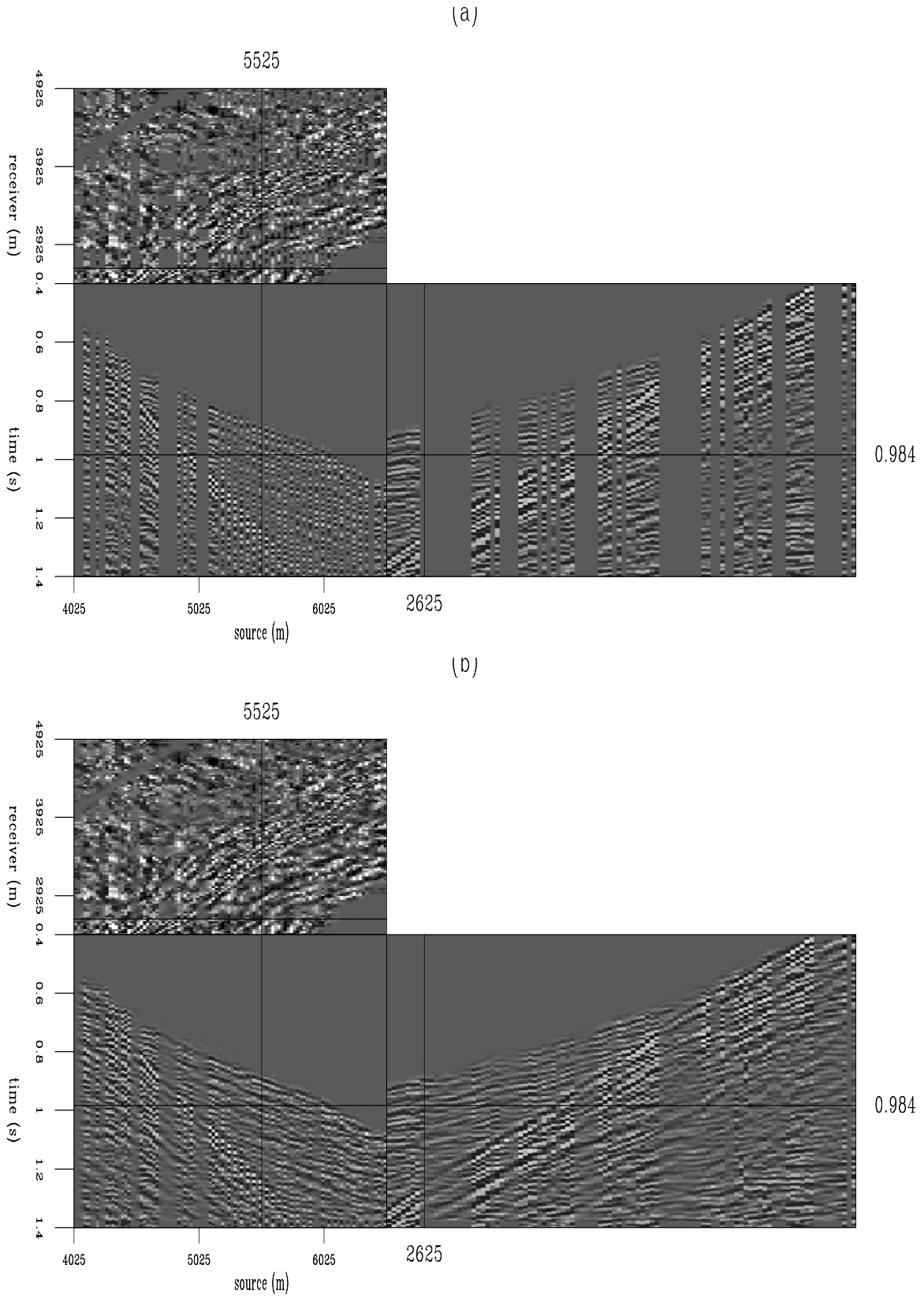


Figure 5: Interpolation in source-receiver coordinates, (a): Original data, (b): Interpolated data. `bill1-sg-interp` [CR,M]

CONCLUSIONS AND FUTURE WORK

Multi-scale PEF-based interpolation in both the cmp-absolute offset and source-receiver coordinates appear to yield acceptable results, although the cmp-absolute offset result is noticeably better. Using CMP-absolute offset coordinates has the benefit of being a smaller space to operate in. However, by using source-receiver coordinates, an interpolation scheme with two 2-D PEFs could be used, which would almost exactly match the distribution of the data compared to the random-sampling assumption made with the multi-scale approach. This would be substantially less expensive as no rescaling would be necessary.

The two most pressing future directions for this work are the applicability of these methods to 3D prestack data, and the effect of the different interpolations on the final migrated image.

ACKNOWLEDGMENTS

I would like to thank Ecopetrol for providing the data used in this paper.

REFERENCES

- Biondi, B., and Vlad, I., 2001, Amplitude preserving prestack imaging of irregularly sampled 3-D data: *SEP-110*, 1–18.
- Chemingui, N., 1999, Imaging irregularly sampled 3D prestacked data: Ph.D. thesis, Stanford University.
- Claerbout, J., 1999, Geophysical estimation by example: Environmental soundings image enhancement: Stanford Exploration Project, <http://sepwww.stanford.edu/sep/prof/>.
- Crawley, S., 2000, Seismic trace interpolation with nonstationary prediction-error filters: Ph.D. thesis, Stanford University.
- Curry, W., and Brown, M., 2001, A new multiscale prediction-error filter for sparse data interpolation: *SEP-110*, 113–122.
- Curry, W., 2002, Non-stationary, multi-scale prediction-error filters and irregularly sampled data: *SEP-111*, 327–337.
- Curry, W., 2003, More fitting equations for PEF estimation on sparse data: *SEP-114*, 171–176.
- Curry, W., 2004, Regularizing madagascar: Pefs from the data space?: *SEP-115*, 347–356.
- Ecker, C., and Berlioux, A., 1995, Flying over the ocean southeast of Madagascar: *SEP-84*, 295–306.

- Fomel, S., 2001, Three-dimensional seismic data regularization: Ph.D. thesis, Stanford University.
- Guittou, A., 2003, Multiple attenuation with multidimensional prediction-error filters: SEP-**113**, 57–74.
- Liu, B., 2004, Multi-dimensional reconstruction of seismic data: Ph.D. thesis, University of Alberta.
- Lomask, J., 1998, Madagascar revisited: A missing data problem: SEP-**97**, 207–216.
- Lomask, J., 2002, Madagascar satellite data: An inversion test case: SEP-**111**, 337–349.
- Lomask, J., 2004, Estimating a 2D stationary PEF on sparse data: SEP-**117**.
- Sacchi, M. D., and Ulrych, T. J., 1995, High-resolution velocity gathers and offset space reconstruction: *Geophysics*, **60**, no. 04, 1169–1177.
- Schonewille, M., 2000, Fourier reconstruction of irregularly sampled seismic data: Ph.d. thesis: Delft University of Technology.
- Spitz, S., 1991, Seismic trace interpolation in the F-X domain: *Geophysics*, **56**, no. 06, 785–794.
- Trad, D., Ulrych, T. J., and Sacchi, M. D., 2002, Accurate interpolation with high-resolution time-variant Radon transforms: *Geophysics*, **67**, no. 2, 644–656.
- Trad, D. O., 2003, Interpolation and multiple attenuation with migration operators: *Geophysics*, **68**, no. 6, 2043–2054.
- Zwartjes, P., and Hindriks, C., 2001, Regularising 3-D data using Fourier reconstruction and sparse inversion: Soc. of Expl. Geophys., 71st Ann. Internat. Mtg, 1906–1909.



Bounds on transport coefficients of porous media

James G. Berryman¹

ABSTRACT

Transport coefficients such as electrical conductivity, thermal conductivity, fluid permeability, etc., can all be treated in mathematically equivalent terms. So an analytical formulation of conductivity bounds by Bergman and Milton can be used in a different way to obtain rigorous bounds on, for example, the real thermal conductivity (which is the particular transport coefficient chosen for the present study) of a fluid-saturated porous material. These bounds do not depend explicitly on the porosity, but rather on two formation factors — one associated with the pore space and the other with the solid frame. The results are then applicable to other physical properties such as fluid permeability. In particular, the formation factors are measures of the microstructure (actually of the tortuosities) of the porous medium, and are therefore the same dimensionless numbers for all these transport processes within the same porous material.

INTRODUCTION

Bounds on various transport coefficients in heterogeneous media have been heavily studied now for over forty years (Hashin and Shtrikman, 1962; Milton, 2002; Torquato, 2002). One of the more interesting developments in this area has been the introduction of rigorous methods for developing bounds on complex constants (closed curves in the complex plane), especially the dielectric constant and conductivity of heterogeneous media (Bergman, 1978, 1980; Milton, 1980, 1981; Bergman, 1982; Korrington and LaTorraca, 1986; Stroud *et al.*, 1986). These methods represent a great technical achievement in this field, but they nevertheless can sometimes be difficult to apply to real data since they require high precision and strong consistency among the data used in computing the bounds. In some cases it would be helpful for applications if some simpler and perhaps more robust methods and results were available.

In this short paper I consider the question of whether it is possible to make use of the analytical methods in a different way to find bounds on transport coefficients. I will limit discussion here to real coefficients, taking thermal conductivity as our main example, but the results apply equally well to other transport coefficients including electrical conductivity and fluid permeability (Berryman, 1992). Furthermore, the resulting bounds depend only on commonly measured quantities in porous media called formation factors (Archie, 1942; Korrington and LaTorraca, 1986), and they show no unusual sensitivity to measurement errors

¹email: berryman@sep.stanford.edu

or any need for careful checking of consistency relations among the measurements.

THE ANALYTICAL FORMULATION

The Bergman-Milton (Bergman, 1978, 1980; Milton, 1980, 1981; Bergman, 1982; Korrington and LaTorraca, 1986; Stroud *et al.*, 1986; Berryman, 1992) analytical approach to understanding some generic effective conductivity g^* of two-component inhomogeneous media shows that

$$g^* = G(g_1, g_2) = g_1 G(1, 0) + g_2 G(0, 1) + \int_0^\infty \frac{dx \mathcal{G}(x)}{\frac{1}{g_1} + \frac{x}{g_2}}, \quad (1)$$

where $G(1, 0)$ and $G(0, 1)$ are constants depending only on the geometry and $\mathcal{G}(x) \geq 0$ is a resonance density also depending only on the geometry. The integral in (1) is known as a Stieltjes integral (Baker, 1975). Although the representation (1) has usually been employed to study the behavior of g^* in the complex plane when g_1 and g_2 are themselves complex (corresponding to mixtures of conductors and dielectrics), I will restrict consideration here – as Bergman did in his early work (Bergman, 1978) – to pure conductors so that g_1 , g_2 , and g^* are all real and nonnegative.

In the limit that one or the other of the two constituents is a perfect insulator ($g_i = 0$), or in the more common case when one of the constituents is much more strongly conducting than the other, I can define two quantities called formation factors (Archie, 1942) by

$$\lim_{g_1 \rightarrow \infty} \frac{g^*}{g_1} = \lim_{g_1 \rightarrow \infty} G(1, g_2/g_1) = G(1, 0) = \frac{1}{F_1}, \quad (2)$$

and, similarly, by

$$\lim_{g_2 \rightarrow \infty} \frac{g^*}{g_2} = \lim_{g_2 \rightarrow \infty} G(g_1/g_2, 1) = G(0, 1) = \frac{1}{F_2}. \quad (3)$$

In a porous material, where solid and pore fluid are each continuously connected throughout the material, both formation factors are finite, and both satisfy $F \geq 1$. The more commonly measured quantity of this type is the electrical formation factor for the continuous fluid component. This measurement has some possible complications due to surface conductance (Johnson *et al.*, 1986; Wildenschild *et al.*, 2000), but it is usually not contaminated by conductance through the bulk solid material because most rock grains can be correctly assumed to be electrically insulating to a very good approximation. Since the formation factor is strictly a measure of the microgeometry of the heterogeneous medium, it is the same number [except for those possible complications already mentioned of surface electrical conduction (Johnson *et al.*, 1986; Wildenschild *et al.*, 2000), which can be eliminated whenever necessary by known experimental methods] for all mathematically equivalent conductivities. For this presentation, I will use F_1 to represent this formation factor associated with the pore space. On the other hand, for thermal conduction the rock grains are the most highly conducting component and the pore fluids tend to be much more poorly conducting – especially so in the case of saturating air. So I will take F_2 to be this formation factor associated with the solid frame of the porous material.

FORMATION FACTOR BOUNDS

To obtain some useful bounds, I again consider the form of (1)

$$G(g_1, g_2) = \frac{g_1}{F_1} + \frac{g_2}{F_2} + \int_0^\infty \frac{dx \mathcal{G}(x)}{\frac{1}{g_1} + \frac{x}{g_2}}. \quad (4)$$

For reasons that will become apparent I want to compare the values of $G(g_1 + 2g_0, g_2 + 2g_0)$ and $G(g_1, g_2) + 2g_0$, where g_0 can take any positive value, but g_0 is limited in the negative range by the limitations that both $g_1 + 2g_0$ and $g_2 + 2g_0$ must always be nonnegative. A straightforward, but somewhat tedious calculation shows that

$$G(g_1 + 2g_0, g_2 + 2g_0) - G(g_1, g_2) - 2g_0 = 2g_0(g_2 - g_1)^2 \int_0^\infty \frac{dx x \mathcal{G}(x)}{(1+x)(g_2+xg_1)[g_2+xg_1+2(1+x)g_0]}. \quad (5)$$

The right hand side of this equation is always positive whenever $g_0 > 0$ and $g_1 \neq g_2$. It vanishes when $g_0 = 0$ or $g_1 = g_2$. If $g_1 < g_2$, then for negative values of the parameter g_0 , allowed values of g_0 lie in the range $0 > 2g_0 \geq -g_1$. For such values of g_0 , the right hand side of (5) is strictly negative.

The limiting case obtained by taking $2g_0 \rightarrow -g_1$ is most useful because, in this limit, $G(g_1 + 2g_0, g_2 + 2g_0) \rightarrow (g_2 - g_1)/F_2$ — thus eliminating the unknown functional $\mathcal{G}(x)$ from this part of the expression. Then, (5) shows that

$$G(g_1, g_2) \geq g_1 + \frac{g_2 - g_1}{F_2} \equiv S_2(g_1, g_2), \quad (6)$$

which is a general lower bound on $G(g_1, g_2)$ without any further restrictions on the measurable quantities $g_1 \leq g_2$, and F_2 .

A second bound can be obtained (again in the limit $2g_0 = -g_1$) by noting that

$$\int_0^\infty \frac{dx x \mathcal{G}(x)}{(1+x)(g_2+xg_1)} \leq \int_0^\infty \frac{dx \mathcal{G}(x)}{g_2+xg_1}, \quad (7)$$

and then recalling that

$$\int_0^\infty \frac{dx \mathcal{G}(x)}{g_2+xg_1} = \frac{1}{g_1 g_2} \left[G(g_1, g_2) - \frac{g_1}{F_1} - \frac{g_2}{F_2} \right]. \quad (8)$$

Substituting (7) into (5) produces an upper bound on $G(g_1, g_2)$. By subsequently substituting (8) and then rearranging the result, the final bound is

$$G(g_1, g_2) \leq g_2 + \frac{g_1 - g_2}{F_1} \equiv S_1(g_1, g_2). \quad (9)$$

Comparing (6) and (9), I see consistency requires that

$$g_1 + \frac{g_2 - g_1}{F_2} \leq g_2 + \frac{g_1 - g_2}{F_1} \quad (10)$$

must be true. Rearranging this expression gives the condition

$$0 \leq (g_2 - g_1) \left(1 - \frac{1}{F_1} - \frac{1}{F_2} \right), \quad (11)$$

the validity of which I need to check. In the limit $g_1 = g_2 = 1$, a sum rule follows from (4), and from this I have:

$$1 - \frac{1}{F_1} - \frac{1}{F_2} = \int_0^\infty \frac{dx \mathcal{G}(x)}{1+x} \geq 0. \quad (12)$$

This shows explicitly that (11) is always satisfied as long as $g_2 \geq g_1$. If this inequality $g_2 \geq g_1$ does not hold, then the sense of the bounding inequalities is changed, so the expressions for the upper and lower bounds trade places.

When $g_2 = \text{const}$ and g_1 varies (as would be expected in a series of thermal conductivity experiments with different fluids in the same porous medium), then (6) and (9) are both straight lines that cross at $g_1 = g_2$. The general bounds are therefore

$$\min(S_1, S_2) \leq G(g_1, g_2) \leq \max(S_1, S_2), \quad (13)$$

where S_1 and S_2 were defined in (6) and (9).

SECOND DERIVATION

Another derivation of the same bounds may provide additional insight into their significance.

Again starting from (4), this time I will go directly to the integral term and start making approximations to it. First, consider

$$\int_0^\infty \frac{dx \mathcal{G}(x)}{\frac{1}{g_1} + \frac{x}{g_2}} = g_1 \int_0^\infty \frac{dx \mathcal{G}(x)}{1 + \frac{xg_1}{g_2}} \geq g_1 \int_0^\infty \frac{dx \mathcal{G}(x)}{1+x}, \quad (14)$$

where the inequality holds whenever $g_1 \leq g_2$. Then, similarly, I have

$$\int_0^\infty \frac{dx \mathcal{G}(x)}{\frac{1}{g_1} + \frac{x}{g_2}} = g_2 \int_0^\infty \frac{dx \mathcal{G}(x)}{\frac{g_2}{g_1} + x} \leq g_2 \int_0^\infty \frac{dx \mathcal{G}(x)}{1+x}, \quad (15)$$

again whenever $g_1 \leq g_2$. I can then make use of the identity in sumrule (12) to replace the integral on the far right in both of these expressions. And, finally, applying (14) to (4) gives exactly the lower bound (6), while applying (15) to (4) gives exactly the upper bound (9). All the same comments about reversal of the sense of the inequalities applies here if instead $g_1 \geq g_2$. So, the final result is again (13).

This derivation has the advantage that it is clear from the inequalities (14) and (15) exactly what approximations have been made in each case to arrive at the bounds on $G(g_1, g_2)$.

Figure 1: Comparison of the formation factor bounds (FF^\pm), the Hashin-Shtrikman bounds (HS^\pm), and thermal conductivity data from Asaad (1955). Data are for sandstone sample B. jim1-gBasaadsmIgwG [NR]

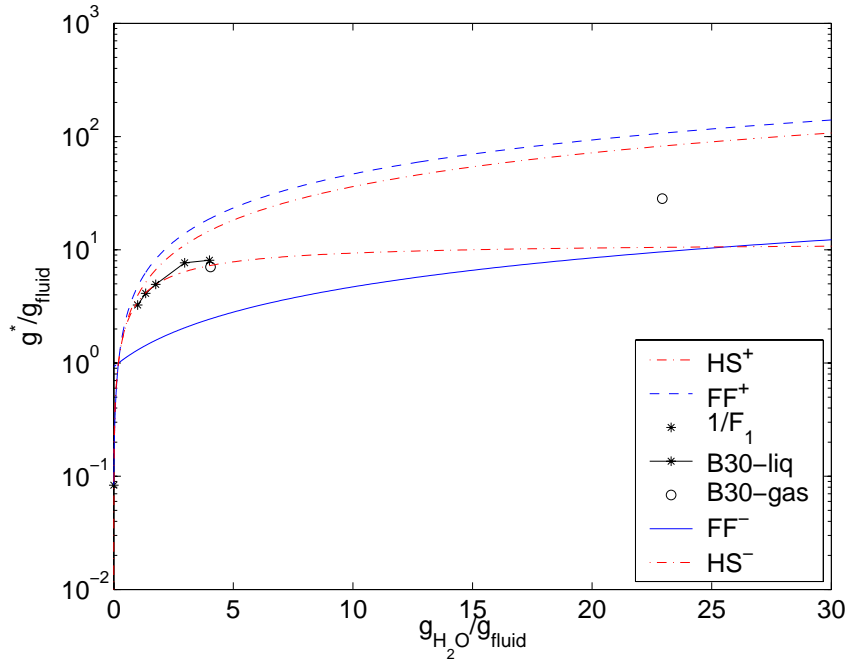


Figure 2: Comparison of the formation factor bounds (FF^\pm), the Hashin-Shtrikman bounds (HS^\pm), and thermal conductivity data from Asaad (1955). Data are for sandstone sample C, including two distinct data sets. jim1-gCasaadIglgwG [NR]

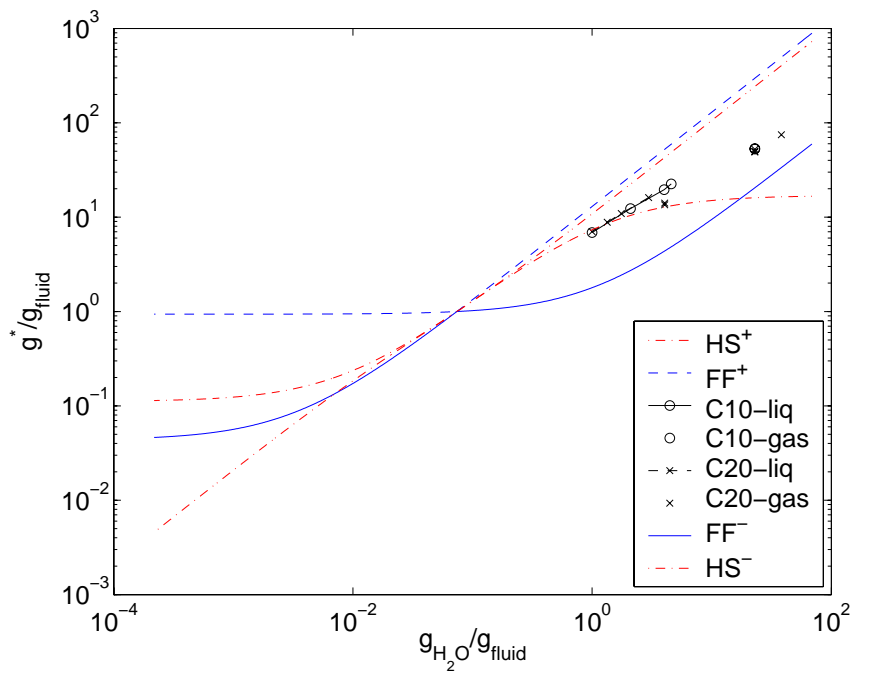
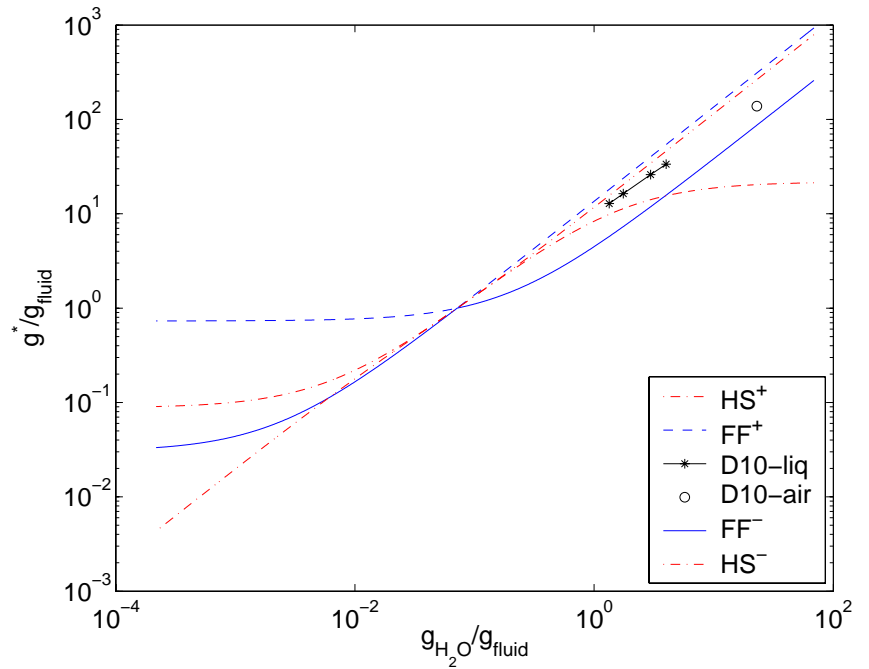


Figure 3: Comparison of the formation factor bounds (FF^\pm), the Hashin-Shtrikman bounds (HS^\pm), and thermal conductivity data from Asaad (1955). Data are for sandstone sample D. jim1-gDasaadlgwg [NR]



NUMERICAL EXAMPLES

Examples shown in Figures 1–3 make use of thermal conductivity and electrical formation factor data from Asaad (1955). Three different sandstones (labelled B, C, D) were studied by Asaad, and several different sets of experiments were performed on each. The Figures show data from experiments B30, C10, C20, and D10. I plot both the new formation factor bounds (FF) and the Hashin-Shtrikman bounds (HS) based on volume fraction information. A selection of the data is displayed in all three cases. Electrical formation factor measurements were made on all three samples ($F_1^B = 12.0$, $F_1^C = 23.0$, $F_1^D = 33.0$). Frame formation factor can be determined from measurements of thermal conductivity when the pores are evacuated. But a value of effective grain thermal conductivity must be found. Asaad (1955) solved this problem — using an extrapolation method — assuming that a certain geometric mean approximation (which is just a straight line on a log-log plot) when fit to the data would then give an accurate estimate of the point at which $G(g_1 = g_2^{\text{eff}}, g_2) \simeq g_2^{\text{eff}}$. Results displayed as they are here on the log-log plots in Figs. 2 and 3 show that Asaad’s method is in fact quite accurate for all these data. Then, $F_2^{\text{eff}} \simeq g_2^{\text{eff}}/G(0, g_2)$, and I find $F_2^B = 13.5$, $F_2^C = 15.9$, $F_2^D = 3.72$. Measured porosity values were $\phi^B = 0.220$, $\phi^C = 0.158$, $\phi^D = 0.126$.

CONCLUSIONS

The results show an interesting common pattern in all three examples. The Hashin-Shtrikman upper bound is always smaller, and therefore a better/tighter bound, than the upper FF bound. But the situation is more complicated for the lower bounds. Near the point where all the bounds cross, the lower Hashin-Shtrikman bounds are just slightly better for higher values of

g_{fluid} , but significantly better for the lower values. On the other hand, far from this convergence point the lower FF bound is clearly superior to Hashin-Shtrikman, both at quite high and quite low values of g_{fluid} . In fact this is not surprising since it is in these asymptotic regimes that the FF bounds tend to become exact estimates. So a reasonable conclusion I reach from these observations is that the combination of the two Hashin-Shtrikman bounds and the lower FF bound provides quite accurate estimates of overall conductivity for the entire range of pore-fluid conductivities.

Future work along these lines will be directed towards improving the estimates obtained from the analytical method by making more direct use of various known constraints on the resonance density \mathcal{G} and its integral moments.

REFERENCES

- Archie, G. E., 1942, The electrical resistivity log as an aid in determining some reservoir characteristics: *Trans. AIME*, **146**, 54–62.
- Asaad, Y., 1955, *A Study of the Thermal Conductivity of Fluid-Bearing Porous Rocks*: Ph. D. Thesis, University of California – Berkeley.
- Baker, G. A., Jr., 1975, *Essentials of Padé Approximants*, Academic, San Diego, California.
- Bergman, D. J., 1978, The dielectric constant of a composite material — A problem of classical physics: *Phys. Rept.*, **43**, 378–407.
- Bergman, D. J., 1980, Exactly solvable microscopic geometries and rigorous bounds for the complex dielectric constant of a two-component composite material: *Phys. Rev. Lett.*, **44**, 1285–1287.
- Bergman, D. J., 1982, Rigorous bounds for the complex dielectric constant of a two-component composite: *Ann. Phys.*, **138**, 78–114.
- Berryman, J. G., 1992, Effective stress for transport properties of inhomogeneous porous rock: *J. Geophys. Res.*, **97**, 17409–17424.
- Hashin, Z., and Shtrikman, S., 1962, A variational approach to the theory of the effective magnetic permeability of multiphase materials: *J. Appl. Phys.*, **33**, 3125–3131.
- Johnson, D. L., Koplik, J., and Schwartz, L. M., 1986, New pore-size parameter characterizing transport in porous media: *Phys. Rev. Lett.*, **57**, 2564–2567.
- Korringa, J., and LaTorraca, G. A., 1986, Application of the Bergman-Milton theory of bounds to the permittivity of rocks: *J. Appl. Phys.*, **60**, 2966–2976.
- Milton, G. W., 1980, Bounds on the complex dielectric constant of a composite material: *Appl. Phys. Lett.*, **37**, 300–303.
- Milton, G. W., 1981, Bounds on the complex permittivity of a two-component composite material: *J. Appl. Phys.*, **52**, 5286–5293.
- Milton, G. W., 2002, *The Theory of Composites*, Cambridge University Press, Cambridge, UK.
- Stroud, D., Milton, G. W., and De, B. R., 1986, Analytical model for the dielectric response of brine-saturated rocks: *Phys. Rev. B*, **34**, 5145–5153.
- Torquato, S., 2002, *Random Heterogeneous Materials: Microstructure and Macroscopic Properties*, Springer, New York.
- Wildenschild, D., Roberts, J. J., and Carlberg, E. D., 2000, On the relationship between microstructure and electrical and hydraulic properties of sand-clay mixtures: *Geophys. Res. Lett.*, **27**, 3065–3068.

Bounds on geomechanical constants for a model of heterogeneous reservoirs

James G. Berryman¹

ABSTRACT

A well-known result due to Hill provides an exact expression for the bulk modulus of any multicomponent elastic composite whenever the constituents are isotropic and the shear modulus is uniform throughout. Although no precise analog of Hill's result is available for the opposite case of uniform bulk modulus and varying shear modulus, it is shown here that some similar statements can be made for shear behavior of random polycrystals composed of laminates of isotropic materials. This model is intended to incorporate characteristics that mimic geomechanical properties of heterogeneous earth reservoirs, including local layering due to sedimentary processes. In particular, the Hashin-Shtrikman-type bounds of Peselnick, Meister, and Watt for random polycrystals composed of hexagonal (transversely isotropic) grains are applied to our model of polycrystals of laminates. An exact product formula relating the Reuss estimate of bulk modulus and an effective shear modulus (of laminated grains composing the system) to products of the eigenvalues for quasi-compressional and quasi-uniaxial shear eigenvectors also plays an important role in the analysis of the overall shear behavior of the random polycrystal. When the bulk modulus is uniform in such a system, the equations are shown to reduce to a simple form that depends prominently on the uniaxial shear eigenvalue — as expected from physical arguments concerning the importance of uniaxial shear in these systems. Applications of the analytical results presented here include benchmarking of numerical procedures used for studying elastic behavior of complex composites, and estimating coefficients needed in up-scaled equations for elasticity and/or poroelasticity of heterogeneous reservoirs.

INTRODUCTION

In the course of analyzing a problem on fluid-dependence of shear modulus in poroelastic systems, the author (Berryman, 2004a) uncovered an unanticipated identity in elasticity that appears to have wider implications for many elastic systems and/or composites. The basic result states that for *any* hexagonal (or transversely isotropic) elastic system there is an exact product formula, namely, $6K_R G_{\text{eff}}^V = \omega_+ \omega_-$, relating the Reuss estimate K_R of the bulk modulus times the Voigt estimate G_{eff}^V of the uniaxial part of the shear modulus to the product of the two system eigenvalues ω_{\pm} for quasi-compressional and quasi-shear modes. There is also

¹email: berryman@sep.stanford.edu

a second product formula with the roles of the Reuss and Voigt averages reversed, but this second identity is somewhat less important as we shall see.

Our goal here will be to show how these facts help to remove in part (although only in one special, but nevertheless interesting, case) the asymmetry in the analysis of elastic composites resulting from the existence of Hill's well-known formula (Hill, 1963, 1964; Milton, 2002) for arbitrary elastic composites, showing that

$$K^* = \left[\sum_{n=1}^N \frac{f_n}{K_n + 4\mu/3} \right]^{-1} - 4\mu/3. \quad (1)$$

Here the bulk modulus of the n -th constituent is K_n , the shear modulus takes the same value $\mu_n = \mu$ for all $n = 1, \dots, N$, and the overall effective bulk modulus is K^* . The volume fractions f_n are all nonnegative, and add up to unity. In general there is in fact no corresponding relationship for the overall shear modulus μ^* , when instead the system has constant bulk modulus $K_n = K$ for all N constituents. But, nevertheless, the existence of formulas quite analogous to (1) for shear will be demonstrated for a model random polycrystal composed of laminated grains.

As always in the theory of composites, there are several clear limitations to the use of the analysis in practice: (a) the continuum hypothesis, (b) the implicit assumption of adequate separation of scales between sizes of grains and of the overall composite, and (c) an assumption of negligible porosity. The continuum hypothesis will clearly be violated if the grain sizes are too small, approaching nanometer sizes and below. The deviations expected in our case are similar to those observed in deviations from the Hall-Petch effect (Hall, 1951; Petch, 1953; Schiötz, 1998), *i.e.*, a softening of the composite as a function of decreasing grain size once the size is below some threshold. This effect is caused in part by a significant increase in grain-to-grain interface area (which is not accounted for by the present theory) in composites when the grains become too small. At still smaller grain sizes, atomic scale effects become important and the continuum theory must clearly fail. At the other extreme, if the grains are too large, then there may not be sufficient numbers of particles in the sample for the separation of scales between composite and grains to be adequate. This issue is related to the question of what is an adequate REV (representative elementary volume) (Bear, 1972; Bourbié, 1987; Drugan and Willis, 1996). If the grains are too large and, therefore, too few, the entire sample may not be large enough to serve as an adequate REV. Finally, when a polycrystal is constructed by assembling many crystalline grains, it is also important that very little porosity remain in the resulting polycrystal. It has been estimated (Berryman, 1994) that as little as 0.5% porosity in a composite is sufficient to make it important to include the porosity in the model. But, except to exclude it thus from consideration, porosity is not discussed here.

The next section introduces the notation and basic results used in the rest of the paper. The third section considers the case of constant bulk modulus, and shows that the Voigt and Reuss averages for shear modulus, although differing in their numerical values, nevertheless depend on simple averages of the shear modulus plus another average comparable to (1). The fourth section considers the general problem for bounds on the moduli of random polycrystals of laminates, with special emphasis on the Peselnick-Meister-Watt bounds (Peselnick and

Meister, 1965; Watt and Peselnick, 1980). The discussion of the fifth section summarizes some practical conclusions about the analysis and also makes a comparison with a “self-consistent” estimate related to the bounds. Two technical Appendices summarize results used in the main text.

ELASTICITY OF LAYERED MATERIALS

We assume that a typical building block of the random system is a small grain of laminate material whose elastic response for such a transversely isotropic (hexagonal) system can be described by:

$$\begin{pmatrix} \sigma_{11} \\ \sigma_{22} \\ \sigma_{33} \\ \sigma_{23} \\ \sigma_{31} \\ \sigma_{12} \end{pmatrix} = \begin{pmatrix} c_{11} & c_{12} & c_{13} & & & \\ c_{12} & c_{11} & c_{13} & & & \\ c_{13} & c_{13} & c_{33} & & & \\ & & & 2c_{44} & & \\ & & & & 2c_{44} & \\ & & & & & 2c_{66} \end{pmatrix} \begin{pmatrix} e_{11} \\ e_{22} \\ e_{33} \\ e_{23} \\ e_{31} \\ e_{12} \end{pmatrix}, \quad (2)$$

where σ_{ij} are the usual stress components for $i, j = 1 - 3$ in Cartesian coordinates, with 3 (or z) being the axis of symmetry (the lamination direction for such a layered material). Displacement u_i is then related to strain component e_{ij} by $e_{ij} = (\partial u_i / \partial x_j + \partial u_j / \partial x_i) / 2$. This choice of definition introduces some convenient factors of two into the 44, 55, 66 components of the stiffness matrix shown in (2).

Although some of the results presented here are more general, we will assume for definiteness that this stiffness matrix in (2) arises from the lamination of N isotropic constituents having bulk and shear moduli K_n, μ_n , in the $N > 1$ layers present in each building block. It is important that the thicknesses d_n always be in the same proportion in each of these laminated blocks, so that $f_n = d_n / \sum_{n'} d_{n'}$. But it is not important what order the layers were added to the blocks, as Backus's formulas (Backus, 1962) for the constants show. For the overall behavior for the quasistatic (long wavelength) behavior of the system we are studying, Backus's results [also see Postma (1955) and Milton (2002)] state that

$$\begin{aligned} c_{33} &= \left\langle \frac{1}{K+4\mu/3} \right\rangle^{-1}, & c_{13} &= c_{33} \left\langle \frac{K-2\mu/3}{K+4\mu/3} \right\rangle, \\ c_{44} &= \left\langle \frac{1}{\mu} \right\rangle^{-1}, & c_{66} &= \langle \mu \rangle, \\ c_{11} &= \frac{c_{13}^2}{c_{33}} + 4c_{66} - 4 \left\langle \frac{\mu^2}{K+4\mu/3} \right\rangle, & c_{12} &= c_{11} - 2c_{66}. \end{aligned} \quad (3)$$

This bracket notation can be correctly viewed: (a) as a volume average, (b) as a line integral along the symmetry axis x_3 , or (c) as a weighted summation $\langle Q \rangle = \sum_n f_n Q_n$ over any relevant physical quantity Q taking a constant value Q_n in the n -th layer.

The bulk modulus for each such building block (or crystalline grain if you like) is that given by the compressional Reuss average K_R of the corresponding compliance matrix s_{ij} [the inverse of the usual stiffness matrix c_{ij} , whose nonzero components are shown in (2)].

The well-known result is $e = e_{11} + e_{22} + e_{33} = \sigma/K_{\text{eff}}$, where $1/K_{\text{eff}} = 1/K_R = 2s_{11} + 2s_{12} + 4s_{13} + s_{33}$. This quantity can be expressed in terms of the stiffness elements as

$$\frac{1}{K_R - c_{13}} = \frac{1}{c_{11} - c_{66} - c_{13}} + \frac{1}{c_{33} - c_{13}}. \quad (4)$$

When $\mu_n = \text{const}$, it is easy to show that (4) implies (1).

Even though K_{eff} is the same for every grain, since the grains themselves are not isotropic, the overall bulk modulus K^* of the random polycrystal is not necessarily the same as K_{eff} for the individual grains (Hill, 1952). Hashin-Shtrikman bounds on K^* for random polycrystals whose grains have hexagonal symmetry (Peselnick and Meister, 1965; Watt and Peselnick, 1980) show in fact that the value K_R lies outside the bounds in many situations. We will say more about this in the fourth section.

In general an upper bound on the overall shear modulus of an isotropic polycrystal (Hill, 1952) is given by the Voigt average over shear of the stiffness matrix, which may be written as

$$\mu_V = \frac{1}{5} (G_{\text{eff}}^V + 2c_{44} + 2c_{66}). \quad (5)$$

This expression can be taken as the definition of G_{eff}^V . Eq. (5) implies that $G_{\text{eff}}^V = (c_{11} + c_{33} - 2c_{13} - c_{66})/3$. G_{eff}^V is the energy per unit volume in a grain when a pure uniaxial shear strain of unit magnitude is applied to the grain along its axis of symmetry (Berryman, 2004a).

CONSTANT BULK MODULUS

As a first result, consider a laminated grain composed of isotropic constituents, all having the same bulk modulus K in each layer, but differing shear moduli. Then, if we define the function [compare (1)]

$$g(\zeta) = \left[\sum_{n=1}^N \frac{f_n}{\mu_n + \zeta} \right]^{-1} - \zeta, \quad (6)$$

we find from (3) that $G_{\text{eff}}^V = g(\zeta)$ with $\zeta = 3K/4$. This function $g(\zeta)$ has the interesting and useful properties that

$$c_{44} = \langle 1/\mu \rangle^{-1} \equiv g_- \leq g(\zeta) \leq g_+ \equiv \langle \mu \rangle = c_{66}. \quad (7)$$

Furthermore, $g(\zeta)$ is a monotonic function, achieving its lower bound when $\zeta = 0$ and approaching its upper bound as $\zeta \rightarrow \infty$. This formula shows in an elementary way how $G_{\text{eff}}^V = g(3K/4)$ — and therefore μ_V — depends on the constant bulk modulus of the system, and also that this component of the Voigt bound on the overall shear modulus increases with increasing magnitude of the bulk modulus. The overall Voigt bound/estimate (5) for shear therefore has very similar character, but the magnitude of the effect is reduced by a factor of 5, since this is only one of the five distinct contributors to the overall shear behavior of the system. So the

largest change in the Voigt shear modulus that variations in bulk modulus can ever induce are expected to be on the order of 20% (or less) of the difference $c_{66} - c_{44}$.

Similarly, the Reuss average for shear is

$$\mu_R = \left[\frac{1}{5} \left(\frac{1}{G_{\text{eff}}^R} + \frac{2}{c_{44}} + \frac{2}{c_{66}} \right) \right]^{-1}, \quad (8)$$

which is also a rigorous lower bound on the overall shear modulus of the polycrystal (Hill, 1952). For each hexagonal grain, the product formulas $3K_R G_{\text{eff}}^V = 3K_V G_{\text{eff}}^R = \omega_+ \omega_- / 2 = c_{33}(c_{11} - c_{66}) - c_{13}^2$ are valid. The symbols ω_{\pm} stand for the quasi-compressional and quasi-uniaxial shear eigenvalues for all the grains (Berryman, 2004). The product formulas show immediately that $G_{\text{eff}}^R = G_{\text{eff}}^V K_R / K_V = G_{\text{eff}}^V$, since $K_R = K_V = K$. Thus, for this relatively simple system, pure compression or tension ($e_{11} = e_{22} = e_{33}$) is an eigenvector corresponding to stiffness eigenvalue $3K$. Uniaxial shear strain ($e_{33} = -2e_{11} = -2e_{22}$) is also an eigenvector and $2G_{\text{eff}}^V = 2G_{\text{eff}}^R$ is the corresponding eigenvalue.

MODEL OF HETEROGENEOUS RESERVOIRS

Returning to the general problem for arbitrary K_n , suppose we construct a random polycrystal by packing small bits of this laminate material into a large container in a way so that the axis of symmetry appears randomly over all possible orientations and also such that no empty volume (porosity) is left in the resulting composite. If the ratio of grain size to overall composite is small enough so the usual implicit assumption of scale separation applies to the composite — but not so small that we are violating the continuum hypothesis — then we have an example of the type of material we want to study.

For each individual grain in this polycrystal, Eqs. (3) are valid locally (*i.e.*, for locally defined coordinates), and the grain bulk modulus K_R is given by (4) for all the grains. The factors $3K_R$ and $2G_{\text{eff}}^V$ are not necessarily eigenvalues of elastic stiffness for individual grains. The Voigt average for shear is again given by (5), which is an upper bound on the isotropic shear modulus of the random polycrystal (Hill, 1952).

The advantage of studying polycrystals of laminates is that we have available an array of theoretical results from which to choose. For example, since each grain is composed of isotropic constituents, standard Voigt and Reuss bounds (Hill, 1952), as well as the more restrictive Hashin-Shtrikman bounds (Hashin and Shtrikman, 1962; 1963) on composites made up of isotropic constituents are all available. Then, we can instead, or in addition, consider Voigt and Reuss bounds on the laminated grain materials. Formulas for these bounds have already been given here in Eqs. (4), (5), and (8), respectively for K_R , μ_V , and μ_R . The remaining formula is well-known to be

$$K_V = [2(c_{11} + c_{12}) + 4c_{13} + c_{33}] / 9. \quad (9)$$

Then, it is useful to distinguish between “correlated” and “uncorrelated” bounds. For example, the most familiar bounds — after the uncorrelated Voigt and Reuss bounds (*i.e.*, the volume

Figure 1: Various bulk modulus bounds: The outer most bounds (blue dot-dash lines) are the standard Hashin-Shtrikman bounds (HS) based only on information about the layer constituents and their volume fractions. The black solid lines are the Voigt and Reuss bounds (XV,XR) obtained from appropriate averages of laminate constants in (3). The inner most bounds (also blue dot-dash lines) are the Peselnick-Meister bounds (PM) for hexagonal polycrystals. For contrast, the Dederich-Zeller bounds (DZ) (see Appendix B) are also shown (dashed red lines).
jim2-K4bounds [NR]

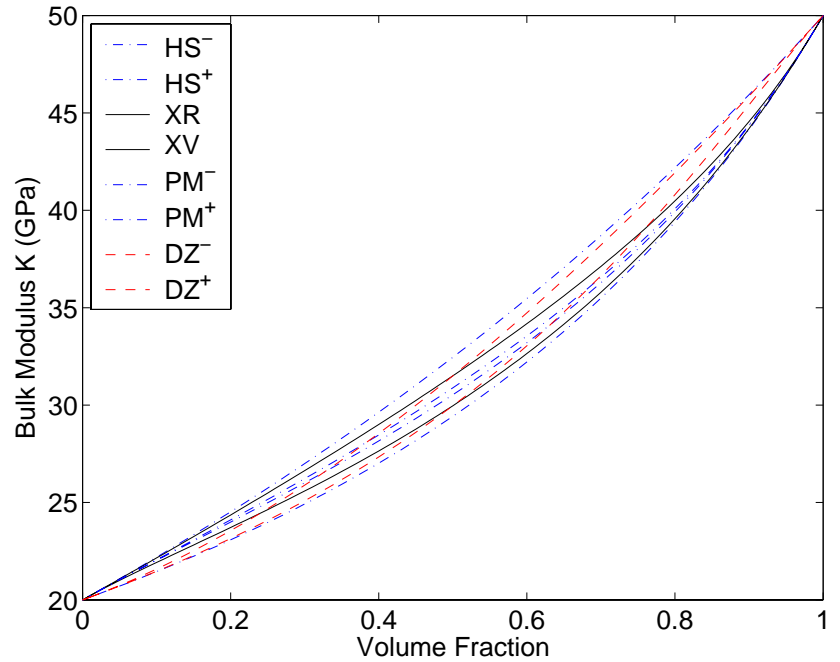
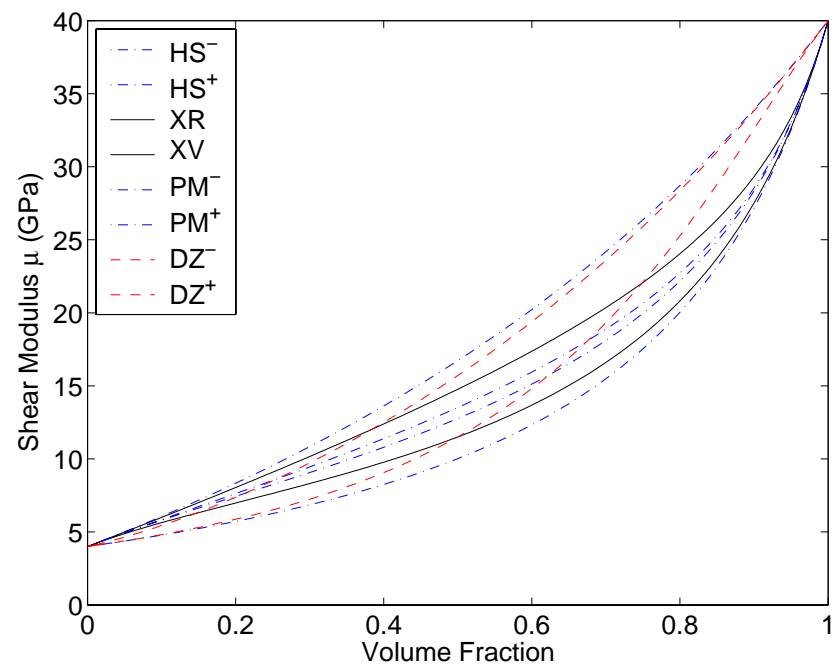


Figure 2: Same as Figure 1 for the various shear modulus bounds.
jim2-mu4bounds [NR]



averaged mean and harmonic mean respectively of the constituents' constants) — are the uncorrelated Hashin-Shtrikman bounds:

$$K_{HS}^{\pm} = \left[\sum_{n=1}^N \frac{f_n}{K_n + 4\mu_{\pm}/3} \right]^{-1} - 4\mu_{\pm}/3 \quad (10)$$

and

$$\mu_{HS}^{\pm} = \left[\sum_{n=1}^N \frac{f_n}{\mu_n + \zeta_{\pm}} \right]^{-1} - \zeta_{\pm}, \quad (11)$$

where

$$\zeta_{\pm} = \frac{\mu_{\pm}}{6} \left(\frac{9K_{\pm} + 8\mu_{\pm}}{K_{\pm} + 2\mu_{\pm}} \right), \quad (12)$$

with K_+ and K_- being the highest and lowest values of K_n in the system, and similarly μ_+ (μ_-) being the highest (lowest) value of the shear modulus. Milton (1981) presented examples of correlated bounds where the correlations were introduced specifically through spatial correlation functions. But here we introduce correlations instead through the laminated grains. The bounds (4), (5), (8), and (9) are then correlated Voigt and Reuss bounds because of the assumed internal grain-like structure.

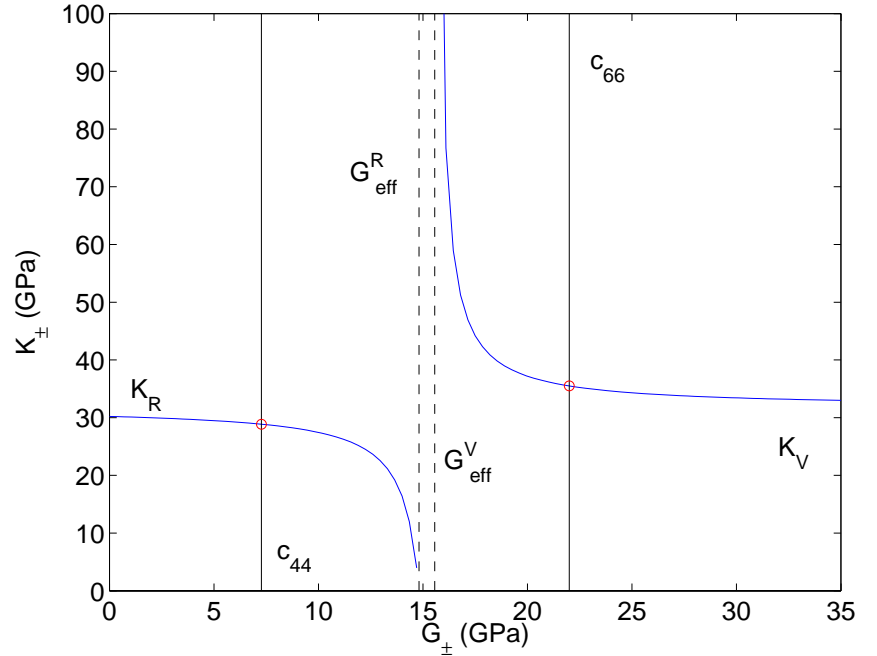
We see in Figures 1 and 2 that these bounds (XR and XV) for the polycrystalline case are fairly substantial improvements over the uncorrelated Hashin-Shtrikman bounds (HS^{\pm}), which are themselves substantial improvements over the uncorrelated version of the Voigt and Reuss bounds (the Voigt bound is not shown here, but is just a straight line in each plot between the end points of these curves).

A correlated version of the Hashin-Shtrikman bounds can be computed also, as has been shown by Peselnick and Meister (1965) and Watt and Peselnick (1980) (see Appendix A for the details of these formulas, but not their derivation). We see that these bounds are very tight indeed in comparison to all the others considered here. In particular, note that K_R computed from (4) falls outside the correlated Voigt and Reuss bounds (curves XV and XR) of Figure 1.

For contrast, Figures 1 and 2 also plot another set of bounds derived by Dederichs and Zeller (1973) that is also intended for use in uncorrelated systems (see Appendix B for the formulas and a brief discussion). The DZ bounds behave quite differently from those of the correlated bounds XR, XV, PM^{\pm} . It is easy to see why this is so. In the laminates, as the volume fractions become small for one constituent at one end of the curves and for the other constituent at the other end, the low volume fraction constituent is approaching a flat disc-like geometry. It is well-known (Milton, 1981) that in this circumstance results for disc-like inclusions tend to dominate the behavior and, therefore, tend to hug the upper Hashin-Shtrikman bound in the lower left-hand limit, and then to hug the lower Hashin-Shtrikman bound in the upper right-hand limit of the Figures. We see that this is so for the correlated bounds XR, XV, PM^{\pm} . But the DZ^{\pm} bounds are uncorrelated and do not show this type of behavior at all.

The best and also most relevant bounds here are obviously the Peselnick-Meister-Watt bounds (Peselnick and Meister, 1965; Watt and Peselnick, 1980), which are presented and

Figure 3: Illustrating the graphical construction leading to the optimum parameters for the comparison material of the lower and upper Peselnick-Meister-Watt bounds: (G_-, K_-) , (G_+, K_+) , shown as red circles. The case shown is for the middle point of the examples shown in Figures 1 and 2 (volume fraction of 0.50). Values of the constants entering the expressions (see Appendix A) are: $K_V = 30.2162$, $c_{44} = 7.2727$, $c_{66} = 22.0000$, $G_{\text{eff}}^R = 14.8082$, and $G_{\text{eff}}^V = 15.5653$, in units of GPa. The two parts of the blue solid curve are determined by (14) and (16). jim2-PMW [NR]



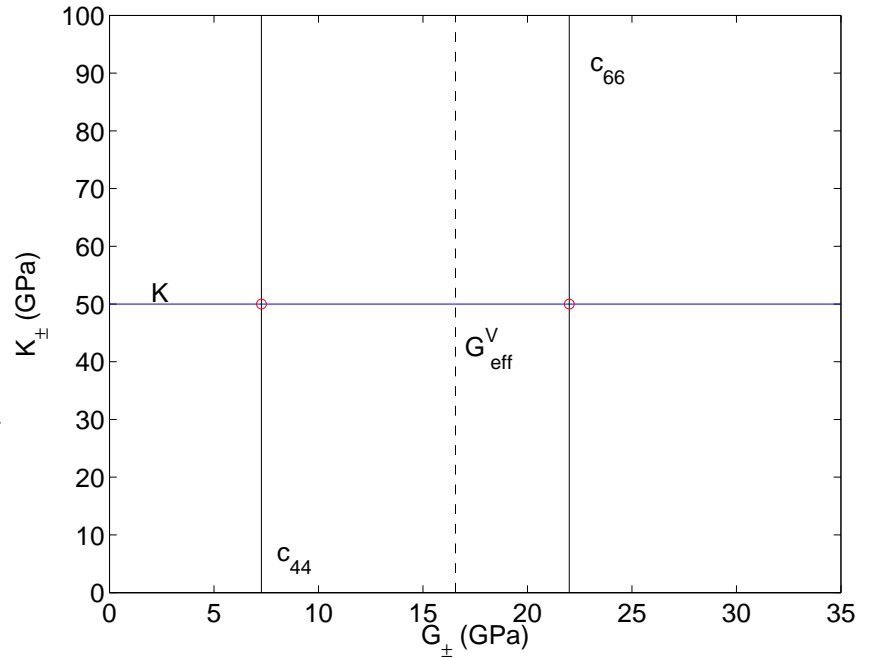
briefly discussed in Appendix A. Figure 3 [following some similar figures in Watt and Peselnick (1980)] shows how the parameter sets for the elastic comparison materials are determined. The allowed regions in Figure 3 are the bounded area in the upper right-hand corner, and the similarly bounded area in the lower left-hand corner. The red circles are therefore the points in the (G_{\pm}, K_{\pm}) -plane that produce the optimum bounds. It is clear that the value of G_{eff}^V plays a very dominant role in the structure of this Figure as the singularity in the blue solid curve occurs exactly at this value.

For the case of constant bulk modulus $K_n = K$, Figure 3 should be contrasted with Figure 4. Obviously, the structure is much simpler, as the singularities in (22) and (24) have disappeared through direct cancelation with the numerator. It is still the case however that the allowed regions in Figure 4 are the bounded areas in upper right-hand corner, and the lower left-hand corner. Again the red circles are the points in the (G_{\pm}, K_{\pm}) -plane that produce the optimum bounds. However, it is no longer clear from this Figure whether G_{eff}^V is playing any role in the analysis or not.

While attempting to find an answer to this question, the author has spent some effort manipulating the form of the equations for the shear modulus bounds and has found what may be a more enlightening form of these equations. (The derivation will not be given here as it is rather straightforward to find the result again, once the final expression is known.) The resulting simplified formula for the Peselnick-Meister-Watt bounds on overall shear modulus of a polycrystal of laminates when $K_n = K$ is:

$$\mu_{PM}^{\pm} = \left[\frac{1}{5} \left(\frac{1}{G_{\text{eff}}^V + \zeta_{\pm}} + \frac{2}{c_{44} + \zeta_{\pm}} + \frac{2}{c_{66} + \zeta_{\pm}} \right) \right]^{-1} - \zeta_{\pm}, \quad (13)$$

Figure 4: As in Figure 3 for the case of constant bulk modulus, in which case $K_V = K_R = K$, and $G_{\text{eff}}^V = G_{\text{eff}}^R$. Values of the constants entering the expressions (see Appendix A) are: $K = 50.0000$, $c_{44} = 7.2727$, $c_{66} = 22.0000$, $G_{\text{eff}}^V = 16.5546$, in units of GPa. `jim2-PMWconK` [NR]



where

$$\zeta_{\pm} = \frac{G_{\pm}}{6} \left(\frac{9K + 8G_{\pm}}{K + 2G_{\pm}} \right) \quad \text{with} \quad G_{\pm} = c_{44} \quad \text{or} \quad c_{66}. \quad (14)$$

Using standard methods, it is not hard to show that, if instead of optimum values of ζ_{\pm} , we use $\zeta_{\pm} = 0$ or ∞ , then (13) reduces to the formulas (8) and (5) for the correlated Reuss and Voigt bounds on the polycrystal's overall shear modulus.

We see that G_{eff}^V still plays a dominant role here — in the company of c_{44} and c_{66} — as one of the three values (after multiplication by 2) that are the shear eigenvalues of the elastic system. Furthermore, G_{eff}^V is determined for this case exactly by Eq. (6).

DISCUSSION

The results obtained so far show that, for the shear modulus G_{eff} of uniaxial shear for a transversely isotropic system, we have $2G_{\text{eff}}^V = \omega_+$ when the bulk modulus of the system is uniform. In this case, the quasi-shear eigenvector is exactly in the same direction as the uniaxial shear component, so the quantity $2G_{\text{eff}}^V$ — while more generally a strict upper bound on the eigenvalue ω_+ — is exactly equal to it in this special case. Thus, the uniaxial shear mode is in this instance an eigenvector of this system. This happens in particular when $K_n = K$ is a constant for random polycrystals of laminates. The simplified formula (13) for the bounds is therefore the main new result of this paper. When compared to (8), it is suggestive that some very simple forms for Hashin-Shtrikman bounds on shear can probably be found for many such polycrystalline systems, and especially so for granular laminates. The constant bulk modulus limit is a most convenient place to begin a search for such simplified expressions for the bounds.

Once these HS bounds are known, it is an elementary operational exercise to determine self-consistent (SC) estimates based just on the analytical form of the bounds. Monotonicity of the functional

$$M(\zeta) = \left[\frac{1}{5} \left(\frac{1}{G_{\text{eff}}^V + \zeta} + \frac{2}{c_{44} + \zeta} + \frac{2}{c_{66} + \zeta} \right) \right]^{-1} - \zeta, \quad (15)$$

appearing in (13), is easy to prove [see Berryman (1982)] for examples of such proofs), and furthermore $\zeta(K, G) = (G/6)(9K + 8G)/(K + 2G)$ is a monotonic functional of both arguments. These facts guarantee that there is a unique solution to the self-consistency relation

$$\mu_{SC} \equiv M(\zeta(K, \mu_{SC})), \quad (16)$$

and, furthermore, this solution always lies between the bounds. To provide an example, consider the case of Figure 4 when the volume fractions are both 50%. Then, $\mu_{44} = 7.2727$, $\mu_{66} = 22.0000$, $G_{\text{eff}} = 16.5546$, $\mu_{PM^-} = 13.1164$, $\mu_{PM^+} = 13.8659$, and $\mu_{SC} = 13.5537$. So the self-consistent estimate is not closely correlated with the value of G_{eff} , which is itself usually found outside the correlated bounds on μ . Figure 5 illustrates these results for the full range of volume fractions with the same choice of constituents.

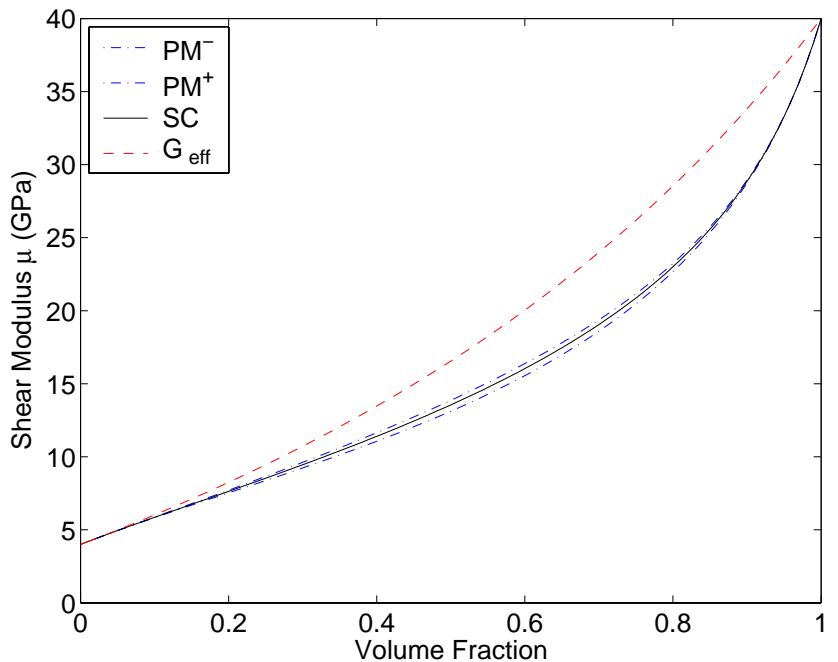


Figure 5: Comparison of the shear modulus estimates over all choices of volume fraction, for the same case considered in Figure 4.

`jim2-mucomparison` [NR]

The results in Fig. 5 show very clearly that self-consistent values fall between the bounds as expected, and that the bounds themselves are in any case very close together for this high contrast example. Thus, an exact result for shear modulus has not been found [so the analogy to Hill's formula (1) is not perfect]. Nevertheless, for most practical purposes, the results show that the predictions of the theory using such correlated bounds — and related self-consistent estimates — will often be as good as, or perhaps better than, the precision of experimental measurements. (Maximum error incurred by using the self-consistent estimate in the example

of Figure 5 is about 2%.) The value of G_{eff} , while playing an important role in the analysis, clearly should not be interpreted as the actual value of the effective overall shear modulus for the random polycrystal. G_{eff} does however contribute about 20% of the overall magnitude of the effective shear modulus.

In conclusion, we note that, applications of the analytical results presented here include benchmarking of numerical procedures used for studying elastic behavior of complex composites, as well as estimating coefficients needed in up-scaled equations for elasticity and/or poroelasticity of heterogeneous systems. In particular, up-scaling methods typically determine the form of the effective equations of motion, but most often do not provide any means (or at least any very useful means) of estimating/computing the elastic/poroelastic coefficients. The methods described here are therefore expected to be especially useful for earth sciences and oil reservoir engineering applications, as well as for obvious uses in the practice and theory of elastic composites and heterogeneous media.

APPENDIX A: PESELNICK-MEISTER-WATT BOUNDS FOR HEXAGONAL SYMMETRY

Hashin-Shtrikman-style bounds (Hashin and Shtrikman, 1962; 1963) on the bulk and shear moduli of isotropic random polycrystals composed of hexagonal grains have been derived by Peselnick and Meister (1965), with later corrections by Watt and Peselnick (1980) The main results are presented here using notation consistent with that of our text, in order to emphasize the connections to the analysis presented. To keep this summary brief, we will merely quote the results and refer the reader to the original papers for the derivations.

Parameters used to optimize the Hashin-Shtrikman bounds are K_{\pm} and G_{\pm} , which have the significance of being the bulk and shear moduli of two isotropic comparison materials. G_{+}, K_{+} are the values used in the formulas for the upper bounds, and G_{-}, K_{-} for the lower bounds. Formulas for the bounds are:

$$K_{PM}^{\pm} = K_{\pm} + \frac{K_V - K_{\pm}}{1 - 2\beta_{\pm}(G_{\text{eff}}^V - G_{\pm})}, \quad (17)$$

and

$$\mu_{PM}^{\pm} = G_{\pm} + \frac{B_2^{\pm}}{1 + 2\beta_{\pm}B_2^{\pm}}, \quad (18)$$

where

$$\alpha_{\pm} = \frac{-1}{K_{\pm} + 4G_{\pm}/3}, \quad \beta_{\pm} = \frac{2\alpha_{\pm}}{15} - \frac{1}{5G_{\pm}}, \quad \gamma_{\pm} = \frac{1}{9}(\alpha_{\pm} - 3\beta_{\pm}), \quad (19)$$

and

$$B_2^{\pm} = \frac{1}{5} \left[\frac{G_{\text{eff}}^V - G_{\pm}}{\mathcal{D}_{\pm}} + \frac{2(c_{44} - G_{\pm})}{1 - 2\beta_{\pm}(c_{44} - G_{\pm})} + \frac{2(c_{66} - G_{\pm})}{1 - 2\beta_{\pm}(c_{66} - G_{\pm})} \right], \quad (20)$$

with

$$\mathcal{D}_{\pm} = 1 - \beta_{\pm}(c_{11} + c_{12} + c_{33} - 3K_{\pm} - 2G_{\pm}) - 9\gamma_{\pm}(K_V - K_{\pm}). \quad (21)$$

Optimum values of the moduli for the comparison materials have been shown to be (in our notation)

$$K_- = \frac{K_V(G_{\text{eff}}^R - G_-)}{(G_{\text{eff}}^V - G_-)} \quad (22)$$

with

$$0 \leq G_- \leq \min(c_{44}, G_{\text{eff}}^R, c_{66}), \quad (23)$$

and

$$K_+ = \frac{K_V(G_+ - G_{\text{eff}}^R)}{(G_+ - G_{\text{eff}}^V)} \quad (24)$$

with

$$\max(c_{44}, G_{\text{eff}}^V, c_{66}) \leq G_+ \leq \infty. \quad (25)$$

Note that, when $G_- = 0$, $K_- = K_R$, because $K_R = K_V G_{\text{eff}}^R / G_{\text{eff}}^V$ from the product formulas (Berryman, 2004). Also, note that, if $K_n = K$ is constant, then $K_{\pm} = K_V = K_R = K$ for any choice of G_{\pm} , since then we also have that $G_{\text{eff}}^V = G_{\text{eff}}^R$.

For the laminated materials considered here, the minimum condition in (23) will never be satisfied by c_{66} except in the trivial case of constant shear modulus. Each of the other two arguments can possibly become the minimum under certain nontrivial circumstances. For the materials considered here, it follows from (7) that the maximum condition in (25) will always be uniquely satisfied by c_{66} , except again for the trivial case of constant shear modulus.

Peselnick and Meister (1965) had originally obtained all the results here except for the additional condition in (23) that permits c_{44} to be replaced in certain circumstances by G_{eff}^R . This new condition was added later by Watt and Peselnick (1980).

APPENDIX B: BOUNDS OF DEDERICHS AND ZELLER FOR MULTIPHASE MEDIA

One of the bounds of Dederichs and Zeller (1973) is based on the assumption that, inside each grain of a multiphase material, the distribution of different phases is independent of the shape of the grain, and also independent of the phases of contiguous grains. Grains are therefore assumed to be completely uncorrelated, both internally and externally. The results obtained for bulk modulus are:

$$K_{DZ}^{\pm} = \left[\sum_{n=1}^N \frac{f_n}{K_n + 4g_{\pm}/3} \right]^{-1} - 4g_{\pm}/3, \quad (26)$$

where

$$g_- = c_{44} \quad \text{and} \quad g_+ = c_{66} \quad (27)$$

in our present notation [see eq. (7)]. Similarly, for shear modulus, we have

$$\mu_{DZ}^{\pm} = \left[\sum_{n=1}^N \frac{f_n}{\mu_n + \zeta_{\pm}} \right]^{-1} - \zeta_{\pm}, \quad (28)$$

where

$$\zeta_- = \frac{c_{44} \langle 9/\mu + 8/K \rangle}{6 \langle 1/\mu + 2/K \rangle} = \frac{g_-}{6} \left(\frac{9 \langle 1/K \rangle^{-1} + 8g_-}{\langle 1/K \rangle^{-1} + 2g_-} \right) \quad (29)$$

and

$$\zeta_+ = \frac{c_{66} \langle 9K + 8\mu \rangle}{6 \langle K + 2\mu \rangle} = \frac{g_+}{6} \left(\frac{9 \langle K \rangle + 8g_+}{\langle K \rangle + 2g_+} \right). \quad (30)$$

These bounds on bulk modulus are the same as those of Beran and Molyneux (1966) and Miller (1969). The upper bound on shear modulus is the same as that of McCoy (1970) and Silnutzer (1972). Because of the simple functional form of both sets of bounds, it is easy to show (Berryman, 1982) that they are always at least as restrictive as — and, for nonnegligible volume fractions of inclusions, normally a significant improvement upon — the Hashin-Shtrikman bounds (Hashin and Shtrikman, 1962; 1963).

We chose to consider these bounds here because they depend only on simple volume averages of the constituent elastic constants, and also because they show — by way of contrast to the other bounds (see Figures 1 and 2) — that it does indeed matter what assumptions are made about the microstructure of the composite.

REFERENCES

- Avellaneda, M., 1987, Iterated homogenization, differential effective medium theory and applications: *Commun. Pure Appl. Math.*, **40**, 527–554.
- Backus, G. E., 1962, Long-wave elastic anisotropy produced by horizontal layering: *J. Geophys. Res.*, **67**, 4427–4440.
- Berryman, J. G., 1980, Long-wavelength propagation in composite elastic media II. Spherical inclusions: *J. Acoust. Soc. Am.*, **68**, 1809–1819.
- Berryman, J. G., 1980, Long-wavelength propagation in composite elastic media II. Ellipsoidal inclusions: *J. Acoust. Soc. Am.*, **68**, 1820–1831.
- Berryman, J. G., 1982, Effective medium theory for elastic composites: in *Elastic Wave Scattering and Propagation*, edited by V. K. Varadan and V. V. Varadan, (Ann Arbor Science, Ann Arbor, Michigan), pp. 111–129.

- Berryman, J. G., 1994, Role of porosity in estimates of composite elastic constants: *Trans. ASME J. Energy Resources Tech.*, **116**, 87–96.
- Berryman, J. G., 2004a, Poroelastic shear modulus dependence on pore-fluid properties arising in a model of thin isotropic layers: *Geophys. J. Int.*, **157**, pp. 415–425.
- Berryman, J. G., 2004b, Bounds on elastic constants of random polycrystals of laminates: in press, to appear in *J. Appl. Phys.*
- Bruggeman, D. A. G., 1935, Berechnung verschiedener physikalischer Konstanten von heterogenen Substanzen: I. Dielectricitätskonstanten und Leitfähigkeiten der Mischkörper aus Isotropen Substanzen: *Ann. Phys. (Leipzig)*, **24**, 636–679.
- Drugan, W. J., and Willis, J. R., 1996, A micromechanics-based nonlocal constitutive equation and estimates of representative volume element size for elastic composites: *J. Mech. Phys. Solids*, **44**, 497–524.
- Einstein, A., 1905, Eine neue Bestimmung der Moleküldimensionen: *Ann. Phys.*, **19**, 289–306.
- Gibiansky, L. V., and Milton, G. W., 1993, On the effective viscoelastic moduli of two-phase media. I. Rigorous bounds on the complex bulk modulus: *Proc. Roy. Soc. London A*, **440**, 163–188.
- Gibiansky, L. V., Milton, G. W., and Berryman, J. G., 1999, On the effective viscoelastic moduli of two-phase media. III. Rigorous bounds on the complex shear modulus in two dimensions: *Proc. Roy. Soc. London A*, **455**, 2117–2149.
- Hashin, Z., and Shtrikman, S., 1961, Note on a variational approach to the theory of composite elastic materials: *J. Franklin Inst.*, **271**, 336–341.
- Hashin, Z., and Shtrikman, S., 1962, On some variational principles in anisotropic and nonhomogeneous elasticity: *J. Mech. Phys. Solids*, **10**, 335–342.
- Hashin, Z., and Shtrikman, S., 1963, A variational approach to the theory of the elastic behavior of multiphase materials: *J. Mech. Phys. Solids*, **11**, 127–140.
- Hill, R., 1952, Elastic properties of reinforced solids: Some theoretical principles: *Proc. Phys. Soc. London A*, **65**, 349–354.
- Maxwell, J. C., 1873, *Treatise on Electricity and Magnetism*: Clarendon Press, Oxford, England.
- Milton, G. W., 1981, Bounds on the electromagnetic, elastic, and other properties of two-component composites: *Phys. Rev. Lett.*, **46**, 542–545.
- Milton, G. W., 1985, The coherent potential approximation is a realizable effective medium scheme: *Comm. Math. Phys.*, **99**, 463–500.

- Milton, G. W., and Berryman, J. G., 1997, On the effective viscoelastic moduli of two-phase media. II. Rigorous bounds on the complex shear modulus in three dimensions: *Proc. Roy. Soc. London A*, **453**, 1849–1880.
- Milton, G. W., 2002, *The Theory of Composites*: Cambridge, University Press, Cambridge, UK, pp. 77-78, 163, 457–498.
- Norris, A. N., 1985, A differential scheme for the effective moduli of composites: *Mech. Mater.*, **4**, 1–16.
- Peselnick, L., and Meister, R., 1965, Variational method of determining effective moduli of polycrystals: (A) Hexagonal symmetry, (B) trigonal symmetry: *J. Appl. Phys.*, **36**, 2879–2884.
- Postma, G. W., 1955, Wave propagation in a stratified medium: *Geophysics*, **20**, 780–806.
- Rayleigh, L., 1892, On the influence of obstacles arranged in a rectangular order upon the properties of medium: *Phil. Mag.*, **34**, 481–502.
- Reuss, A., 1929, Berechnung der Fließgrenze von Mischkristallen auf Grund der Plastizitätsbedingung für Einkristalle: *Z. Angew. Math. Mech.*, **9**, 49–58.
- Voigt, W., 1928, *Lehrbuch der Kristallphysik*: Teubner, Leipzig, 964 pp.
- Walpole, L. J., 1966, On bounds for the overall elastic moduli of inhomogeneous systems I.: *J. Mech. Phys. Solids*, **14**, 151–162.
- Watt, J. P., and Peselnick, L., 1980, Clarification of the Hashin-Shtrikman bounds on the effective elastic moduli of polycrystals with hexagonal, trigonal, and tetragonal symmetries: *J. Appl. Phys.*, **51**, 1525–1531.

Short Note

Fault tolerant parallel SEPlib

Robert G. Clapp¹

INTRODUCTION

In the past few years, several papers have been written dealing with SEP's attempts to run on Beowulf style clusters. The initial work involved the use of the Open Multi-Processing (OMP) library (Biondi et al., 1999). As we increased the number of nodes at SEP, we switched to, or added on support for, MPI to many of our programs (Sava and Clapp, 2002). This proved to be a somewhat successful strategy with a few notable drawbacks. First, it required each program to include MPI specific coding. Clapp (2003b) described an effort to minimize the repetitive portions by introducing a library that did MPI-like operations on SEPlib files.

Another problem was that we relied on mounting, or in our case automounting, of disks. Each process would open the history file (and in most cases the binary file) of each input SEPlib file. This posed two problems. First it doesn't scale well to a large number of nodes (100 processes opening up the same file will often fail). Second, automount isn't particularly stable on Linux. Clapp (2004a) was an attempt to address this problem. It worked in a master-slave manner. The master process would read a sepfile and pass along its description and contents to worker nodes. In addition, it introduced the concept of a distributed SEPlib dataset. A SEPlib file could be broken into sections along one of its axes and various parts could sit on different nodes. It provided routines to partition and collect the distributed dataset. Unfortunately this left one glaring problem, node instability. When running a MPI program if a node becomes inoperable the entire job will die either immediately or at the first communication attempt. The solution, to add to each application the ability to 'restart' itself can be extremely challenging, especially in large, global inversion applications (Sava and Biondi, 2003; Clapp, 2003a).

In this paper I describe a library, written in Python, that allows auto-parallelization with a high-level of fault tolerance for almost any SEPlib program. Instead of handling parallelization within a compiled code at the library level, the parallelization is done at the script level which sits on top of the executables. The Python library distributes and collects the datasets, keeps track of what portion of the parallel job are done, and monitors the state of the nodes. The distribution and collection are done through MPI but individual jobs are all serial codes. The

¹email: bob@sep.stanford.eda

code is written using Python's object oriented capabilities so it is easily expandable. A parallel job is described by a series of files and a series of tasks.

PARALLEL JOB

The controlling process for a parallel job is the `SEP.parjob` object. I will begin by going over the objects it inherits properties from. Then I will discuss its initialization and finally go over its execution sequence.

Inheritance

A parallel job is a Python class object that inherits from three other classes. The first is the `SEP.status.sep_status` class. At the most basic level this class simply reads and writes to an ASCII text file. This text file is what keeps track of the progress for the job. Each line of the status file is a ':' separated list. The first item is the text descriptor, the *jobid*, for each task. The second item is the status of the job (`todo`, `sent`, `running`, `finished`, `collected`). The third is what machine (if any) the job is running on/ran on. The final two are progress indicators for the job (to enable restarting), and the number of times the job has failed. In the course of a parallel job, several different processes will need to read and/or write to the status file. In order to avoid clobbering of the file contents, each process can get an exclusive lock on the status file.

The parallel job class also inherits from a class that handles socket communication `sep_socket.sep_server`. The socket class knows how to find a free socket number, and how to run a socket server that takes actions based on simple string messages. Finally it inherits from a class, `SEP.par_log.jobs`, that stores the stdout and stderr of the various jobs.

Initialization

There are two required parameters and several optional parameters to initialize a parallel job. The first required parameter is (`sect_pars`) a Python dictionary that links the *jobid* mentioned before, with a parameter object `SEP.par.sep_pars`. This class knows how to read, write, add, and return a list of parameters. An example of where a job might need different parameters is if you are creating an output cube that scans over a parameter space. The second required parameter is a dictionary of parallel files that are needed for the job. A dictionary rather than a list is used to enable a parallel job to be used in inversion. When inverting the model and data vectors will change depending on the inversion process. `key` in the dictionary enables an easy way to locate (and possibly change Clapp (2004b)) the parallel file. The `value` in the dictionary is a parallel file object discussed below.

Below is a list of some of the useful optional parameters:

program The serial code that you want to run on each node. This is an optional, rather

than required parameter, because it is possible, and in some cases useful, to extend the `SEP.parjob.parjob` class's job creation mechanism.

restart Whether or not we are restarting a job. When restarting the status file will be read instead of created.

global_pars A list of of parameters to run with every job, again a `SEP.par.sep_par` object.

attempts The number of attempts (defaulted to 2) to attempt to start a job (on different nodes) before failing.

restart_com A parameter that needs to be added to the calling sequence when restarting a job.

mfile The machine file to read the available nodes from (in the same status convention as an MPI machine file. Defaults to a file name `mfile`.

njobs The maximum number of jobs to run simultaneously. Defaults to the number of processors described in `mfile`.

verb The level of verbosity.

The initialization creates a machine class object (also inherited from the status class). This object keeps track of the available machines. An obvious extension of this class is discussed in the future work section.

Running

When a parallel job is started it first checks the status of all of the nodes, removing any that aren't functioning properly from its potential list. A second thread is then created.

This new thread handles job distribution. It requests a list of free nodes from the machine class. It then finds the list of the jobs that haven't been completed. It matches the job to the available nodes and requests from the parallel file object a SEPlib tag for a version, or portion, of the parallel file given the requestion section and node. It then builds a command string for the job. In addition to a `rsh` call to the machine and the program name the command string includes the global parameters and section parameters discussed above along with information on how to communicate with the server process. The job and machine's status files are then updated to note what job was sent to what node.

These jobs are started by a series of forked processes. These forked processes will run the job and record in the status file if they ran to completion or failed with an error. These processes will then exit. The job creation thread will run in a loop, checking for available machines and occasionally (every 5 minutes) checking to see if a node has become inaccessible.

The original thread starts an `INET` server socket. It receives communication, in the form of small ASCII strings, from the slave processes. It recognize four different messages: job

started, job finished, error in the job, and progress of the job. How the serial code sends these messages is discussed later. If the socket server receives a start message it changes the status of the job from `sent` to `running`. A progress message is added in status file. A finish message changes the job status to `finished` and marks the node as available. A failure message results in the node status being checked, the job being re-listed as ‘todo’, and an updating of an internal list to insure that the same job is not sent to the same node. In addition the last 100 lines of stdout and stderr of the failed job are sent to stdout. All messages are also recorded in each parallel file’s status file.

When the job creation thread notes that all jobs have run to completion it exits. Finally, when the socket server notes that all jobs have been finished it loops through all of the parallel files. Each output file is combined, and the job is exited.

PARALLEL FILE

The key building block for a parallel job is the parallel file.

Initialization

A parallel file is initialized by a series of required and optional parameters. The following are all required to initialize a parallel file.

name The name of the sepfile.

tag The tag used by the serial program (e.g. `<`, `>`, `tag2=`).

usage How the file is to be used as input (`INPUT`) or output (`OUTPUT`).

isect_dict A python dictionary object that links the job descriptor with the section number it corresponds to.

In addition there several optional parameters available.

type The distribution method for the file. Currently three options are available:

`BLOCK`, different elements of the distributed axis are grouped together;

`SPREAD`, elements along the axis are distributing in a round robin fashion; or

`COPY`, the file is shared among all of the sections. If input, the file will be copied to all the nodes. If output, the sectioned files were added together to form the final output. The file will also be shared among all processes running on the node. In order to avoid multiple processes overwriting themselves a simple file locking mechanism is available (see the programming section).

axis The axis the data is distributing along. Required for all distribution methods except `COPY`.

reuse_par A parameter string to include when the file is being reused. This is only applicable in the case of `COPY` distribution type.

Functions

A parallel file is also derived from the status object. The `sent`, `is running`, `finished`, or `failed` messages received and recorded by the parallel job status file are also recorded in the parallel file status file. In addition the parallel job object has the ability to distribute and collect itself. Both of the operations are done through MPI using the external SEPlib function `Partition` and `Collect` programs.

PROGRAM FUNCTIONS

There are two required and three optional function available to the programmer. The required functions go near the beginning and ending of the program. The first, `sep_begin_prog`, tells the server that the program has started successfully. It should be used when it is safe to start another instance of the program on the same node. This latter requirement is important when sharing an output space (`COPY`) on a node. If you are adding to the output space you need insure that the output file has been created by the first instance of the program. The other required function is `sep_end_prog`. This should be used after all of the output files have been completely written to. The server interprets as a sign of completion for the job.

The `sep_progress` function enables effective job restarting. The programmer can use this function to signify a checkpoint in the code. When restarting a job, both the restart flag and the last progress message will be passed as arguments for the restarting job. In the case when you sharing an output space, you should use this function whenever you write to the shared file. The final two functions are when you are sharing an output space. The `sep_open_lock(tag)` locks (if already locked waits for the file to become available) a seplib tag. The `sep_close_lock(tag)` functions frees a tag so another process can safely read or write to it. All of these commands perform no function when not a portion of a parallel job.

FUTURE WORK

There are five additional features that would be useful to add to the parallel infrastructure. These changes need to be made to the dataset collection, the machine selection, and the file distribution options.

Currently datasets are collected only at the completion of the job. It would be useful to be able to concatenate at various time intervals. This would make QCing easier and make the job less susceptible to disks going bad, requiring the rerunning of portions of the job. The

problem with implementing this feature is when the output file is of the `COPY` type. The file is being continually updated by processes running on the node. In order to get an accurate picture of what is collected all writing to the node would have to be frozen and/or insure that no processes is running on the node. The second change is in the actual methodology of the collection. Currently a binary tree sum is done using the `MPI_collect` routine. For large datasets this approach quickly swamps the network switch. A more efficient collection method should be implemented.

Another feature would be to expand on the current `COPY`, `BLOCK`, and `SPREAD` methods. It would be useful to be able to distribute over multiple axes, and to have the distributed portions overlap (patching).

Finally, a couple changes to the way the machines are chosen needs to be made. Instead of the list of available machines being read from a file it would be useful to have it read from a global server. In this way you could have dynamic control over the number of nodes a job was running on. In addition in some special cases it is necessary to guarantee that jobs run on specific nodes. Wave equation migration velocity analysis (Sava and Biondi, 2003) is an example of this. The downward continued wave-field is pre-stored on the nodes. You must be able to insure that each frequency is sent to the node that contains the wave-field at that frequency.

The object oriented way that the library was implemented makes these changes relatively easy. For example, to insure that a specific job is spent to a specific node would involve inheriting the parallel job class, and overriding the routine that matches jobs with available machines.

CONCLUSION

A fault tolerant, parallel job environment is created within python. Serial codes can be in parallel with minimal changes. The object oriented nature of the library makes it easily extendable to solve almost any coarse grained problem.

REFERENCES

- Biondi, B., Clapp, R. G., and Rickett, J., 1999, Testing linux multiprocessors for seismic imaging: SEP-102, 235-248.
- Clapp, M. L., 2003a, Velocity sensitivity of subsalt imaging through regularized inversion: SEP-114, 57-66.
- Clapp, R. G., 2003b, MPI in SEPlib: SEP-113, 491-500.
- Clapp, R. G., 2004a, Parallel datasets in seplib: SEP-115, 479-488.
- Clapp, R. G., 2004b, A python solver for out of core, fault tolerant inversion: SEP-117.

Sava, P., and Biondi, B., 2003, Wave-equation mva: Born rytov and beyond: SEP-**114**, 83–94.

Sava, P., and Clapp, R. G., 2002, Wei: a Wave-Equation Imaging library: SEP-**111**, 383–395.

APPENDIX A

The following is a simple example parallel job. In this case a file is split along the third axis and the SEPlib program `Scale` is run on each section, then the files combined to form the final output.

```
njobs =4          #the number of jobs we are going to break the problem into
isect_dict={}    #an empty dictionary object relating the section and jobid
par_list={}     #an empty dictionary object relating parameters and jobid
for i in range(njobs):          #loop over the jobs
    isect_dict[str(i)]=ia       #form the jobid:isect dictionary ('1':1)
    par_list[str(i)]=SEP.par.sep_pars(name=str(i)) #form an empty parameter list

file={}         #the files dictionary
#create the input: first command line is the name of the file, referenced with<
file["input"]=SEP.parfile.parfile(name=sys.argv[1],
    tag="<",isect_dict=isect_dict, usage="INPUT",axis=3,verb=verb)
#create the output parallel file object
file["output"]=SEP.parfile.parfile(name=sys.argv[2],tag=">",
isect_dict=isect_dict, usage="OUTPUT",axis=3,verb=verb)
#create the parallel job
test1=SEP.parjob.parjob(files=file,sect_pars=par_list,program="Scale",
    log_level=2,verb=verb,njobs=njobs)
#run the job
test1.run_job()
#clean: remove all the temporary and status files
test1.clean()
```

Short Note

A Python solver for out-of-core, fault tolerant inversion

Robert G. Clapp¹

INTRODUCTION

In the last ten years SEP has seen a progression in the way it does inversion. Earlier version of Claerbout (1999) coded the conjugate gradient loop within a FORTRAN 77 main program. Later, with the adoption of FORTRAN 90, the solver became a subroutine, operators were in modules, and vectors were 1-D arrays of floats (and later complex). This solution proved effective for a large range of problems. It was an ineffective for other problems and resulted in several additional FORTRAN 90 packages. To handle non-linear problems Clapp and Brown (1999) and Guitton (2000) introduced non-linear solvers. To handle problems that could not fit within core memory, Sava (2001) introduced a out of core solver. All of these packages have been used extensively at SEP over the years, but they all suffer some weaknesses that are related to coding in Fortran 90.

During the same period we have seen people in the geophysical community take a more object-oriented approach to the problem than FORTRAN 90 allows. Deng et al. (1996), Gockenbach and Symes (1999), and Harlan (2004b) used C++ as their controlling inversion framework. Schwab and Schroeder (1997); Schwab (1998) and Harlan (2004b) designed inversion systems within Java. For at least Deng et al. (1996) and Gockenbach and Symes (1999), memory limits was one of the reasons for the object-oriented language choice.

The size and complexity of the inversion problems at SEP has dramatically increased. These problems now involve operators that can take days to weeks to run (Sava and Biondi, 2003; Clapp, 2003b) and can involve multiple instances of complex operations (Clapp, 2003a). Running these problems on Beowulf clusters poses a problem. The odds of a multi-week job running without a node failing is low. In addition, multiple instances of the same, or similar operator, is problematic (increasing with the complexity of the problem) in FORTRAN 90.

In this paper I discuss a new solution to the instability and complex problem description. I describe a Python inversion library which uses abstract vector and operator descriptions. From these abstract classes I derive specific classes to handle out-of-core problems. Operators become wrappers around SEPlib programs and vectors wrappers around SEPlib files. Deng et al. (1996) is a similar solution using C++ and SU. The difference is my Python library is built

¹email: bob@sep.stanford.eda

upon the framework described in Clapp (2004), which handles fault tolerance within parallel programs, and provides the building blocks for easy restarting of inversions.

I will begin by discussing the abstract vector and object design. I will then discuss the specific cases of out-of-core vectors and operators. I will conclude with a simple example of using the library.

ABSTRACT CLASSES

A linear inverse system general involves three basic classes. The vector class is a collector class for a series of numbers. The operator class is some type of mapping between vector objects. The solver class does the actual inversion by calling the operator objects given an initial model and data vector.

Vectors and super vectors

Vectors are composed of two parts: an array of numbers and a description of the space the reside in. The space they reside in is arbitrary but all vectors must be able to perform some basic mathematical operations. They must be able to be scaled by a number, able to add, multiply, and take the dot product of themselves and another vector in the same space. In addition, they must be able to perform some operations related to the space they reside in. They need to be able clone themselves and they need to be able to check whether or not another vector resides in the same space.

For coding simplicity I expanded this minimal set. Each derived vector class must define the following functions.

clone Make a copy of both the space the vector resides in and the vector values.

clone_space Make a copy of just the space the vector resides in.

zero Fill the vector values with zeros.

random Fill the vector values with random numbers.

scale Scale the vector by a number.

add Add the vector to another vector.

scale_add Add the vector to another vector multiplied by a scalar.

scale_addscale Scale the vector and add it to another vector scaled by some scalar.

dot Return the dot product of the vector with another vector.

load Given a vector space, read/or create the vector values.

size A rudimentary method to check vector space similarity.

clean Remove all remnants of the vector.

In addition to the `SEP.vector.vector` described above, an additional arbitrary class is necessary. This class, `SEP.vector.super`, is collection of vectors. Take for example a regularized inversion problem,

$$\begin{aligned} \mathbf{d} &\approx \mathbf{Lm} \\ \mathbf{0} &\approx \epsilon \mathbf{Am}, \end{aligned} \tag{1}$$

where \mathbf{L} relates the data \mathbf{d} and the \mathbf{m} , \mathbf{A} is a regularization operator, $\mathbf{0}$ is a vector filled with 0s existing in the range space of \mathbf{A} , and ϵ is some twiddle parameter. A super vector would be the combination of \mathbf{d} and $\mathbf{0}$.

Operators and combination operators

When it comes to writing an object oriented conjugate gradient based inversion library there are two schools of thought. One is a Bayesian approach that correlates vectors with their decorrelators. In the Bayesian approach, Harlan (2004b,a) being one example, an inverse covariance function is associated with each vector. The approach taken in this library, and the approach taken by Gockenbach and Symes (1999) among others, think more in terms of operators. Operators know the space that their domain and range vectors reside in. For this library I took the latter approach. My decision was based more on code complexity issue more than anything else. When building complex inversion operators, the programmer has to be much more careful if the component operators do not know the space of their domain and range vectors.

The abstract class `SEP.operator.operator` is initialized with a string descriptor, domain vector, and a range vectors. The space these vectors exist in are stored in the operator. The operator has several additional functions.

init_op(restart) Initialize the operator.

job_desc(iter) Return an ASCII string describing the operator given the current iteration. This will be used to keep track of the progress of the inversion.

forward_op(model,data,add,restart) Run the forward operation possibly by adding to the data, and with the ability to signify a restart of the operation.

adjoint_op(model,data,add,restart) Run the adjoint operation possibly by adding to the model, and with the ability to signify a restart of the operation.

check_operator(domain,range) A function to check to make sure the domain and range vector conform to the domain and range vectors with which the operator was initialized.

forward(domain,range,status,iter,add,restart) A wrapper for running the forward operation. The additional status and iter parameters are used to record the starting and finished of forward operation to enable restarting.

adjoint(domain,range,status,iter,add,restart) The same idea as the forward function, this time for wrapping the adjoint operation.

To build more complex operations there are two component operator classes `SEP.vector.chain` and `SEP.vector.array`. Both of the complex operators are initialized by a string descriptor and an array of operators. The `SEP.vector.chain` chains two operators, an example is the preconditioning problem,

$$\begin{aligned} \mathbf{d} &\approx \mathbf{LSp} \\ \mathbf{0} &\approx \epsilon \mathbf{p}, \end{aligned} \quad (2)$$

where \mathbf{S} is the preconditioning operator and \mathbf{p} is a vector in the domain of \mathbf{S} . In this case `SEP.vector.chain` would be formed from \mathbf{L} and \mathbf{S} . A condition of forming this operator is that the range vector of operator i must exist in the same space as the domain vector of $i+1$. When this operator is initialized it will automatically create all of the intermediate spaces. The other class, `SEP.vector.array` creates a new operator which is a matrix of existing operators. For examples we can think of the regularization inverse problem in terms of the matrices,

$$\begin{pmatrix} \mathbf{d} \\ \mathbf{0} \end{pmatrix} = \begin{pmatrix} \mathbf{L} \\ \epsilon \mathbf{A} \end{pmatrix} (\mathbf{m}). \quad (3)$$

The `SEP.vector.array` is initialized by the array of operators and the number of collums and rows in the new array operator. In forming the operator the library makes sure that all of the domain and range vectors make sense (for the regularization problem the domain of \mathbf{L} and \mathbf{A} must be the same. From these two building blocks any inverse problem can be described.

Solver

With the ease in forming complex operators, the solver becomes a rather trivial code. All of the linear solvers are derived from a basic `SEP.solver.solver` class. This class is initialized with a model vector, residual vector, an operator, a step function, the number of iterations to run, and optional verbosity flag, and whether or not the job is being restarted. The initialization process is limited to first cloning model vector and the residual vector to form the gradient and the vector resulting from \mathbf{Lg} . It then initializes the step function, calculates and stores (or in the case of restarts, reads) the tasks it needs to perform. Taking a linear step becomes the following trivial code fragment.

```
def step(self, iter):
    self.op.adjoint(self.g, self.rr, self.status, iter)
    self.op.forward(self.g, self.gg, self.status, iter)
    self.status.update_status(str(iter)+".step", ["started"])
```

```

if not self.stepper.step(self.x,self.g,self.rr,self.gg): return None
self.status.update_status(str(iter)+".step",["finished"])
return 1

```

Three solvers are derived from this base class: `SEP.solver.smp`, `SEP.solver.reg`, and `SEP.solver.prec`. These classes simply form the objects needed by the solver class.

OUT-OF-CORE EXTENSION

The vector and operator classes described above were extended to perform an out-of-core inversion.

Vector

From the `SEP.vector.vector` class, and a class that knows how to read SEPlib description files (`SEP.file.sep_file`), the `SEP.sep_vector.sfloat` and `SEP.sep_vector.scmplx` were created. These classes use the SEPlib program `Math` to do the required vector operation. The space cloning and check is done by accessing functions derived from `SEP.file.sep_file`.

Operator

Out of core operations are done by the `SEP.operator.oc`. This class inherits from both the `SEP.operator.operator` class and `SEP.operator.run_oc`. The `SEP.operator.run_oc` class handles building the command line. The class has no required options but several optional arguments.

pars A `SEP.par.sep_pars` object containing the list of command line arguments to run with operator call.

add_com The argument to add to the function call when adding (defaults to `add=y`).

restart_com The argument to add to the function call when restarting.

adjoint_com The argument to add to the function call when running the adjoint (defaults to `adj=y`)

data_tag The tag associated with the data (defaults to `data=`)

model_tag The tag associated with the model (defaults to `model=`)

The `SEP.operator.oc` is initialized by the name of the program to run and a domain and range vectors of the type `sep_vector`, and arbitrary additional arguments. The additional arguments are passed to initialize the `SEP.operator.oc_run`. The `adjoint_op` and `forward_op` use the `SEP.operator.oc_run` class to build the commands string and then executes the program.

Parallel operator

To understand this section it useful to refer to Clapp (2004). If an operator is in fact a parallel operator then the `SEP.operator.oc_par` class should be used. This class inherits from the `SEP.operator.oc`. The parallel operator is initialized with a parallel job object. It expects the domain and range vectors to have been specified in the job creation with the keys 'domain' and 'range'. The forward and adjoint operation function are defined in the same manner described above with the exception that domain and range vectors are turned into `parfile` objects and running the job involves executing `parjob.run`.

EXAMPLE

This example is taken from Claerbout (1999) and is completely inappropriate for an out-of-core solver. It is a simple 1-D interpolation problem that takes a second to run on a modern computer and takes 5 minutes to run out-of-core. I am using it because of the simplicity of the concepts. We begin by grabbing all of the command line arguments and checking to make sure `data` and `model` are specified.

```
args=SEP.par.sep_args() #get arguments
dname=args.par("data",error=1)
mname=args.par("model",error=1)
```

We then create the data and model float vectors. In the case of the data is read from a file and the model is defined.

```
data =SEP.sep_vector.sfloat(tag=dname)
model=SEP.sep_vector.sfloat(name=mname)
model.set_axis(200,0.,.4)
```

We then write out the description of the model to disk and zero the file.

```
model.write_file()
model.zero()
```

Our data fitting operator is simple linear interpolation. It takes the coordinates of the data as input and we direct the stdout to `/dev/null`.

```
interp_args=SEP.par.sep_pars(name="interp")
interp_args.add_string("coord=coord.H")
interp_args.add_param(">", "/dev/null")
```

We create the argument list for the preconditioner. In this case we just need to direct stdout to `/dev/null` and specify the type of filter.

```
precpars=SEP.par.sep_pars(name="devnull")
precpars.add_param("filter",2)0
precpars.add_param(">", "/dev/null")0
```

Next we create our operator objects. In both cases the domain vector is the model. In the case of the interpolation operator the range is the data. For the preconditioning the range is also described by the model space.

```
interp=SEP.operator.oc("Interpl.x",model,data,pars=interp_args)
prec=SEP.operator.oc("prec.x",model,model,pars=precpars)
```

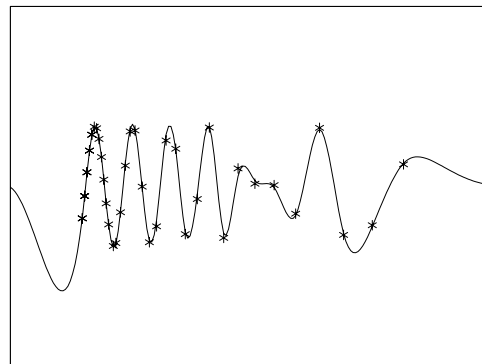
We create our step function.

```
step=SEP.cgstep.cgstep("matcg")
```

Finally we create our solver object and iterate for 20 iterations. Figure 1 shows the result of the inversion. The '*' are the known data and the line is the estimated curve.

Figure 1: A simple linear interpolation result using the out-of-core library. The '*' are the known data and the line is the estimated curve.

`bob2-inverse` [CR]



```
solver=SEP.solver.prec("interp1d",model,data,interp,prec,step,20,.1,verb=0)
if not solver.solve():
    SEP.util.err("Trouble iterating")
```

CONCLUSION

Fortran 90 is ill-suited for handling complex inversion problems and dealing with hardware instability for multi-week jobs. Using Python and treating programs as operators offers an attractive alternative to completely rewriting code.

REFERENCES

- Claerbout, J., 1999, Geophysical estimation by example: Environmental soundings image enhancement: Stanford Exploration Project, <http://sepwww.stanford.edu/sep/prof/>.
- Clapp, R. G., and Brown, M., 1999, Applying SEP's latest tricks to the multiple suppression problem: SEP-102, 91-100.
- Clapp, M. L., 2003a, Directions in 3-D imaging - Strike, dip, both?: SEP-113, 363-368.
- Clapp, M. L., 2003b, Velocity sensitivity of subsalt imaging through regularized inversion: SEP-114, 57-66.
- Clapp, R. G., 2004, Fault tolerant parallel SEPlib: SEP-117.
- Deng, H. L., Gouveia, W., and Scales, J. A., 1996, The cwp object-oriented optimization library: http://www.cwp.mines.edu/html_reports/coool/main.html.
- Gockenbach, M. S., and Symes, W. W., 1999, The hilbert class library: <http://www.trip.caam.rice.edu/txt/hcldoc/html/index.html>.
- Guitton, A., 2000, Implementation of a nonlinear solver for minimizing the Huber norm: SEP-103, 281-289.
- Harlan, W. S., 2004a, C++ implementation of gauss-newton and conjugate-gradients optimization: http://billharlan.com/pub/code/conjugate_gradients/.
- Harlan, W. S., 2004b, Gauss-newton and conjugate-gradient optimization: <http://billharlan.com/pub/code/inv/>.
- Sava, P., and Biondi, B., 2003, Wave-equation mva: Born rytov and beyond: SEP-114, 83-94.
- Sava, P., 2001, oclib: An out-of-core optimization library: SEP-108, 199-224.
- Schwab, M., and Schroeder, J., 1997, A seismic inversion library in Java: SEP-94, 363-381.
- Schwab, M., 1998, Enhancement of discontinuities in seismic 3-D images using a Java estimation library: Ph.D. thesis, Stanford University.

Chapter 7

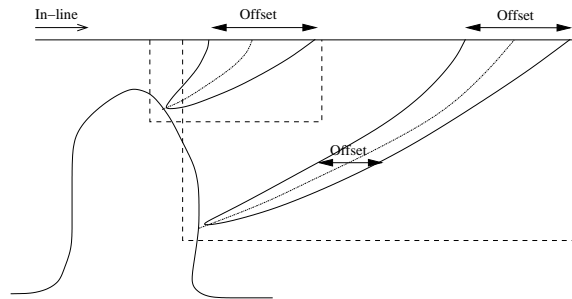
Efficient wavefield-continuation methods for prestack migration

Wavefield-continuation methods can be more accurate for 3-D prestack migration than methods based on the Kirchhoff integral. Their computational cost is the main hurdle that discourages the usage of wavefield methods in a majority of the imaging project. Wavefield-propagation algorithms are the most efficient when the computational grid is regular, and it has an horizontal extent similar to the horizontal coverage of the recorded data that are being propagated. The first, but not the most challenging, difficulty to overcome is that realistic 3-D data acquisition geometries are not regular (Chapter 1). The data geometry must be thus regularized before migration by applying a data-regularization algorithm, such as the methods described in Chapter 9, or methods that achieve similar results.

Wavefield-continuation methods can be extremely inefficient when there is a mismatch between the geometry of the recorded data and the geometry of the computational grid that the imaging algorithm requires. This problem is difficult to avoid when shot-gather migration is applied, as described in Chapter 4, in particular when the data are narrow-azimuth, such as marine streamer data. The sketch shown in Figure 7.1 illustrates the challenges faced by shot-gather migration when imaging deep and steeply dipping targets. It represents the geometry of the prestack imaging process for two targets, one shallow and the other deep. Each threesome of rays corresponds to the propagation paths for the events recorded at zero and maximum offset. The dashed boxes show the boundary of the computational domain required for imaging the events of interest. From the figure, it is apparent that for imaging the deep and steeply dipping event, a shot-gather migration would require a computational domain with horizontal extent much wider than the original maximum offset of the recorded data. In practice, the recorded shot gather must be padded all around with an enormous amount of zero traces. For example, if padding by a factor of four is needed on either side of the receiver array, and along both the in-line and the cross-line axes, the computational domain would be larger than the original shot gather by a factor of 81 $((4 + 1 + 4)^2 = 81)$. If computational cost are reduced by

¹In this chapter the figures whose caption contain an explicit reference to another SEP's report or to a SEP's thesis are marked as Non-Reproducible[NR]. I refer to the original documents for their reproducibility.

Figure 7.1: Schematic representing the ray-paths, projected along the in-line direction, for two prestack events recorded from two steeply-dipping reflectors, one shallow and the other deep. The dashed boxes show the boundaries of the minimum-sized computational domains required to image the events. The box for the deep events is substantially wider than the in-line offset, indicating potential computational inefficiencies when shot-gather migration is applied. `comaz-in-line-shot` [NR]



using a narrower computational domain, steeply dipping deep events might be lost.

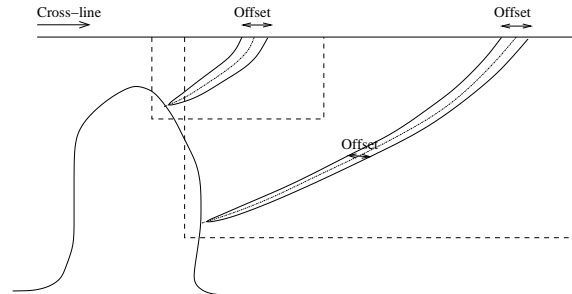
Several solutions to this computational-efficiency challenge have been proposed. The most of them fall in one of the following two categories: 1) variations of the source-receiver downward-continuation migration transformed into the midpoint-offset coordinates (Section 4.2.2), or 2) “synthesis” of common-source gathers with wide horizontal extent that are obtained by weighted sums of the shot gathers recorded in the field.

The algorithms that belong to the first category can be extremely efficient, in particular for marine streamer data, because they exploit the fact that the offset axes tend to shrink monotonically with depth. This phenomenon is illustrated by the sketch in Figure 7.1. Therefore, the offset axes at surface need to be only as wide as the data offset axes, and can be additionally trimmed down with depth. Furthermore, the cross-line offset of marine streamer data is narrow at the surface, as illustrated by the sketch in Figure 7.2, and thus the computational domain can be reduced further along the cross-line offset axis. At the limit, it can be reduced to just one sample, as in the common-azimuth algorithm presented in Section 7.2.2. In that section, I present a family of algorithms that achieve high efficiency by taking advantage of the narrow-azimuth nature of streamer data.

The main drawback of source-receiver migration is that it is not as flexible as shot-gather migration is. Its main limitation is that it is intrinsically incapable of imaging overturned events, since for such events there is always at least one depth level at which the horizontal offset between the downward-continued sources and receivers is not defined. In other words, for overturned events either the source path or the receiver path overturns shallower than the other one, making its correct propagation impossible within a source-receiver migration framework, at least in its conventional definition presented in Section 4.2.2.

In contrast with the methods based on source-receiver migration, the algorithms based on the synthesis of common-source gathers enjoy the same flexibility of the original shot-gather migration. However, they do not provide as much computationally efficiency as the

Figure 7.2: Schematic representing the geometry of the same two prestack events represented in Figure 7.1, but now projected along the cross-line direction. The cross-line offset is narrow at the surface because a marine streamer geometry is assumed. If a source-receiver migration transformed into midpoint-offset coordinates is applied to migrate the data, the computational domain can be much smaller than the one required by a shot-gather migration (dashed boxes).



comaz-cross-line-shot [NR]

one belonging to the first category, because they cannot (at least in the form known at the moment of writing this book) fully exploit the narrowness of the offset axes (in particular of the cross-line axis) and the fact that the offset axes shrink with depth, as the source-receiver based algorithms do. Section 7.1 discusses the general principles underlying all the algorithms in this second category, and briefly demonstrate how they can be simply adapted to migrate overturned events by propagating the source and receiver wavefields along a tilted Cartesian grid.

7.1 Migration of synthesized common-source gathers

An effective method to tackle the computational inefficiency of shot-gather migration discussed above is to combine the data from several gathers recorded from point sources (shot gathers) and synthesize equivalent gathers from spatially-extended source. I will refer to these synthesized gathers as **common-source gathers**. The common-source gathers generated by this process have a wide horizontal extent, at the limit covering the whole survey area, for both the equivalent source function and the synthesized data. Imaging of these common-source gathers using a shot-gather migration method; that is, the independent propagation of the source and receiver wavefields [equations (4.5)–(4.6)] and imaging at depth by applying the imaging condition in equation (4.7), avoids some of the inefficiencies encountered when imaging point-source gathers.

The imaging of the combined common-source gathers is based on the linearity of the acoustic wave equation with respect to the propagating wavefield. Linearity is a common property of all approximations of the wave-equation that we commonly use, such as the one-way wave equation used for downward-continuation migration and the two-ways wave equation used for reverse-time migration. Because of linearity, the wavefield obtained at depth by

propagating a common-source gather is the same as the wavefield that we would have obtained by independently propagating each recorded shot gather, and then combining the propagated wavefields at depth. In the general case, the combination of wavefields generates “cross-talks” artifacts in the image; these artifacts are caused by spurious correlation of source and receiver wavefields that are related to different shot gathers. However, when a large number of combined common-source gathers are migrated, these cross-talks artifacts can be attenuated, and at the limit they vanish. The accuracy of the results obtained by imaging several common-source gathers depends on the method used for the combination (i.e. the choice of the algorithm to determine the summation weights), and the total number of the common-source gathers synthesized and imaged. Depending on the scheme used for determining the summation weights, the errors can be alternatively analyzed as caused by “cross-talks” or as caused by an incomplete (aliased) representation of the source functions.

The synthesis of the common-source gathers is performed by the following sum of N shot gathers weighted by the complex coefficients $w_{i,j}(\omega)$:

$$\widehat{P}^g(\omega, x, y; j) = \sum_{i=1}^N w_{i,j}(\omega) P^g(\omega, x, y; \mathbf{s}_i) \quad (7.1)$$

to create the j -th combined receiver common-source gather, $\widehat{P}^g(\omega, x, y; j)$. Similarly, the j -th combined-source function, $\widehat{P}^s(\omega, x, y; j)$, is created by the following weighted sums of N source functions:

$$\widehat{P}^s(\omega, x, y; j) = \sum_{i=1}^N w_{i,j}(\omega) P^s(\omega, x, y; \mathbf{s}_i). \quad (7.2)$$

The weighted sums expressed in equations (7.1) and (7.2) can be repeated to create M common-source gathers and M combined-sources functions. In the following I will assume, for the sake of simplicity, that N is equal to the total number of shot gathers in the survey, but this assumption is not necessary. Equations (7.1) and (7.2) are in the temporal-frequency domain ω , but obviously the same procedure could be performed in the time domain if we substitute convolution along the time axis for the multiplication in the frequency domain.

The summation weights $w_{i,j}(\omega)$ in equations (7.1) and (7.2) are written as general functions of the temporal frequency ω , the original shot-gather index, i , and the combined common-source gather index, j . The choice of the functional form of these weights determine the name and the characteristics of the migration method. There are two main families of methods: the **phase-encoding migration** methods presented in the next section, and the **plane-wave migration** methods presented in Section 7.1.2.

7.1.1 Phase-encoding migration

The phase-encoding migration methods rely on the application of different phase shifts to the original shot gathers (i.e. phase encoding) to decrease the amount of cross-talks artifacts caused by migrating the combined gathers (Morton and Ober, 1998; Romero et al., 2000). The

summation weights are phase-only complex numbers and are independent from the spatial coordinates; they can be expressed as follows:

$$w_{i,j}(\omega) = \frac{e^{i\phi_{i,j}(\omega)}}{\sqrt{M}}, \quad (7.3)$$

where $\phi_{i,j}(\omega)$ is a real phase function. Because the summation weights are independent from the spatial coordinates, their application to the wavefields commutes with the application of the propagation operators, and the prestack image cube that is obtained by applying shot-gather migration (either by downward continuation or by reverse-time migration) to the M common-source gathers can be written as:

$$\begin{aligned} I(z, x, y, x_h, y_h) &= \sum_{\omega} \sum_{j=1}^M \widehat{P}_z^g(\omega, x + x_h, y + y_h; j) \overline{\widehat{P}_z^s(\omega, x - x_h, y - y_h; j)} \\ &= \sum_{\omega} \sum_{i=1}^N \sum_{j=1}^M |w_{i,j}(\omega)|^2 P_z^g(\omega, x + x_h, y + y_h; \mathbf{s}_i) \overline{P_z^s(\omega, x - x_h, y - y_h; \mathbf{s}_i)} \\ &+ \sum_{\omega} \sum_{k=1; k \neq l}^N \sum_{l=1}^N \sum_{j=1}^M w_{l,j}(\omega) \overline{w_{k,j}(\omega)} P_z^g(\omega, x + x_h, y + y_h; \mathbf{s}_l) \overline{P_z^s(\omega, x - x_h, y - y_h; \mathbf{s}_k)} \\ &= \sum_{\omega} \sum_{i=1}^N \widehat{w}_{i,i}(\omega) P_z^g(\omega, x + x_h, y + y_h; \mathbf{s}_i) \overline{P_z^s(\omega, x - x_h, y - y_h; \mathbf{s}_i)} \\ &+ \sum_{\omega} \sum_{k=1; k \neq l}^N \sum_{l=1}^N \widehat{w}_{l,k}(\omega) P_z^g(\omega, x + x_h, y + y_h; \mathbf{s}_l) \overline{P_z^s(\omega, x - x_h, y - y_h; \mathbf{s}_k)}, \end{aligned} \quad (7.4)$$

$$(7.5)$$

where the subscript z indicates the wavefields propagated from the surface down to depth z , and where

$$\widehat{w}_{l,k}(\omega) = \sum_{j=1}^M w_{l,j}(\omega) \overline{w_{k,j}(\omega)}, \quad (7.6)$$

and consequently

$$\widehat{w}_{i,i}(\omega) = \sum_{j=1}^M |w_{i,j}(\omega)|^2. \quad (7.7)$$

The image cube computed by equation (7.5) is equal to the image obtained by conventional shot-gather migration of the original shot-gathers [equation (4.7)] when the sum in equation (7.7) is equal to one, and when the cross-talk contributions vanish; that is, when the sum in equation (7.6) is equal to zero. The choice of the particular form for the weights expressed in equation (7.3) assures that the sum in equation (7.7) is always equal to one.

Several strategies have been proposed to minimize the “cross-talk” term. Because of the particular form of the weights, the sum in equation (7.6) can be re-written as follows:

$$\widehat{w}_{l,k}(\omega) = \frac{1}{M} \sum_{j=1}^M e^{i(\phi_{l,j}(\omega) - \phi_{k,j}(\omega))}. \quad (7.8)$$

One way for assuring that the sum in equation (7.8) approaches zero as M increases is to choose the phase function $\phi_{i,j}(\omega)$ to be a random variable equally distributed in the interval $0 - 2\pi$ (Morton and Ober, 1998; Bonomi and Cazzola, 1999; Romero et al., 2000). This choice for the weights is effective when the number, N , of shot gathers combined to create each common-source gather is large, but it is less effective when N is small. In this case deterministic algorithms for designing the weights can be more effective (Jing et al., 2000; Romero et al., 2000).

When random phase shifts are chosen for the summation weights, the cross-talk noise tends to be incoherent and zero-mean. It can be also shown that its total energy decreases as $1/\sqrt{M}$. One attractive application of random phase-encoding is the reduction of computational cost of the iterative migrations needed by Migration Velocity Analysis (MVA) procedures (Chapter 11). Many of the methods that we apply during MVA for extracting velocity information from the migrated images are based on curvature scans (e.g. semblance spectra function of ρ), which are robust to incoherent noise in the prestack image. Therefore, the application of phase encoding with small values of M is likely to be sufficient for MVA purposes.

Another intriguing application of random phase encoding is the reduction of computational cost of wavefield-based MVA methods (Chapter 12). In these methods, the result of cross-correlating two wavefields (e.g. “imaging” in shot-gather migration) is a velocity-updating function, which is usually smoothed by the introduction of a regularization term. We should be able to get accurate smooth velocity-updates by using a small value for M , because the cross-talk noise is incoherent and zero-mean and thus it should be greatly attenuated by the spatial smoothing of the velocity updates.

7.1.2 Plane-wave migration

The idea of imaging seismic data after decomposition in their plane-wave components has been introduced in the early days of seismic imaging (Schultz and Claerbout, 1978; Stoffa et al., 1981; Treitel et al., 1982; Temme, 1984). However, results of plane-waves depth migrations of real data have been published only more recently (Whitmore and Garing, 1993), and plane-waves migration methods have become popular thanks to their computational efficiency for wavefield-continuation migration of 3-D prestack marine data (Duquet et al., 2001; Notfors et al., 2003). Whitmore (1995) provides an excellent introduction to the basic concepts of plane-wave migration.

The decomposition of prestack data in plane-wave components according to the ray parameters at the source, (p_{x_s}, p_{y_s}) , can be seen as a particular case of phase encoding, when the resulting combined source functions are plane waves with different value of the ray parameters p_{x_s} and p_{y_s} , and the common-source gathers are computed by slant stacks of common-receiver gathers (Liu et al., 2002). To achieve this result, the phase function in equation (7.3) is expressed as follows:

$$\phi_{i,j}(\omega) = \omega [p_{x_s,j}(x_0 - x_{s,i}) + p_{y_s,j}(y_0 - y_{s,i})], \quad (7.9)$$

where x_0 and y_0 are arbitrary horizontal coordinates that are the same for all the values of i and j .

Also in this case we can apply the quantitative analysis of the cross-talk noise developed in equations (7.4) and (7.5). The summation in equation (7.6) can be written as follows:

$$\sum_{j=1}^M w_{l,j}(\omega) \bar{w}_{k,j}(\omega) = \frac{1}{M} \sum_{j=1}^M e^{i\omega[p_{x_s,j}(x_{s,k}-x_{s,l})+p_{y_s,j}(y_{s,k}-y_{s,l})]}. \quad (7.10)$$

The sum in equation (7.10) vanishes if the ranges of the ray parameters p_{x_s} and p_{y_s} are: 1) wide enough with respect to the minimum distances between shots, $(x_{s,k} - x_{s,l})$ and $(y_{s,k} - y_{s,l})$, and 2) sampled densely enough to assure that the oscillatory argument of the summation over j in equation (7.10) is not aliased. Not surprisingly, the criterion for eliminating the cross-talk noise turns into a sampling criterion for a plane-wave representation of a function defined at the original shot locations of the survey. These sampling criteria are the ones usually applied when discussing the accuracy of plane-wave migration (Whitmore, 1995; Duquet et al., 2001; Notfors et al., 2003).

An interesting variations of the plane-wave migration that is cost-effective for 3-D marine streamer data is the **conical-wave migration** first discussed by Whitmore (1995), and first applied to 3-D data by Duquet et al. (2001). This method takes advantage of both the narrow-azimuth nature of marine data and of the large distance between parallel sail lines of typical 3-D marine surveys to achieve higher computational efficiency than a full 3-D plane-wave migration could achieve (Duquet et al., 2001; Notfors et al., 2003). Each sail line in a 3-D survey is assumed to be a common-azimuth line; that is, with zero cross-line offset. The 3-D acquisition geometries used in the field are not strictly common-azimuth, but we can transform the data into an ensemble of common-azimuth lines by a pre-processing step such as the AMO process presented in Section 3.3. The shot gathers in each common-azimuth line are then combined according to the in-line source ray parameter p_{x_s} , and imaged independently into a 3-D volume. The name of the method derives from the fact that the wavefield originated by the line-source functions for each p_{x_s} , propagates as a conical wave in a 3-D volume.

Imaging overturned waves by plane-wave migration in tilted coordinates

The computational advantages of plane-wave migration can be substantial when the inaccuracies caused by limiting the number of plane-wave components do not interfere with the final goals of the imaging project. However, the most promising application of plane-wave migration might be the migration of overturned events by one-way propagation operators. One-way extrapolation has many advantages over two-way propagation. It is computationally more efficient and less memory demanding because it can be easily performed in the temporal frequency domain and the depth-stepping length is not limited by stringent stability constraints as the time-stepping length is in explicit finite-difference two-ways solvers. Furthermore, when using one-way propagators, sharp velocity boundaries do not cause the artifacts that are created by reverse-time migration and that I discussed in Section 4.1. The main limitation of

one-way extrapolators is that they cannot handle events that propagate along both directions of the extrapolation axis; such as overturned events.

Higginbotham et al. (1985) proposed a simple method for imaging overturned events reflected by a specific interface, such as a salt flank, by a zero-offset migration that uses a one-way propagator. The idea is to tilt the propagation axis from the conventional depth direction to a direction that better matches the propagation of the events of interest. This idea is simple and powerful, but it is difficult to generalize to prestack migration when the overturned events have not a preferred propagation direction, as it happens in complex 3-D geology. The creation of common-source gathers identified by the take-off angle of the source wavefields at the surface achieves an approximate separation of the events according to their prevailing propagation direction, and thus enables the determination of an “optimal” tilt angle for imaging each plane wave component. Both the combined source function and the combined common-source gather can be effectively continued by one-way propagators advancing along the tilted direction defined by the take-off angle at the source (Etgen, 2003; Shan and Biondi, 2004), or even at slightly steeper angle when the velocity is known to increase monotonically with depth.

Figure 7.3 illustrates this idea for one plane wave component. It shows that both the source and the receiver legs of an overturned event have much better chance to be properly imaged by one-way propagation along an axis tilted in the same direction as the take-off angle of the source, than by conventional extrapolation along the depth axis. For events not reflected at normal-incidence, the propagation direction of the receiver wavefield does not coincide with the propagation direction of the source wavefield, but the relative “angular distance” between these two directions is approximately bound by the aperture angle at the reflection point, which is limited by the maximum offset of the recording geometry.

Shan and Biondi (2004) describe an implementation of this idea, and show that overturned events generated by vertical salt edge can be imaged by using a one-way propagator as well as by using a reverse time-migration algorithm. Furthermore, they applied the geometric understanding of the kinematics of angle-domain CIG of overturned events presented by Biondi and Shan (2002) and Biondi and Shan (2002) to define a simple algorithm for computing high-quality ADCIGs for the overturned events imaged using the **tilted-coordinates plane-wave migration** method. As discussed by Biondi and Shan (2002) and Biondi and Symes (2003), the quality of the ADCIGs obtained from horizontal-offset CIGs degrades progressively as the geological dip increases, and, at the limit, it degenerates when events overturn. The propagation in tilted coordinates enables a simple solution to this problem. The offset-domain CIGs are computed along the x' directions and then transformed to equivalent CIGs computed on both the x and z directions. The contributions from all the source plane-wave components are merged, and then transformed to angle domain (Shan and Biondi, 2004).

Figures 7.4 and 7.5 show the quality of the stacked images and of the CIGs that can be obtained by applying a plane-wave migration in tilted coordinates. The data set is a 2-D line extracted from a 3-D marine survey recorded in the North Sea. A vertical salt edge generates overturned events that cannot be migrated by using downward-continuation migration. This data set is thus a good test bed for migration methods aiming to image overturned events.

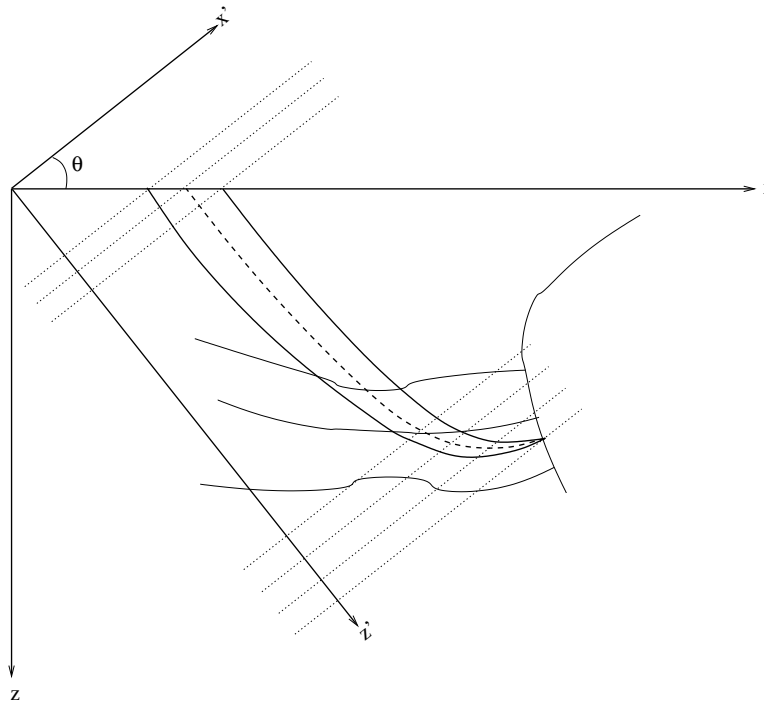


Figure 7.3: Schematic showing the geometry of an overturned event reflected from a salt flank. The event cannot be properly imaged by a downward-continuation method propagating the wavefields along the depth axis z . In contrast, it can be properly imaged by a plane-wave migration propagating the wavefields along the z' propagation direction, which is rotated by the tilt angle θ with respect to z . The tilt angle θ can be different for different plane-wave components. The dotted lines represent the “horizontal” direction in the tilted coordinates; they help to visually verify that neither of the two legs of the event overturns with respect to the z' propagation direction. `comaz-tilt-over` [NR]

Figure 7.4 compares the migration results for three different prestack migration methods. Figure 7.4a shows the image obtained by a conventional downward-continuation migration. Figure 7.4b shows the image obtained by a reverse-time migration (Biondi and Shan, 2002), and Figure 7.4c shows the image obtained by plane-wave migration with tilted coordinates. The fan of rays shown in Figure 7.4d is traced through the migration velocity model starting from the vertical salt-edge reflection. Notice that the reverse-time migration image (panel b) is sampled more coarsely than either of the other two images (panels a and c). The vertical salt edge is imaged equally well by the plane-wave migration (panel c) as by the reverse-time migration (panel b). Whereas the salt-edge reflectors are discontinuous and attenuated in the downward-continuation migration results (panel a), they are continuous and with strong amplitudes in the plane-wave migration (panel c).

Figure 7.5 compares the CIGs obtained by reverse-time migration with the CIGs obtained by plane-wave migration, extracted at a surface location, $x = 4,000$ meters, where the reflectors are only mildly dipping. Figure 7.5a and Figure 7.5b compare the offset-domain CIGs, whereas Figure 7.5c and Figure 7.5d compare the angle-domain CIGs. The two sets of CIGs

are similar, though there are slight differences mostly due to the different spatial sampling between the images computed by reverse-time migration and the ones computed by plane-wave migration.

7.2 Source-receiver migration in midpoint-offset coordinates

The methods presented in the previous section achieve high computational efficiency when the number of synthesized common-source gathers, M , is substantially lower than the total number of shot gathers to be imaged (Cazzola et al., 2004); otherwise, the computational gain might be modest (Stork and Kapoor, 2004). Whether this condition is fulfilled depends on many parameters, such as the required image accuracy, the structure of the target, and the data-acquisition geometry.

Another effective way to reduce the computational cost of wavefield-continuation migration is to take advantage of the fact that, because of practical and economical limitations, the data are always acquired with a limited extent of the offset axes, as compared to the total horizontal extents of the survey (Figures 7.1–7.2). Furthermore, the most of the data-acquisition geometries on both land and the ocean have an anisotropic distribution of the offset vectors (Chapter 1), with the offset range substantially wider in one direction (i.e.; the in-line direction) than the other (i.e.; the cross-line direction).

Source-receiver migration transformed into midpoint-offset coordinates can take advantage of the limited offset ranges in a simple and straightforward way, because the computational domain can be easily restricted to encompass only the existing offsets. From Section 4.2.2, the whole prestack wavefield expressed in the frequency and wavenumber domain, $P_z(\omega, \mathbf{k}_m, \mathbf{k}_h)$, can be downward-continued from depth z to depth $z + \Delta z$ by the following phase-shift:

$$P_{z+\Delta z}(\omega, \mathbf{k}_m, \mathbf{k}_h) = e^{-ik_z \Delta z} P_z(\omega, \mathbf{k}_m, \mathbf{k}_h), \quad (7.11)$$

where the vertical wavenumber k_z is evaluated using the following midpoint-offset wavenumber DSR equation:

$$\begin{aligned} k_z = & \sqrt{\frac{\omega^2}{v^2(\mathbf{s}, z)} - \frac{1}{4} \left[(k_{x_m} - k_{x_h})^2 + (k_{y_m} - k_{y_h})^2 \right]} \\ & + \sqrt{\frac{\omega^2}{v^2(\mathbf{g}, z)} - \frac{1}{4} \left[(k_{x_m} + k_{x_h})^2 + (k_{y_m} + k_{y_h})^2 \right]}. \end{aligned} \quad (7.12)$$

The prestack image is computed by applying the imaging condition (4.12); that is, by evaluating the downward-propagated wavefield at zero time (i.e. summation over frequencies).

As demonstrated in Section 4.2.3, the prestack image obtained by source-receiver migration is equivalent to the one obtained by shot-gather migration. Therefore, I will refer to the migration algorithm defined by equations (7.11), (7.12), and (4.12) as **full-azimuth migration**. Full-azimuth migration can be fairly efficient, but there are two main practical obstacles for full-azimuth migration achieve absolute efficiency: 1) the downward continuation must be

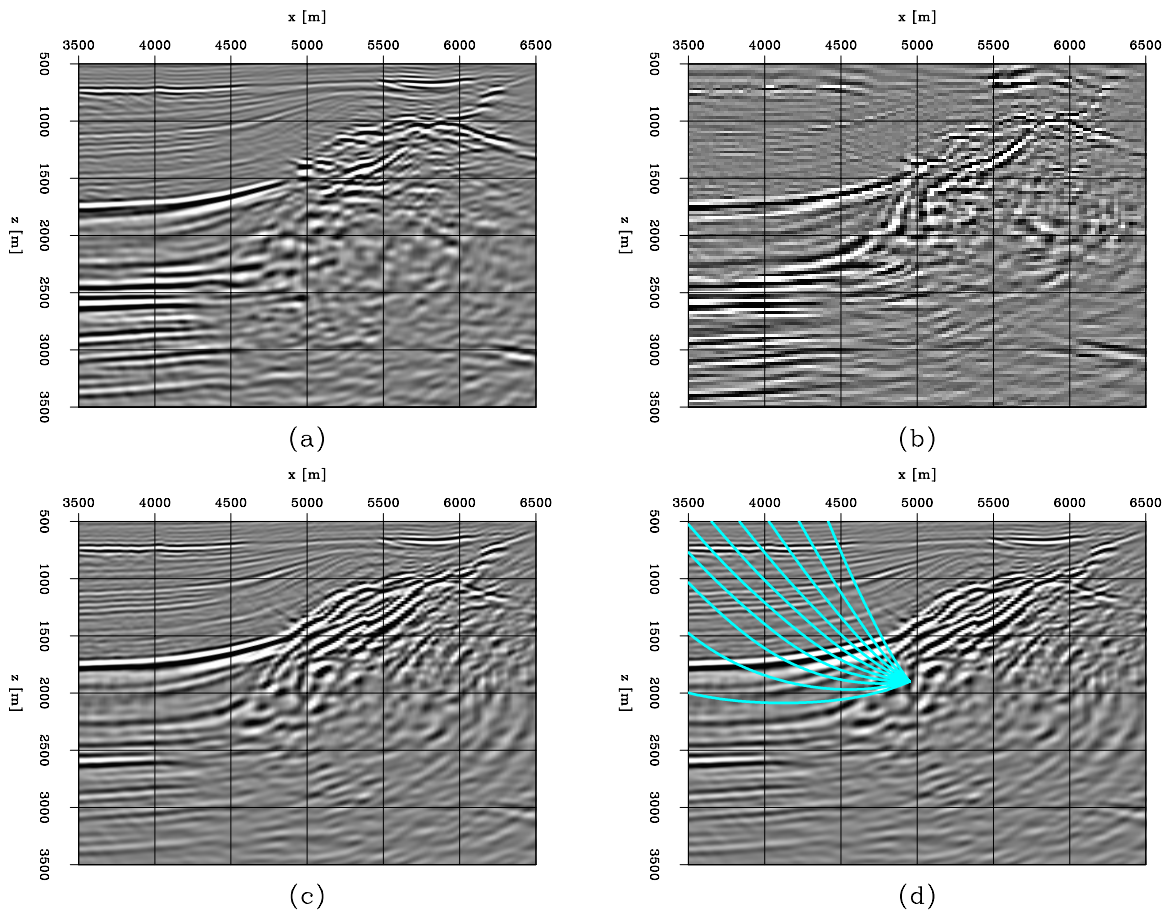
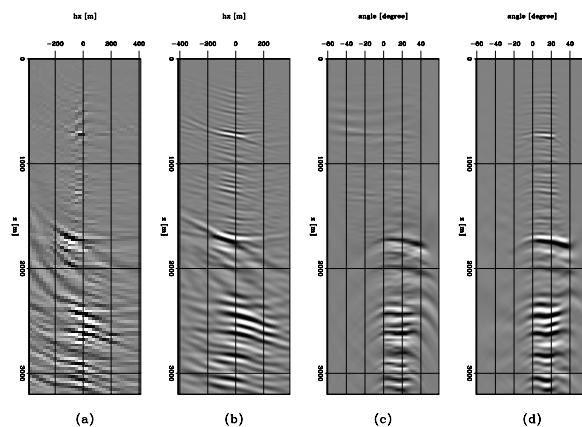


Figure 7.4: Migration of a North Sea real dataset in the proximity of a vertical salt edge: (a) the image from downward-continuation migration; (b) the image from reverse-time migration; (c) the image from plane-wave migration in tilted coordinates; (d) same image as in (c), with superimposed a fan of rays corresponding to overturned events reflected from the salt edge. (This figure is from Shan and Biondi (2004).) `comaz-elf.image` [NR]

Figure 7.5: CIGs extracted from the prestack images at $x = 4,000$ meters: (a) offset-domain CIGs obtained by reverse-time migration; (b) offset-domain CIGs obtained by plane-wave migration in tilted coordinates; (c) ADCIGs obtained by reverse-time migration; (d) ADCIGs obtained by plane-wave migration in tilted coordinates. (This figure is from Shan and Biondi (2004).) `comaz-elf.cig` [NR]



performed on 4-D data sets (constant-frequency slices) and thus require either a large amount of memory or out-of-core computations, and 2) computational efficiency demands that the cross-line offset range is as narrow as possible, but still to be sufficiently wide to “capture” all the useful propagation paths and to avoid boundary artifacts. Several variations of full-azimuth migration have been proposed for addressing these issues and improve computational efficiency. Because of their practical importance, in particular for the imaging of 3-D marine data, I will dedicate the rest of this chapter to analyze these methods.

7.2.1 Offset plane-wave downward-continuation and migration

The **offset plane-wave migration** (Mosher et al., 1997) is the most efficient method among the variations of full-azimuth migration that we consider. This method is a generalization to 3-D depth migration of the 2-D time migration methods originally proposed by Ottolini and Claerbout (1984). It is based on the decomposition of each CMP gather into offset plane waves by slant stacks as a function of the offset ray parameters p_{x_h} and p_{y_h} . After slant-stacking, each offset plane-wave component can be downward-continued independently by applying the following expression of the DSR operator:

$$k_z = \sqrt{\frac{\omega^2}{v^2(\mathbf{s}, z)} - \frac{1}{4} \left[(k_{x_m} - \omega p_{x_h})^2 + (k_{y_m} - \omega p_{y_h})^2 \right]} + \sqrt{\frac{\omega^2}{v^2(\mathbf{g}, z)} - \frac{1}{4} \left[(k_{x_m} + \omega p_{x_h})^2 + (k_{y_m} + \omega p_{y_h})^2 \right]}, \quad (7.13)$$

that is obtained by substituting $k_{x_h} = \omega p_{x_h}$ and $k_{y_h} = \omega p_{y_h}$ in equation (7.12).

The independent imaging of the offset plane-wave components solves the practical challenges of full-azimuth migration discussed above; that is; the large-memory requirements and the boundary artifacts along narrow offset axes. The number of offset-plane waves needed to achieve the desired imaging accuracy is an important parameter influencing the computational efficiency. For narrow-azimuth data sets, the number of required offset plane waves is substantially lower than the number of source plane waves needed for the plane-waves migration presented in Section 7.1.2.

The price to pay for the efficiency gained with the independent downward-continuation of the offset plane waves is inaccuracy in depth migration with complex velocity models. The offset plane waves should actually mix during downward-continuation, to take into account the differences in ray bending between the source and the receiver legs that occur in media with laterally-varying velocity. Whereas in layered media the horizontal ray parameters, $(p_{x_s}, p_{y_s}, p_{x_g}, p_{y_g})$, are constant with depth, the ray parameters change when later inhomogeneities are encountered, and consequently the offset ray parameters should be allowed to change as well. An alternative way for understanding the same issue is to notice that in laterally varying media the operators represented by the square roots in the DSR operator are not “diagonal” in the frequency-wavenumber domain; they become convolutional operators that mix the wavefield components corresponding to different wavenumbers; that is, they mix different offset plane waves.

7.2.2 Common-azimuth downward-continuation and migration

The vast majority of marine data sets acquired with streamers have a narrow cross-line offset range. The **common-azimuth migration** method takes advantage of this characteristic to reduce the dimensionality of the computational domain of full-azimuth migration (Biondi and Palacharla, 1996). It assumes that all the data have zero cross-line offset; that is, all the traces in the data share the same azimuth, hence the common-azimuth name. By reducing the cross-line offset axis to only one sample, common-azimuth solves both issues of full-azimuth migration discussed above: the constant-frequency slices become smaller (3-D instead of 4-D), and the problem of boundary artifacts along the cross-line offset axis disappears.

Since the actual data are not common-azimuth, a pre-processing step is necessary to transform all the data into equivalent common-azimuth data (Section 3.3.3). In principle, this pre-processing step might introduce errors, but usually the amount of azimuth rotation required to convert real geometries into true common-azimuth geometries is very small, and consequently the errors introduced by the rotation are also small. As I will discuss later in this section, inaccuracies of common-azimuth images are less likely to be caused by the initial azimuthal rotation than by the approximation involved in forcing the downward-continued wavefield to be common-azimuth at every depth level.

The analytical derivation of the common-azimuth downward-continuation operator takes advantage explicitly of the reduced dimensionality of the data space so that it derives a continuation operator with only four dimensions. The general downward-continuation step of equation (7.11) can be rewritten as the following common-azimuth continuation:

$$\begin{aligned}
 P_{z+\Delta z}(\omega, \mathbf{k}_m, k_{x_h}, y_h = 0) &= \int_{-\infty}^{+\infty} dk_{y_h} P_z(\omega, \mathbf{k}_m, k_{x_h}, y_h = 0) e^{-ik_z \Delta z} \\
 &= P_z(\omega, \mathbf{k}_m, k_{x_h}, y_h = 0) \left\{ \int_{-\infty}^{+\infty} dk_{y_h} e^{-ik_z \Delta z} \right\} \\
 &\approx P_z(\omega, \mathbf{k}_m, k_{x_h}, y_h = 0) A(\omega, \mathbf{k}_m, k_{x_h}) e^{-i\hat{k}_z \Delta z}, \tag{7.14}
 \end{aligned}$$

where the integration over the cross-line offset wavenumber k_{y_h} evaluates the wavefield along the plane $y_h = 0$. Because the data is independent from k_{y_h} the integral can be pulled inside, and applied only to the operator itself and not to the data. The integral can be then approximated by a stationary-phase method (Bleistein, 1984); the result is a dispersion relation that does not depend on k_{y_h} , and that thus represents a four-dimensional operator instead of a five-dimensional one.

The expression for the common-azimuth operator is derived by substituting the “stationary path”,

$$\hat{k}_{y_h} = k_{y_m} \frac{\sqrt{\frac{\omega^2}{v^2(\mathbf{g},z)} - \frac{1}{4}(k_{x_m} + k_{x_h})^2} - \sqrt{\frac{\omega^2}{v^2(\mathbf{s},z)} - \frac{1}{4}(k_{x_m} - k_{x_h})^2}}{\sqrt{\frac{\omega^2}{v^2(\mathbf{g},z)} - \frac{1}{4}(k_{x_m} + k_{x_h})^2} + \sqrt{\frac{\omega^2}{v^2(\mathbf{s},z)} - \frac{1}{4}(k_{x_m} - k_{x_h})^2}}, \tag{7.15}$$

into the expression for the full DSR of equation (7.12); that is,

$$\begin{aligned} \widehat{k}_z &= \sqrt{\frac{\omega^2}{v^2(\mathbf{s}, z)} - \frac{1}{4} \left[(k_{x_m} - k_{x_h})^2 + (k_{y_m} - \widehat{k}_{y_h})^2 \right]} \\ &+ \sqrt{\frac{\omega^2}{v^2(\mathbf{g}, z)} - \frac{1}{4} \left[(k_{x_m} + k_{x_h})^2 + (k_{y_m} + \widehat{k}_{y_h})^2 \right]}. \end{aligned} \quad (7.16)$$

Common-azimuth migration can be accurately implemented with mixed-domain (ω - k/ω - x) downward-continuation methods, such as an extended split-step algorithm (Section 5.2), as long as the implementation takes properly into account the fact that the “stationary path” expressed in equation (7.15) is function of the interval velocities at the source and receiver locations.

The common-azimuth dispersion relation of equation (7.16) can be recast, after some algebraic manipulations, as a cascade of two dispersion relations. The first is that for 2-D prestack downward-continuation along the in-line direction,

$$k_{z_x} = \sqrt{\frac{\omega^2}{v^2(\mathbf{s}, z)} - \frac{1}{4} (k_{x_m} - k_{x_h})^2} + \sqrt{\frac{\omega^2}{v^2(\mathbf{g}, z)} - \frac{1}{4} (k_{x_m} + k_{x_h})^2}, \quad (7.17)$$

and the second is the one for 2-D zero-offset downward continuation along the cross-line axis,

$$\widehat{k}_z = \sqrt{k_{z_x}^2 - k_{y_m}^2}. \quad (7.18)$$

This in-line and cross-line separation of the common-azimuth dispersion relation is an alternative proof of the full-separability of the 3-D prestack migration operator derived in Chapter 3. If the propagation velocity in equation (7.17) and equation (7.18) is assumed to be constant, these dispersion relations can be directly used for cascading two 2-D Stolt migrations (Stolt, 1978).

The cost function of a mixed-domain implementation of common-azimuth migration is

$$\begin{aligned} \text{PreCaz} &\propto \kappa_{\text{PreCaz}} \\ &\times (\text{Nz}_\xi \times \text{Nx}_\xi \times \text{Ny}_\xi \times \text{Nf} \times \log_2 \text{Nx}_\xi \times \log_2 \text{Ny}_\xi \times \log_2 \text{Nf}) \times (\text{Nt}). \end{aligned} \quad (7.19)$$

For full-volume imaging of deep targets this cost function is more attractive than the equivalent cost function for Kirchhoff migration [equation (2.12)], because it is proportional only to the square of the target depth ($\text{Nz}_\xi \times \text{Nt}$), as opposed to the cube.

Figures 7.6–7.7 demonstrate the effectiveness of common-azimuth migration to depth-image 3-D data in the presence of a complex velocity function. The data were recorded in the North Sea over a salt diapir with an overhang. The figures shows an in-line section extracted from migrated cube imaged by common-azimuth migration (Figure 7.6) and Kirchhoff migration (Figure 7.7). Notice that below the overhang the common-azimuth results are cleaner and the termination of the sediments against the salt are better imaged.

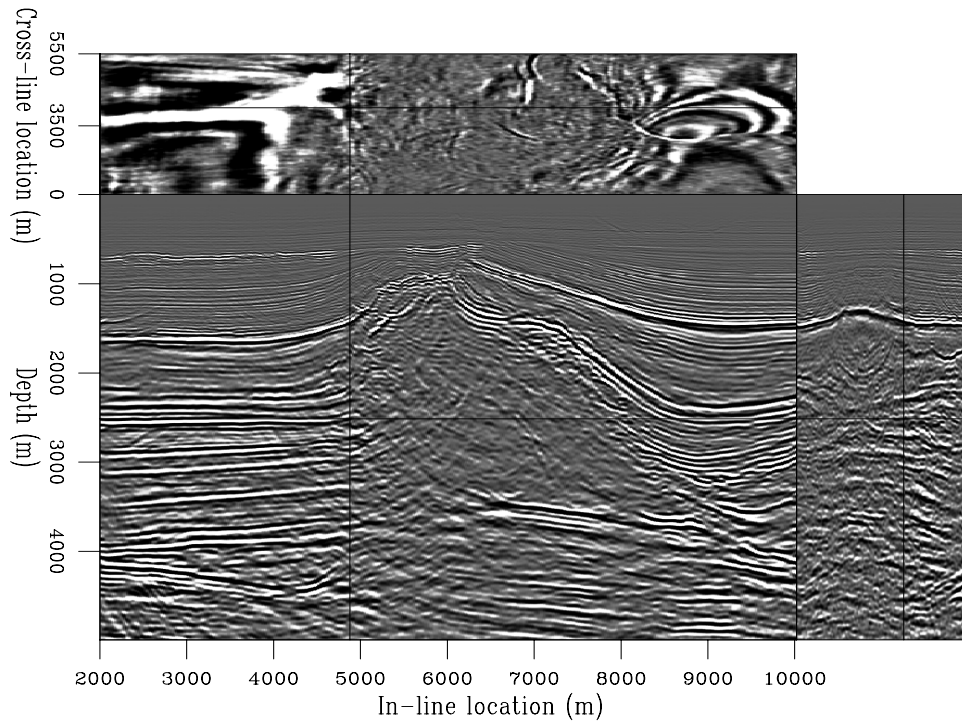


Figure 7.6: In-line section extracted from a migrated cube imaged by common-azimuth migration. (This figure is from Vaillant and Calandra (2000).) `comaz-L7d-wave-120` [NR,M]

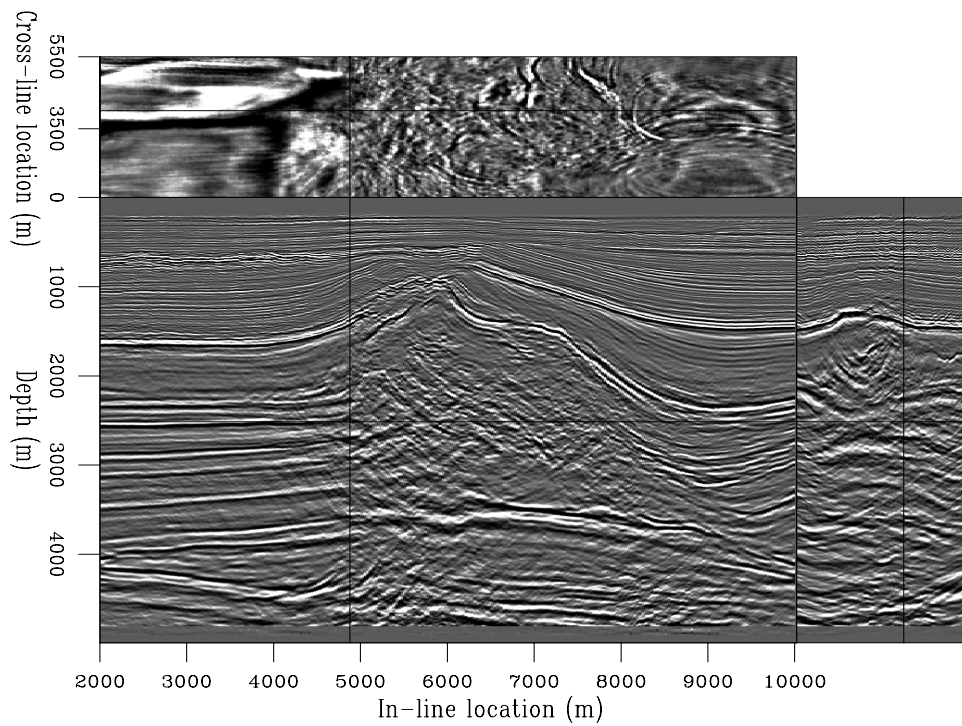


Figure 7.7: In-line section extracted from a migrated cube imaged by Kirchhoff migration. This section as the same cross-line coordinate as the section shown in Figure 7.6. (This figure is from Vaillant and Calandra (2000).) `comaz-L7d-kir-120` [NR,M]

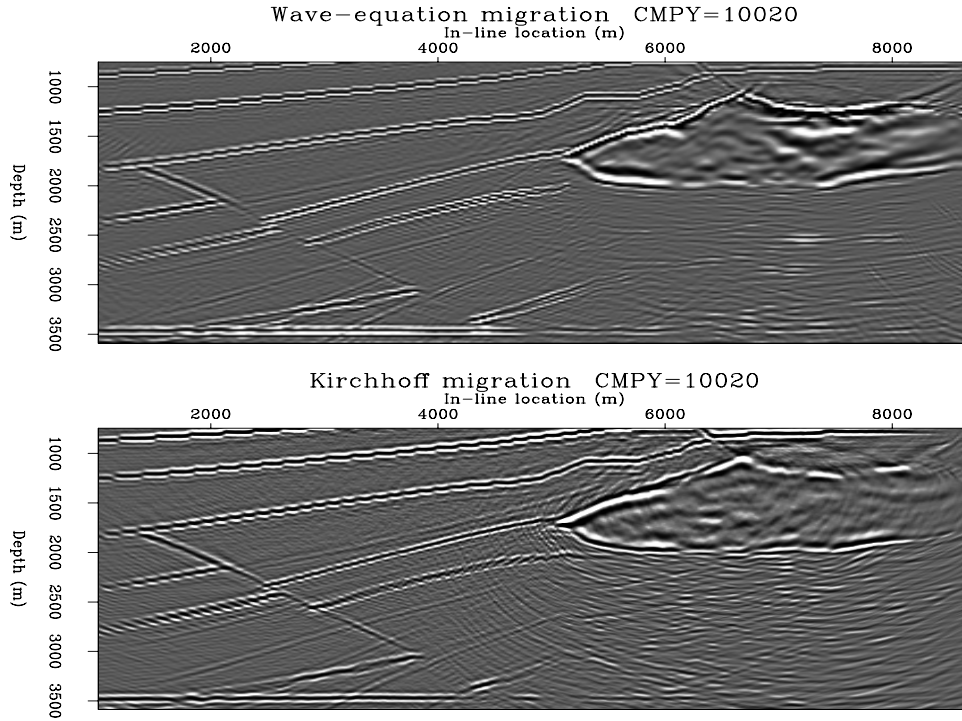


Figure 7.8: Common-azimuth migration (top) compared with Kirchhoff migration (bottom). (This figure is from Biondi (1999a).) `comaz-Both-salt-under-y10020` [NR]

Figure 7.8 shows similar advantages for common-azimuth migration over Kirchhoff migration, but for the SEG-EAGE salt data set, for which the velocity model is known. Figure 7.8 compares two in-line sections. The structure under the salt is better imaged by common-azimuth migration.

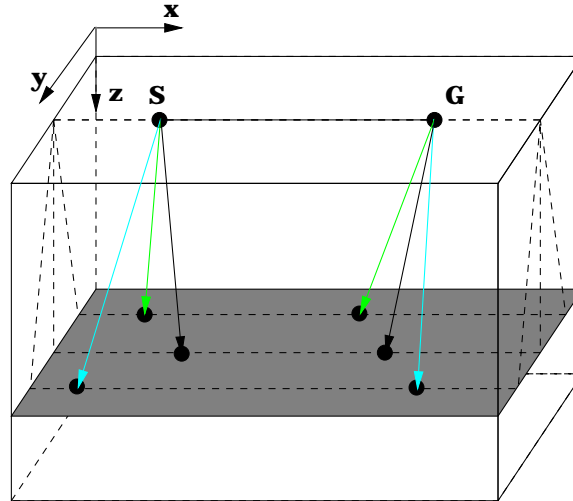
Geometric interpretation of common-azimuth downward continuation

The common-azimuth downward-continuation operator, which was derived analytically by the stationary-phase method, has a straightforward geometric interpretation that relates the propagation directions of the rays of the continued wavefield. Biondi and Palacharla (1996) demonstrate in the Appendix of their paper that the expression for the stationary path of equation (7.15) is equivalent to the following relationship:

$$\frac{p_{y_s}}{p_{z_s}} = \frac{p_{y_g}}{p_{z_g}}, \quad (7.20)$$

among the ray parameters for the rays downward-propagating the sources, $(p_{x_s}, p_{y_s}, p_{z_s})$, and the ray parameters for the rays downward-propagating the receivers, $(p_{x_g}, p_{y_g}, p_{z_g})$. This relationship between the ray parameters constrains the direction of propagation of the source and receiver rays, for each possible pair of rays. In particular, the source ray and the receiver ray must lie on the same plane, with all the possible propagation planes sharing the

Figure 7.9: Geometry of the source and receiver rays for one depth step of common-azimuth downward continuation. For each pair of source ray and receiver ray, both rays are constrained to lie on the same slanted plane. All the propagation planes share the line connecting the source and the receiver locations. `comaz-comaz-down` [NR]



line that connects the source and receiver location at each depth level. This geometric relationship constrains the sources and receivers at the new depth level to be aligned along the same azimuth as the source and receivers at the preceding depth level; this constraint is consistent with the condition that we imposed when deriving analytically the common-azimuth downward-continuation operator [equation (7.14)].

Figure 7.9 is a graphical representation of the geometric interpretation of one depth step of a common-azimuth downward continuation. The source ray and the receiver ray must lie on any of the slanted planes that share the line connecting the source and receiver locations. Notice that this coplanarity constraint applies only to one depth step at the time. The propagation of any given event can occur on different planes at each depth step; that is, the tilt angles of the propagation planes can arbitrarily vary with depth.

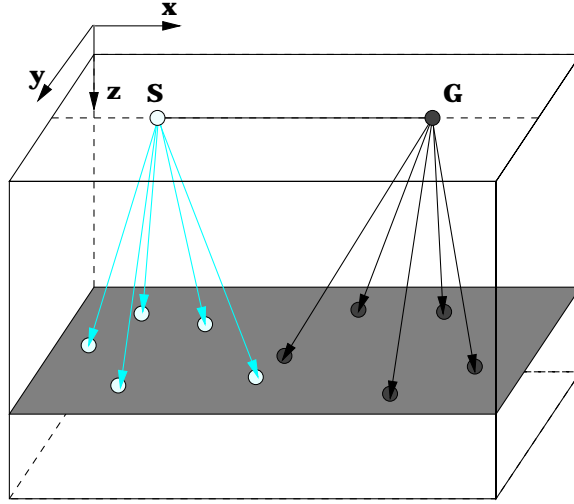
Notice that in Section 6.2.1, I used this geometric interpretation of the relationship between the temporal frequency and the spatial wavenumbers defined by the stationary path (7.15) when discussing 3-D ADCIGs. I called this relationship the coplanarity condition, and used it to define the plane of coplanarity for events imaged by 3-D ADCIGs.

In contrast with common-azimuth downward continuation, the full-azimuth downward-continuation operator represented by the DSR equation propagates the source and the receiver rays in all directions. Figure 7.10 shows the ray geometry in the general case. The generality of this downward-continuation operator requires a full five-dimensional computational space, instead of the four-dimensional space required by common-azimuth migration.

Significance of the coplanarity condition

The coplanarity condition in equation (7.15) determines the cross-line offset dips of events as a function of their dips along the midpoint axes and the in-line offset axis. These dips are equal to zero only for events that are exactly dipping in either the in-line direction ($k_{ym} = 0$) or the cross-line direction ($k_{xm} = 0$ and consequently the numerator vanishes). For all other

Figure 7.10: Geometry of the source and receiver rays for one depth step of a full-azimuth 3-D prestack downward continuation. The source and the receiver rays propagate in all directions. `comaz-dsr-down` [NR]



events $k_{y_h} \neq 0$, although $y_h = 0$. This is somewhat counter-intuitive and we could be tempted to approximate the value provided by the stationary path (7.15) with zero. If we used this approximation for \hat{k}_{y_h} , the DSR operator in equation (7.16) becomes:

$$\bar{k}_z = \sqrt{\frac{\omega^2}{v^2(\mathbf{s}, z)} - \frac{k_{y_m}^2}{4} - \frac{1}{4}(k_{x_m} - k_{x_h})^2} + \sqrt{\frac{\omega^2}{v^2(\mathbf{g}, z)} - \frac{k_{y_m}^2}{4} - \frac{1}{4}(k_{x_m} + k_{x_h})^2}. \quad (7.21)$$

It is easy to verify that if we assume $v(\mathbf{s}, z) \approx v(\mathbf{g}, z) = v(\mathbf{m}, z)$, the dispersion relation of equation (7.21) can be expressed as the cascade of a zero-offset downward continuation along the cross-line direction:

$$k_{z_y} = \sqrt{\frac{\omega^2}{v^2(\mathbf{m}, z)} - \frac{k_{y_m}^2}{4}} \quad (7.22)$$

and the second is the one for 2-D prestack downward continuation along the in-line axis,

$$\bar{k}_z = \sqrt{k_{z_y}^2 - \frac{1}{4}(k_{x_m} - k_{x_h})^2} + \sqrt{k_{z_y}^2 - \frac{1}{4}(k_{x_m} + k_{x_h})^2}. \quad (7.23)$$

In constant velocity, the use of the dispersion relation of equation (7.21) is thus equivalent to a constant-velocity cross-line zero-offset migration, followed by a constant-velocity in-line prestack migration. The order between these migrations is thus reversed with respect to the correct order for two-pass migration derived in Section 3.4.

To analyze the implications of this order reversal I show the equivalent 3-D prestack Kirchhoff migration impulse response (spreading surface) obtained by applying two-pass migration in the wrong order, to be compared with the spreading surface shown in Figure 3.30 computed with the correct two-pass migration. Figure 7.11 compares the exact impulse response of 3-D prestack migration and the approximate impulse response corresponding to using the approximate DSR operator in equation (7.21). The gray surface shown in the left panel of Figure 7.11 is the exact spreading surface for an impulse recorded at 2.5 seconds, at an offset of 4,000 meters, and assuming a constant velocity of 2,500 m/s. The inner set of contour lines corresponds

to the exact summation surface, while the outer one corresponds to the surface defined by the approximation. The right panel of Figure 7.11 shows the same contour lines in plane view. The solid lines correspond to the exact spreading surface, while the dashed lines correspond to the approximate spreading surface. It is apparent that the approximation is worse for shallow reflectors dipping at 45 degrees with respect to the acquisition axes. This qualitative analysis is confirmed by the following numerical results obtained on the SEG-EAGE salt data set.

Figure 7.12 compares the cross-line sections cut through the images obtained by common-azimuth migration (panel a) and by using the approximate DSR operator in equation (7.21) (panel b). Both the right and left flank of the salt are better imaged by migration (a) than by migration (b). Migration (a) produces also a better image of the two normal faults.

Limitations of common-azimuth migration

Kinematics of common-azimuth migration are only approximately correct when the velocity varies. The errors are related to the departure of the reflected events wavepaths from the common-azimuth geometry. This phenomenon can be easily understood by analyzing the raypaths of reflections. Figure 7.13 shows an example of raypaths for an event bouncing off a reflector dipping at 60 degrees and oriented at 45 degrees with respect to the offset direction. The offset is equal to 2.9 km, and the velocity function is $V(z) = 1.5 + .5z$ km/s. The projections of the rays on the cross-line plane clearly show the raypaths departure from the common-azimuth geometry. Notice that the source ray (light gray) is close to overturn. A dipping reflector oriented at 45 degrees with rays close to overturn is the worst-case scenario for common-azimuth migration.

The event modeled with raytracing can also be imaged using raytracing by a simple process that I will identify as raytracing migration. Starting from the initial conditions at the surface given by modeling, both the shot and the receiver rays are traced downward until the sum of their traveltimes is equal to the traveltime of the reflected event. When raytracing migration is performed using the exact equation derived from an asymptotic approximation of the double-square root equation, the rays are exactly the same as the rays shown in Figure 7.13. On the contrary, if the common-azimuth approximation is introduced in the raytracing equations, the rays will follow the paths shown in Figure 7.14. As expected, the projections of the rays on the cross-line plane overlap perfectly, confirming that the rays follow a common-azimuth geometry. However, in Figure 7.14 it is also apparent that the common-azimuth rays do not meet at the ending points. This discrepancy in the kinematics causes errors in the migration.

To connect the kinematic analysis with migration errors, I migrated a data set with similar characteristics as the events analyzed above. The data set is the same synthetic common-azimuth data set used in Section 6.2.3 to illustrate the concept of 3-D ADCIGs. The reflectivity field consists of a set of five dipping planes, from zero dip to 60 degrees dip. The azimuth of the planes is 45 degrees with respect to the direction of the acquisition. The velocity was $V(z) = 1.5 + .5z$ km/s, which roughly corresponds to typical gradients found in the Gulf of Mexico. The maximum source-receiver offset was 3 km. Figure 6.22 shows the geometry of the reflectors.

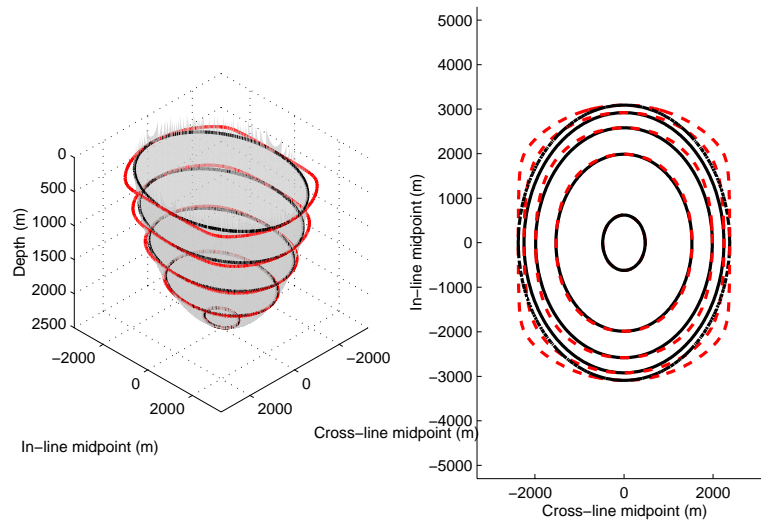


Figure 7.11: The gray surface shown in the left panel is the exact spreading surface for an impulse at at 2.5 seconds, an offset of 4,000 meters, and assuming a constant velocity of 2,500 m/s. The solid contour lines correspond to the exact spreading surface, while the dashed contour lines correspond to the approximate spreading surface. (This figure is from Biondi (1999b).) `comaz-planeellips` [NR]

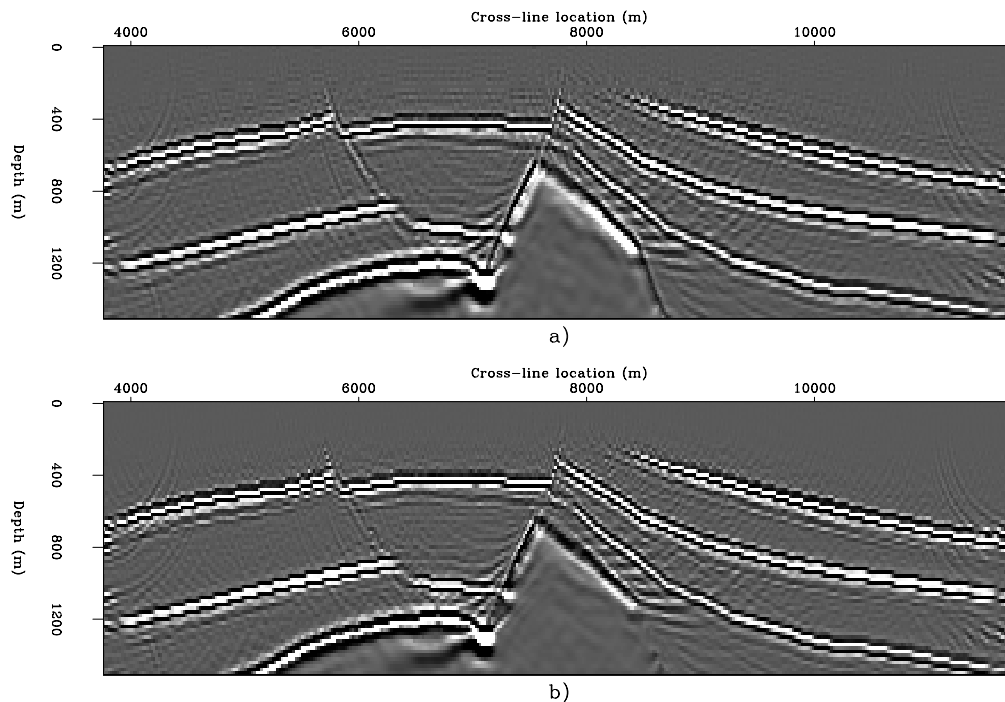


Figure 7.12: Cross-line sections ($x_m = 4,420$ meters) from the images obtained with a) common-azimuth migration, b) migration obtained by using the approximate DSR operator in equation (7.21). The shallow faults and the salt flanks are better imaged in (a) than in (b). (This figure is from Biondi (1999b).) `comaz-Both-salt-over-y4420` [NR]

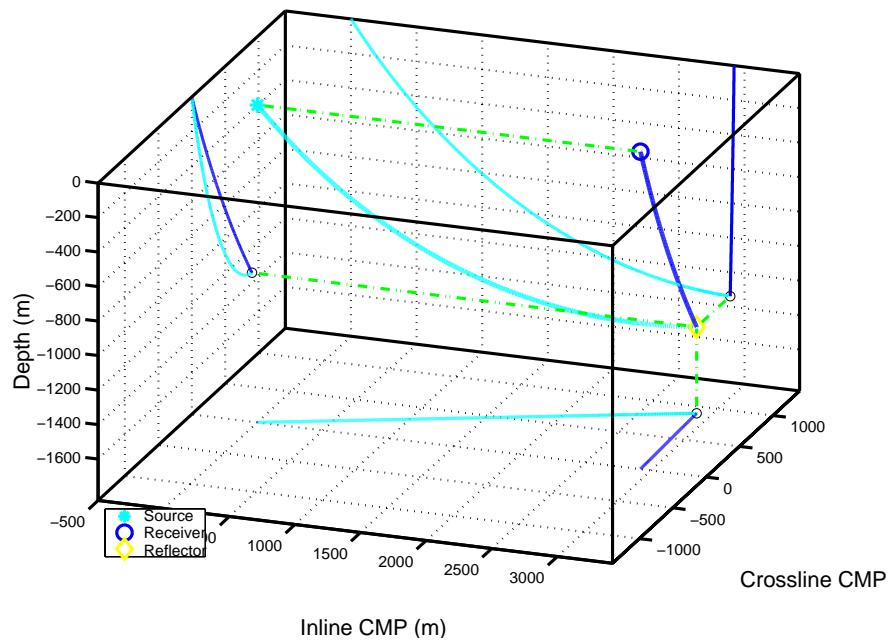


Figure 7.13: Ray corresponding to an event reflected by a reflector dipping at 60 degrees and oriented at 45 degrees with respect to the offset. The offset is 2.9 km offset, and $p_{x_h} = .00045$ s/m. The velocity function is $V(z) = 1.5 + .5z$ km/s. Notice the small, but finite, cross-line offset of the rays at depth. Also notice that the source ray (light gray) is close to overturn. (This figure is from Biondi (2003).) `comaz-sem1` [NR]

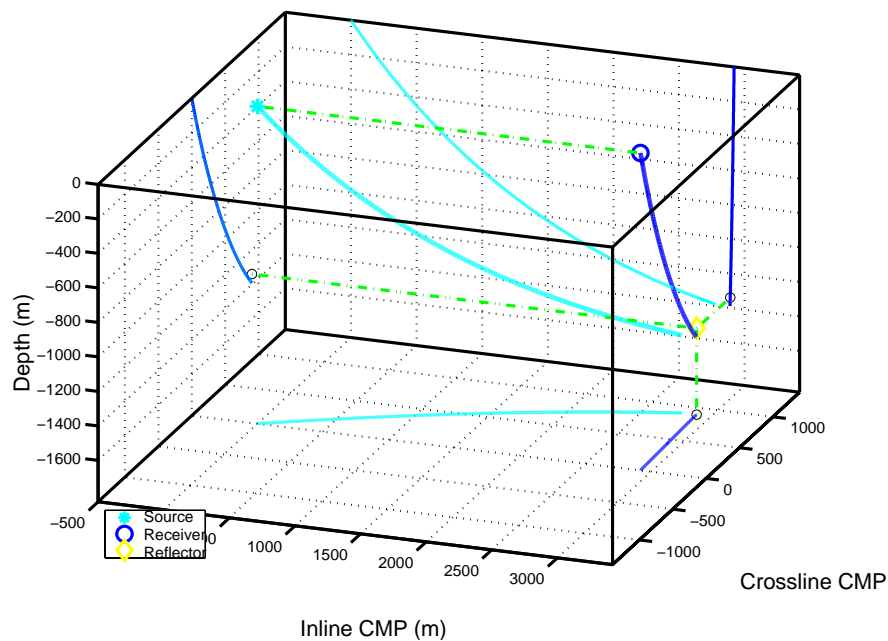


Figure 7.14: Equivalent common-azimuth rays for the same event shown in Figure 7.13. The common-azimuth rays are similar to the true rays shown in Figure 7.13, but the end points do not meet, causing a mispositioning of the migrated image. (This figure is from Biondi (2003).) `comaz-sem2` [NR]

Figure 7.15 shows a subset of the migration results. The front face of the cube displayed in the figure is an in-line section through the stack. The other two faces are sections through the prestack image as a function of the offset ray parameter p_{x_h} . The three events in the right panel of Figure 7.15 correspond to the planes dipping at 30, 45 and 60 degrees. Notice that the events are almost perfectly flat as a function of the offset ray parameter p_{x_h} , except for the reflections from the 60 degrees dipping plane with large offset ray parameters (i.e. large reflection angle). Figures 7.13–7.14 show the rays corresponding to one of these events; in particular the one corresponding to $p_{x_h}=.00045$ s/m. Figure 7.16 shows the three orthogonal projections of these rays. The black (blue in colors) rays are the exact rays, while the light gray (red in colors) rays are the common-azimuth rays for the same events recorded at the surface. The solid (magenta in colors) dot corresponds to the imaging location for the common-azimuth migration. It is at the midpoint between the end points of the two rays. It is deeper than the correct one by $\Delta_z=48$ m, and laterally shifted by $\Delta_x=-56$ m and $\Delta_y=-2$ m. However, at fixed horizontal location, the dot is shallower by $\Delta_{z-\text{plane}}=-21$ m than the reflecting plane. This is about the same vertical shift that is observable on the corresponding event in the ADCIG gather shown in Figure 7.15.

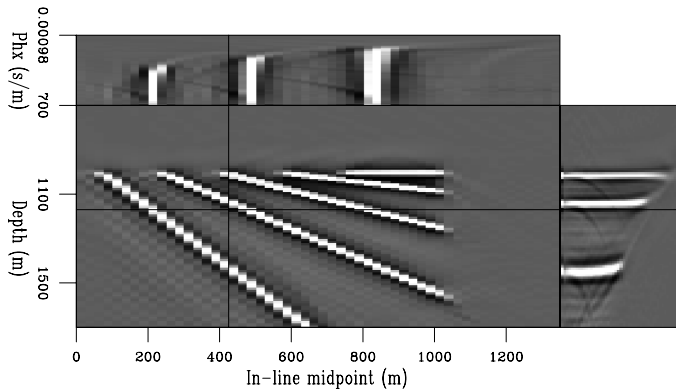
The maximum cross-line offset of the exact rays is about 200 meters. This maximum offset occurs at the intersection between the cross-line offset ray parameter (p_{y_h}) curves shown on the top-right panel in Figure 7.16. This small value for the maximum cross-line offset (about 7% of the maximum in-line offset), suggests that this event could be exactly downward continued by expanding the computational domain in a narrow strip around the zero cross-line offset. On the other hand, the value for the cross-line offset ray parameter p_{y_h} is about .00018 s/m; that is, p_{y_h} is about 40% of the in-line offset ray parameter ($p_{x_h}=.00045$ s/m). To minimize the number of cross-line offsets needed to adequately sample the cross-line-offset dips (p_{y_h}), it is important to define an optimal range of p_{y_h} that is not symmetric around the origin. In the next section I will discuss how to use the common-azimuth migration equations for defining such a range.

7.2.3 Narrow-azimuth downward-continuation and migration

The kinematic analysis presented in the previous section suggests a generalization of common-azimuth migration based on the downward continuation of a narrow strip around the zero cross-line offset. The computational cost of such a generalization is obviously proportional to the number of cross-line offsets used to represent this narrow strip. The minimum width of the strip needed to properly image all events depends on the reflector geometry and on the velocity model. The maximum sampling in the cross-line offset direction depends on the cross-line-offset dip spectrum; the common-azimuth relationship (7.15), or its equivalent in term of reflection angles (6.19), provides a guideline for the cross-line dip spectrum as a function of the reflector geometry.

To achieve computational efficiency, the cross-line offset range must be as narrow as possible and still “capture” all the useful propagation paths and avoid boundary artifacts. This goal can be best accomplished by applying two complementary procedures: 1) definition of an “optimal” range of cross-line-offset wavenumbers, k_{y_h} , for the downward continuation, and 2) window the ADCIGs along the azimuth axis to limit the effects of the boundary artifacts

Figure 7.15: Subset of the results of common-azimuth migration of the synthetic data set. The front face of the cube is an in-line section through the stack. The other two faces are sections through the prestack image. The three events in the ADCIG (right panel) correspond to the planes dipping at 30, 45 and 60 degrees. Notice that the events are almost perfectly flat in the ADCIG, with the exception of the large offset ray parameters (i.e. large reflection angle) of the 60 degrees dipping plane. (This figure is from Biondi (2003).)



comaz-CA-pull-WKBJ-stat-vp

[NR]

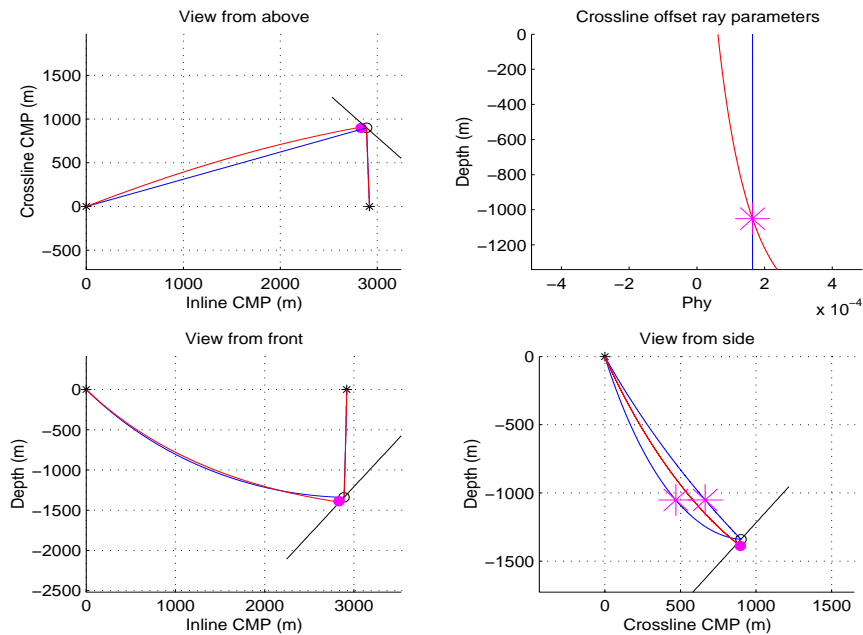


Figure 7.16: Orthogonal projections of rays shown in Figure 7.13 and Figure 7.14. The imaging point of common-azimuth migration (solid, red in colors, dot) is deeper than the correct one by $\Delta_z=48$ m, and laterally shifted by $\Delta_x=-56$ m and $\Delta_y=-2$ m. However, the dot is shallower by $\Delta_{z-plane}=-21$ m than the plane at the same horizontal location. This vertical shift is consistent with the shift observed in the ADCIG gather shown in Figure 7.15. The maximum cross-line offset of the exact rays is about 200 m. The top-right panel shows the cross-line offset ray parameters as a function of depth. (This figure is from Biondi (2003).)

comaz-sem3

[NR]

on the final migrated image.

To define an optimal range of cross-line-offset wavenumbers we need to take into account that, as demonstrated in the previous section, for dipping reflectors the dip spectrum is not centered around the zero dip ($k_{y_h} = 0$), and thus a symmetric range around zero would be wasteful. The information provided by the common-azimuth equation can be exploited to define a range of cross-line-offset dips that corresponds to propagation azimuths centered around the zero-azimuth direction defined by the common-azimuth stationary path. For this reason, and because we can window the ADCIGs along the azimuth axis, the resulting migration method is called **narrow-azimuth migration**.

The definition of an optimal cross-line offset-wavenumber range is based on the common-azimuth stationary path, where the center of the range, \bar{k}_{y_h} is defined by equation (7.15), or an approximation of equation (7.15). In equation (7.15), the cross-line offset-wavenumber k_{y_h} is function of the velocity (at the source, $v(\mathbf{s}, z)$, and at the receiver $v(\mathbf{g}, z)$), the temporal-frequency, ω , and of the wavenumbers, $k_{x_m}, k_{y_m}, k_{x_h}$. The dependency on velocity makes the direct application of equation (7.15) to depth migration cumbersome; furthermore, the dependency on the temporal frequency is also inconvenient when we want to compute ADCIGs after imaging, since the dependency on ω is lost during the imaging step. We therefore use an approximation of equation (7.15).

A practical approximation of equation (7.15) can be achieved by setting the values of the velocity and the frequency to be constant and equal to average values, \bar{v} and $\bar{\omega}$. In this way the ratio α between the cross-line offset-wavenumber k_{y_h} and the cross-line midpoint wavenumber k_{y_m} is dependent only on the in-line wavenumbers k_{x_m} and k_{x_h} ; that is:

$$\alpha_{y_h}(k_{x_m}, k_{x_h}) = \frac{\sqrt{\frac{\bar{\omega}^2}{\bar{v}^2} - \frac{1}{4}(k_{x_m} + k_{x_h})^2} - \sqrt{\frac{\bar{\omega}^2}{\bar{v}^2} - \frac{1}{4}(k_{x_m} - k_{x_h})^2}}{\sqrt{\frac{\bar{\omega}^2}{\bar{v}^2} - \frac{1}{4}(k_{x_m} + k_{x_h})^2} + \sqrt{\frac{\bar{\omega}^2}{\bar{v}^2} - \frac{1}{4}(k_{x_m} - k_{x_h})^2}}. \quad (7.24)$$

To avoid singularities when the denominator in equation (7.24) becomes small, it is also appropriate to set a limit on the maximum magnitude of α_{y_h} , so that $|\alpha_{y_h}| \leq \alpha_{y_h}^{\max}$. The center of the k_{y_h} range can thus be set as:

$$\bar{k}_{y_h}(k_{x_m}, k_{y_m}, k_{x_h}) = \begin{cases} -k_{y_m} \alpha_{y_h}^{\max} & \text{if } \alpha_{y_h}(k_{x_m}, k_{x_h}) \leq -\alpha_{y_h}^{\max} \\ k_{y_m} \alpha_{y_h}(k_{x_m}, k_{x_h}) & \text{if } |\alpha_{y_h}(k_{x_m}, k_{x_h})| < \alpha_{y_h}^{\max} \\ k_{y_m} \alpha_{y_h}^{\max} & \text{if } \alpha_{y_h}(k_{x_m}, k_{x_h}) \geq \alpha_{y_h}^{\max} \end{cases}, \quad (7.25)$$

and the the range is defined as:

$$\bar{k}_{y_h}(k_{x_m}, k_{y_m}, k_{x_h}) - \left(\frac{N_{y_h}}{2} - 1\right) dk_{y_h} \leq k_{y_h} \leq \bar{k}_{y_h}(k_{x_m}, k_{y_m}, k_{x_h}) + \frac{N_{y_h}}{2} dk_{y_h}, \quad (7.26)$$

where N_{y_h} is the number of cross-line offsets and the cross-line offset-wavenumber sampling dk_{y_h} is

$$dk_{y_h} = \frac{2\pi}{N_{y_h} \Delta y_h}. \quad (7.27)$$

When computing 3-D ADCIGs from the results of narrow-azimuth migration, it is important to take into account the shift in the cross-line offset-wavenumber range defined by equation (7.25). This task is straightforward to accomplish when applying equation (6.19) (Section 6.2.1) to convert offset ray parameters into angles. It is also easy to accomplish when computing ADCIGs after imaging by applying equation (6.25) (Section 6.2.2), because we approximated the stationary path (7.15) with an expression that is independent from the temporal frequency ω .

Narrow-azimuth migration of synthetic data sets

The migration example shown in Figure 7.15 illustrates the limitation of common-azimuth migration in a simple situation that can be effectively analyzed by raytracing (Figures 7.13–7.14 and 7.16). The next set of figures shows the comparison between the images obtained by full-azimuth migration, narrow-azimuth migration, and common-azimuth migration on the same data set. In particular I focus on the same ADCIG shown in the right panel of Figure 7.15 and then analyzed by raytracing. To create data sets with more than one cross-line offset I padded the original common-azimuth data with zeros. The differences between the results are thus exclusively due to differences between the migration algorithms.

Figure 7.17 shows four ADCIGs, all extracted at the same horizontal location, but corresponding to four different migrations. The full-azimuth migration and the narrow-azimuth migration show the ADCIGs at the “true” reflection azimuth ($\phi = 12$ degrees) for the event of interest; that is, the reflection from the deepest reflector. The shallower events are reflected at azimuths smaller than 12 degrees, and thus they are not flat in the ADCIGs, except for the common-azimuth ADCIG.

Figure 7.17a shows the ADCIG obtained by full-azimuth migration with $N_{y_h} = 32$, $\bar{k}_{y_h} = 0$, and $\Delta y_h = 50$ meters. Figure 7.17b shows the ADCIG obtained by narrow-azimuth migration with $N_{y_h} = 32$ and $\Delta y_h = 100$ meters. The center of the k_{y_h} range, \bar{k}_{y_h} , was set by using equations (7.24) and (7.25) with $\bar{\omega} = 2\pi 25 \text{ s}^{-1}$, $\bar{v} = 1,500 \text{ m/s}$, and $\alpha_{y_h}^{\max} = 2$. Figure 7.17c shows the ADCIG obtained by full-azimuth migration with $N_{y_h} = 32$, $\bar{k}_{y_h} = 0$, and $\Delta y_h = 100$ meters, and Figure 7.17d shows the ADCIG obtained by common-azimuth migration. In Figure 7.17a and Figure 7.17b all events are correctly imaged, even the wide-aperture angle reflection from the reflector dipping at 60 degrees, which shows the upward departure from flatness in the common-azimuth migration. Notice that the same event in Figure 7.17c has not been correctly imaged, because the cross-line offset sampling was too coarse, $\Delta y_h = 100$ meters, for the full-azimuth migration. In contrast, narrow-azimuth migration with the same value of Δy_h (Figure 7.17b) images the event correctly, because it uses the computational domain more efficiently by shifting the center of the range according to equation (7.25).

Figures 7.18–7.20 shows slices taken from the same ADCIGs shown in Figure 7.17, at the constant depth of $z = 1,430$ meters; this depth corresponds to the deepest reflector shown in Figure 7.17. The reflection amplitudes are shown as functions of both the aperture angle (γ) and the reflection azimuth (ϕ). Because the common-azimuth ADCIG lacks the azimuthal dimension, the depth-slice obtained by common-azimuth migration is omitted.

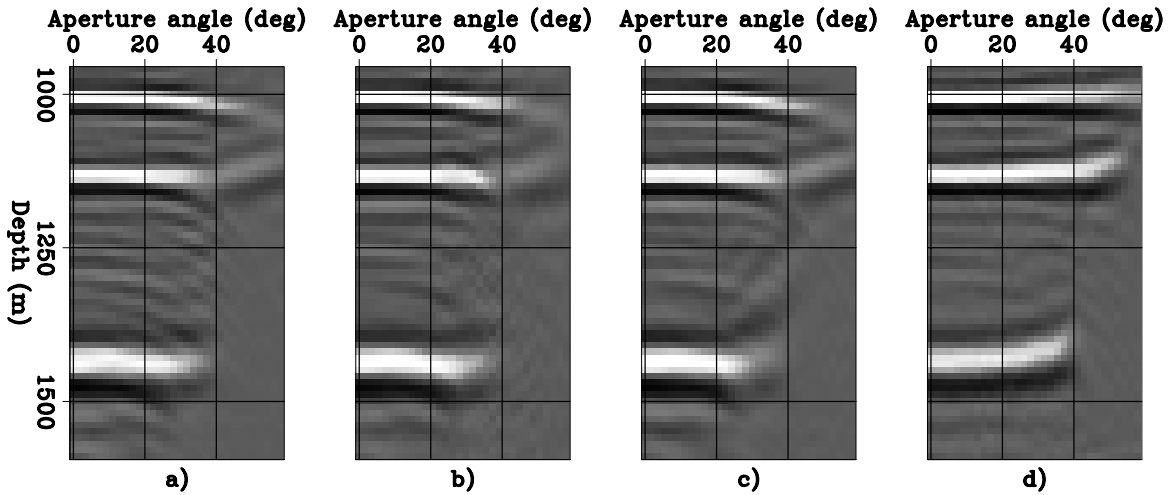


Figure 7.17: Four ADCIGs, all extracted at the same horizontal location, but corresponding to four different migrations: (a) ADCIG obtained by full-azimuth migration with $N_{y_h} = 32$, $\bar{k}_{y_h} = 0$, and $\Delta y_h = 50$ meters, (b) ADCIG obtained by narrow-azimuth migration with $N_{y_h} = 32$ and $\Delta y_h = 100$ meters, (c) ADCIG obtained by full-azimuth migration with $N_{y_h} = 32$, $\bar{k}_{y_h} = 0$, and $\Delta y_h = 100$ meters, (d) ADCIG obtained by common-azimuth migration. The full-azimuth migration and the narrow-azimuth migration show the ADCIGs at the “true” reflection azimuth for the deepest reflector; that is, $\phi = 12$ degrees. `comaz-cig-az12-azim` [CR]

Figure 7.18 shows the image obtained by full-azimuth migration when the cross-line offset axis is sufficiently sampled (depth slice of ADCIG shown in Figure 7.17a). Figure 7.19 shows the image obtained by narrow-azimuth migration (depth slice of ADCIG shown in Figure 7.17b). Figure 7.20 shows the image obtained by full-azimuth migration when the cross-line offset axis is not sufficiently sampled (depth slice of ADCIG shown in Figure 7.17c). The adequately-sampled full-azimuth image (Figure 7.18) and the narrow-azimuth image (Figure 7.19) are similar and show coherent events up to $\gamma \approx 40$ degrees, though the narrow-azimuth image is slightly more noisy than the wide-azimuth image. The coarsely-sampled full-azimuth image (Figure 7.20) shows coherent events only up to $\gamma \approx 30$ degrees.

REFERENCES

- Biondi, B., and Palacharla, G., 1996, 3-D prestack migration of common-azimuth data: *Geophysics*, **61**, 1822–1832.
- Biondi, B., and Shan, G., 2002, Prestack imaging of overturned reflections by reverse time migration: 72nd Ann. Internat. Meeting, Soc. of Expl. Geophys., 1284–1287.
- Biondi, B., and Symes, W. W., 2003, Angle-domain common-image gathers for migration velocity analysis by wavefield-continuation imaging: *Geophysics*: accepted for publication.
- Biondi, B., 1999a, Subsalt imaging by common-azimuth migration: *SEP*–**100**, 113–125.

Figure 7.18: Full-azimuth ADCIG as a function of aperture angle (γ) and reflection azimuth (ϕ) at constant depth ($z = 1,430$ meters). The cross-line offset sampling ($\Delta y_h = 50$ meters) was adequate for imaging the events with large γ .

`comaz-zaz-60-60-dense-all-v4-data8`

[CR]

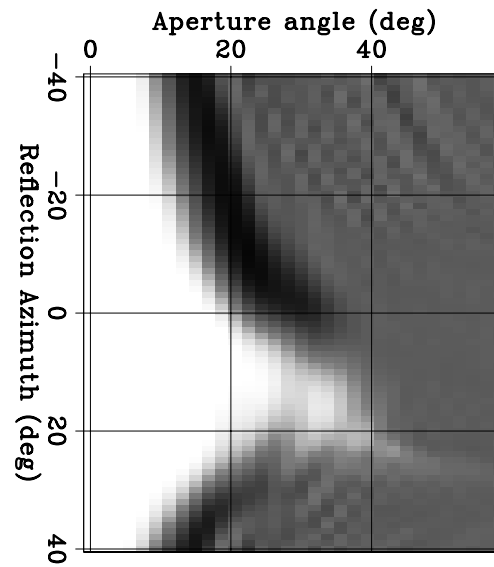


Figure 7.19: Narrow-azimuth ADCIG as a function of aperture angle (γ) and reflection azimuth (ϕ) at constant depth ($z = 1,430$ meters). The events with large γ are correctly imaged.

`comaz-zaz-60-60-dense-nam-pos-all-v5-data8`

[CR]

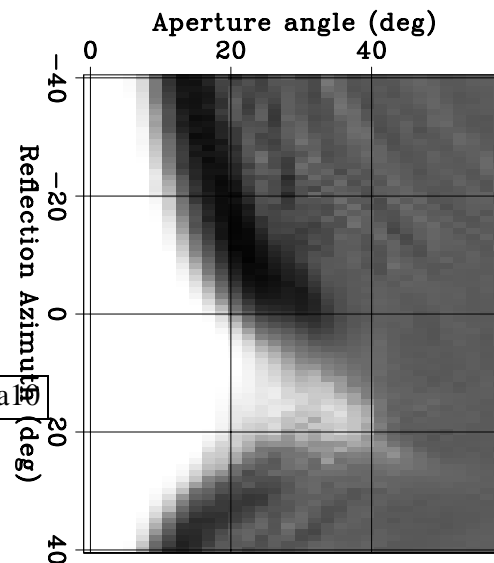
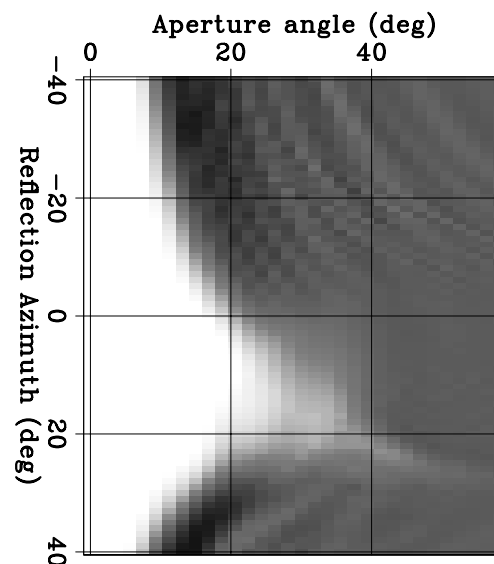


Figure 7.20: Full-azimuth ADCIG as a function of aperture angle (γ) and reflection azimuth (ϕ) at constant depth ($z = 1,430$ meters). The cross-line offset sampling ($\Delta y_h = 100$ meters) was too coarse for imaging the events with large γ .

`comaz-zaz-60-60-dense-all-v4-data9`

[CR]



- Biondi, B., 1999b, Offset plane waves vs. common-azimuth migration for sub-salt imaging: SEP-102, 15–34.
- Biondi, B., 2003, Narrow-azimuth migration of marine streamer data: SEP-113, 107–121.
- Bleistein, N., 1984, *Mathematical methods for wave phenomena*: Academic Press.
- Bonomi, E., and Cazzola, L., 1999, Prestack imaging of compressed seismic data: A Monte Carlo approach: 69th Ann. Internat. Meeting, Soc. of Expl. Geophys., 1914–1917.
- Cazzola, L., Pizzaferrì, L., Ratti, L., Cardone, G., and Bonomi, E., 2004, An example of wavefield depth migration and Monte Carlo imaging in West Africa deep waters: 74th Ann. Internat. Mtg., Soc. of Expl. Geophys., Expanded Abstracts, accepted for publication.
- Duquet, B., Lailly, P., and Ehinger, A., 2001, 3-D plane wave migration of streamer data: 71st Ann. Internat. Meeting, Soc. of Expl. Geophys., 1033–1036.
- Etgen, J. T., 2003, private communication.
- Higginbotham, J. H., Shin, Y., and Sukup, D. V., 1985, Directional depth migration (short note): *Geophysics*, **50**, 1784–1796.
- Jing, X., Finn, C., Dickens, T., and Willen, D., 2000, Encoding multiple shot gathers in prestack migration: 70th Ann. Internat. Meeting, Soc. of Expl. Geophys., 786–789.
- Liu, F., Stolt, R., Hanson, D., and Day, R., 2002, Plane wave source composition: An accurate phase encoding scheme for prestack migration: 72nd Ann. Internat. Meeting, Soc. of Expl. Geophys., 1156–1159.
- Morton, S. A., and Ober, C. C., 1998, Faster shot-record migrations using phase encoding: 68th Ann. Internat. Meeting, Soc. of Expl. Geophys., 1131–1134.
- Mosher, C. C., Foster, D. J., and Hassanzadeh, S., 1997, Common angle imaging with offset plane waves: 67th Annual Internat. Mtg., Soc. Expl. Geophys., Expanded Abstracts, 1379–1382.
- Notfors, C., Gray, S., Sun, J., Young, J., Zhang, Y., and Chernis, L., 2003, Delayed-shot 3D prestack depth migration: 73rd Ann. Internat. Meeting, Soc. of Expl. Geophys., 1027–1030.
- Ottolini, R., and Claerbout, J. F., 1984, The migration of common-midpoint slant stacks: *Geophysics*, **49**, 237–249.
- Romero, L. A., Ghiglia, D. C., Ober, C. C., and Morton, S. A., 2000, Phase encoding of shot records in prestack migration: *Geophysics*, **65**, 426–436.
- Schultz, P. S., and Claerbout, J. F., 1978, Velocity estimation and downward-continuation by wavefront synthesis: *Geophysics*, **43**, 691–714.
- Shan, G., and Biondi, B., 2004, Imaging overturned waves by plane-wave migration in tilted coordinates: 74th Ann. Internat. Mtg., Soc. of Expl. Geophys., Expanded Abstracts, accepted for publication.

- Stoffa, P. L., Buhl, P., Diebold, J. B., and Wenzel, F., 1981, Direct mapping of seismic data to the domain of intercept time and ray parameter - A plane-wave decomposition: *Geophysics*, **46**, 255–267.
- Stolt, R. H., 1978, Migration by Fourier transform: *Geophysics*, **43**, 23–48.
- Stork, C., and Kapoor, J., 2004, How many P values do you want to migrate for delayed shot wave equation migration?: 74th Ann. Internat. Mtg., Soc. of Expl. Geophys., Expanded Abstracts, accepted for publication.
- Temme, P., 1984, A comparison of common-midpoint single-shot and plane-wave depth migration: *Geophysics*, **49**, 1896–1907.
- Treitel, S., Gutowski, P. R., and Wagner, D. E., 1982, Plane-wave decomposition of seismograms: *Geophysics*, **47**, 1375–1401.
- Vaillant, L., and Calandra, H., 2000, Common-azimuth migration and Kirchhoff migration for 3-D prestack imaging: A comparison on North Sea data: *SEP*–**103**, 139–147.
- Whitmore, N. D., and Garing, J. D., 1993, Interval velocity estimation using iterative prestack depth migration in the constant angle domain: *The Leading Edge*, **12**, 757–762.
- Whitmore, N. D., 1995, An imaging hierarchy for common-angle plane wave seismograms: Ph.D. thesis, University of Tulsa.

Chapter 12

Migration Velocity Analysis by wavefield methods

Every velocity estimation method presented in Chapters 10 and 11 is based, explicitly or implicitly, on a ray-tracing modeling of the kinematics of the reflections. When estimating velocity, a ray approximation is convenient for several reasons. First, it is faster to trace rays than propagating waves, and thus an inversion method based on rays has a large computational advantage. An even more important advantage is the intuitive nature of the link that rays establish between the velocity function and the kinematics of the reflections.

Ray-based velocity-estimation methods, however, have serious drawbacks for complex depth imaging problems. In Chapter 11 we have seen that when the subsurface geology is structurally complex, the velocity estimation and the migration steps are interdependent, and velocity estimation and migration are applied iteratively in a Migration Velocity Analysis (MVA) procedure. In the presence of complex wave propagation (i.e. multipathing and geometrical dispersion), ray-based migration methods are often not capable of producing high-quality images, while wavefield-continuation methods, such as the ones introduced in Chapter 4, yield better images. To ensure that the MVA iterative imaging process converges to a satisfactory model, it is crucial that the migration and the velocity estimation are as consistent with each other as possible. Consistency with migration is an important attribute for velocity-estimation methods, because the final goal is to improve the quality of the migrated image. When wavefield-continuation migration is required, we should consider using velocity-estimation methods that go beyond the asymptotic approximations required by ray-based methods.

Imaging under rugged salt bodies is an important case where ray-based MVA methods are not reliable. An important practical difficulty encountered when using rays to estimate velocity below rugose salt bodies is the instability of ray tracing. Rough salt topography creates poorly illuminated areas, or even shadow zones, in the subsalt region (Section 9.3). The spatial distribution of these poorly illuminated areas is very sensitive to the velocity func-

¹In this chapter the figures whose caption contain an explicit reference to another SEP's report or to a SEP's thesis are marked as Non-Reproducible[NR]. I refer to the original documents for their reproducibility.

tion. Therefore, it is often extremely difficult to trace rays connecting a given point in the poorly illuminated areas with a given point at the surface (two-point ray-tracing). In contrast, wavefield-extrapolation methods are also stable in poorly illuminated areas.

A related and more fundamental problem with ray-based MVA is that rays poorly approximate actual **wavepaths** when a band-limited seismic wave propagates through the rugose top of a salt body. Figure 12.1 illustrates this issue by showing three band-limited (1 – 26 Hz) wavepaths, also known in the literature as **fat rays** (Woodward, 1992; Pratt, 1999; Dahlen et al., 2000), for subsalt events propagating through a synthetic model of a salt body (Sigsbee 2A). The fat rays link perturbations in the image with perturbations in the velocity, and are thus the **sensitivity kernels** of wavefield MVA. Each of these three wavepaths is associated with the same point source located at the surface but corresponds to a different sub-salt “event”. The top panel in Figure 12.1 shows a wavepath that could be reasonably approximated using the method introduced by Lomax (1994) to trace fat rays using asymptotic methods. In contrast, the wavepaths shown in both the middle and bottom panels in Figure 12.1 cannot be well approximated using Lomax’s method. The amplitude and shapes of these wavepaths are significantly more complex than the simple fattening of a geometrical ray could ever describe. The bottom panel illustrates the worst-case scenario for ray-based tomography, because the variability of the top salt topology is at the same scale as the spatial wavelength of the seismic wave. The fundamental reason why true wavepaths cannot be approximated using fattened geometrical rays is that the wavepaths are frequency dependent. Figure 12.2 illustrates this dependency by depicting the wavepath shown in the bottom panel of Figure 12.1 as a function of the temporal bandwidth: 1 – 5 Hz (top), 1 – 16 Hz (middle), and 1 – 64 Hz (bottom). The width of the wavepath decreases as the frequency bandwidth increases, and the focusing/defocussing of energy varies with the frequency bandwidth.

In 3-D, wavepaths are even more complex than in 2-D. Figure 12.3 displays three orthogonal slices of a 3-D slowness model containing a salt body. Figure 12.4 shows the sensitivity kernel related to a perturbation of the phase of subsalt event, imaged from a point source on the surface with a frequency range of 1 – 16 Hz. The shapes of the kernels are complicated, which is an expression of the multipathing occurring as waves propagate through rough salt bodies. The horizontal slice indicates multiple paths linking the source point on the surface with the image perturbation in the subsurface. One noticeable characteristic is that the sensitivity kernels shown in Figure 12.4 shows little or no sensitivity along the central path; therefore, fat rays look more like “doughnuts” than “bananas” This phenomenon was discussed by Dahlen et al. (2000) and by Marquering et al. (1999) in the context of finite-frequency traveltimes tomography.

Notwithstanding the potential advantages of using wavefield-continuation methods to estimate propagation velocity, these methods are seldom applied in practice. Computational cost has been a major hurdle in the past, but it is going to be less and less important in the future as the cost-effectiveness of high-performance computers increases. A more fundamental limitation of wavefield-based tomography or MVA is represented by the challenges of linearizing the wave equation for evaluating velocity updates. As we will discuss in detail in Section 12.2, the most convenient, and therefore popular, linearization of the wave equation is based on the truncation of the Born scattering series to the first order term (Born approximation). If the

phase differences between the modeled and recorded wavefields are larger than a fraction of the wavelet, then the assumptions made under the Born approximation are violated, and the velocity-inversion methods diverge (Woodward, 1992; Pratt, 1999; Dahlen et al., 2000; Hung et al., 2000). Overcoming these limitations is crucial for a practical MVA tool. This goal is easier to accomplish with methods that optimize an objective function defined in the image space (Symes and Carazzone, 1991; Biondi and Sava, 1999; Shen et al., 2003) than with methods that optimize an objective function defined in the data space (Tarantola, 1984; Mora, 1987; Pratt, 1999). However, even methods that optimize an image-space objective function are not automatically immune from the pitfalls related to the Born approximation, and therefore the objective function needs to be carefully designed.

In this chapter I present a general framework for improving the migrated image by updating the migration velocity using a wavefield-continuation operator. This general methodology could be used to optimize any of the image-space objective functions presented in the literature, such as the Differential Semblance Optimization (DSO) (Symes and Carazzone, 1991; Shen et al., 2003), the Multiple Migration Fitting (Chavent and Jacewitz, 1995), and the Wave-Equation Migration-Velocity Analysis (WEMVA) (Biondi and Sava, 1999; Sava and Biondi, 2004a,b). In the second part of this chapter, I focus on the WEMVA method, because it is conceptually related to the ray-based MVA methods described in Chapter 11, and it can be applied by leveraging the same robust work-flows currently used for conventional MVA.

12.1 Objective function of wavefield migration velocity analysis

The goal of all MVA methods is to maximize the quality of the migrated image by iteratively updating the velocity function. The coherency between partial prestack images in Common-Image Gathers (CIG) is customarily used as a measure of image quality, but the focusing of the reflections along the physical dimensions can be also a useful metric (Section 11.2.2). The “optimal” migration velocity is estimated by solving an optimization problem defined by an objective function that mathematically expresses the goals of MVA. Since Angle-Domain CIGs (ADCIGs) are the most natural CIGs for wavefield-continuation migration (Chapter 6), the objective functions of wavefield-based MVA methods are usually defined for prestack images transformed to the angle domain.

The objective function of ray-based MVA methods [equation (11.19)] is defined in terms of the kinematics of the migrated images. In particular, it aims at minimizing the RMO function measured from the CIGs, or, as we discussed at the end of Section 11.4.1, it drives the RMO function toward a “target” RMO function that is zero for all reflectors and at all angles (offsets). The objective function of wavefield-based MVA methods has a similar goal (i.e. flattening the ADCIGs), but is defined in terms of the whole image, including kinematics *and* amplitudes. It aims at driving the migrated image, \mathbf{I} , toward a “target” image, $\hat{\mathbf{I}}$, that has the desired properties (i.e.; flat ADCIGs and well-focused reflections). Conceptually, such an objective function could be written as follows:

$$J_{\text{reg}}(\mathbf{s}) = \|\mathbf{I}(\mathbf{s}) - \hat{\mathbf{I}}\|_2 + \mathbf{s}' \mathbf{C}_s^{-1} \mathbf{s}, \quad (12.1)$$

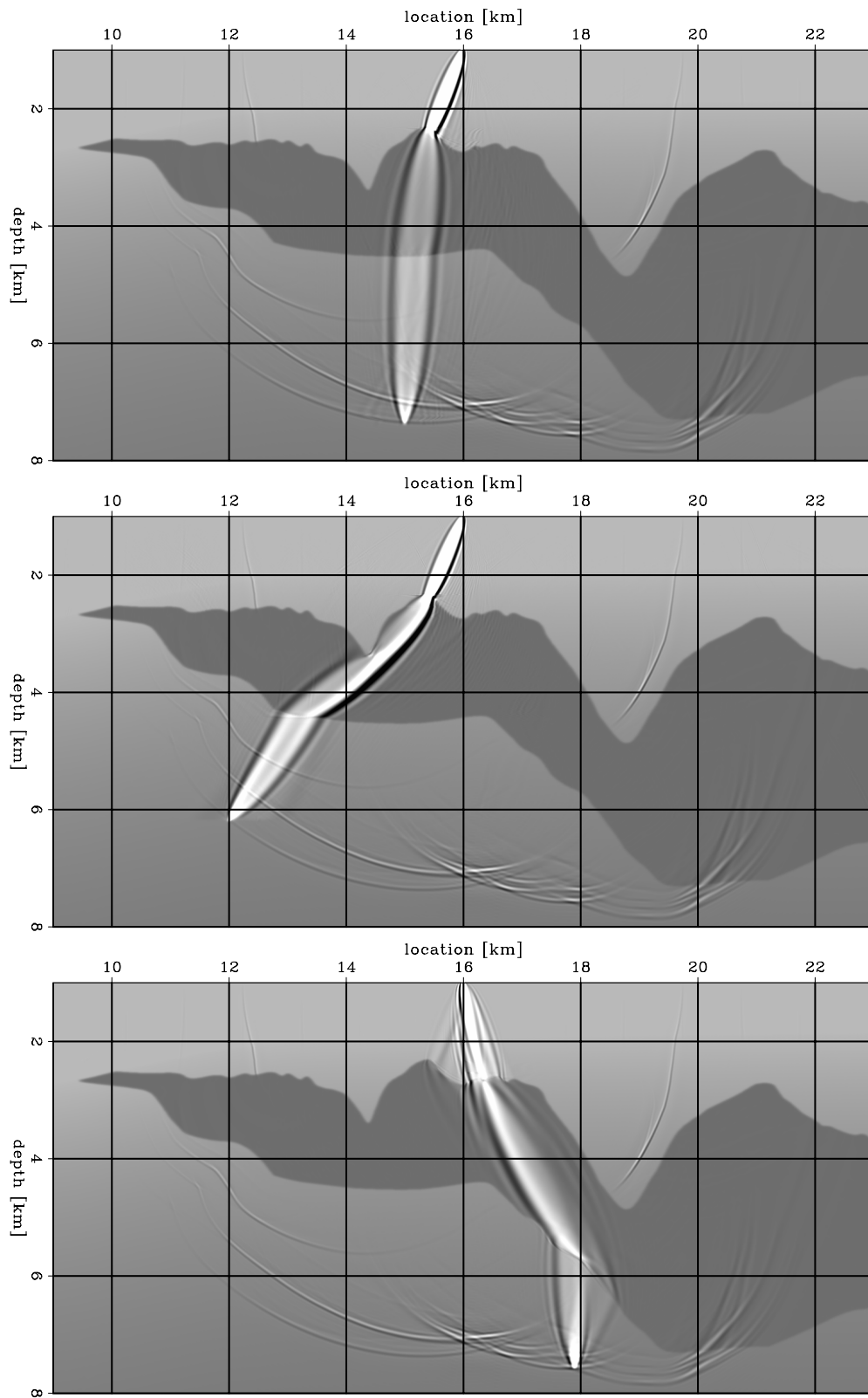


Figure 12.1: Wavepaths for frequencies between 1 and 26 Hz connecting a point on the surface with various locations in the image. Each panel is an overlay of three elements: the slowness model, the wavefield corresponding to a point source on the surface at $x = 16$ km, and wavepaths from a point in the subsurface to the source. (This figure is from Sava and Biondi (2004c).) `wemva-zifat` [NR]

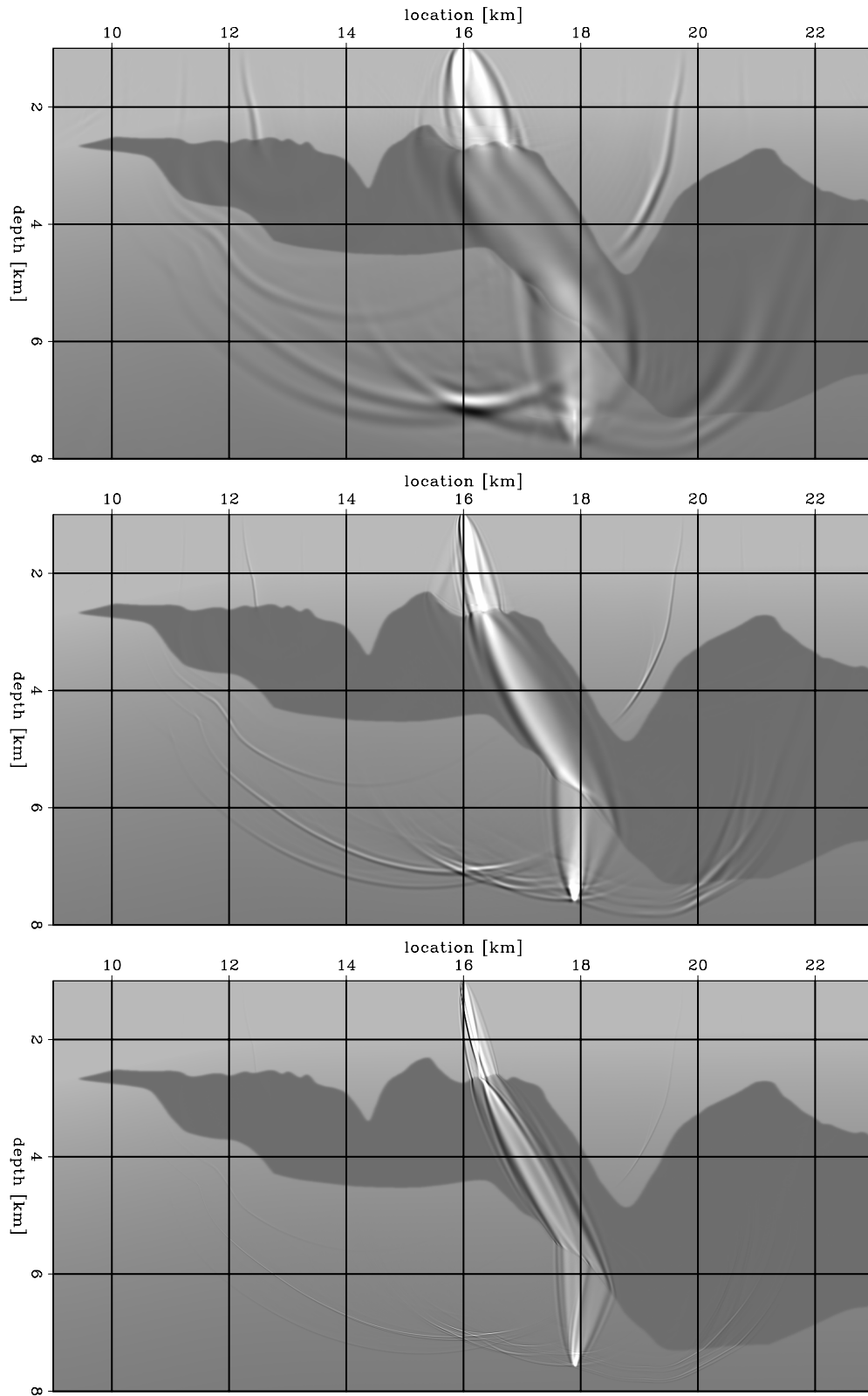


Figure 12.2: Frequency dependence of wavepaths between a location in the image and a point on the surface. Each panel is an overlay of three elements: the slowness model, the wavefield corresponding to a point source on the surface at $x = 16$ km, and wavepaths from a point in the subsurface to the source. The different wavepaths correspond to frequency bands of 1 – 5 Hz (top), 1 – 16 Hz (middle) and 1 – 64 Hz (bottom). The larger the frequency band, the narrower the wave-path. The end member for an infinitely wide frequency band corresponds to an infinitely thin geometrical ray. (This figure is from Sava and Biondi (2004c).) wemva-zifrq2

Figure 12.3: Orthogonal slices cut through a 3-D slowness model containing a salt body. (This figure is from Sava and Biondi (2004c))

`wemva-fat3.sC` [NR]

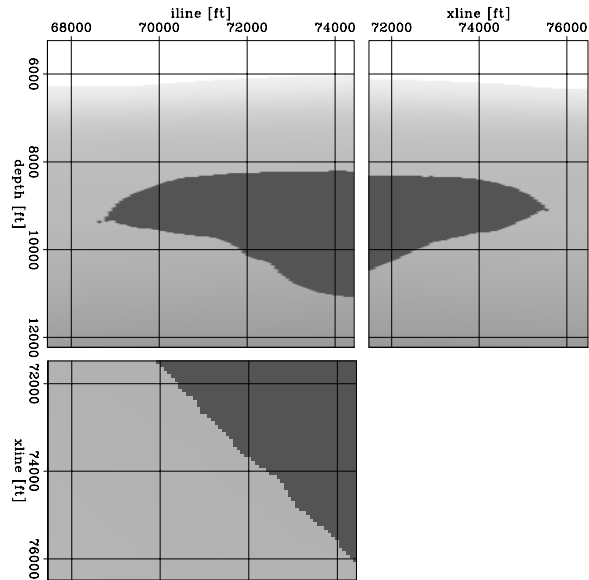
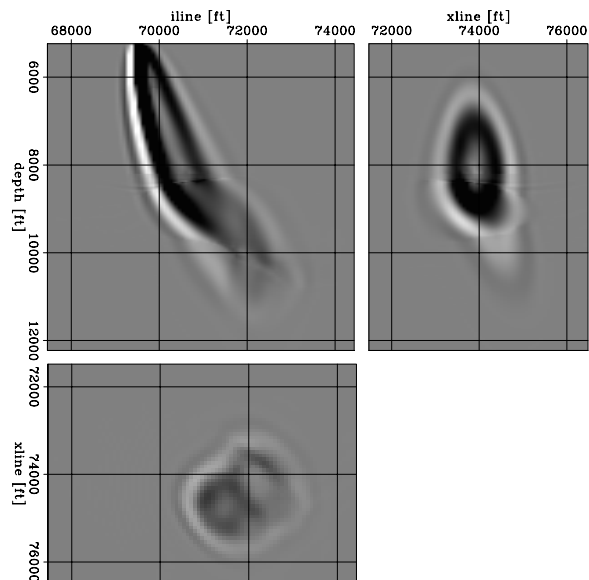


Figure 12.4: Orthogonal slices cut through the 3-D sensitivity kernel for wave-equation MVA. The frequency range is 1 – 16 Hz. The kernels are complicated by the multipathing occurring as waves propagate through the salt body. (This figure is from Sava and Biondi (2004c).)

`wemva-fat3.fp3` [NR]



where \mathbf{s} is the slowness function, and \mathbf{C}_s is an estimate of the covariance matrix of the slowness function, as discussed for ray-based MVA in Chapter 11.

In practice, defining an objective function for both the amplitudes and the kinematics of the image that can be effectively optimized is more challenging than for the simple kinematics. In the case of ray-based MVA, the target is defined as an RMO function that is zero for all angles, but the target image in equation (12.1) cannot be simply set to zero. In practice, the target image must be a function of the migrated image. In general, the target image is the result of enhancing the migrated image by the application of a non-linear “image-enhancing” operator \mathcal{K}_w to the migrated image. Therefore, the objective function of an effective MVA method must be written in a slightly more general form:

$$J_{\text{reg}}(\mathbf{s}) = \|\mathbf{W}_w \{\mathbf{I}(\mathbf{s}) - \mathcal{K}_w[\mathbf{I}(\mathbf{s})]\|_2 + \mathbf{s}' \mathbf{C}_s^{-1} \mathbf{s}, \quad (12.2)$$

where \mathbf{W}_w is a weighting operator that enhances the image components that we want to penalize (or reward), so that the optimization problem defined by the objective function (12.2) becomes tractable with gradient-based methods.

The properties of the operators \mathcal{K}_w and \mathbf{W}_w are the main distinguishing elements among existing wavefield-based MVA methods. The following list summarizes the choices of three well-known approaches:

- In the Differential Semblance Optimization (DSO) method (Symes and Carazzone, 1991; Shen et al., 2003), the linear operator \mathbf{W}_w is a differential operator acting along the angle axes in the ADCIGs, and $\mathcal{K}_w = 0$. The rationale for this choice of objective function is that by minimizing the differences between the migrated images of contiguous angles we drive the optimization process toward flat ADCIGs.
- In the Multiple Migration Fitting (MMF) method (Chavent and Jacewitz, 1995) the linear operator \mathbf{W}_w is a stacking operator along the angle axes in the ADCIGs, and $\mathcal{K}_w = 0$. The MMF objective function is maximized, instead of being minimized. By maximizing the stack power along angles, we reward well-focused images, and images that are coherent along the angle axes.
- In the Wave-Equation MVA (WEMVA) method (Biondi and Sava, 1999; Sava and Biondi, 2004a,b), the target image $\hat{\mathbf{I}}$ is an improved version of the migrated image \mathbf{I} , and \mathbf{W}_w is the identity operator. In this case, \mathcal{K}_w is represented by an operator performing residual moveout (Section 11.2.1) or residual migration (Section 11.2.2), as a function of spatially varying values of ρ . For a fixed value of ρ , these residual imaging operators are linear with respect to the image, and thus they can be represented by the linear operator $\mathbf{K}_w(\rho)$. The non-linearity of \mathcal{K}_w derives from the fact that the values of ρ are determined based on the migrated image itself.

The objective function expressed in equation (12.2) is highly non-quadratic. It could be optimized by applying algorithms specifically designed for non-quadratic problems. A good choice could be a version of the quasi-Newton algorithm (Gill et al., 1981) that does not

require the storage of the complete Hessian; Guitton and Symes (2003) describe a useful seismic application of such an algorithm (BFGS-L). Alternatively, a version of the conjugate-gradient algorithm that is effective for non-quadratic problems, such as the conjugate-direction algorithm, can also be used (Claerbout, 2004).

As I discussed in Section 11.4.4, the convergence of the velocity estimation process greatly benefits when some crucial tasks, such as the determination of RMO parameters and the estimation of the covariance of the slowness function, are performed in conjunction with the interpretation of the migrated images. Because the interpretation of prestack images can be realistically carried out only a limited number of times during the estimation process, the use of fully automated optimization algorithms is challenging in practice. Therefore, in my analysis I follow the same approach used for ray-based MVA (Section 11.4), and address the non-quadratic nature of the problem by repeatedly solving the quadratic optimization problems obtained by linearizing the objective function (12.2).

After each linearization, the perturbed image can be approximated as a linear function of the slowness perturbation ${}_i\Delta\mathbf{s}$, as follows:

$$I({}_{i-1}\hat{\mathbf{s}} + {}_i\Delta\mathbf{s}) \approx {}_{i-1}\mathbf{I} + {}_i\mathbf{M}_w {}_i\Delta\mathbf{s}, \quad (12.3)$$

where the left subscript i indicates the iteration number, ${}_{i-1}\hat{\mathbf{s}}$ is the current background slowness, ${}_{i-1}\mathbf{I}$ is the background image obtained by prestack migration with ${}_{i-1}\hat{\mathbf{s}}$, and ${}_i\mathbf{M}_w$ is a linearization of the prestack migration functional at ${}_{i-1}\hat{\mathbf{s}}$.

Substituting the expression (12.3) into the objective function (12.2), we obtain the following quadratic objective function:

$$\begin{aligned} J_{\text{reg}}({}_i\Delta\mathbf{s}) &= \|\mathbf{W}_w({}_{i-1}\mathbf{I} + {}_i\mathbf{M}_w {}_i\Delta\mathbf{s} - {}_i\mathbf{K}_w {}_{i-1}\mathbf{I})\|_2 + ({}_{i-1}\hat{\mathbf{s}} + {}_i\Delta\mathbf{s})' {}_i\mathbf{C}_s^{-1} ({}_{i-1}\hat{\mathbf{s}} + {}_i\Delta\mathbf{s}) = \\ &= \|\mathbf{W}_w({}_i\mathbf{M}_w {}_i\Delta\mathbf{s} - {}_i\Delta\mathbf{I})\|_2 + ({}_{i-1}\hat{\mathbf{s}} + {}_i\Delta\mathbf{s})' {}_i\mathbf{C}_s^{-1} ({}_{i-1}\hat{\mathbf{s}} + {}_i\Delta\mathbf{s}), \end{aligned} \quad (12.4)$$

where ${}_i\mathbf{C}_s$ is the current estimate of the slowness covariance, ${}_i\mathbf{K}_w$ is the image-enhancing operator determined by analyzing the current migrated image ${}_{i-1}\mathbf{I}$, and

$${}_i\Delta\mathbf{I} = ({}_i\mathbf{K}_w {}_{i-1}\mathbf{I} - {}_{i-1}\mathbf{I}) = ({}_i\mathbf{K}_w - \mathbf{1}) {}_{i-1}\mathbf{I} \quad (12.5)$$

is the actual image perturbation fitted during each linearized iteration. In equation (12.5) the symbol $\mathbf{1}$ stands for the identity operator, to avoid confusion with the image \mathbf{I} .

To assure that a gradient-based optimization converges to a useful estimate of the slowness perturbations, it is necessary for ${}_i\Delta\mathbf{I}$ to be consistent with the linearization of the wave-propagation process that we use to evaluate ${}_i\mathbf{M}_w$. The next section presents a method for evaluating ${}_i\mathbf{M}_w$ for downward-continuation migration, and the following section addresses the issue of computing a ${}_i\Delta\mathbf{I}$ that is consistent with ${}_i\mathbf{M}_w$.

12.2 Linearization of wave propagation with respect to the velocity function

To solve the quadratic optimization problem defined by the objective function (12.4), we need an algorithm for applying the linearized wavefield-MVA operator, \mathbf{M}_w , to a slowness-perturbations vector, $\Delta\mathbf{s}$, and computing the corresponding image-perturbations vector, $\Delta\mathbf{I}$.

Similarly, we must be able to apply its adjoint, \mathbf{M}'_w , to an image-perturbations vector, $\Delta\mathbf{I}'$, and compute the corresponding slowness-perturbations vector, $\Delta\mathbf{s}'$.

A crucial component of the evaluation of \mathbf{M}_w is the linearization of wave propagation. Two ways to linearize wave propagation with respect to velocity perturbations (**wavefield scattering**) have been developed and applied in the literature: the **Born linearization** and the **Rytov linearization**. The two methods can be derived using the same mathematical formalism; both methods are derived by truncating after the first-order term the Taylor series of the total perturbed wavefield, expanded as a function of the velocity perturbation. The zero-order term in the Taylor expansion represents the **background wavefield**, and the first-order term represents the **single-scattered wavefield**.

The main difference between the two approximations is that when the Born approximation is derived, the Taylor expansion is defined in terms of the amplitudes (real and imaginary) of the complex-valued wavefield, whereas for the Rytov approximation, the Taylor expansion is defined in terms of the complex phase (i.e. complex logarithm of the complex amplitude) of the wavefield (Devaney, 1981).

The Born approximation underlies most of the migration methods (Cohen and Bleistein, 1979; Clayton and Stolt, 1981; Stolt and Weglein, 1985; Stolt and Benson, 1986). However, for the purposes of velocity analysis, the Rytov approximation is more appealing at first sight, because it better approximates phase delays caused by large velocity anomalies (Devaney, 1981; Woodward, 1990). However, the Rytov approximation has severe shortcomings when complex multipathing occurs in the background wavefield, because phase perturbations are not additive. Furthermore, practical applications of the Rytov linearization require phase unwrapping, which is a task prone to errors with complex and noisy data. In contrast, the Born approximation has no difficulties with multipathing in the background wavefield, and does not require phase unwrapping. Furthermore, the evaluation and propagation of the scattered wavefield is fairly straightforward. However, the Born linearization fails when the phase differences between the perturbed and background wavefields are larger than a fraction of the wavelet, making it difficult to properly handle large velocity perturbations. The preceding brief discussion of the issues relating the Born and Rytov linearizations of the wave-equation is by necessity incomplete: *Fundamentals of Seismic Tomography* (Lo and Inderweisen, 1994) provides a succinct but clear description of both approximations, and Woodward (1990) clearly discusses the advantages and disadvantages of both approximations.

Most of the wavefield-MVA methods that have been presented in the literature are based on the Born approximation as is the evaluation of the linearized wavefield-MVA operator presented in this section. The challenge is to avoid the Born approximation's limitations, and to devise an MVA method that is capable of correctly handling large velocity perturbations. Section 12.3 analyzes this issue for the DSO, MMF, and WEMVA methods, applying the insight into the Born approximation gained by the detailed analysis presented in this section. Section 12.4 presents a solution that solves this challenge for the WEMVA method. In this section I present the method introduced by Biondi and Sava (1999), for evaluating \mathbf{M}_w and its adjoint for source-receiver migration. The same concepts can be easily applied for shot-profile migration (Shen et al., 2003), or any other downward-continuation migration.

12.2.1 Application of \mathbf{M}_w and \mathbf{M}'_w by downward continuation

The development of the algorithm for the evaluation of \mathbf{M}_w is somewhat intricate, because the two perturbations vectors, $\Delta\mathbf{s}$ and $\Delta\mathbf{I}$, are not directly linked. They are connected through two intermediary vector fields: the background wavefield, \mathbf{P} , and the scattered wavefield, $\Delta\mathbf{P}$. Three operators also play a role in this algorithm: the downward-continuation operator, \mathbf{E} , the imaging operator, $\mathbf{\Sigma}$, and the **scattering operator**, \mathbf{G} . The downward-continuation operator and the imaging operator are the familiar components of downward-continuation migration (Chapter 4), whereas the scattering operator is described in detail in this section.

The flow-chart in Figure 12.5 summarizes the algorithm for evaluating \mathbf{M}_w and its adjoint. The three components are labeled as A, B and C on the chart. Box A corresponds to the computation of the background wavefield, based on the surface data, \mathbf{D} , and background slowness, $\hat{\mathbf{s}}$. Boxes B and C correspond respectively to the forward and adjoint \mathbf{M}_w operator.

Computation of the background wavefield

Imaging by source-receiver migration (Section 4.2.2) is based on the following recursive continuation of the wavefields, \mathbf{P}_z , from a given depth level, z , to the next, $z + \Delta z$, by means of the Double Square Root operator, $\mathbf{E}(\hat{\mathbf{s}}_z)$, which is function of the slowness vector, $\hat{\mathbf{s}}_z$:

$$\mathbf{P}_{z+\Delta z} = \mathbf{E}_z(\hat{\mathbf{s}}_z)\mathbf{P}_z. \quad (12.6)$$

All the steps of this recursive extrapolation can also be expressed in matrix form as follows:

$$\begin{pmatrix} \mathbf{P}_0 \\ \mathbf{P}_1 \\ \mathbf{P}_2 \\ \vdots \\ \mathbf{P}_n \end{pmatrix} = \begin{pmatrix} \mathbf{0} & \mathbf{0} & \mathbf{0} & \cdots & \mathbf{0} & \mathbf{0} \\ \mathbf{E}_0 & \mathbf{0} & \mathbf{0} & \cdots & \mathbf{0} & \mathbf{0} \\ \mathbf{0} & \mathbf{E}_1 & \mathbf{0} & \cdots & \mathbf{0} & \mathbf{0} \\ \vdots & \vdots & \vdots & \vdots & \vdots & \vdots \\ \mathbf{0} & \mathbf{0} & \mathbf{0} & \cdots & \mathbf{E}_{n-1} & \mathbf{0} \end{pmatrix} \begin{pmatrix} \mathbf{P}_0 \\ \mathbf{P}_1 \\ \mathbf{P}_2 \\ \vdots \\ \mathbf{P}_n \end{pmatrix} + \begin{pmatrix} \mathbf{D}_0 \\ 0 \\ 0 \\ \vdots \\ 0 \end{pmatrix}, \quad (12.7)$$

where \mathbf{D}_0 is the data recorded at the surface. Or, in a more compact notation,

$$\mathbf{P} = \mathbf{E}(\hat{\mathbf{s}})\mathbf{P} + \mathbf{D}. \quad (12.8)$$

Here and hereafter, I use the subscripts z and $z + \Delta z$ to distinguish the quantities measured at a particular depth level (e.g. \mathbf{P}_z), from the corresponding vectors denoting such quantities at all depth levels (e.g. \mathbf{P}). The recursive relationship in equation (12.8) can be formally solved as follows:

$$\mathbf{P} = [\mathbf{1} - \mathbf{E}(\hat{\mathbf{s}})]^{-1} \mathbf{D}, \quad (12.9)$$

where $\mathbf{1}$ stands for the identity operator.

After wavefield extrapolation, we obtain an image by applying, at every depth level, an imaging operator, $\mathbf{\Sigma}_z$, to the extrapolated wavefield \mathbf{P}_z :

$$\mathbf{I}_z = \mathbf{\Sigma}_z \mathbf{P}_z, \quad (12.10)$$

where \mathbf{I}_z stands for the image at the z level. A commonly used imaging operator involves summation over the temporal frequencies (Section 4.2.2). We can write the same relation in compact matrix form:

$$\mathbf{I} = \mathbf{\Sigma} \mathbf{P} = \mathbf{\Sigma} [\mathbf{1} - \mathbf{E}(\hat{\mathbf{s}})]^{-1} \mathbf{D}, \quad (12.11)$$

where \mathbf{I} stands for the image, and $\mathbf{\Sigma}$ stands for the imaging operator which is applied to the extrapolated wavefield \mathbf{P} at all depth levels.

The downward-continuation expression (12.8) and the imaging expression (12.11) summarize the computation of the background wavefield and the background image that is represented by Box A in Figure 12.5. The background wavefield is an important component of the wavefield-MVA operator. This wavefield plays a role analogous to the one played in travelttime tomography by the ray-field obtained by ray tracing in the background model. The wavefield is the carrier of information and defines the wavepaths along which we spread the velocity errors measured from the migrated images, which are obtained using the background slowness function. Unlike a ray-field, which describes propagation of waves with an infinite frequency band, the wavefield is band-limited. It provides a more accurate description of wave propagation through complicated media than a corresponding ray-field (Figures 12.1 and 12.2). Typical applications are salt bodies characterized by large velocity contrasts, where ray tracing is both unstable and inaccurate.

Application of the forward operator

At each depth level, the interaction of the propagating wavefield with a slowness perturbation creates a scattered wavefield, which is summed to the scattered wavefield created at the depth levels above. When computing the scattered wavefield at each depth level, we should consider the interaction between the total propagating wavefield (background and scattered) and the velocity perturbations. However, to maintain the linearity of the relationship, we limit the computations only to the contributions of the background wavefield to the scattering process, neglecting the contributions of the scattered wavefield created at the previous depth levels. These contributions are considered second-order; their omission constitutes the first-order Born approximation discussed above. Because of the first-order approximation, we can also neglect the scattered wavefield propagating in the direction opposite to the propagation direction of the background wavefield. Therefore, we consider only the forward-scattered wavefield, and we propagate the scattered wavefield in the same direction as the background wavefield; that is, only toward increasing depths.

The contribution to the scattered wavefield, $\Delta \mathbf{U}_{z+\Delta z}$, is generated by the interaction of the background wavefield, \mathbf{P}_z , with a perturbation of the velocity model, $\Delta \mathbf{s}_z$, which is then propagated from z to $z + \Delta z$; that is,

$$\Delta \mathbf{U}_{z+\Delta z} = \mathbf{E}_z(\hat{\mathbf{s}}_z) \mathbf{G}_z(\mathbf{P}_z, \hat{\mathbf{s}}_z) \Delta \mathbf{s}_z, \quad (12.12)$$

where the scattering operator \mathbf{G}_z is function of both the incident background wavefield and the local background slowness function $\hat{\mathbf{s}}_z$. After scattering occurs, the scattered wavefield is propagated downward using the same operator, \mathbf{E}_z , and background slowness, $\Delta \mathbf{s}_z$, that are

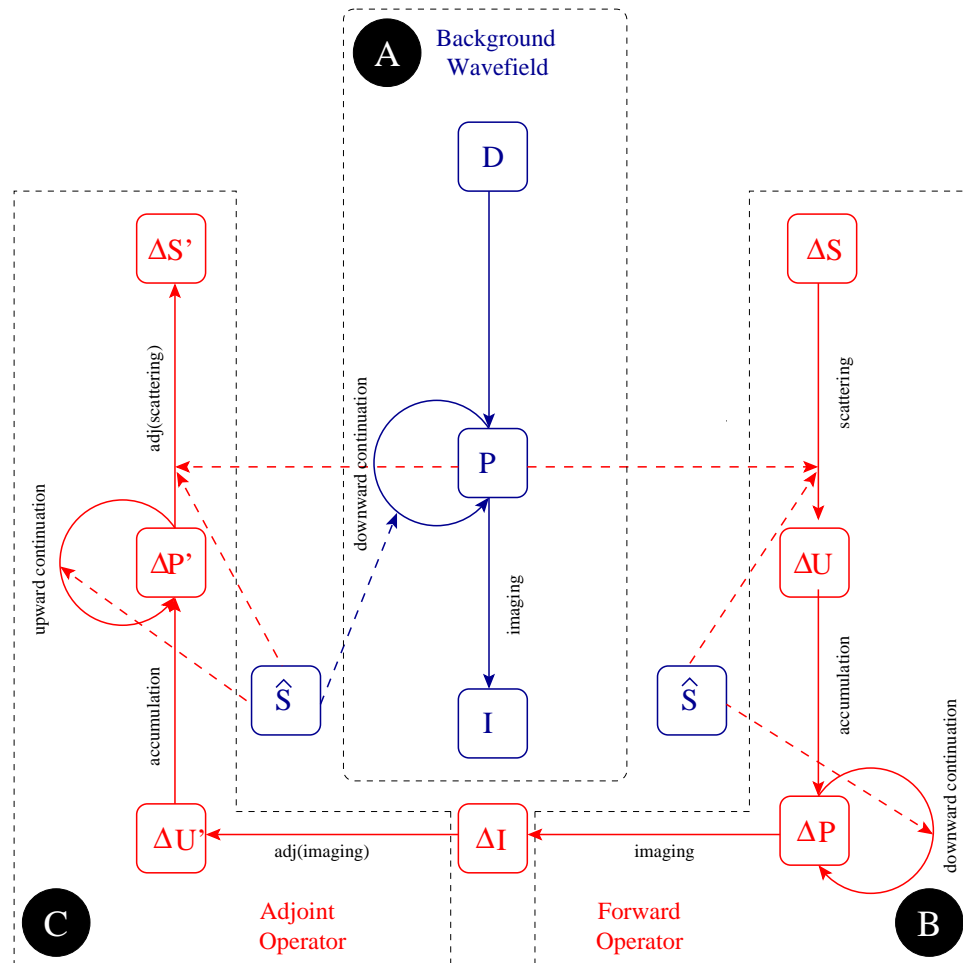


Figure 12.5: Box A – Background Wavefield: The data recorded at the surface (**D**) are extrapolated in depth using the background slowness (\hat{s}), generating the background wavefield (**P**); the background wavefield (**P**) is transformed into the background image (**I**) using an imaging operator. Box B - Forward Operator: The background wavefield (**P**) interacts with a slowness perturbation (Δs), generating a scattered wavefield (ΔU); after depth extrapolation, the locally scattered wavefield is accumulated into a total scattered wavefield (ΔP), which is transformed into an image perturbation (ΔI) using an imaging operator. Box C - Adjoint Operator: The image perturbation (ΔI) is transformed into the scattered wavefield ($\Delta U'$) using the adjoint of the imaging operator. The locally scattered wavefield is accumulated into the adjoint-state scattered wavefield ($\Delta P'$), which is upward continued, and at every depth level it is transformed into an adjoint slowness perturbation ($\Delta s'$), by applying the adjoint of the scattering operator. wemva-wemva_chart-v5 [NR]

used to propagate the background wavefield. Therefore, the scattered wavefield propagates along the same wavepaths as the background wavefield.

The total scattered wavefield at depth $z + \Delta z$, $\Delta \mathbf{P}_{z+\Delta z}$, is the result of downward continuation from z to $z + \Delta z$ of the sum of $\Delta \mathbf{U}_{z+\Delta z}$ with the total scattered wavefield at depth z , $\Delta \mathbf{P}_z$; that is,

$$\Delta \mathbf{P}_{z+\Delta z} = \mathbf{E}_z(\hat{\mathbf{s}}_z) \Delta \mathbf{P}_z + \Delta \mathbf{U}_{z+\Delta z}. \quad (12.13)$$

Substituting equation (12.12) into equation (12.13) we obtain,

$$\Delta \mathbf{P}_{z+\Delta z} = \mathbf{E}_z(\hat{\mathbf{s}}_z) \Delta \mathbf{P}_z + \mathbf{E}_z(\hat{\mathbf{s}}_z) \mathbf{G}_z(\mathbf{P}_z, \hat{\mathbf{s}}_z) \Delta \mathbf{s}_z, \quad (12.14)$$

which also can be written in matrix form as follows:

$$\begin{pmatrix} \Delta \mathbf{P}_0 \\ \Delta \mathbf{P}_1 \\ \Delta \mathbf{P}_2 \\ \vdots \\ \Delta \mathbf{P}_n \end{pmatrix} = \begin{pmatrix} \mathbf{0} & \mathbf{0} & \mathbf{0} & \cdots & \mathbf{0} & \mathbf{0} \\ \mathbf{E}_0 & \mathbf{0} & \mathbf{0} & \cdots & \mathbf{0} & \mathbf{0} \\ \mathbf{0} & \mathbf{E}_1 & \mathbf{0} & \cdots & \mathbf{0} & \mathbf{0} \\ \vdots & \vdots & \vdots & \ddots & \vdots & \vdots \\ \mathbf{0} & \mathbf{0} & \mathbf{0} & \cdots & \mathbf{E}_{n-1} & \mathbf{0} \end{pmatrix} \begin{pmatrix} \Delta \mathbf{P}_0 \\ \Delta \mathbf{P}_1 \\ \Delta \mathbf{P}_2 \\ \vdots \\ \Delta \mathbf{P}_n \end{pmatrix} + \begin{pmatrix} \mathbf{0} & \mathbf{0} & \mathbf{0} & \cdots & \mathbf{0} & \mathbf{0} \\ \mathbf{E}_0 & \mathbf{0} & \mathbf{0} & \cdots & \mathbf{0} & \mathbf{0} \\ \mathbf{0} & \mathbf{E}_1 & \mathbf{0} & \cdots & \mathbf{0} & \mathbf{0} \\ \vdots & \vdots & \vdots & \ddots & \vdots & \vdots \\ \mathbf{0} & \mathbf{0} & \mathbf{0} & \cdots & \mathbf{E}_{n-1} & \mathbf{0} \end{pmatrix} \begin{pmatrix} \mathbf{G}_0 & \mathbf{0} & \mathbf{0} & \cdots & \mathbf{0} \\ \mathbf{0} & \mathbf{G}_1 & \mathbf{0} & \cdots & \mathbf{0} \\ \mathbf{0} & \mathbf{0} & \mathbf{G}_2 & \cdots & \mathbf{0} \\ \vdots & \vdots & \vdots & \ddots & \vdots \\ \mathbf{0} & \mathbf{0} & \mathbf{0} & \cdots & \mathbf{G}_n \end{pmatrix} \begin{pmatrix} \Delta \mathbf{s}_0 \\ \Delta \mathbf{s}_1 \\ \Delta \mathbf{s}_2 \\ \vdots \\ \Delta \mathbf{s}_n \end{pmatrix},$$

or in a more compact notation as follows:

$$\Delta \mathbf{P} = \mathbf{E}(\hat{\mathbf{s}}) \Delta \mathbf{P} + \Delta \mathbf{U} = \mathbf{E}(\hat{\mathbf{s}}) \Delta \mathbf{P} + \mathbf{E}(\hat{\mathbf{s}}) \mathbf{G}(\mathbf{P}, \hat{\mathbf{s}}) \Delta \mathbf{s}, \quad (12.15)$$

where the vector $\Delta \mathbf{s}$ stands for the slowness perturbation at all depths, and the vector $\Delta \mathbf{U}$ stands for the contributions to the scattered wavefields at all depths. The formal solution of the recursive equation (12.15) is

$$\Delta \mathbf{P} = [\mathbf{1} - \mathbf{E}(\hat{\mathbf{s}})]^{-1} \mathbf{E}(\hat{\mathbf{s}}) \mathbf{G}(\mathbf{P}, \hat{\mathbf{s}}) \Delta \mathbf{s}. \quad (12.16)$$

By applying the imaging operator to the scattered wavefield, $\Delta \mathbf{P}$, we obtain a linear relationship between the image perturbations, $\Delta \mathbf{I}$, and the slowness perturbations, $\Delta \mathbf{s}$, and consequently, an expression for the forward operator \mathbf{M}_w :

$$\Delta \mathbf{I} = \boldsymbol{\Sigma} [\mathbf{1} - \mathbf{E}(\hat{\mathbf{s}})]^{-1} \mathbf{E}(\hat{\mathbf{s}}) \mathbf{G}(\mathbf{P}, \hat{\mathbf{s}}) \Delta \mathbf{s} = \mathbf{M}_w \Delta \mathbf{s}. \quad (12.17)$$

Notice the parallelism between equation (12.11) and equation (12.17), or analogously between the recursive relationships (12.8) and (12.15). In equation (12.15), the scattered wavefield $\Delta \mathbf{U}$ that is generated by the interactions of the background wavefield with the slowness perturbations acts as “source term” at each depth level. In the conventional downward-continuation process, equation (12.8), the recorded data acts as a source at the surface. The process for evaluating the forward operator, \mathbf{M}_w , is summarized in Box B in Figure 12.5.

Application of the adjoint operator

To optimize the MVA objective function (12.4), we need to evaluate the adjoint operator, \mathbf{M}'_w , that backprojects the image perturbations $\Delta \mathbf{I}'$ into slowness perturbations $\Delta \mathbf{s}'$. Its application could be computed by applying the general **adjoint-state methodology**, as defined by Lions (1971), but the formal derivation of the adjoint operator from equation (12.17) is the most

straightforward. If we take the adjoint of the operator expressed in equation (12.17), we can write the following expression:

$$\Delta \mathbf{s}' = \mathbf{G}'(\mathbf{P}, \hat{\mathbf{s}}) \mathbf{E}'(\hat{\mathbf{s}}) [\mathbf{1} - \mathbf{E}'(\hat{\mathbf{s}})]^{-1} \Sigma' \Delta \mathbf{I}'. \quad (12.18)$$

This formal expression for the adjoint operator can be unraveled and written as an upward continuation of an **adjoint-state scattered wavefield**, $\Delta \mathbf{P}'$,

$$\Delta \mathbf{P}' = \mathbf{E}'(\hat{\mathbf{s}}) \Delta \mathbf{P}' + \Delta \mathbf{U}', \quad (12.19)$$

where $\Delta \mathbf{U}' = \Sigma' \Delta \mathbf{I}'$, followed by an “imaging” step,

$$\Delta \mathbf{s}' = \mathbf{G}'(\mathbf{P}, \hat{\mathbf{s}}) \mathbf{E}'(\hat{\mathbf{s}}) \Delta \mathbf{P}'. \quad (12.20)$$

The combination of equations (12.19) and (12.20) provides an algorithm for applying the adjoint operator \mathbf{M}'_w to image perturbations $\Delta \mathbf{I}'$ and computing slowness perturbations $\Delta \mathbf{s}'$. Box C in Figure 12.5. summarizes the process for evaluating \mathbf{M}'_w .

Although it is not obvious at first sight, the operation represented by equation (12.20) is indeed an imaging-like step. It represents a correlation between the adjoint-state scattered wavefield, $\Delta \mathbf{P}'$, and the background wavefield phase-rotated by 90 degrees, $i\mathbf{P}$, as shown by the expression of the scattering operator, \mathbf{G} , in equation (12.23). If the phases of $i\mathbf{P}$ (or $-i\mathbf{P}$) and $\Delta \mathbf{P}'i$ are close to each other, approximately within a ± 45 degree interval, the correlation generates coherent positive (or negative) slowness perturbations that provide useful search directions for the optimization algorithm. If the phases are not close to one another, the correlation generates incoherent slowness perturbations, possibly even with the wrong sign.

In equation (12.19) the image perturbations $\Delta \mathbf{I}'$ act as source term, and thus the phase of $\Delta \mathbf{P}'$ is related to the phase of $\Delta \mathbf{I}'$, whereas the phase of \mathbf{P} is related to the phase of \mathbf{I} through the imaging condition (12.10). Therefore, the relative phase delay of the adjoint-state scattered wavefield with respect to the background wavefield depends on the distance between the events in the image perturbation $\Delta \mathbf{I}'$ and the background image \mathbf{I} . If the reflectors in the two images are sufficiently close, a velocity-estimation process based on the Born approximation converges; otherwise it may diverge.

The scattering operator

The scattering operator, \mathbf{G} , enters into the computation of both the forward and the adjoint wavefield-MVA operators. It can be derived by physical considerations or can be simply derived by a formal linearization of the depth-propagation operator. This formal derivation is related to the Taylor expansion of the SSR equation introduced in Section 5.2.2, but in this case the entire wavefield, and not just the exponent, is linearized. From the approximation of the SSR operator in equation 5.4 we write

$$\mathbf{P}_{z+\Delta z} = e^{ik_z \Delta z} \mathbf{P}_z \approx e^{\left(i \Delta z \hat{k}_z + i \Delta z \frac{dk_z}{ds} \Big|_{s=\hat{\mathbf{s}}}\right) \Delta \mathbf{s}} \mathbf{P}_z \approx e^{i \Delta z \hat{k}_z} \mathbf{P}_z + e^{i \Delta z \hat{k}_z} \left(i \Delta z \frac{dk_z}{ds} \Big|_{s=\hat{\mathbf{s}}} \right) \mathbf{P}_z \Delta \mathbf{s}, \quad (12.21)$$

where

$$\left. \frac{dk_z}{ds} \right|_{s=\hat{s}} = \frac{\omega}{\sqrt{1 - \frac{|\mathbf{k}|^2}{\omega^2 \hat{s}^2}}}. \quad (12.22)$$

By comparing the last term in equation (12.21) with the last term in equation (12.14), we can write the scattering operator as follows:

$$\mathbf{G}(\mathbf{P}, \hat{s}) = i \Delta z \left. \frac{dk_z}{ds} \right|_{s=\hat{s}} \mathbf{P}_z = \frac{i \omega \Delta z}{\sqrt{1 - \frac{|\mathbf{k}|^2}{\omega^2 \hat{s}^2}}} \mathbf{P}_z. \quad (12.23)$$

The scattering operator expressed in equation (12.23) is a linear function of the background wavefield \mathbf{P}_z , and a non-linear function of the background slowness \hat{s} . Because the background slowness is a spatially varying function, the dip-dependent weight expressed by the denominator in equation (12.23) is spatially non-stationary, and the expression in equation (12.23) is a mixed-domain representation of \mathbf{G} . Its numerical implementation presents challenges similar to those encountered implementing the SSR operator for downward-continuing wavefields in laterally varying media. However, in contrast with the downward-continuation case, the scattering operator is not applied recursively. Therefore, the implementation of \mathbf{G} is not subject to the same stringent stability requirements as the SSR operator is; the computations of \mathbf{G} do not diverge even if its magnitude is not uniformly less than one for all wavenumbers.

A straightforward method for applying the scattering operator was proposed by Huang et al. (1999) in the context of approximating the SSR for downward continuation. Whereas this numerical method is unstable when applied to downward continuation, it is appropriate for applying \mathbf{G} . The method is based on the following Taylor series expansion (Sava and Biondi, 2004a):

$$i \Delta z \left. \frac{dk_z}{ds} \right|_{\hat{s}} \mathbf{P}_z \approx i \omega \Delta z \left[1 + \frac{1}{2} \left(\frac{|\mathbf{k}|}{\omega \hat{s}} \right)^2 + \frac{3}{8} \left(\frac{|\mathbf{k}|}{\omega \hat{s}} \right)^4 + \frac{5}{16} \left(\frac{|\mathbf{k}|}{\omega \hat{s}} \right)^6 + \frac{35}{128} \left(\frac{|\mathbf{k}|}{\omega \hat{s}} \right)^8 + \dots \right] \mathbf{P}_z. \quad (12.24)$$

The even powers of $|\mathbf{k}|$ represent spatial-derivative operators that can be applied either in the space domain by finite-difference approximations, or in the Fourier domain.

Simple examples of the application of \mathbf{M}_w and \mathbf{M}'_w

Figures 12.6 and 12.7 illustrate the flow-chart in Figure 12.5, by showing its application to two simple examples. In the first example (Figure 12.6), I use a monochromatic wavefield, whereas in the second one (Figure 12.7), I use a wide-band wavefield. For both examples the data are recorded above a planar horizontal reflector.

Figure 12.6a shows a snapshot (taken at time zero) of the monochromatic background wavefield obtained by downward continuation of an incident plane wave in a constant medium. Figure 12.6b shows a slowness perturbation that, under the influence of the incident wavefield (a), generates a wavefield perturbation (c). The snapshots at zero time shown in panels (a) and

(c) can also be regarded as images. Finally, I back-propagate the image perturbation (c) and obtain the adjoint slowness perturbation (d).

Figure 12.7 shows panels analogous to those shown in Figure 12.6, but for wide-band data. Figure 12.7a shows the image obtained by wavefield extrapolation of a wide-band plane wave in the background medium. From the same slowness perturbation (b) as in the preceding example, I obtain an image perturbation (c), from which I generate an adjoint slowness perturbation (d) using the background wavefield used to compute the background image.

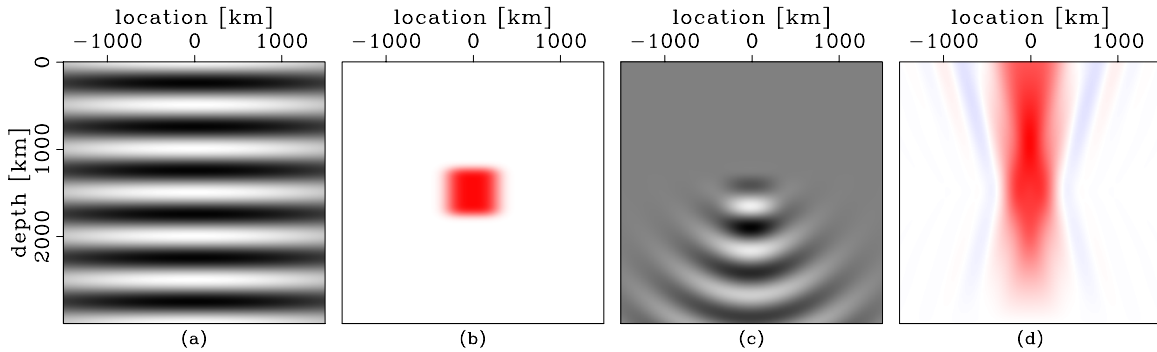


Figure 12.6: Monochromatic WEMVA example: background wavefield (a), slowness perturbation (b), wavefield perturbation (c), slowness backprojection (d). (This figure is from Sava (2004).) `wemva-SCATbas1.scats` [NR]

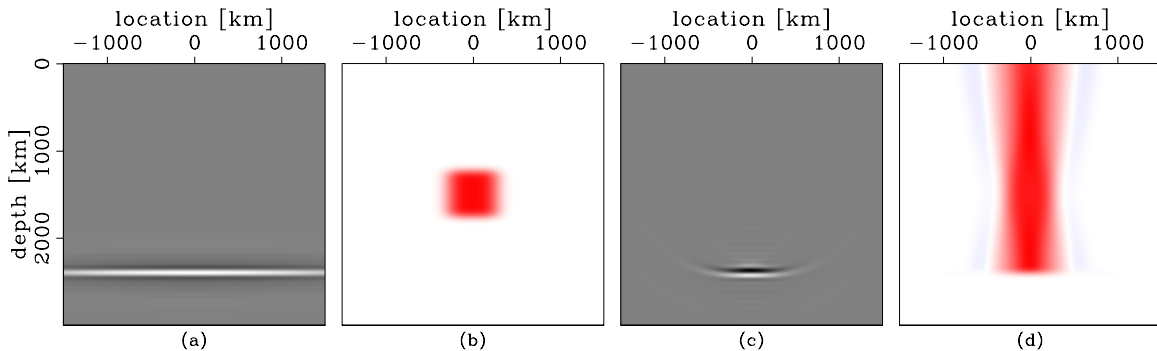


Figure 12.7: Wide-band WEMVA example: background image (a), slowness perturbation (b), image perturbation (c), slowness backprojection (d). (This figure is from Sava (2004).) `wemva-SCATbasN.scats` [NR]

12.3 Convergence of wavefield migration velocity analysis

In the previous section (Section 12.2), I presented a general approach for computing the linearized MVA operator, \mathbf{M}_w , associated with downward-continuation migration, and a specific algorithm to for source-receiver migration. This methodology can be applied to the velocity-estimation problem defined by the the non-quadratic objective function (12.2), and by the

linearized objective function (12.4). These objective functions define a family of wavefield-MVA methods; a specific method within this family is determined by the choice of the two operators \mathcal{K}_w and \mathbf{W}_w . In Section 12.1 I briefly discussed three choices for the operators \mathbf{W}_w and \mathcal{K}_w that correspond to three known methods for wavefield MVA: DSO, MMF and WEMVA. In this section I will further discuss these three methods in light of the properties of \mathbf{M}_w discussed in Section 12.2. In particular, I address the important issue of whether a specific choice for \mathcal{K}_w and \mathbf{W}_w yields an MVA method that converges even in presence of large errors in the background velocity function.

To analyze the issue of convergence, I consider the gradient direction computed by back-projecting the image perturbations into the slowness model. This back-projection is performed by applying the adjoint operator \mathbf{M}'_w to the image perturbations $\Delta\mathbf{I}$. As discussed in (Section 12.2.1), we expect a useful gradient direction when the phase difference between the background image \mathbf{I} and the image perturbation $\Delta\mathbf{I}$ is sufficiently small to fulfill the assumptions of the Born approximation.

The general form of the image perturbation ${}_i\widetilde{\Delta\mathbf{I}}$ that is actually back-projected at the i -th linearized iteration can be directly derived from the objective function (12.4) as follows:

$${}_i\widetilde{\Delta\mathbf{I}} = \mathbf{W}'_w \mathbf{W}_w ({}_i\mathbf{M}_w {}_i\Delta\mathbf{s} - {}_i\Delta\mathbf{I}) = \mathbf{W}'_w \mathbf{W}_w [{}_i\mathbf{M}_w {}_i\Delta\mathbf{s} - ({}_i\mathbf{K}_w - \mathbf{1}) {}_{i-1}\mathbf{I}], \quad (12.25)$$

For the sake of simplicity, I analyze the gradient direction at the first linearized iteration, when ${}_i\Delta\mathbf{s} = 0$. In this case, equation (12.25) simplifies into

$${}_i\widetilde{\Delta\mathbf{I}} = \mathbf{W}'_w \mathbf{W}_w ({}_i\mathbf{K}_w - \mathbf{1}) {}_{i-1}\mathbf{I}. \quad (12.26)$$

In both the DSO and MMF cases, ${}_i\mathbf{K}_w = 0$, and equation (12.26) further simplifies into

$${}_i\widetilde{\Delta\mathbf{I}} = \mp \mathbf{W}'_w \mathbf{W}_w {}_{i-1}\mathbf{I}. \quad (12.27)$$

The sign is negative for DSO and positive for MMF, because in one case the objective function is minimized, whereas in the other it is maximized.

In the DSO case, \mathbf{W}_w is a differential operator operating along the angle axes in the ADCIGs. Shen et al. (2003) demonstrate that this differential operator in the angle domain is equivalent to a zero-phase (i.e. real diagonal) operator in the subsurface-offset domain. Consequently, the image perturbation ${}_i\widetilde{\Delta\mathbf{I}}$ and the background image ${}_{i-1}\mathbf{I}$ are, by construction, in phase with each other, and the back-projection operator provides useful slowness perturbations.

In contrast, in the MMF case the \mathbf{W}_w operator stacks the background image over angles, whereas its adjoint \mathbf{W}'_w spreads the result of stacking back along the angles. In the presence of large errors in the background velocity function, the ADCIGs show a significant curvature, and thus at wide-aperture angles the reflectors in the stacked image are shifted substantially with respect to the reflectors in the background image. Under these conditions, the relative phase differences between ${}_i\widetilde{\Delta\mathbf{I}}$ and ${}_{i-1}\mathbf{I}$ can exceed the narrow range in which the Born approximation is valid, and the MVA method based on the MMF objective function may never converge toward a satisfactory solution.

In the WEMVA method, the choice of the “image enhancing” operator \mathcal{K}_w plays an important role, whereas \mathbf{W}_w is set to be the identity operator. Ideally the target image would be an image with flat ADCIGs and well-focused reflections in the physical space. Biondi and Sava (1999) proposed to use residual prestack migration (Section 11.2.2) to obtain the target image. Alternatively, residual moveout can be used in place of residual migration to flatten the ADCIGs, albeit without improving the focusing of the reflections (Section 11.2.1). In either case, an “optimal” value for the parameter ρ is measured for all the locations in the image space, and the background image is transformed by using a residual imaging operator ${}_i\mathbf{K}_w(\rho)$, which is a function of ρ . However, a residual imaging operator significantly shifts the image of the reflectors for which $\Delta\rho = \rho - 1$ is sufficiently large. For these reflectors, the relative phase differences between ${}_i\widetilde{\Delta\mathbf{I}}$ and ${}_{i-1}\mathbf{I}$ can easily exceed the narrow range in which the Born approximation is valid, and the WEMVA method based on this choice of \mathcal{K}_w may never converge toward a satisfactory solution. This problem is illustrated in the following sequence of four figures, and its solution is described in Section 12.4.

Illustration of wavefield MVA challenges in the presence of large velocity errors

Large velocity errors present challenges to both the MMF and WEMVA methods as defined in the previous section. The following four figures illustrate the problem faced by WEMVA with a simple example. Figure 12.8 shows three impulse responses of the migration operator. For the sake of simplicity the following figures show the results of zero-offset experiments. The velocity is constant, and the data are represented by an impulse in space and time. We consider two slowness models: the background slowness s , and the “correct” (perturbed) slowness $s_c = s + \Delta s$. The two slownesses are related by a scale factor $\rho = s/s_c$. For Figures 12.8 and 12.9 we consider $\rho = .999$ to ensure that we do not violate the limits imposed by the Born approximation.

Figure 12.8a shows the migration impulse response computed with the background slowness. Figure 12.8b shows the difference between the migration with the background slowness (Figure 12.8a) and the migration with the correct slowness s_c . Figure 12.8c shows the image perturbation computed by applying the forward operator \mathbf{M}_w to the slowness perturbation Δs . Since the slowness perturbation is very small, the conditions imposed by the Born approximation are fulfilled, and the two images in Figures 12.8b and 12.8c are identical. The image perturbations are phase-rotated by 90 degrees relative to the background image.

Figure 12.9 illustrates the back-projection process. The image perturbations shown in Figures 12.9b and 12.9c are created by extracting a small subset from the impulse responses shown in Figures 12.8b and 12.8c, respectively. In this way, the data correspond to a single point on the surface, and the image perturbation corresponds approximately to a single point in the subsurface. Panel (b) shows the image perturbation computed as an image difference, whereas panel (c) shows the image perturbation computed with the forward operator \mathbf{M}_w . By back-projecting the image perturbations in Figures 12.9b and 12.9c with the adjoint operator \mathbf{M}'_w , we obtain identical “fat rays” shown in Figures 12.9d and 12.9e, respectively. The results of the back-projection of the image perturbations shown in Figures 12.9d and 12.9e are identical, because the slowness ratio ρ is close to one ($\rho = .999$). The phase differences

between the background image (Figure 12.9a) and the image perturbation computed as a difference between images (Figure 12.9b) are small, well within the limits imposed by the Born approximation.

In contrast, if we decrease ρ to $\rho = .83$, we obtain a significantly different, and troublesome, result, as shown in Figures 12.10 and 12.11. The panels in these two figures are homologous with the panels shown in Figures 12.8 and 12.9. In this case, the phase differences between the background image (Figure 12.11a) and the image perturbation computed as a difference between images (Figure 12.11b) are large. The image perturbation shown in Figure 12.11b contains two distinct events, whereas the image perturbation obtained by the forward operator \mathbf{M}_w (Figure 12.11c) shows only one event. The only difference between the image perturbations shown in Figure 12.11c and in Figure 12.9c is a scale factor proportional to the ratio between the respective magnitudes of the slowness perturbations.

Because of the large phase differences between the background image and the image perturbation computed as a difference between images, the result computed by applying the adjoint operator \mathbf{M}'_w to the image perturbation, shown in Figure 12.11b, is negatively affected by the limitation of the Born approximation. The polarity of the central part of the fat ray shown in Figure 12.11c is opposite to the polarity of the fat ray shown in Figure 12.11e, which is the same as the true slowness perturbation. We also see the two characteristic migration ellipsoidal side-events, indicating cycle-skipping (Woodward, 1992).

12.4 A robust WEMVA method

The root of the problem illustrated by the previous example is that the Born approximation is derived by linearizing the wavefield scattering phenomenon in terms of the amplitudes of the wavefield, whereas large velocity errors cause large phase errors. Therefore, when the events in the background image are significantly shifted with respect to the image perturbation, the Born approximation breaks down.

In this section, I present an alternative method for computing the image perturbation (Sava and Biondi, 2004a), that overcomes the limitations imposed by the Born approximation. The events in the image perturbation produced by this method are phase-rotated by ± 90 degrees, not phase shifted, with respect to the background image. The crucial component of the new method is the approximation of the residual prestack migration operator by its linearization with respect to the amplitude of the image. This amplitude linearization “parallels” the amplitude linearization performed when defining the linearized forward modeling operator \mathbf{M}_w . It produces image perturbations that can be effectively inverted by using \mathbf{M}_w in a gradient-based algorithm.

The residual prestack migration operator $\mathbf{K}_w(\rho)$ can be expanded in Taylor series with respect to ρ as follows:

$$\mathbf{K}_w(\rho) \approx \widehat{\mathbf{K}}_w(\rho) = \mathbf{1} + \Delta\rho \left. \frac{d\mathbf{K}_w}{d\rho} \right|_{\rho=1} = \mathbf{1} + \Delta\rho \left. \frac{d\mathbf{K}_w}{dk_z} \frac{dk_z}{d\rho} \right|_{\rho=1} = \mathbf{1} + \widehat{\mathbf{K}}_w^d, \quad (12.28)$$

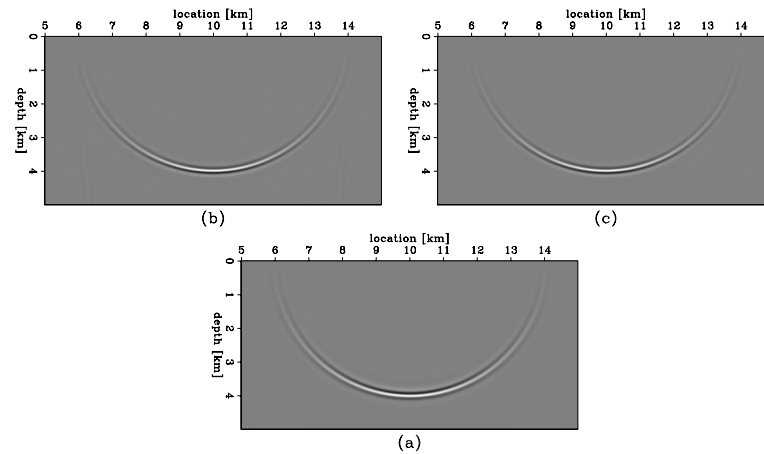


Figure 12.8: Comparison of image perturbations obtained as a difference between two migrated images (b) and as the result of the forward operator \mathbf{M}_w applied to the known slowness perturbation (c). Panel (a) shows the background image corresponding to the background slowness. Since the slowness perturbation is small (0.1%), the image perturbations in panels (b) and (c) are practically identical. (This figure is from Sava (2004).) `wemva-WEPI.imag` [NR]

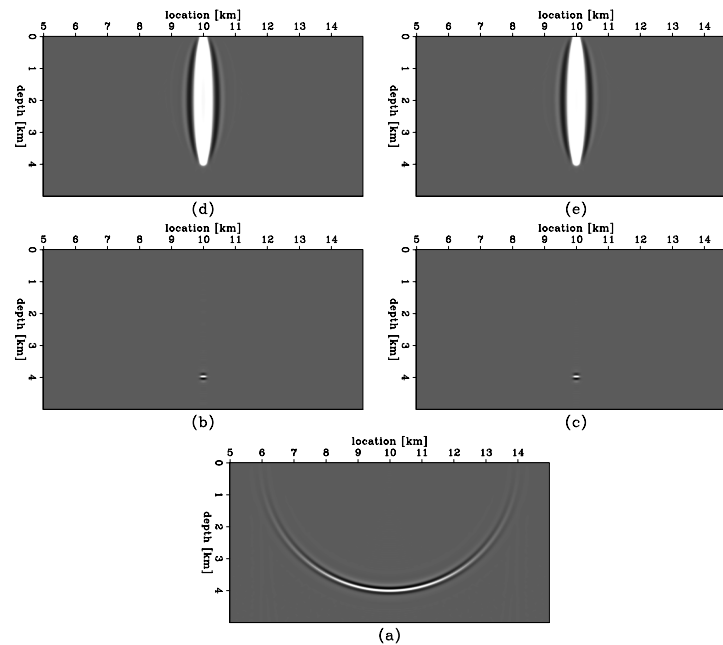


Figure 12.9: Comparison of back-projections of image perturbations into the slowness model using the adjoint operator \mathbf{M}'_w . Slowness perturbation (d) computed from image perturbations obtained as a difference between two migrated images (b). Slowness perturbation (e) computed from image perturbations obtained by applying the forward operator \mathbf{M}_w to a known slowness perturbation (c). Panel (a) shows the background image corresponding to the background slowness. Since the slowness perturbation is small (0.1%), the image perturbations in panels (b) and (c), and the fat rays in panels (d) and (e) are practically identical. (This figure is from Sava (2004).) `wemva-WEPI.rays.scaled` [NR]

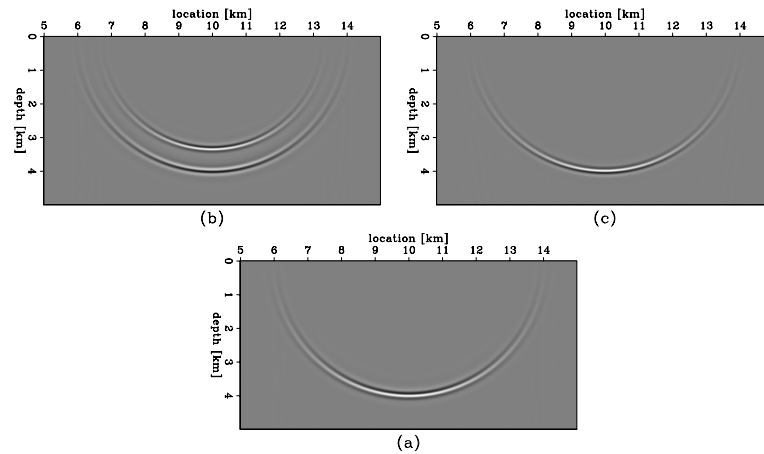


Figure 12.10: Comparison of image perturbations obtained as a difference between two migrated images (b) and as the result of the forward operator \mathbf{M}_w applied to the known slowness perturbation (c). Panel (a) shows the background image corresponding to the background slowness. Since the slowness perturbation is large (20%), the image perturbations in panels (b) and (c) are different from each other. (This figure is from Sava (2004).) `wemva-WEP2.imag` [NR]

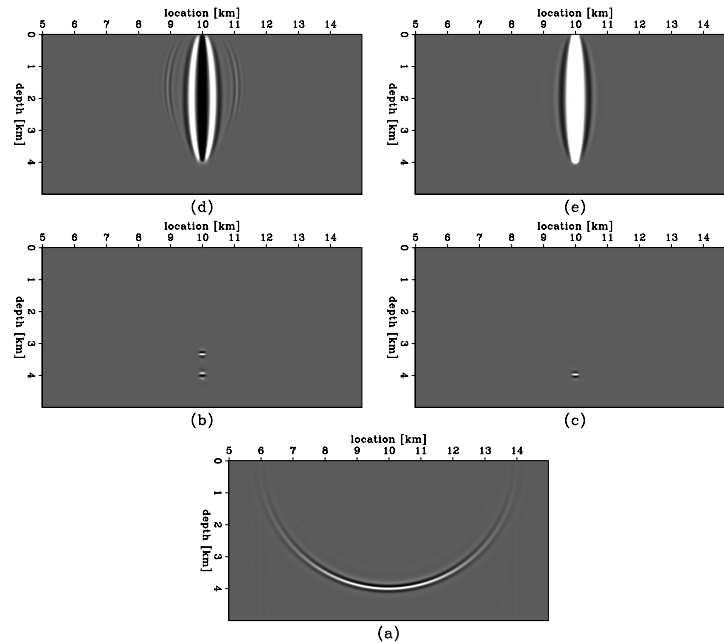


Figure 12.11: Comparison of back-projections of image perturbations into the slowness model using the adjoint operator \mathbf{M}'_w . Slowness perturbation (d) computed from image perturbations obtained as a difference between two migrated images (b). Slowness perturbation (e) computed from image perturbations obtained by applying the forward operator \mathbf{M}_w to a known slowness perturbation (c). Since the slowness perturbation is large (20%), the image perturbations in panels (b) and (c) and the fat rays in panels (d) and (e) are substantially different. Panel (d) shows the typical behavior associated with the breakdown of the Born approximation. (This figure is from Sava (2004).) `wemva-WEP2.rays.scaled` [NR]

where the notation $\widehat{\mathbf{K}}_w^d$ reminds us that the operator is the result of differentiation. From expression (12.5), the image perturbation ${}_i\Delta\mathbf{I}$ can be expressed as the operator ${}_i\widehat{\mathbf{K}}_w^d$ applied to the background image ${}_{i-1}\mathbf{I}$; that is,

$${}_i\Delta\mathbf{I} = ({}_i\mathbf{K}_w - \mathbf{1}) {}_{i-1}\mathbf{I} = {}_i\widehat{\mathbf{K}}_w^d {}_{i-1}\mathbf{I}. \quad (12.29)$$

Expression (12.28) suggests that the linearized residual migration operator ${}_i\widehat{\mathbf{K}}_w^d$ can be applied to the background image ${}_{i-1}\mathbf{I}$ as the cascade of two operators: the first is applied in the wavenumber domain, and the second is applied in the space domain.

The full expression for the first operator can be easily derived by taking the first derivative of the Stolt remapping of the vertical wavenumber, k_z , expressed in equation (11.14). This remapping can be written as follows:

$$k_z(\rho) = \sqrt{\frac{1}{\rho^2}\lambda - \frac{1}{4}|\mathbf{k}_m + \mathbf{k}_h|^2} + \sqrt{\frac{1}{\rho^2}\lambda - \frac{1}{4}|\mathbf{k}_m - \mathbf{k}_h|^2}, \quad (12.30)$$

where

$$\lambda = \frac{(k_{z\rho}^2 + |\mathbf{k}_m|^2)(k_{z\rho}^2 + |\mathbf{k}_h|^2)}{4k_{z\rho}^2}. \quad (12.31)$$

The first derivative with respect to ρ of the mapping (12.30) is

$$\frac{dk_z}{d\rho} = -\frac{\lambda}{\rho^3} \left(\frac{1}{\sqrt{\frac{\lambda}{\rho^2} - \frac{1}{4}|\mathbf{k}_m + \mathbf{k}_h|^2}} + \frac{1}{\sqrt{\frac{\lambda}{\rho^2} - \frac{1}{4}|\mathbf{k}_m - \mathbf{k}_h|^2}} \right), \quad (12.32)$$

which when evaluated at $\rho = 1$ simplifies into

$$\left. \frac{dk_z}{d\rho} \right|_{\rho=1} = \frac{-\lambda}{\sqrt{\lambda - \frac{1}{4}|\mathbf{k}_m + \mathbf{k}_h|^2}} + \frac{-\lambda}{\sqrt{\lambda - \frac{1}{4}|\mathbf{k}_m - \mathbf{k}_h|^2}}. \quad (12.33)$$

Equation (12.33) expresses a wavenumber-dependent scaling of the migrated image. The scaling depends on the propagation direction of the source and receiver wavepaths in a constant-velocity medium. For each reflected event, this scaling is proportional to the sum of the down-going and upgoing wavepath lengths, divided by the depth of the reflector. It is straightforward to verify that in the special case of flat reflectors, equation (12.33) is the linearization around $\rho = 1$ of the mapping functions presented in equations (11.15) and (11.16), and thus is related to the angle-domain RMO function expressed in equation (11.11).

The second operator, $d\mathbf{K}_w/dk_z$, is applied by taking the derivative of the weighted image with respect to k_z . It is efficiently applied in the space domain as follows:

$$\frac{d\mathbf{K}_w}{dk_z} = -iz. \quad (12.34)$$

The crucial component of the operator expressed in equation (12.34) is the 90-degree phase rotation performed by i . This phase rotation ensures coherent cross-correlation between the

background wavefield \mathbf{P} and the scattered wavefield $\Delta\mathbf{P}'$, which is part of the “imaging” step of the adjoint operator \mathbf{M}'_w expressed in equation (12.20). The depth-scaling is simply to restore the proper scaling of the downgoing and upgoing wavepath lengths that were “lost” in equation (12.33).

Finally, according to equation (12.28), the phase-rotated image is multiplied in the space domain by the value of $\Delta\rho$. This multiplication scales the image perturbation according to the measured curvature of the migrated ADCIGs. The events with large curvature in the ADCIGs (i.e. large velocity errors) are emphasized over events with a small curvature. At the limit, where the ADCIGs are flat in the migrated image, the image perturbation is zeroed.

The substitution of the linearized residual migration operator, $\mathbf{1} + \widehat{\mathbf{K}}_w$, for the residual migration operator, \mathbf{K}_w , achieves our goal of making the WEMVA method robust to large velocity errors. The shifts of the reflectors performed by \mathbf{K}_w are replaced with the phase rotations of the reflectors performed by $\widehat{\mathbf{K}}_w$. This exchange makes the image perturbation computed using $\widehat{\mathbf{K}}_w$ consistent with the Born approximation used to define the linearized operator \mathbf{M}_w . The next numerical example demonstrates that, in the simple case of constant background slowness and constant velocity errors, the image perturbation computed by applying $\widehat{\mathbf{K}}_w$ is identical to the one computed using the forward linearized operator \mathbf{M}_w .

The application of the linearized residual prestack migration to the computation of image perturbations is illustrated by Figure 12.12. The panels in this figure are homologous with the panels shown in Figures 12.9 and 12.11. The slowness error is large, with $\rho = .83$, the same as for Figure 12.11. However, in this case the residual prestack migration operator is approximated by the the linearized residual migration operator $\widehat{\mathbf{K}}_w^d$. The image perturbation computed by applying $\widehat{\mathbf{K}}_w^d$ to the background image (panel b) is identical to the image perturbations computed by applying the forward operator \mathbf{M}_w to the known slowness perturbation (c). Similarly, the results of the back-projection of the image perturbations using the adjoint operator \mathbf{M}'_w are also identical. Figure 12.12. demonstrates that, at least for the simple example under study, the computation of the image perturbation by $\widehat{\mathbf{K}}_w^d$ overcomes the problems related to the Born approximation.

It should be noticed that applying the linearized residual migration operator $\widehat{\mathbf{K}}_w$ as a cascade of operators in the wavenumber and space domain assumes that these operators are stationary along both the wavenumber and space axes. This assumption is approximately fulfilled for the operators that are derived analytically and expressed in equations (12.33) and (12.34). In contrast, the measured $\Delta\rho$ function is not guaranteed to be smooth. In practical applications, it should be smoothed to assure its semi-stationarity on the scale of the wavelength of the reflectors.

The concepts applied to the derivation of the linearized residual-migration operator presented in this section can be also applied to the linearization of several residual prestack-imaging operators, such as the RMO functions introduced in Chapter 11, and the common-azimuth migration introduced in Chapter 7, as presented by Sava (2004). When the residual-imaging operator measures relative shifts between the normal-incidence events and the events at finite aperture and azimuth (e.g. RMO function), the expression of the linearized operator \mathbf{M}_w should be modified to take into account this characteristic of the measured data. This

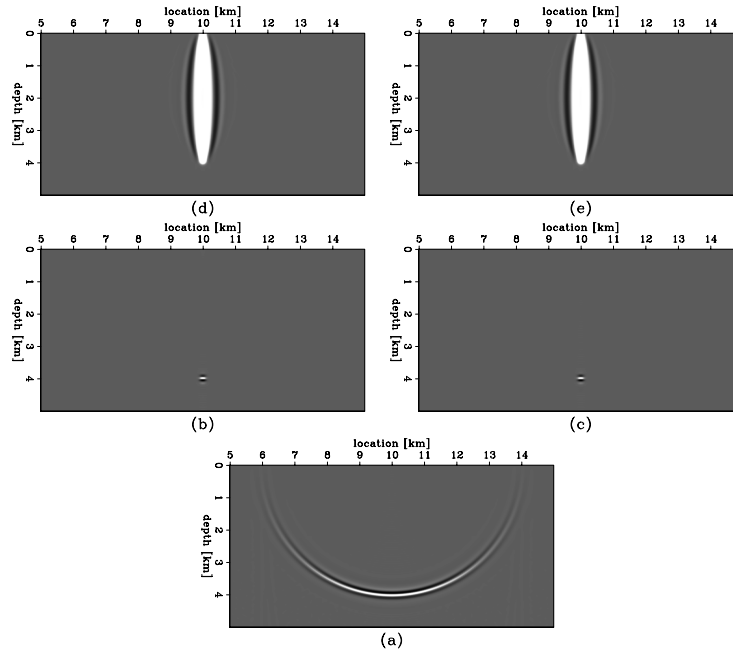


Figure 12.12: Comparison of image perturbations obtained by applying the linearized residual migration operator $\widehat{\mathbf{K}}_w^d$ (b), and by applying the forward operator \mathbf{M}_w to the known slowness perturbation (c). Despite the fact that the slowness perturbation is large (20%), the image perturbations in panels (b) and (c) and the fat rays in panels (d) and (e) are practically identical, both in shape and in magnitude. (This figure is from Sava (2004).) `wemva-WEP2.raan.scaled` [NR]

task can be accomplished by adding another component to \mathbf{M}_w that subtracts the image perturbation at normal incidence, following a theoretical development that is similar to the one followed in Section 10.4.2 for the traveltime tomography method, and in Section 11.4.2 for the ray-based MVA method.

Wavefield-continuation MVA methods hold the promise of improving the resolution of MVA methods, because they are, at least in theory, capable of using all the velocity information present in band-limited data, as illustrated by the wavepaths shown in Figure 12.2. However, by measuring the velocity errors using a residual-imaging operator defined by only one parameter (ρ), even if the parameter is spatially varying, we substantially limit our ability to exploit this potential advantage of wavefield methods over ray methods. This limitation can be an important shortcoming of the WEMVA method presented in this section, when compared with the DSO and MMF objective functions discussed previously in this chapter.

As I briefly discussed in Section 12.3, the DSO objective function has attractive properties of global convergence, because the gradient direction is well behaved even in presence of large velocity errors. In contrast, the MMF objective function cannot be used in presence of large velocity errors, but it has attractive local convergence properties, and it is sensitive to small relative shifts in the ADCIGs. These characteristics are complementary to the robust global convergence properties of the WEMVA method presented in this section. We can combine the

stacking operator with a global residual imaging operator, \mathbf{K}_w , which removes the large shifts from the migrated ADCIGs, and derive the following expression for computing the image perturbation ${}_i\Delta\mathbf{I}$:

$${}_i\Delta\mathbf{I} = \left\{ {}_i\widehat{\mathbf{K}}_w^d({}_i\rho) + \epsilon \left[{}_i\mathbf{K}_w^{-1}({}_i\rho)\mathbf{S}'_w\mathbf{S}_w{}_i\mathbf{K}_w({}_i\rho) - \mathbf{1} \right] \right\} {}_{i-1}\mathbf{I}, \quad (12.35)$$

where \mathbf{S}_w its a stacking operator over angles, like the one used by the MMF objective function, and ϵ is an appropriate scaling factor. Notice that both the residual-imaging operator ${}_i\mathbf{K}_w$ and the linearized residual-imaging operator ${}_i\widehat{\mathbf{K}}_w^d$ are determined by the same slowness-ratio function ${}_i\rho$.

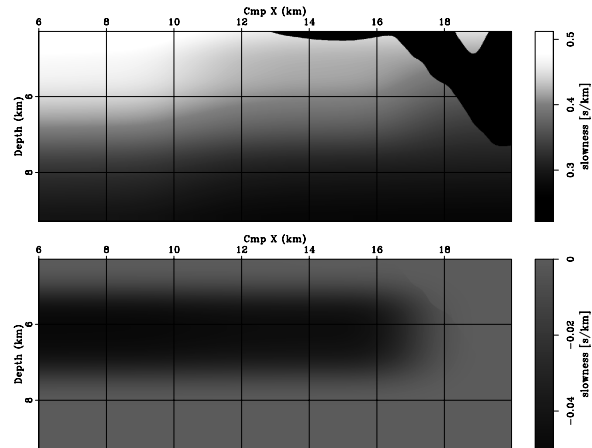
Expression (12.35) has attractive characteristics that should yield a velocity-estimation method that avoids the pitfalls of the Born approximation while achieving the high-resolution potential of wavefield methods. When the gathers display a curvature, but the residual moveouts are well corrected by the one-parameter residual-imaging operator ${}_i\mathbf{K}_w$, the image perturbation defined by equation (12.35) is equivalent to the one defined by equation (12.29). However, when the residual moveouts are not sufficiently corrected by the one-parameter residual-imaging operator ${}_i\mathbf{K}_w$ – that is, when after the application of ${}_i\mathbf{K}_w$ the migrated ADCIGs display small positive and negative shifts – the use of the image perturbation defined by equation (12.35) should enable the estimation of the velocity anomalies responsible for these small shifts.

At the limit, if the ADCIGs are close to flat, and the measured ${}_i\rho$ function is approximately equal to one everywhere, the contributions from the first operator (${}_i\widehat{\mathbf{K}}_w^d$) in equation (12.35) become negligible, and the operator ${}_i\mathbf{K}_w$ becomes close to the identity operator. In this case, the gradient direction computed starting from the perturbation expressed in equation (12.35), and the gradient direction computed for the MMF functional [equation (12.27) with the plus sign and $\mathbf{W}_w = \mathbf{S}_w$] are the same, since the application of the adjoint operator \mathbf{M}'_w to the background image ${}_{i-1}\mathbf{I}$ is approximately zero.

12.5 Examples of subsalt wave-equation MVA

Subsalt imaging is one of the most promising applications for wavefield MVA methods, as discussed in the introduction to this Chapter. Primarily, wavefield methods should provide more robust and stable convergence than ray methods in the subsalt environment because of the challenges presented by multi-pathing and shadow zones. Secondly, they may provide higher-resolution estimates because of their potential at exploiting the frequency dispersion that is caused by complex velocity functions. Therefore, I will use two subsalt examples, one from a synthetic 2-D data set (Sigsbee 2A) and another from a 2-D line taken from a 3-D data set acquired in the deep waters of the Gulf of Mexico.

Figure 12.13: Sigsbee 2A synthetic model. The background slowness model (top) and the correct slowness perturbation (bottom). (This figure is from Sava (2004).) `wemva-SIG.slo` [NR]



12.5.1 Synthetic example

The data set that I use in this example is based on the same velocity model (Sigsbee 2A) that I used to compute the wavepaths shown in Figures 12.1 and 12.2. This model has been designed to be similar to real salt bodies found in the deep waters of the Gulf of Mexico (Paffenholz et al., 2002). In this section, I concentrate on the lower part of the model, under the salt body. The top panel in Figure 12.13 shows the background slowness model, and the bottom panel shows the slowness perturbation of the background model relative to the correct slowness. Therefore, I simulate a common subsalt velocity analysis situation, where the shape of the salt is known, but the smoothly varying subsalt slowness is not fully known.

The original data set was computed with a typical marine off-end recording geometry. Preliminary studies of the data demonstrated that in some areas the complex overburden causes events to be reflected with negative reflection angles (i.e. the source and receiver wavepaths cross before reaching the reflector). To avoid losing these events, I applied the reciprocity principle and created a split-spread data set from the original off-end data set. This modification of the data set leads to the computation of symmetric ADCIGs that are easier to visually analyze than the typical one-sided ADCIGs obtained from marine data. Therefore, I display the symmetric ADCIGs in Figure 12.16 and Figures 12.20-12.22. Doubling the dataset also doubles the computational cost of the velocity-estimation process.

Figure 12.14 shows the migrated image using the correct slowness model. The top panel shows the zero offset of the prestack migrated image, and the bottom panel shows ADCIGs at equally spaced locations in the image. Each ADCIG corresponds roughly to the location right above it.

This image highlights several characteristics of this model that make it a challenge for migration velocity analysis. Most of them are related to the complicated wavepaths in the subsurface under rough salt bodies. First, the angular coverage under the salt ($x_m > 11$ km) is much smaller than in the sedimentary section uncovered by salt ($x_m < 11$ km). Second, the subsalt region is marked by many illumination gaps or shadow zones, the most striking being located at $x_m = 12$ and $x_m = 19$ km. In Section 11.2.2 I used the same synthetic dataset to

illustrate the illumination problem caused by salt edges. The main consequence is that velocity analysis in the poorly illuminated areas is much less constrained than in the well illuminated zones.

The process starts by migrating the data with the background slowness (Figure 12.15). As before, the top panel shows the zero offset of the prestack migrated image, and the bottom panel shows ADCIGs at equally spaced locations in the image. Since the migration velocity is incorrect, the image is defocused, and the angle-gathers show significant moveout. Furthermore, the diffractors at depths $z = 7.5$ km and the fault at $x_m = 15$ km are defocused.

As described in Section 11.2.2, prestack residual migration is performed for several values of the slowness-ratio parameter ρ within the range of 0.625 and 1.1, which ensures that a fairly wide range of the velocity space is spanned. Although residual migration operates on the entire image globally, for illustration purposes I extract one gather at $x_m = 10$ km. Figure 12.16 shows at the top the ADCIGs for all velocity ratios and at the bottom the semblance panels computed from the ADCIGs. The semblance maxima are picked at all locations and all depths (Figure 12.17), together with an estimate of the reliability of every picked value. This estimate is used to weight the image residuals during inversion. These weights enter the WEMVA objective function expressed in equation (12.5) as a diagonal weighting matrix, \mathbf{W}_w . The panel at the bottom of Figure 12.17 shows the weights. Where the image is poorly illuminated, the weights are low, because the ADCIGs are affected by illumination artifacts. This a typical example where poor illumination interferes with our ability to estimate velocity.

Based on the picked velocity ratio, the image perturbation $\Delta\mathbf{I}$ is computed by using equation (12.29), and the slowness perturbation is estimated by minimizing the objective function (12.5). The bottom panel of Figure 12.18 shows the estimated slowness perturbation. For comparison, the top panel of Figure 12.18 shows the correct slowness perturbation relative to the correct slowness. We can clearly see the effects of different angular coverage in the subsurface: at $x_m < 11$ km, the inverted slowness perturbation is better constrained vertically than it is at $x_m > 11$ km.

Finally, the data are remigrated with the updated slowness model (Figure 12.19). As before, the top panel shows the zero offset of the prestack migrated image, and the bottom panel shows ADCIGs at equally spaced locations in the image. With this updated velocity, the reflectors have been repositioned to their correct locations, the diffractors at $z = 7.5$ km are focused, and the ADCIGs are flatter than in the background image, indicating that the slowness update has improved the quality of the migrated image.

Figures 12.20-12.22 enable a more detailed analysis of the results of the WEMVA method by displaying the ADCIGs at three locations in the image. In each figure, the panels correspond to migration with the correct slowness (left), the background slowness (center), and the updated slowness (right). Figure 12.20 corresponds to an ADCIG at $x_m = 8$ km, in the region that is well illuminated. The angle gathers are clean, with clearly identifiable moveouts that are corrected after inversion. Figure 12.21 corresponds to an ADCIG at $x_m = 10$ km, in the region with illumination gaps, clearly visible on the strong reflector at $z = 9$ km, at a reflection aperture angle of about 20 degrees. The gaps are preserved in the ADCIG from the image mi-

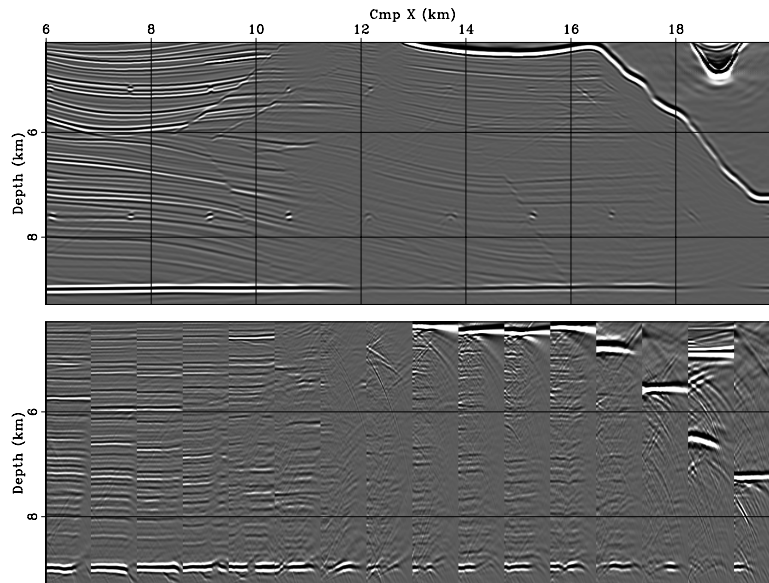


Figure 12.14: Migration with the correct slowness. The zero offset of the prestack migrated image (top) and ADCIGs at equally spaced locations in the image (bottom). Each ADCIG corresponds roughly to the location right above it. (This figure is from Sava (2004).)

wemva-SIG.imgC [NR]

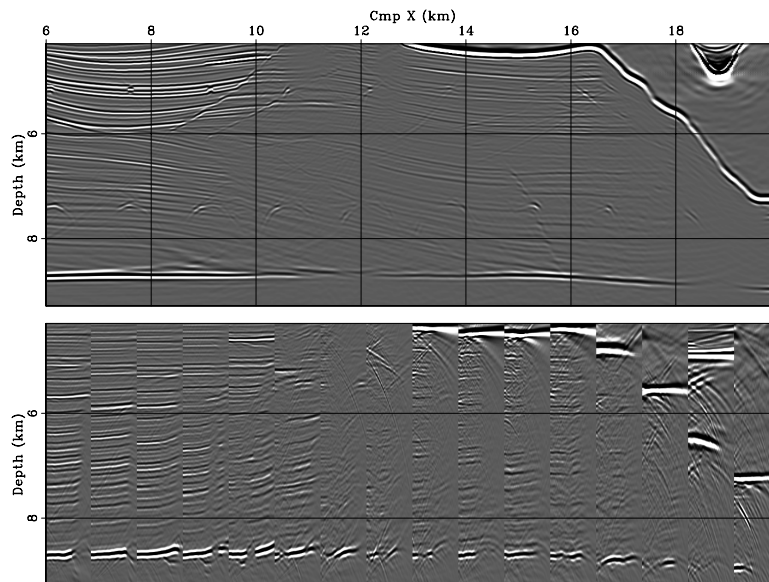
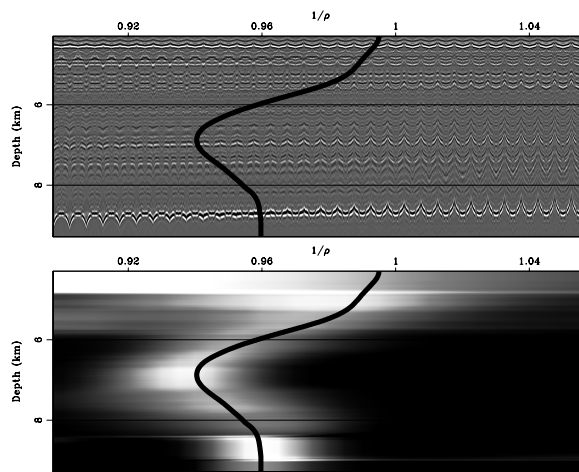


Figure 12.15: Migration with the background slowness. The zero offset of the prestack migrated image (top) and ADCIGs at equally spaced locations in the image (bottom). Each ADCIG corresponds roughly to the location right above it. (This figure is from Sava (2004).)

wemva-SIG.img1 [NR]

Figure 12.16: Residual migration for an ADCIG at $x_m = 10$ km. The top panel shows ADCIGs for all values of the inverse of the velocity ratio $1/\rho$, and the bottom panel shows semblance panels used for picking. All gathers are stretched along the depth axis to eliminate the vertical movement corresponding to different migration velocities. The overlaid line indicates the picked values at all depths. (This figure is from Sava (2004).) `wemva-SIG.srm.fix` [NR]



grated with the background slowness, but the moveouts are still easy to identify and correct. Finally, Figure 12.22 corresponds to an ADCIG at $x_m = 12$ km, in a region that is poorly illuminated. In this case, the ADCIG is much noisier and the moveouts are harder to identify and measure. This region also corresponds to the lowest reliability, as indicated by the low weight of the picks (Figure 12.17). The gathers in this region contribute less to the inversion, and the resulting slowness perturbation is mainly controlled by regularization. Despite the noisier gathers, after slowness update and re-migration, we recover an image reasonably similar to the one obtained by migration with the correct slowness.

A simple visual comparison of the middle panels with the right and left panels in Figures 12.20-12.22 unequivocally demonstrates that the WEMVA method overcomes the limitations related to the linearization of the wave equation with the first-order Born approximation. The images obtained using the initial velocity model (middle panels) are vertically shifted by several wavelengths with respect to the images obtained using the true velocity (left panels) and the estimated velocity (right panels). If the Born approximation limited the magnitude and spatial extent of the velocity errors that could be estimated with the WEMVA method, we

Figure 12.17: The top panel shows the values of $-\Delta\rho/\rho$ at all locations, and the bottom panel shows a weight indicating the reliability of the picked values at every location. The picks in the shadow zone around $x_m = 12$ km are less reliable than the picks in the sedimentary region around $x_m = 8$ km. All picks inside the salt are disregarded. (This figure is from Sava (2004).) `wemva-SIG.pck` [NR]

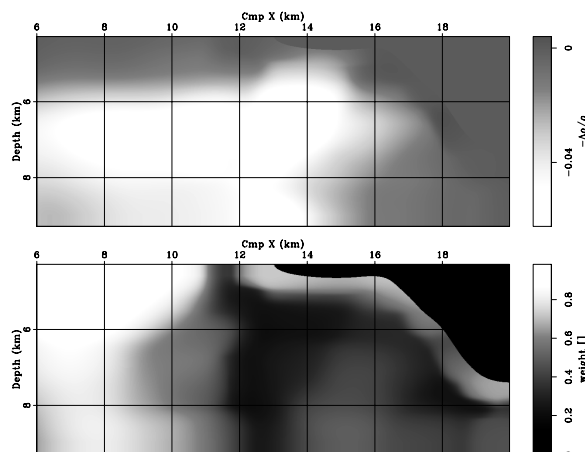
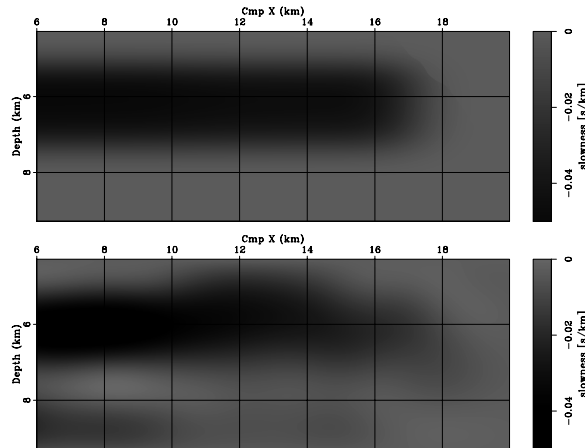


Figure 12.18: The correct slowness perturbation (top) and the inverted slowness perturbation (bottom). (This figure is from Sava (2004).) `wemva-SIG.dsl` [NR]



would have been unable to estimate a velocity perturbation sufficient to improve the ADCIGs from the middle panels to the right panels.

12.5.2 Gulf of Mexico data example

The next example concerns a 2-D line extracted from a 3-D subsalt dataset from the Gulf of Mexico. I follow the same methodology as used for the preceding synthetic example. In this case, however, we run several non-linear iterations of WEMVA, each involving wavefield linearization, residual migration and inversion.

Figure 12.23 (top) shows the image migrated with the background velocity superimposed on the background slowness. This image serves as a reference against which we check the results of our velocity analysis. Two regions of interest are labeled A and B in the figure. The right edge of the model corresponds to a salt body. The top edge of the image is not at the surface, because the surface data were datumed to a depth below the well-imaged overhanging salt body.

The procedure is like the one in the previous example. We run residual migration and analyze the moveouts of ADCIGs. This analysis is repeated at every location, from which we obtain two maps: a map of the residual migration parameter $\Delta\rho$ at every location in the image (Figure 12.23 middle), and a map of the weight indicating the reliability of the measured values of $\Delta\rho$ (Figure 12.23 bottom). In the map shown in the middle panel of Figure 12.23, the whiter regions indicate flatter ADCIGs. The stack of the background image is overlaid on to both of these panels to facilitate identification of image features. Next, we generate an image perturbation based on the $\Delta\rho$ values shown in Figure 12.23 (middle) and estimate the slowness perturbation using the weights shown in Figure 12.23 (bottom), as a measure of the reliability of the measured image perturbation.

The results obtained after two non-linear iterations of WEMVA are shown in Figure 12.24. As in Figure 12.23, the three panels show the migrated image superimposed on slowness (top), the values of $\Delta\rho$ measured from the migrated image (middle), and weights of the image

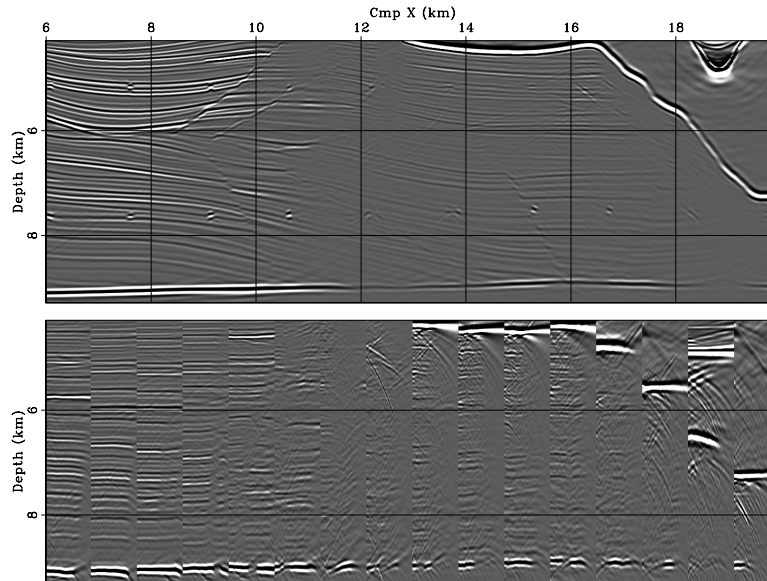


Figure 12.19: Migration with the updated slowness. The zero offset of the prestack migrated image (top) and ADCIGs at equally spaced locations in the image (bottom). Each ADCIG corresponds roughly to the location right above it. (This figure is from Sava (2004).) wemva-SIG.img2 [NR]

perturbations (bottom). Two regions in which changes occur are labeled A and B.

The residual migration picks converge toward $\Delta\rho = 0$, indicating flatter ADCIGs, and therefore better-focused images. Reflectors in both regions shift vertically, according to the slowness changes. A notable feature is the improved continuity of the strongest reflectors in the region labeled B.

The comparison of the images and ADCIGs shown in Figures 12.25 and 12.26 confirm that the two non-linear iterations of the WEMVA process yield an improvement in the velocity function. The ADCIG obtained by using the starting migration velocity (bottom of Figure 12.25) “smiled” upward in region A, and “frowned” downward in region B. The ADCIG obtained by using the estimation results (bottom of Figures 12.26) are flatter in both of these regions. In the poorly illuminated area (left of “B”) the ADCIGs are affected by artifacts, but they seem to be slightly more coherent in Figure 12.26 than in Figure 12.25. Correspondingly, the weights shown in the bottom panel of Figure 12.24 are slightly higher than the weights shown the bottom panel of Figure 12.23. However, in the poorly illuminated area, the weights are still fairly low, indicating that the WEMVA process is only partially using the velocity information provided in the reflectors.

As in the synthetic example shown in the previous section, poor illumination hampers the velocity estimation. Whereas WEMVA provides a robust method for inverting velocity measurements of reflections that have propagated through complex overburden, it is generally less effective in poorly illuminated regions.

Figure 12.20: Angle-domain common-image gathers at $x = 8$ km. Each panel corresponds to a different migration velocity: migration with the correct velocity (left), migration with the background velocity (center) and migration with the updated velocity (right). (This figure is from Sava (2004).) `wemva-SIG.ang08.fix` [NR]

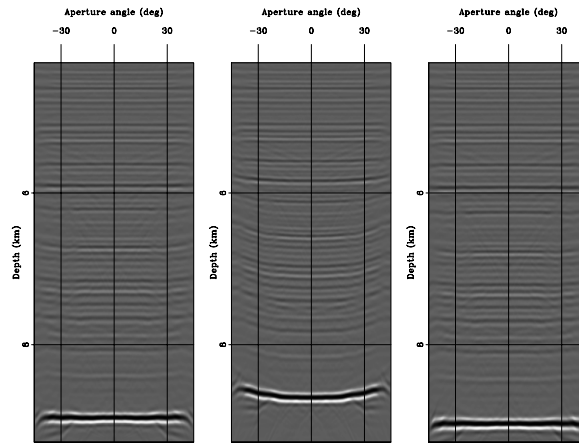


Figure 12.21: Angle-domain common-image gathers at $x = 10$ km. Each panel corresponds to a different migration velocity: migration with the correct velocity (left), migration with the background velocity (center) and migration with the updated velocity (right). (This figure is from Sava (2004).) `wemva-SIG.ang10.fix` [NR]

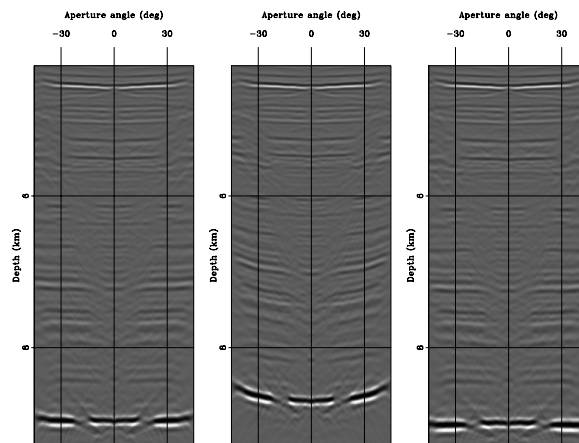
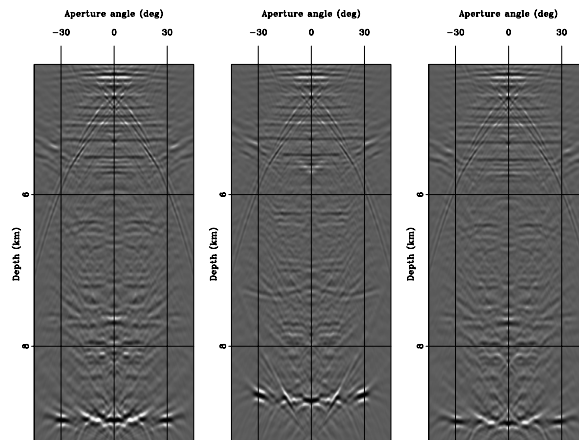


Figure 12.22: Angle-domain common-image gathers at $x = 12$ km. Each panel corresponds to a different migration velocity: migration with the correct velocity (left), migration with the background velocity (center) and migration with the updated velocity (right). (This figure is from Sava (2004).) `wemva-SIG.ang12.fix` [NR]



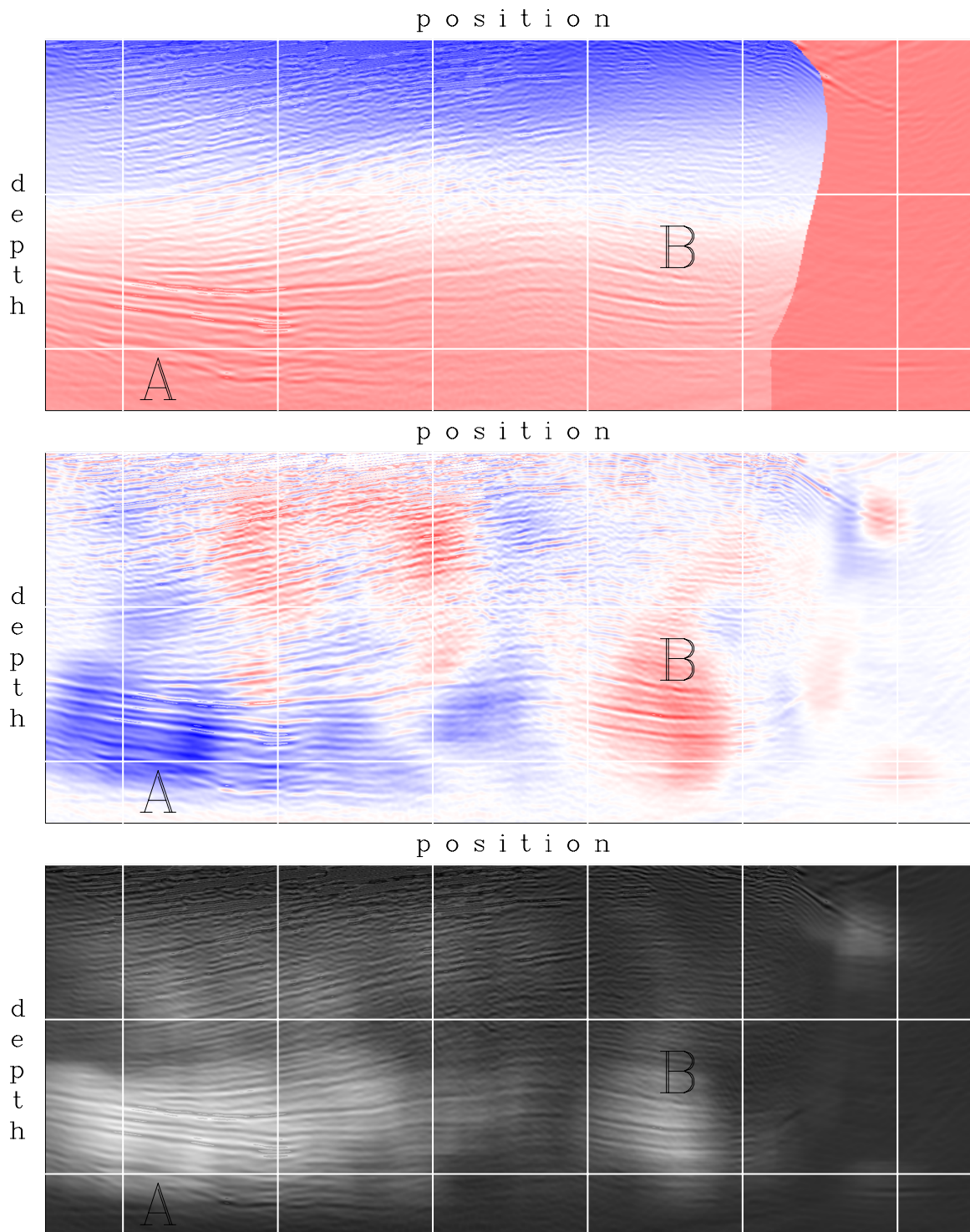


Figure 12.23: Gulf of Mexico data. Migrated image superimposed on slowness (top), residual migration picks (middle), and picking weight (bottom). The migration corresponds to the background slowness. (This figure is from Sava (2004).) `wemva-BPGOM.it0` [NR]

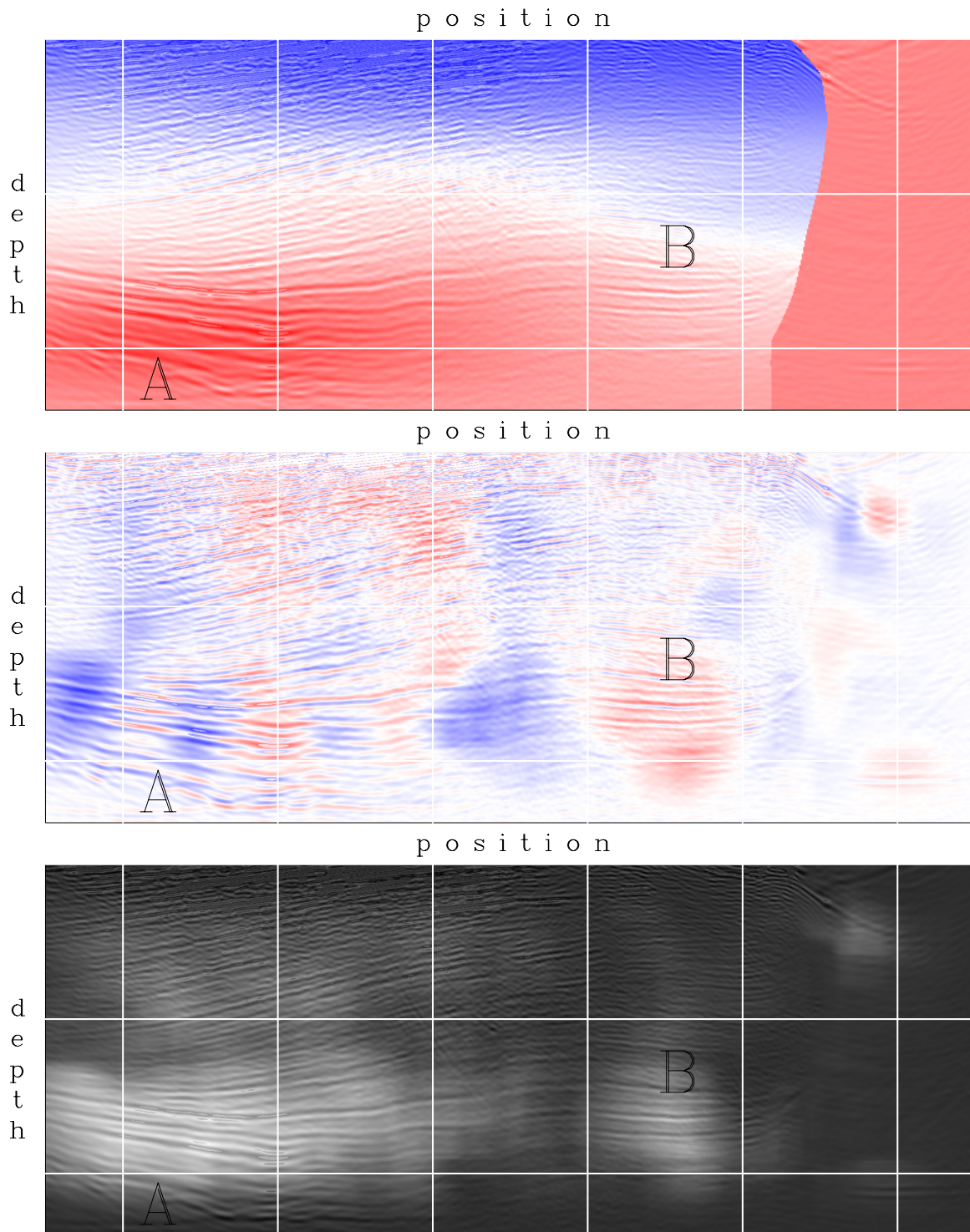


Figure 12.24: Gulf of Mexico data. Migrated image superimposed on slowness (top), residual migration picks (middle), and picking weight (bottom). The migration corresponds to the updated slowness after two iterations. Compare with Figure 12.23. (This figure is from Sava (2004).) `wemva-BPGOM.it2` [NR]

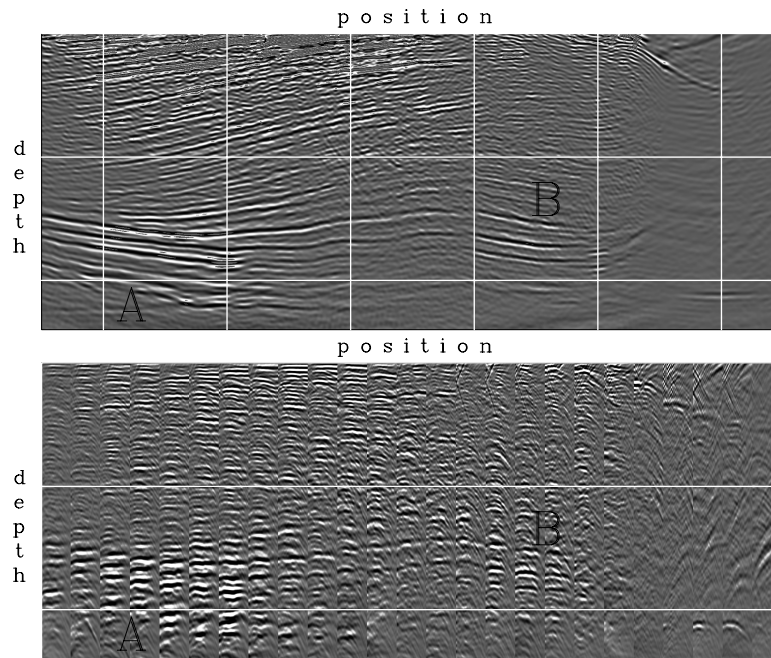


Figure 12.25: Migration results of the Gulf of Mexico data using the background slowness. Stack of the migrated image (top), and ADCIGs at regularly spaced locations (bottom). (This figure is from Sava (2004).) `wemva-BPGOM.iman0` [NR]

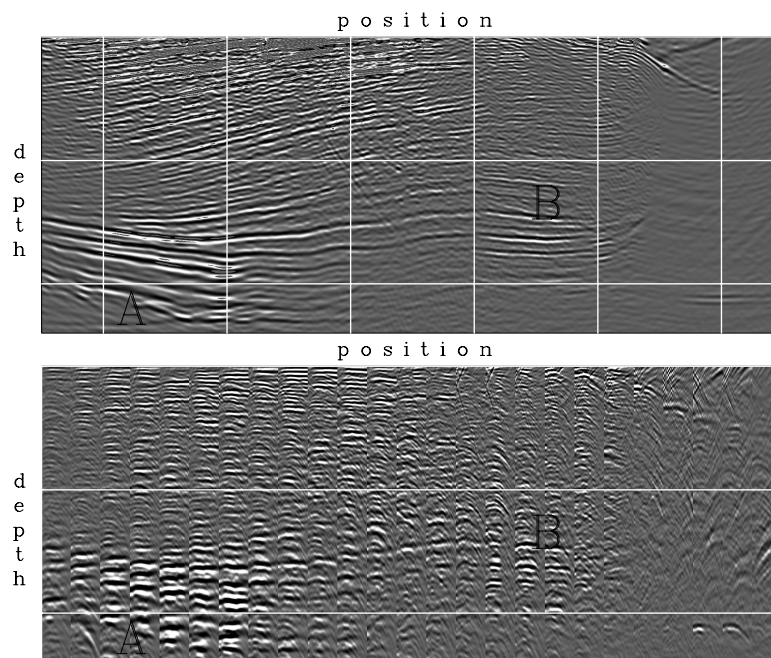


Figure 12.26: Migration results of the Gulf of Mexico data using the updated slowness after two WEMVA iterations. Stack of the migrated image (top), and ADCIGs at regularly spaced locations (bottom). (This figure is from Sava (2004).) `wemva-BPGOM.iman2` [NR]

REFERENCES

- Biondi, B., and Sava, P., 1999, Wave-equation migration velocity analysis: 69th Ann. Internat. Meeting, Soc. of Expl. Geophys., Expanded Abstracts, 1723–1726.
- Chavent, G., and Jacewitz, C. A., 1995, Determination of background velocities by multiple migration fitting: *Geophysics*, **60**, 476–490.
- Claerbout, J. F., 2004, Image Estimation by Example: <http://sepwww.stanford.edu/sep/prof/index.html>.
- Clayton, R. W., and Stolt, R. H., 1981, A Born-WKBJ inversion method for acoustic reflection data: *Geophysics*, **46**, 1559–1567.
- Cohen, J. K., and Bleistein, N., 1979, Velocity inversion procedure for acoustic waves: *Geophysics*, **44**, 1077–1087.
- Dahlen, F. A., Hung, S. H., and Nolet, G., 2000, Frechet kernels for finite frequency traveltimes—I. Theory: *Geophys. J. Int.*, **141**, 157–174.
- Devaney, A. J., 1981, Inverse-scattering theory within the Rytov approximation: *Optics Letters*, **6**, 374–376.
- Gill, P. E., Murray, W., and Wright, M. H., 1981, *Practical optimization*: Academic Press.
- Guitton, A., and Symes, W. W., 2003, Robust inversion of seismic data using the Huber norm: *Geophysics*, **68**, 1310–1319.
- Huang, L. Y., Fehler, M. C., and Wu, R. S., 1999, Extended local Born Fourier migration method: *Geophysics*, **64**, 1524–1534.
- Hung, S. H., Dahlen, F. A., and Nolet, G., 2000, Frechet kernels for finite frequency traveltimes—II. Examples: *Geophys. J. Int.*, **141**, 175–203.
- Lions, J. L., 1971, *Optimal control of systems governed by partial differential equations*: Springer Verlag.
- Lo, T. W., and Inderweisen, P. L., 1994, *Fundamentals of seismic tomography*., Tulsa, OK.
- Lomax, A., 1994, The wavelength-smoothing method for approximating broad-band wave propagation through complicated velocity structures: *Geoph. J. Int.*, **117**, 313–334.
- Marquering, H., Dahlen, F. A., and Nolet, G., 1999, Three-dimensional sensitivity kernels for finite-frequency traveltimes: the banana-doughnut paradox: *Geophys. J. Int.*, **137**, 805–815.
- Mora, P. R., 1987, Nonlinear two-dimensional elastic inversion of multioffset seismic data: *Geophysics*, **52**, 1211–1228.
- Paffenholz, J., McLain, B., Zaskie, J., and Keliher, P., 2002, Subsalt multiple attenuation and imaging: Observations from the Sigsbee2B synthetic dataset: 72nd Ann. Internat. Meeting, Soc. of Expl. Geophys., Expanded Abstracts, 2122–2125.

- Pratt, R. G., 1999, Seismic waveform inversion in the frequency domain, part 1: Theory and verification in a physical scale model: *Geophysics*, **64**, 888–901.
- Sava, P., and Biondi, B., 2004a, Wave-equation migration velocity analysis—I: Theory: *Geophysical Prospecting*, accepted for publication.
- Sava, P., and Biondi, B., 2004b, Wave-equation migration velocity analysis—II: Examples: *Geophysical Prospecting*, accepted for publication.
- Sava, P., and Biondi, B., 2004c, Sensitivity kernels for wave-equation migration velocity analysis: *SEP-Report*, **115**, 199–212.
- Sava, P., 2004, Migration and velocity analysis by wavefield extrapolation: Ph.D. thesis, Stanford University.
- Shen, P., Symes, W. W., and Stolk, C. C., 2003, Differential semblance velocity analysis by wave-equation migration: 73rd Ann. Internat. Meeting, Soc. of Expl. Geophys., Expanded Abstracts, 2132–2135.
- Stolt, R. H., and Benson, A., 1986, *Seismic migration - theory and practice*: Geophysical Press, London - Amsterdam.
- Stolt, R. H., and Weglein, A. B., 1985, Migration and inversion of seismic data: *Geophysics*, **50**, 2458–2472.
- Symes, W. W., and Carazzone, J. J., 1991, Velocity inversion by differential semblance optimization: *Geophysics*, **56**, 654–663.
- Tarantola, A., 1984, Inversion of seismic reflection data in the acoustic approximation: *Geophysics*, **49**, 1259–1266.
- Woodward, M., 1990, Wave equation tomography: Ph.D. thesis, Stanford University.
- Woodward, M. J., 1992, Wave-equation tomography: *Geophysics*, **57**, 15–26.

SEP ARTICLES PUBLISHED OR IN PRESS

- Alkhalifah, T., and Biondi, B., 2004, Numerical analysis of the azimuth moveout operator for vertically inhomogeneous media: *Geophysics*, **69**, 554–561.
- Alvarez, G., and Larner, K., 2004, Relative performance of moveout-based multiple-suppression methods for amplitude variation with offset (AVO) analysis and common mid-point (CMP) stacking: *Geophysics*, **69**, no. 1, 275–285.
- Alvarez, G., Biondi, B., and Guitton, A., 2004a, Attenuation of diffracted multiples in angle domain common image gathers: 74th Ann. Internat. Mtg., Soc. of Expl. Geophys., Expanded Abstracts.
- Alvarez, G., Pereyra, V., and Carcione, L., 2004b, Model-based 3D seismic survey design as an optimization problem: 74th Ann. Internat. Mtg., Soc. of Expl. Geophys., Expanded Abstracts.
- Biondi, B., and Bevc, D., 2004, Seismic imaging of complex structures by reflection seismic data *in* Levander, A., and Nolet, G., Eds., *Data Analysis and Imaging with Global and Local Arrays*:: American Geophysical Union, submitted.
- Biondi, B., and Symes, W., 2004, Angle-domain common-image gathers for migration velocity analysis by wavefield-continuation imaging: *Geophysics*, in press.
- Biondi, B., and Tisserant, T., 2004, 3-D angle-domain common-image gathers for migration velocity analysis: submitted for publication in *Geophysical Prospecting*.
- Biondi, B., Tisserant, T., and Symes, W., 2003, Wavefield-continuation angle-domain common-image gathers for migration velocity analysis: 73rd Ann. Internat. Mtg., Soc. of Expl. Geophys., Expanded Abstracts, 2104–2107.
- Biondi, B., 2003a, Equivalence of source-receiver migration and shot-profile migration: *Geophysics*, **68**, 1340–1347.
- Biondi, B., 2003b, Narrow-azimuth migration of marine streamer data: 73rd Ann. Internat. Mtg., Soc. of Expl. Geophys., Expanded Abstracts, 897–900.
- Brown, M., and Guitton, A., 2004a, Efficient prestack modeling and imaging of pegleg multiples: 74th Ann. Internat. Mtg., Soc. of Expl. Geophys., Expanded Abstracts.
- Brown, M., and Guitton, A., 2004b, Least-squares joint imaging of multiples and primaries: 74th Ann. Internat. Mtg., Soc. of Expl. Geophys., Expanded Abstracts.
- Brown, M., 2003, HEMNO, a time-imaging operator for pegleg multiples in 2-D and 3-D: 65th Mtg., Eur. Assoc. Geosc. Eng., Abstracts.
- Clapp, M. L., Biondi, B., and Clapp, R. G., 2004a, Regularized least-squares inversion for 3-D subsalt imaging: 74th Ann. Internat. Mtg., Soc. of Expl. Geophys., Expanded Abstracts.

- Clapp, R. G., Biondi, B., and Claerbout, J. F., 2004b, Geologically constrained migration velocity analysis: *Geophysics*, **69**, 533–546.
- Draganov, D., Wapenaar, K., Artman, B., and Biondi, B., 2004, Migration methods for passive seismic data: 74th Ann. Internat. Mtg., Soc. of Expl. Geophys., Expanded Abstracts.
- Fomel, S., Sava, P., Rickett, J., and Claerbout, J. F., 2003, The Wilson-Burg method of spectral factorization with application to helical filtering: *Geophysical Prospecting*, **51**, 409–420.
- Guitton, A., and Claerbout, J., 2004, Interpolation of bathymetry data from the Sea of Galilee: a noise attenuation problem: *Geophysics*, **69**, 608–616.
- Guitton, A., and Symes, W. W., 2003, Robust inversion of seismic data using the Huber norm: *Geophysics*, **68**, 1310–1319.
- Guitton, A., and Verschuur, D. J., 2004, Adaptive subtraction of multiples with the ℓ^1 norm: *Geophysical Prospecting*, **52**, 27–38.
- Guitton, A., Claerbout, J., and Lomask, J., 2004, First order lateral interval velocity estimates without picking: 74th Ann. Internat. Mtg., Soc. of Expl. Geophys., Expanded Abstracts.
- Guitton, A., 2003a, Amplitude and kinematic corrections of migrated images for non-unitary imaging operators: 73rd Ann. Internat. Mtg., Soc. of Expl. Geophys., Expanded Abstracts, 933–936.
- Guitton, A., 2003b, Multiple attenuation with multidimensional prediction-error filters: 73rd Ann. Internat. Mtg., Soc. of Expl. Geophys., Expanded Abstracts, 1945–1948.
- Guitton, A., 2003c, What can we do with a model of the multiples?: 65th Mtg., Eur. Assoc. Geosc. Eng., Abstracts.
- Guitton, A., 2004a, Amplitude and kinematic corrections of migrated images for non-unitary imaging operators: accepted for publication in *Geophysics*.
- Guitton, A., 2004b, Multidimensional multiple attenuation in complex geology: illustration on the Sigsbee2B dataset: 74th Ann. Internat. Mtg., Soc. of Expl. Geophys., Expanded Abstracts.
- Haines, S., Guitton, A., Biondi, B., and Pride, S., 2003a, Development of experimental methods in electroseismics: 73rd Ann. Internat. Mtg., Soc. of Expl. Geophys., Expanded Abstracts, 560–563.
- Haines, S., Klemperer, S., Brown, L., Guo, J., Mechie, J., Meissner, R., Ross, A., and Zhao, W., 2003b, INDEPTH III seismic data: From surface observations to deep crustal processes in tibet: *Tectonics*, **22**, no. 1.
- Haines, S., Pride, S., Klemperer, S., and Biondi, B., 2004, Development of electroseismic experimental methods: Symposium on the Application of Geophysics to Engineering and Environmental Problems, Environmental and Engineering Geophysical Society, Proceedings, 1490–1503.

- Liner, C. L., and Clapp, R. G., 2004, Nonlinear pairwise alignment of seismic traces: Geophysics, in press.
- Lomask, J., 2003, Flattening 3-D seismic cubes without picking: 73rd Ann. Internat. Mtg., Soc. of Expl. Geophys., Expanded Abstracts, 1402–1405.
- Rosales, D., and Biondi, B., 2004a, Multicomponent azimuth moveout: submitted for publication in Geophysics.
- Rosales, D. A., and Biondi, B., 2004b, Acquisition geometry regularization for multicomponent data: Soc. of Expl. Geophys., Expanded Abstracts.
- Sava, P., and Biondi, B., 2003a, Analytical image perturbations for wave-equation migration velocity analysis: 65th Mtg., Eur. Assoc. Geosc. Eng., Abstracts.
- Sava, P., and Biondi, B., 2003b, Migration velocity analysis by recursive wavefield extrapolation: EAGE/SEG Research Workshop, Eur. Assoc. Expl. Geophys., Abstracts.
- Sava, P., and Biondi, B., 2003c, Wave-equation migration velocity analysis by inversion of differential image perturbations: 73rd Ann. Internat. Mtg., Soc. of Expl. Geophys., Expanded Abstracts, 2124–2127.
- Sava, P., and Biondi, B., 2004a, Wave-equation migration velocity analysis - I: Theory: Geophysical Prospecting, in press.
- Sava, P., and Biondi, B., 2004b, Wave-equation migration velocity analysis - II: Subsalt imaging examples: Geophysical Prospecting, in press.
- Sava, P., and Fomel, S., 2003, Angle-domain common image gathers by wavefield continuation methods: Geophysics, **68**, no. 3, 1065–1074.
- Sava, P., and Fomel, S., 2004a, Seismic imaging using Riemannian wavefield extrapolation: submitted for publication in Geophysics.
- Sava, P., and Fomel, S., 2004b, Seismic modeling with Riemannian wavefield extrapolation: 66th Mtg., Eur. Assoc. Geosc. Eng., Abstracts.
- Sava, P., and Fomel, S., 2004c, Wavefield extrapolation in Riemannian coordinates: 74th Ann. Internat. Mtg., Soc. of Expl. Geophys., Expanded Abstracts.
- Sava, P., and Guitton, A., 2003a, Multiple attenuation after migration: EAGE/SEG Research Workshop, Eur. Assoc. Expl. Geophys., Abstracts.
- Sava, P., and Guitton, A., 2003b, Multiple attenuation in the image space: 73rd Ann. Internat. Mtg., Soc. of Expl. Geophys., Expanded Abstracts, 1933–1936.
- Sava, P., and Guitton, A., 2004, Multiple attenuation in the image space: Geophysics, in press.
- Sava, P., Biondi, B., and Fomel, S., 2003, Wave-equation migration velocity analysis: SIAM Conference on Mathematical and Computational Issues in the Geosciences, Society of Industrial and Applied Mathematics, Abstracts.

- Sava, P., Biondi, B., and Etgen, J., 2004a, Diffraction-focusing migration velocity analysis: 74th Ann. Internat. Mtg., Soc. of Expl. Geophys., Expanded Abstracts.
- Sava, P., Biondi, B., and Etgen, J., 2004b, Diffraction-focusing migration velocity analysis with application to seismic and GPR data: submitted for publication in Geophysics.
- Sava, P., 2003, Prestack residual migration in the frequency domain: *Geophysics*, **67**, no. 2, 634–640.
- Shan, G., and Biondi, B., 2004, Imaging overturned waves by plane-wave migration in tilted coordinates: 74th Ann. Internat. Mtg., Soc. of Expl. Geophys., Expanded Abstracts.
- Shan, G., and Guitton, A., 2004, Migration of surface-related multiples: tests on the Sigsbee2B dataset: 74th Ann. Internat. Mtg., Soc. of Expl. Geophys., Expanded Abstracts.
- Shan, G., 2003, Source-receiver migration of multiple reflections: 73rd Ann. Internat. Mtg., Soc. of Expl. Geophys., Expanded Abstracts, 1008–1011.
- Shragge, J., and Sava, P., 2004, Adaptive phase-rays wavefield extrapolation: 74th Ann. Internat. Mtg., Soc. of Expl. Geophys., Expanded Abstracts.
- Tisserant, T., and Biondi, B., 2004, Residual move-out analysis with 3-D angle-domain common-image gathers: 74th Ann. Internat. Mtg., Soc. of Expl. Geophys., Expanded Abstracts.
- Valenciano, A. A., Brown, M., Guitton, A., and Sacchi, M. D., 2004, Interval velocity estimation using edge-preserving regularization: 74th Ann. Internat. Mtg., Soc. of Expl. Geophys., Expanded Abstracts.
- Vlad, I., and Biondi, B., 2004, Velocity estimation for seismic data exhibiting focusing-effect AVO: Soc. of Expl. Geophys., Expanded Abstracts.
- Wolf, K., Rosales, D., Guitton, A., and Claerbout, J., 2004, Robust moveout without velocity picking: Soc. of Expl. Geophys., Expanded Abstracts.

SEP PHONE DIRECTORY

Name	Phone	Login Name
Alvarez, Gabriel	724-0461	gabriel
Artman, Brad	723-6007	brad
Berryman, James	724-0461	berryman
Biondi, Biondo	723-1319	biondo
Claerbout, Jon	723-3717	jon
Clapp, Bob	725-1334	bob
Clapp, Marie	725-1334	marie
Curry, Bill	723-5911	bill
Guitton, Antoine	723-6007	antoine
Lau, Diane	723-1703	diane
Lomask, Jesse	723-6006	lomask
Rosales, Daniel	723-1250	daniel
Sava, Paul	723-0463	paul
Shan, Guojian	723-0463	shan
Shragge, Jeff	724-0461	jeff
Valenciano, Alejandro	723-6006	valencia
Vlad, Ioan	723-1250	nick
Wilson, Charlie	725-2234	wilsonck

SEP fax number: (650) 723-0683

E-MAIL

Our Internet address is "sep.stanford.edu"; i.e., send Jon electronic mail with the address "jon@sep.stanford.edu".

WORLD-WIDE WEB SERVER INFORMATION

Sponsors who have provided us with their domain names are not prompted for a password when they access from work. If you are a sponsor, and would like to access our restricted area away from work, visit our website and attempt to download the material. You will then fill out a form, and we will send the username/password to your e-mail address at a sponsor company.

STEERING COMMITTEE MEMBERS, 2004-2005

Name	Company	Telephone	E-Mail
Raymond Abma	BP	(281) 366-4604	abmar1@bp.com
Francois Audebert	CGG	(281) 646-2524	faudebert@cgg.com
Dimitri Bevc	3DGeo	(650) 969-3886	dimitri@3dgeo.com
Biondo Biondi	SEP	(650) 723-1319	biondo@sep.stanford.edu
Luis Canales	WesternGeco	(713) 806-5271	lcanales@houston.westerngeco.slb.com
Jon Claerbout	SEP	(650) 723-3717	jon@sep.stanford.edu
Richard Cook (Co-chair, 2nd year)	Shell	(713) 245-7195	richard.cook@shell.com
Helmut Jakobowicz (Co-chair, 1st year)	Veritas DGC	(44) 1293 443219	helmut_jakobowicz@veritasdgc.com
Stewart Levin	Landmark Graphics	(303) 779-8080	salevin@lgc.com
Simon Spitz	CGG	(281) 646-2502	sspitz@cgg.com

Research Personnel

James G. Berryman received a B.S. degree in physics from Kansas University (Lawrence) in 1969 and a Ph.D. degree in physics from the University of Wisconsin (Madison) in 1975. He subsequently worked on seismic prospecting at Conoco. His later research concentrated on seismic waves in rocks and sediments – at AT&T Bell Laboratories (1978-81) and at Lawrence Livermore National Laboratory (1981-), where he is currently a physicist in the Earth Sciences Division. Continuing research interests include acoustic, seismic, and electrical methods of geophysical imaging and waves in porous media containing fluids. He is a member of ASA, AGU, APS, and SEG.



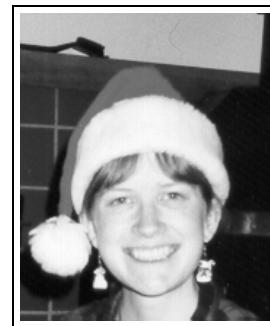
Biondo L. Biondi graduated from Politecnico di Milano in 1984 and received an M.S. (1988) and a Ph.D. (1990) in geophysics from Stanford. SEG Outstanding Paper award 1994. During 1987, he worked as a Research Geophysicist for TOTAL, Compagnie Francaise des Petroles in Paris. After his Ph.D. at Stanford, Biondo worked for three years with Thinking Machines Co. on the applications of massively parallel computers to seismic processing. After leaving Thinking Machines, Biondo started 3DGeo Development, a software and service company devoted to high-end seismic imaging. Biondo is now Associate Professor (Research) of Geophysics and leads SEP efforts in 3-D imaging. He is a member of SEG and EAGE.



Robert Clapp received his B.Sc. (Hons.) in Geophysical Engineering from Colorado School of Mines in May 1993. He joined SEP in September 1993, received his Masters in June 1995, and his Ph.D. in December 2000. He is a member of the SEG and AGU.



Marie Clapp, formerly Marie Prucha, received her B.Sc. in Geophysical Engineering from Colorado School of Mines in May 1997. She joined SEP in September 1997 and received her M.S. in June 1999. She married one of her fellow SEPer in 2001 and finally changed her last name in the summer of 2002. She is currently edging towards a Ph.D. in geophysics. She is a member of SEG.



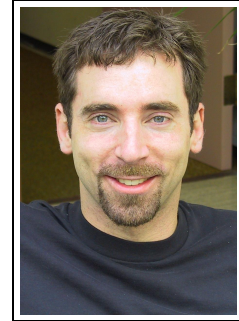
William Curry has been with SEP since 2000. He graduated in 2000 from the University of Alberta with a B.Sc. (Hons.) in Geophysics, and received his M.S. from SEP in 2002. From 1998-1999, he worked as a seismic interpreter with Jet Energy Corporation in Calgary, Canada, and during the summer of 2002 with Marathon Oil in Houston. Bill is a student member of the AGU, CGU, CSEG, EAGE, IEEE, SEG, and SIAM.



Antoine Guitton received a M.Sc. in geophysics from Universite de Strasbourg, France in 1996 and from Stanford University in 2000. Received a "Diplome d'ingenieur de L'Ecole de Physique du Globe de Strasbourg" in 1996. He received the Best Student Paper Award from the SEG in 1999. Assistant research geophysicist at the Institut Francais du Petrole (Paris-1996/97) working on well seismic imaging. Assistant research geophysicist at CGG Houston (1997-98) working on multiples attenuation. He joined SEP in September 1998. Current research topics are nonlinear inversion and noise attenuation. He is a member of the SEG.



Jesse Lomask graduated in 1993 with a B.S. in Geology from Temple University in Philadelphia. He then worked as a field engineer for Anadrill-Schlumberger in the Gulf of Mexico for two years. In 1998, he completed a Masters in Exploration and Development at Stanford which included a summer internship at Mobil Exploration and Producing in Houston. He then worked as a staff geophysicist for Occidental Oil and Gas at Elk Hills, California, where he interpreted recently acquired 3D seismic survey. In the fall of 2001, he returned to Stanford to join SEP.



Daniel A. Rosales received his B.S. in Geophysics from Universidad Simon Bolivar, Venezuela, in 1997. From 1996 to 1998, he worked at PDVSA-INTEVEP S.A. in seismic modeling, 2-D prestack depth migration, and velocity estimation by wave-field downward continuation. In 1998, he joined Simon Bolivar University as an instructor in geophysics. He obtained his M.Sc in geophysics from Stanford University in June 2001, and is currently working towards his Ph.D. in geophysics with the Stanford Exploration Project. He is a member of SEG and AAPG.



Paul Sava received an engineering degree (1995) from the University of Bucharest and an M.Sc. (1998) from Stanford University. He is currently with Stanford Exploration Project working toward a Ph.D. in Geophysics. He worked for Schlumberger GeoQuest (1995-1997) and for BP Upstream Technology Group (2001). He is a recipient of an Honorable Mention in the category Best Paper in Geophysics for "Angle-domain common-image gathers by wavefield continuation methods" published in 2003 and co-authored with Sergey Fomel. He is also a recipient of two SEG awards of merit for best student presentations (1999, 2001). His main research interests are in seismic imaging and velocity analysis using wavefield extrapolation techniques. He is a member of SEG, EAGE, SIAM, AGU, and RSG.



Guojian Shan received his B.Sc. in Mathematics School of Peking University in July, 1998. From 1998 to 2001, he studied in Institute of Computational Mathematics and Scientific/Engineering Computing, Chinese Academy of Sciences (CAS), and received his M.S. in Applied Mathematics in July, 2001. He joined SEP in 2001 and is currently working towards a Ph.D. in geophysics. He is a member of the SEG.



Jeff Shragge graduated in 1998 with a BScH in Honours Physics from Queen's University in Kingston, Canada. After completing a MSc degree in 2001 in teleseismic imaging at the UBC in Vancouver, Canada, he spent 2001 and 2002 working for a small geophysical consulting company based out of Woburn, MA. He joined SEP in 2002, and is working towards a Ph.D. in Geophysics. His main research interest is migration and wavefield inversion. He is a member of SEG and AGU.



Alejandro A. Valenciano received a B.Sc. degree in Physics from Havana University (Cuba) in 1994, and a M.Sc. in Physics from Simon Bolivar University (Venezuela) in 1998. He worked in the Earth Science Department of PDVSA-INTEVEP from 1995 to 2001. He joined SEP to work towards a Ph.D in geophysics in the Fall of 2001.



Ioan Vlad graduated in June 2000 with an Engineer Diploma (5-year degree) in Geophysics from the University of Bucharest, with a thesis on gravity and geodynamical modeling of the lithosphere. He joined SEP in 2000 and is currently working towards a Ph.D. in geophysics at Stanford. He is a member of SEG.



Charlie Wilson received his B.Sc. degree in geology from the University of Arizona in 1998 and a Ph.D. in Geophysics from the University of Colorado, Boulder in 2003. His thesis was on imaging the continental lithosphere using teleseismic earthquakes to solve tectonic problems. He joined the Stanford Geophysics Department as a Post-Doc in December 2003 and is currently working on several projects related to tectonics and earthquake imaging. He is a member of AGU.



SPONSORS OF THE STANFORD EXPLORATION PROJECT, 2003-2004

Amerada Hess Corporation
One Allen Center
500 Dallas St.
Houston, TX 77002
USA
tel: (713) 609-5829
fax: (713) 609-5666
contact: Scott A. Morton
email: morton@hess.com

ChevronTexaco Corporation
935 Gravier St., Room 1668
New Orleans, LA 70112
USA
tel: (504) 592-6153
fax: (504) 592-6742
contact: Ming Zhao
email: ming.zhao@chevrontexaco.com

Aramco Services Company
Saudi Aramco
Geophysics Technology
P.O. Box 750, EXPEC Bldg., X-1370
Dhahran 31311
Saudi Arabia
tel: 966 (3) 874 7262
fax: 966 (3) 874 1020
contact: Mohammed N. Alfaraj
email: mohammed.faraj@aramco.com

ConocoPhillips Inc.
P.O. Box 2197
Lobo 3000
Houston, TX 77252
USA
tel: (281) 293-5696
fax: (281)
contact: Robert M. Habiger
email: Rob.M.Habiger@ConocoPhillips.com

BP America Inc.
200 Westlake Park Blvd., #1018
Houston, TX 77079
USA
tel: (281) 366-3611
fax: (281) 366-5856
contact: John T. Etgen
email: john.etgen@bp.com

Ecopetrol-ICP
Laboratorio de Geofisica
A.A. 4185 Bucaramanga
Colombia
tel: (57) 76 445420
fax: (57) 76 445444
contact: Alfredo Tada
email: atada@ecopetrol.com.co

CGG Americas Inc.
16430 Park Ten Place
Houston, TX 77079
USA
tel: (281) 646-2525
fax: (281) 646-2620
contact: Francois S. Audebert
email: faudebert@cgg.com

ENI - E & P Division
Dept. RIGE
via Unione Europea 3
20097 S. Donato Milanese
Italy
tel: 39 (02) 520 55308
fax: 39 (02) 520 45694
contact: Vittorio De Tomasi
email: vittorio.detomasi@agip.it

SPONSORS OF THE STANFORD EXPLORATION PROJECT, 2003-2004

- | | |
|---|--|
| ExxonMobil Upstream Research Company
Seismic Processing Research
URC-GW3-834A
P.O. Box 2189, 3319 Mercer St.
Houston, TX 77081-2189
USA
tel: (713) 431-6011
fax: (713) 431-6161
contact: Thomas A. Dickens
email: tom.a.dickens@exxonmobil.com | Norsk Hydro Produksjon as
PB 7190
Sandsliveien 90
Bergen, N-5020
Norway
tel: (47) 5599 6861
fax: (47) 5599 6970
contact: Arnfinn Sagehaug
email: Arnfinn.Sagehaug@nho.hydro.com |
| Fairfield Industries Inc.
14100 Southwest Fwy.
Suite 100
Sugar Land, TX 77478
USA
tel: (281) 275-7597
fax: (281) 275-7660
contact: Bill Schneider, Jr.
email: bschneiderjr@fairfield.com | Paradigm Geophysical Corporation
Two Memorial Plaza
820 Gessner, Suite 400
Houston, TX 77024
USA
tel: (713) 393-4979
fax: (713) 393-4801
contact: Orhan Yilmaz
email: yilmaz@ParadigmGeo.com |
| GX Technology Corporation
5847 San Felipe
Suite 3500
Houston, TX 77057-3010
USA
tel: (713) 789-7250
fax: (713) 789-7201
contact: Nick Bernitsas
email: nxb@gxt.com | Petrobras S.A.
Avenida Chile 65, s/1302
Rio de Janeiro
20031-912 RJ
Brazil
tel: 55 (21) 2534-2706
fax: 55 (21) 2534-1076
contact: Carlos A. Cunha Filho
email: ccunha@petrobras.com.br |
| Landmark Graphics Corporation
1805 Shea Center Dr.
Suite 400
Highlands Ranch, CO 80129-2258
USA
tel: (303) 779-8080
fax: (303) 796-0807
contact: Stewart A. Levin
email: salevin@lgc.com | PGS Technology Division
10550 Richmond Ave.
Suite 250
Houston, TX 77042
USA
tel: (713) 735-6322
fax: (713) 532-6774
contact: Ruben D. Martinez
email: ruben.martinez@pgs.com |

SPONSORS OF THE STANFORD EXPLORATION PROJECT, 2003-2004

Shell International E&P Inc.
 3737 Bellaire Blvd.
 P.O. Box 481
 Houston, TX 77001-0481
 USA
 tel: (713) 245-7195
 fax: (713) 245-7339
 contact: Richard W. Cook
 email: richard.cook@shell.com

Deepwater USA, UNOCAL
 14141 Southwest Fwy.
 Sugar Land, TX 77478
 USA
 tel: (281) 287-7481
 fax: (281) 287-5360
 contact: Philip S. Schultz
 email: phil.schultz@unocal.com

Statoil ASA
 Arkitekt Ebbellsvei 10
 Rotvoll
 Trondheim, N-7005
 Norway
 tel: (47) 73584917
 fax: (47) 73584665
 contact: Constantin Gereaa
 email: geco@statoil.com

Veritas DGC Ltd.
 Crompton Way
 Manor Royal Estate
 Crawley, West Sussex RH10 2QR
 England
 tel: 44 (1293) 443219
 fax: 44 (1293) 443010
 contact: Helmut Jakubowicz
 email: Helmut_Jakubowicz@veritasdgc.com

3DGeo Development Inc.
 4633 Old Ironsides Dr.
 Suite 401
 Santa Clara, CA 95054
 USA
 tel: (408) 450 7840, x102
 fax: (408) 450 7809
 contact: Dimitri Bevc
 email: dimitri@3dgeo.com

Weinman GeoScience
 17103 Preston Road
 Suite 200 N.
 Dallas, TX 75248
 USA
 tel: (972) 818-2550
 fax: (972) 818-2553
 contact: Barry L. Weinman
 email: barryw@weinmangeosciencecom

TOTAL E&P USA, Inc.
 800 Gessner
 Suite 700
 Houston, TX 77024
 USA
 tel: (713) 647-3940
 fax: (713) 647-3875
 contact: Henri Calandra
 email: henri.calandra@total.com

WesternGeco
 Houston Technology Center
 10001 Richmond Ave.
 Houston, TX 77042-4299
 USA
 tel: (713) 806-5271
 fax: (713) 689-5757
 contact: Luis L. Canales
 email: LCanales@houston.westerngeco.slb.com

